

AD-A187 261

AN ANALYSIS OF THE MOTION AND EFFECTS OF HAIRPIN
VORTICES(U) LEHIGH UNIV BETHLEHEM PA DEPT OF MECHANICAL
ENGINEERING AND M. T HON ET AL. JUN 87 FH-11

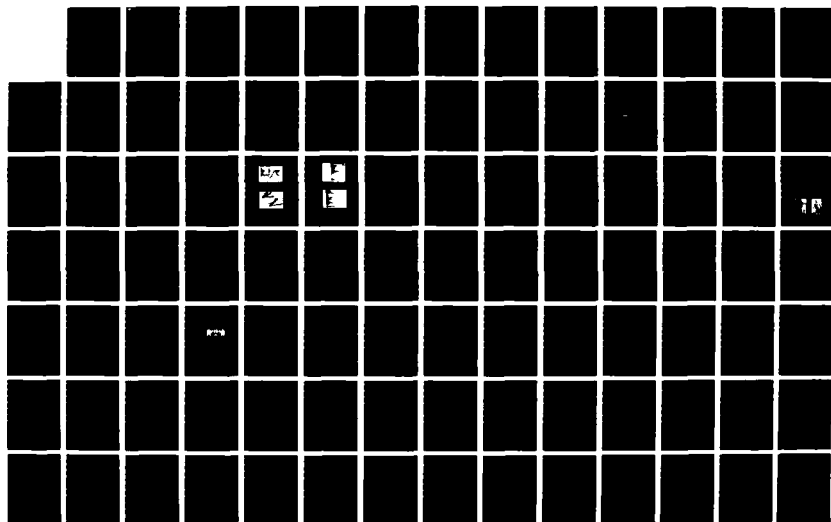
1/3

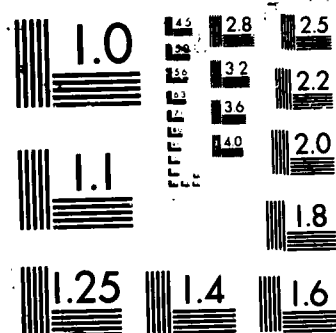
UNCLASSIFIED

AFOSR-TR-87-1389 F49620-85-C-0100

F/G 20/4

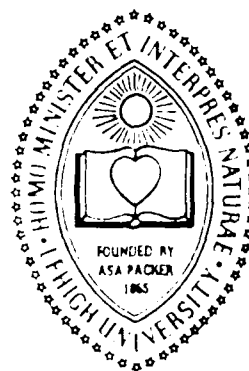
NL





AD-A187 261

Lehigh University



2

AN ANALYSIS OF THE MOTION AND EFFECTS OF HAIRPIN VORTICES

by

T.-L. Hon and J.D.A. Walker

Report FM-11

May 1987

Approved for public release
distribution unlimited.

AIR FORCE OFFICE OF SCIENTIFIC RESEARCH (AFOSR)
NOTICE OF FINANCIAL SUPPORT
THE AIR FORCE OFFICE OF SCIENTIFIC RESEARCH (AFOSR) has provided financial support for this research and is pleased to publish the results.
MATTHEW J. KERBER
Chief, Technical Information Division

Prepared Under Financial Support of the
U.S. Air Force Office of Scientific Research
Contract F49620-85-C-0108

Department of Mechanical Engineering & Mechanics
Lehigh University, Bethlehem, PA 18015

8

UNCLASSIFIED

SECURITY CLASSIFICATION OF THIS PAGE

REPORT DOCUMENTATION PAGE

1a. REPORT SECURITY CLASSIFICATION UNCLASSIFIED			1b. RESTRICTIVE MARKINGS	
2a. SECURITY CLASSIFICATION AUTHORITY			3. DISTRIBUTION/AVAILABILITY OF REPORT UNCLASSIFIED/UNLIMITED	
2b. DECLASSIFICATION/DOWNGRADING SCHEDULE				
4. PERFORMING ORGANIZATION REPORT NUMBER(S) FM-11			5. MONITORING ORGANIZATION REPORT NUMBER(S) AFOSR-TR- 87-1389	
6a. NAME OF PERFORMING ORGANIZATION LEHIGH UNIVERSITY		6b. OFFICE SYMBOL (If applicable)	7a. NAME OF MONITORING ORGANIZATION AFOSR/NA	
6c. ADDRESS (City, State and ZIP Code) DEPT. OF MECHANICAL ENGINEERING, LEHIGH U., BETHLEHEM, PA 18015			7b. ADDRESS (City, State and ZIP Code) BOLLING AFB DC Bk1 410 20332-6448	
8a. NAME OF FUNDING/SPONSORING ORGANIZATION AFOSR		8b. OFFICE SYMBOL (If applicable) NA	9. PROCUREMENT INSTRUMENT IDENTIFICATION NUMBER F49620-85-C-0108	
8c. ADDRESS (City, State and ZIP Code) Bk1 410 BOLLING AIR FORCE BASE, WASHINGTON, D.C. 20332			10. SOURCE OF FUNDING NOS.	
			PROGRAM ELEMENT NO.	PROJECT NO.
			TASK NO.	
			WORK UNIT NO.	
11. TITLE (Include Security Classification) AN ANALYSIS OF THE MOTION AND EFFECTS OF HAIRPIN VORTICES			61102F 2307 A2	
12. PERSONAL AUTHOR(S) HON, THON-LON and WALKER, JAMES DAVID				
13a. TYPE OF REPORT INTERIM		13b. TIME COVERED FROM 7/85 TO 7/87		14. DATE OF REPORT (Yr., Mo., Day) 1987 JUNE
15. PAGE COUNT 205				
16. SUPPLEMENTARY NOTATION				
17. COSATI CODES			18. SUBJECT TERMS (Continue on reverse if necessary and identify by block number)	
FIELD	GROUP	SUB. GR.	TURBULENT BOUNDARY LAYERS, HAIRPIN VORTICES, VISCOUS- INVISCID INTERACTION, FLUID MECHANICS	
19. ABSTRACT (Continue on reverse if necessary and identify by block number)				
<p>Recent experimental studies strongly suggest that the hairpin vortex plays an important, and possibly dominant, role in the dynamics of turbulent flows near walls. In this study, various aspects of the motion of hairpin vortices near solid walls are addressed on a theoretical basis. In particular the following topics are of interest: (1) the nature of the evolution of hairpin vortices in a shear flow; (2) the type of flow induced near a wall by a convected hairpin vortex; (3) the character of the viscous response near a wall to the hairpin vortex motion and (4) the nature of the interaction of two hairpin vortices.</p> <p>In the first phase of this study, a numerical procedure is developed to allow the accurate evaluation of the trajectory of a three-dimensional vortex for vortices having small cores. The integration method is based on a numerical approximation to the Biot-Savart integral; most existing vortex calculation methods have severe stability problems for vortices with small cores. The stability problem is overcome with the present method and</p>				
20. DISTRIBUTION/AVAILABILITY OF ABSTRACT UNCLASSIFIED/UNLIMITED <input checked="" type="checkbox"/> SAME AS RPT. <input type="checkbox"/> DTIC USERS <input type="checkbox"/>			21. ABSTRACT SECURITY CLASSIFICATION UNCLASSIFIED	
22a. NAME OF RESPONSIBLE INDIVIDUAL Dr. JAMES MCMICHAEL			22b. TELEPHONE NUMBER (Include Area Code) 202-767-4935	22c. OFFICE SYMBOL AFOSR/NA

19.

the technique is applied to compute the evolution of convected vortex loops and hairpin vortices, both in a uniform flow and in a shear flow above a wall. For the case of hairpin vortices evolving in a shear flow, a regenerative process is observed wherein secondary hairpin vortices form outboard of the original hairpin vortex in a manner consistent with experimental observations. Calculations for two hairpin vortices, which are initially close to one another in a shear flow show that the vortices interact in a manner so as to reinforce one another. Simulations are carried out to compute the evolution of hydrogen bubble lines as a hairpin vortex passes and these show that such vortices can give rise to wall-layer streaks.

In the second phase of this study, the response is computed for a viscous flow near a wall due to the motion of a hairpin vortex above the wall. The results reveal that a complex, unsteady boundary-layer flow develops near the wall which ultimately develops a very strong local outward growth. The final stages of this development are expected to lead to a boundary-layer eruption and the creation of a secondary hairpin vortex by a strong viscous-inviscid interaction with the outer flow. This mode of regeneration is believed to be a fundamental process wherein new vorticity from the wall region is continually introduced into the turbulent boundary layer.

AN ANALYSIS OF THE MOTION AND EFFECTS
OF HAIRPIN VORTICES

by

T.-L. Hon and J.D.A. Walker

Department of Mechanical Engineering and Mechanics
Lehigh University, Bethlehem, Pennsylvania

Technical Report FM-11

May 1987

Accession For	
NTIS CS&I	<input checked="checked" type="checkbox"/>
DTIC TAB	<input type="checkbox"/>
Unannounced	<input type="checkbox"/>
Justification	
By	
Date	
Av. (1) (2) (3) (4) (5) (6) (7) (8) (9) (10) (11) (12)	
Dist	
A-1	

Distribution of this Document is Unlimited

ABSTRACT

Recent experimental studies strongly suggest that the hairpin vortex plays an important, and possibly dominant, role in the dynamics of turbulent flows near walls. In this study, various aspects of the motion of hairpin vortices near solid walls are addressed on a theoretical basis. In particular the following topics are of interest: (1) the nature of the evolution of hairpin vortices in a shear flow; (2) the type of flow induced near a wall by a convected hairpin vortex; (3) the character of the viscous response near a wall to the hairpin vortex motion and (4) the nature of the interaction of two hairpin vortices.

In the first phase of this study, a numerical procedure is developed to allow the accurate evaluation of the trajectory of a three-dimensional vortex for vortices having small cores. The integration method is based on a numerical approximation to the Biot-Savart integral; most existing vortex calculation methods have severe stability problems for vortices with small cores. The stability problem is overcome with the present method and the technique is applied to compute the evolution of convected vortex loops and hairpin vortices, both in a uniform flow and in a shear flow above a wall. For the case of hairpin vortices evolving in a shear flow, a regenerative process is observed wherein secondary hairpin vortices form outboard of the original hairpin vortex in a manner consistent with experimental observations. Calculations for two

hairpin vortices, which are initially close to one another in a shear flow, show that the vortices interact in a manner so as to reinforce one another. Simulations are carried out to compute the evolution of hydrogen bubble lines as a hairpin vortex passes and these show that such vortices can give rise to wall layer streaks.

In the second phase of this study, the response is computed for a viscous flow near a wall due to the motion of a hairpin vortex above the wall. The results reveal that a complex, unsteady boundary-layer flow develops near the wall which ultimately develops a very strong local outward growth. The final stages of this development are expected to lead to a boundary-layer eruption and the creation of a secondary hairpin vortex by a strong viscous-inviscid interaction with the outer flow. This mode of regeneration is believed to be a fundamental process wherein new vorticity from the wall region is continually introduced into the turbulent boundary layer.

ACKNOWLEDGEMENTS

The authors wish to thank the Air Force Office of Scientific Research for providing financial support under the contract F49620-85-C-0108. The present investigation is part of a larger overall program which is aimed at developing an understanding of the physical processes that occur in turbulent boundary-layer flows. The contract monitor during the period of this study was Dr. James McMichael; the authors would like to express their appreciation to Dr. McMichael for his encouragement during the course of this work.

The authors would also like to thank Mrs. Constance Weaver for her patient and careful typing of this report.

TABLE OF CONTENTS

	Page
ABSTRACT	i
ACKNOWLEDGEMENTS	iii
TABLE OF CONTENTS	iv
LIST OF FIGURES	vii
CHAPTER 1 - INTRODUCTION	1
1.1 Background	1
1.2 Experimental Studies	3
1.3 Theoretical Background	12
1.3.1 Inviscid Vortex Dynamics	12
1.3.2 Influence of Convecting Vortices on Viscous Flow Near Walls	17
1.4 Summary and Overview	20
CHAPTER 2 - THE VORTEX CALCULATION METHOD	25
2.1 Introduction	25
2.2 The Biot-Savart Law	25
2.3 Previous Calculation Methods	29
2.4 An Instability Associated With the Moore-Rosenhead Method	38
2.5 Present Method	41
CHAPTER 3 - THE INFLUENCE OF MOVING VORTEX LOOPS	48
3.1 INTRODUCTION	48

	Page
3.2 The Trajectory of Vortex Loops	49
3.3 Simulation of Hydrogen Bubble Lines	52
3.4 Calculated Results	57
3.5 Conclusions	69
CHAPTER 4 - THE EVOLUTION OF A HAIRPIN VORTEX	75
4.1 Introduction	75
4.2 Equation of Motion	76
4.3 Numerical Methods	83
4.4 The Evolution of a Hairpin Vortex in Stagnant Flow	83
4.5 The Evolution of a Hairpin Vortex in Shear	88
4.6 Discussion	94
4.7 Influence of a Hairpin Vortex on Dye Markers	98
4.8 The Velocity Signature of a Hairpin Vortex	108
4.9 Interaction of Two Hairpin Vortices	120
CHAPTER 5 - THE BOUNDARY LAYER INDUCED BY A MOVING HAIRPIN VORTEX	132
5.1 Introduction	132
5.2 The Inviscid Velocity Distribution	133
5.3 The Boundary Layer Problem	141
5.4 The Transformed Boundary-Layer Problem	148
5.5 Numerical Methods	154

	Page
5.6 Calculated Results	158
5.7 Conclusions	187
CHAPTER 6 - CONCLUSIONS	190
REFERENCES	194
APPENDIX A	200
APPENDIX B	203

LIST OF FIGURES

		Page
Figure 1.1	- A schematic sketch of dye collected into low-speed streaks in a turbulent flow near a wall.	4
Figure 1.2	- Schematic sketch of wall-layer bursting process when visualized by dye injection through the wall.	5
Figure 1.3	- Effect of Reynolds number on eddies (a) very slow Re (vortex loops); (b) low-moderate Re (horseshoes); (c) moderate-high Re (hairpins).	9
Figure 1.4	- Side view comparison between hairpin vortex and turbulent boundary layer patterns.	13
Figure 1.5	- Top view comparison between hairpin vortex and turbulent boundary layer patterns.	14
Figure 1.6	- Schematic diagram of two methods of hairpin vortex regeneration.	22
Figure 2.1	- A portion of a vortex filament (Shown for $\Gamma < 0$).	27
Figure 2.2	- Trajectory of a vortex ring (viewed from the side) approaching a wall; the results are computed using Moore's method (1972) and show the development of numerical instability.	40
Figure 2.3	- Behavior of integrand in the first integral in equation (2.14) for (a) 100 and (b) 200 total points.	42
Figure 2.4	- Comparison of local approximation to the integrand $R(s, s_0)$ to the exact answer for a ring vortex.	44
Figure 2.5	- Results for the trajectory of a vortex ring (viewed from the side) approaching a wall using the present method.	46

	Page
Figure 3.1 - Initial vortex ring configuration.	50
Figure 3.2 - Side view of the trajectory of vortex loop convected with speed $V = 5$ ($\alpha=135^\circ$).	53
Figure 3.3 - Trajectory of a vortex ring moving normal to the wall.	54
Figure 3.4 - Schematic diagram of hydrogen bubble line simulation.	55
Figure 3.5 - Side view of the trajectory of a vortex ring convected with speed $V = 6$ ($\alpha=0^\circ$).	58
Figure 3.6 - Temporal development of the simulated hydrogen bubble lines due to a convected ring ($V=6$).	59
(a) $t=.2$ and (b) $t=.5$	59
(c) $t=1.$ and (d) $t=2.$	60
Figure 3.7 - Side view of the development of simulated hydrogen bubble lines due to a convected ring ($V=6$).	62
Figure 3.8 - End view of the development of simulated hydrogen bubble lines due to a convected ring ($V=6$).	63
Figure 3.9 - Side view of the trajectory of a vortex ring convected with speed $V=3$.	64
Figure 3.10 - Temporal development of the simulated hydrogen bubble lines due to a convected ring ($V=3$).	65
(a) $t=.2$ and (b) $t=.5$	65
(c) $t=1.$ and (d) $t=2.$	66
Figure 3.11 - Side view of the development of simulated hydrogen bubble lines due to a convected ring ($V=3$).	67

	Page
Figure 3.12 - End view of the development of simulated hydrogen bubble lines due to a convected ring ($V=3$).	68
Figure 3.13 - Side view of the trajectory of a vortex loop convected with speed $V=10$ ($\alpha=135^\circ$).	70
Figure 3.14 - Temporal development of the simulated hydrogen bubble lines due to a convected vortex loop ($V=10$).	71
(a) $t=.2$ and (b) $t=.5$	71
(c) $t=1.$ and (d) $t=2.$	72
Figure 3.15 - Side view of the development of simulated hydrogen bubble lines due to a convected vortex loop with speed $V=10$ ($\alpha=135^\circ$).	73
Figure 3.16 - End view of the development of simulated hydrogen bubble lines due to a convected vortex loop with speed $V=10$ ($\alpha=135^\circ$).	74
Figure 4.1 - Vortex motion above a wall.	77
Figure 4.2 - Temporal development for a hairpin vortex in a stagnant flow. Case 1 ($\alpha=45^\circ$, $A=0.5$, $\beta=20$); the vortex position is plotted every 40 time steps ($\Delta t=0.0002$).	85
Figure 4.3 - Temporal development for a hairpin vortex in a stagnant flow. Case 2 ($\alpha=45^\circ$, $A=1.$, $\beta=20$); the vortex position is plotted every 20 time steps ($\Delta t=0.0002$).	87
Figure 4.4 - Temporal development for a hairpin vortex in a stagnant flow. Case 3 ($\alpha=0^\circ$, $A=0.5$, $\beta=20$); the vortex position is plotted every 30 time steps ($\Delta t=0.0002$).	89

	Page
Figure 4.5 - Temporal development for a hairpin vortex in a shear flow ($V=50$). Case 4 ($\alpha=45^\circ$, $A=0.5$, $\beta=20$); the vortex position is plotted every 20 time steps ($\Delta t=0.0005$).	91
Figure 4.6 - Temporal development for a hairpin vortex in a shear flow ($V=150$). Case 5 ($\alpha=45^\circ$, $A=0.5$, $\beta=20$); the vortex position is plotted every 20 time steps ($\Delta t=0.0003$).	93
Figure 4.7 - Temporal development for a hairpin vortex in a shear flow ($V=250$). Case 6 ($\alpha=45^\circ$, $A=0.5$, $\beta=20$); the vortex position is plotted every 30 time steps ($\Delta t=0.0002$).	95
Figure 4.8 - Continuation of integration for Case 6; the vortex position is plotted every 15 time steps ($\Delta t=0.0002$).	96
Figure 4.9 - Flow visualization sequence reproduced from Acalar and Smith (1984) showing a hairpin vortex moving toward the observer; the visualization is accomplished with a hydrogen bubble wire.	99
Figure 4.10 - The simulated hydrogen bubble lines due to a convected hairpin vortex (Case 6) at $t = 0.3$; initial bubble lines were located at $y = .8$.	102
Figure 4.11 - The simulated hydrogen bubble lines due to a convected hairpin vortex (Case 6) at $t = 0.6$; initial bubble lines were located at $y = .8$.	103
Figure 4.12 - The simulated hydrogen bubble lines due to a convected hairpin vortex (Case 6) at $t = .07$; initial bubble lines were located at $y = .8$.	104
Figure 4.13 - The simulated hydrogen bubble lines due to a convected hairpin vortex (Case 6) at $t = .03$; initial bubble lines were located at $y = .7$.	105

	Page
Figure 4.14 - The simulated hydrogen bubble lines due to a convected hairpin vortex (Case 6) at $t = .06$; initial bubble lines were located at $y = .7$.	106
Figure 4.15 - The simulated hydrogen bubble lines due to a convected hairpin vortex (Case 6) at $t = .07$; initial bubble lines were located at $y = .7$.	107
Figure 4.16(a) - Side view of hairpin vortex (at $t = 0.1$ for Case 4 of Section 4.5) and instantaneous streamwise measuring locations.	109
Figure 4.16(b) - Instantaneous streamwise velocity fluctuations at stations indicated in Figure 4.16(a).	110
Figure 4.16(c) - Instantaneous streamwise velocity profiles at stations indicated in Figure 4.16(a).	111
Figure 4.17(a) - Side view of the developing hairpin vortex for Case 4 at various times.	113
Figure 4.17(b) - Instantaneous velocity fluctuations of the measuring station indicated in Figure 4.17(a); note the shifted origins.	114
Figure 4.17(c) - Instantaneous velocity profiles at the measuring station indicated in Figure 4.17(a).	115
Figure 4.18(a) - Side view of hairpin vortex (at $t = 0.78$ for Case 6 of Section 4.5) and instantaneous streamwise measuring locations.	116
Figure 4.18(b) - Instantaneous streamwise velocity fluctuations at stations indicated in Figure 4.18(a).	117
Figure 4.19(a) - Side view of the developing hairpin vortex for Case 6 at various time.	118

	Page
Figure 4.19(b) - Instantaneous velocity fluctuations at the measuring station indicated in Figure 4.19(a); note the shifted origins.	119
Figure 4.20 - Profiles of (a) velocity and (b) velocity fluctuation of hairpin vortex over a cycle as obtained from hydrogen bubble flow visualization pictures on plane of symmetry of the hairpin vortex.	121
Figure 4.21 - Initial configuration for two hairpin vortices in shear.	124
Figure 4.22 - Development of the two hairpin vortices at $t = .01$.	125
Figure 4.23 - Development of the two hairpin vortices at $t = .02$.	126
Figure 4.24 - Development of the two hairpin vortices at $t = .015$.	129
Figure 4.25 - Development of the two hairpin vortices at $t = .04$.	130
Figure 4.26 - Development of the two hairpin vortices at $t = .048$.	131
Figure 5.1 - Inviscid streamwise velocity on the symmetry plane near the wall induced by a moving hairpin vortex in shear.	137
Figure 5.2 - Schematic sketch of a hairpin vortex after deformation in a shear flow.	139
Figure 5.3 - Temporal development of the spanwise velocity distribution near the symmetry plane induced by the moving hairpin vortex in shear.	140
Figure 5.4 - Inviscid streamwise velocity distribution on the symmetry plane near the wall induced by a moving hairpin vortex in a stagnant flow.	142
Figure 5.5 - Temporal development of the spanwise velocity distribution near the symmetry plane induced by a moving hairpin vortex in a stagnant flow.	143

	Page
Figure 5.6 - Temporal evolution of θ_1 and θ_2 , the decomposition of θ_∞ .	147
Figure 5.7(a) - Streamlines in the symmetry plane at $t = 0.001$.	160
Figure 5.7(b) - Lines of constant θ at $t = 0.001$.	161
Figure 5.7(c) - Limiting surface streamlines in the xz plane at $t = 0.001$.	162
Figure 5.8(a) - Streamlines in the symmetry plane at $t = 0.01$.	164
Figure 5.8(b) - Lines of constant θ at $t = 0.01$.	165
Figure 5.8(c) - Limiting surface streamlines in the xz plane at $t = 0.01$.	166
Figure 5.9(a) - Streamlines in the symmetry plant at $t = 0.02$.	168
Figure 5.9(b) - Lines of constant θ at $t = 0.02$.	169
Figure 5.9(c) - Limiting surface streamlines in the xz plane at $t = 0.02$.	170
Figure 5.10(a) - Streamlines in the symmetry plane at $t = 0.03$.	171
Figure 5.10(b) - Lines of constant θ at $t = 0.03$.	172
Figure 5.10(c) - Limiting surface streamlines in the xz plane at $t = 0.03$.	173
Figure 5.11(a) - Streamlines in the symmetry plane at $t = 0.04$.	174
Figure 5.11(b) - Lines of constant θ at $t = 0.04$.	175
Figure 5.11(c) - Limiting surface streamlines in the xz plane at $t = 0.04$.	176
Figure 5.12(a) - Streamlines in the symmetry plane at $t = 0.05$.	178
Figure 5.12(b) - Lines of constant θ at $t = 0.05$.	179
Figure 5.12(c) - Limiting surface streamlines in the xz plane at $t = 0.05$.	180

	Page
Figure 5.13(a) - Streamlines in the symmetry plane at $t = 0.06$.	181
Figure 5.13(b) - Lines of constant θ at $t = 0.06$.	182
Figure 5.13(c) - Limiting surface streamlines in the xz plane at $t = 0.06$.	183
Figure 5.14(a) - Streamlines in the symmetry plane at $t = 0.07$.	184
Figure 5.14(b) - Lines of constant θ at $t = 0.07$.	185
Figure 5.14(c) - Limiting surface streamlines in the xz plane at $t = 0.07$.	186
Figure 5.15 - Temporal development of displacement thickness.	188

CHAPTER I

INTRODUCTION

1.1 Background

Most flows occurring in nature and in engineering application are turbulent. The atmospheric boundary layer as well as ocean currents are generally in turbulent motion. The major portion of boundary layers which form and grow on such devices as turbine blades and aircraft wings are turbulent. Turbulence is usually present in most channel and pipe flows as well as in most combustion processes. The study and prediction of turbulent flow phenomena is thus an extremely important area of basic research.

Generally turbulence cannot sustain itself without some source of energy. For incompressible flows, the production of new turbulence is generally observed to be associated with the presence of shear in the mean flow; the most common location where mean shear occurs is near solid walls where the flow must be reduced to relative rest to satisfy the no slip condition. The role of shear in the production process appears to be important for if turbulence arrives in an environment where there is no shear (or some other maintenance mechanism), it decays. Unfortunately, the production process is not well understood. A common view is that vortex motions play an important role in the transport of turbulence; the large scale eddies are thought to extract energy from the mean flow

(see for example Tennekes and Lumley, 1972, p. 41 or Hinze, 1975, p. 74) and then to transfer energy to smaller scale eddies through vortex stretching. Ultimately the smaller eddies dissipate energy into heat through viscous dissipation. Although this statement of the processes in turbulence is commonly accepted, it does not shed much light on the complex dynamics that occur in the production mechanisms near walls.

In recent years, there has been considerable experimental interest in the structure of turbulent boundary-layer flow near walls and it has become apparent that such flows are not comprised of random fluctuations in velocity; rather an ordered (but complex) cyclic sequence of events appears to take place in the flow near the wall. This apparently deterministic sequence is usually referred to as the coherent structure or the coherent behavior of the wall-layer flow; here the wall layer is understood to imply that portion of a turbulent flow between the wall and locations where the mean profile is logarithmic in y , the distance from the wall. There are two features which are observed to dominate the dynamics of the wall-layer flow, namely the low speed streaks and the bursting phenomenon. When a visualization medium, such as dye or hydrogen bubbles, is introduced into the wall-layer flow it is observed to collect into low-speed streaks near the wall which are aligned in the streamwise direction and which persist over relatively long distances; the streaks are referred to as "low-speed" because the streamwise velocity near the streaks is generally observed to be

less than the velocity distribution corresponding to the mean profile. A schematic sketch of the observed phenomenon is given in Figure 1.1.

The second important feature of the wall-layer flow is the bursting process wherein the wall-layer fluid is observed to erupt, at isolated spanwise and streamwise locations, into the outer region of the flow. The event is observed to initiate near a wall layer streak and in its primary stages is characterized by a lifting of the low-speed streak from the wall; an apparently oscillatory behavior then starts to develop in the streak and then a violent chaotic eruption of wall-layer fluid is observed. A schematic diagram of the various stages of the process, as viewed from the side and which is adapted from Kline (1978), is shown in Figure 1.2.

The physical cause of the wall-layer streaks and the bursting phenomenon is not well understood. In this study, the possibility that the observed effects are due to convected vortex motion will be considered. In particular the major thrust of this study is an investigation of the cause and effect relationships generated by a convecting hairpin vortex.

1.2 Experimental Studies

It is commonly believed that the vortex motions that are clearly observable in boundary-layer turbulence, play an important role in the dynamics of the turbulence and a variety of model vortex

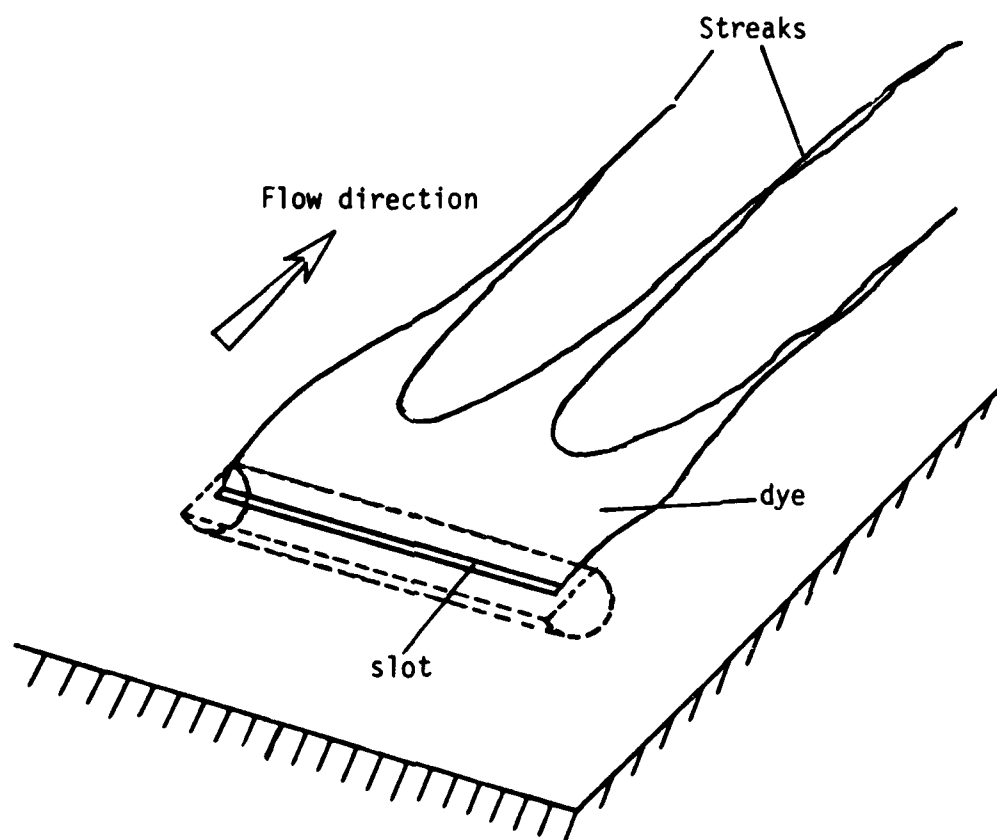


Figure 1.1 - A schematic sketch of dye collected into low-speed streaks in a turbulent flow near a wall.

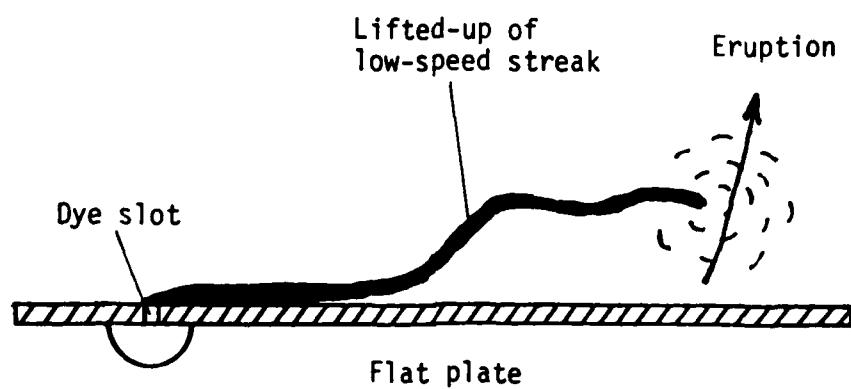


Figure 1.2 - Schematic sketch of wall-layer bursting process when visualized by dye injection through the wall.

motions have been suggested. In an early study by Nychas, Hershey and Brodkey (1973) it was suggested that (what appeared to be) large transverse convecting vortices in the outer layer were somehow associated with the bursting events near the wall. Bakewell and Lumley (1967) and later Blackwelder (1978) and Blackwelder and Eckelmann (1979) suggested that long counter-rotating streamwise vortex pairs are an important feature in the time-dependent flow near the wall. Falco (1981,1982) has proposed that convected ring-like vortices are an important dynamical feature of turbulent boundary layers. Perhaps the most popular vortex model is the hair-pin vortex which has been proposed as a basic feature of wall-layer turbulence by Theodorsen (1952), Willmarth and Tu (1967), Kline et al (1967), Offen and Kline (1973,1975), Smith (1978), Wallace (1982), Head and Bandyopadhyay (1981), Perry, Lim and Teh (1981), Perry and Chong (1982), Smith and Metzler (1983) and Acarlar and Smith (1984, 1987a, 1987b) among others.

In the study by Nychas, Hershey and Brodkey (1973), small solid particles were suspended in a water flow and the particle motions were photographed using a high-speed motion-picture camera which moved in the flow direction. It is difficult to get a clear three-dimensional picture of the sequence of events with this approach. Nevertheless, Nychas et al (1973) observed what appeared to be transverse vortices convecting in the outer layer. Such vortices induced a decelerated flow near the wall followed by a

region of acceleration. It was concluded, on the basis of the visual observations, that ejection events at the wall were closely associated with the presence of transverse vortices in the outer flow; the clear suggestion of this work is that the transverse vortices induce conditions in the wall region that cause an ejection. A similar mechanism is suggested by the studies of Falco (1981,1982) and Falco and Wiggert (1980); in these experiments, the flow structure of the turbulent boundary layer was visualized by using smoke in air and compact vortex structures, which appeared to be similar to vortex rings, were observed; the ring-like vortices were believed to induce eruptions of the wall-layer flow. Detailed experiments involving vortex rings moving toward a wall by Cerra and Smith (1982), Walker, Smith, Cerra and Doligalski (1987) and Didden and Ho (1986) confirm that vortex rings moving toward a wall do induce eruptive behavior and the production of secondary vortices through an unsteady separation effect with the boundary layer near the wall. This mechanism will be discussed in more detail in Section 1.3.

Another picture of the flow near the wall in turbulent boundary layer has been proposed by Bakewell and Lumley (1967); these authors examined the near-wall region of a pipe flow and on the basis of measurements with a hot-film anemometer concluded that the most energetic velocity fluctuations were associated with pairs of counter-rotating vortices. Bakewell and Lumley (1967) suggested

that the dominant structures in the wall-layer region consist of randomly distributed counter-rotating vortices which are elongated in the streamwise direction. A similar model was proposed by Blackwelder and Eckelmann (1979) who suggested that long streamwise vortices are present in the wall-layer flow; in this model, the role of the counter-rotating vortex pairs is to pump low momentum fluid away from the wall and to lead to the formation of the low-speed streaks. It was conjectured that the process terminates with the arrival of a sweep of high speed flow from the outer region which was supposed to lead to a highly inflectional streamwise profile near the low-speed streaks. The inflectional velocity profile is believed to be a highly unstable situation and the bursting event was considered to be the outcome of the instability. This type of model is purely kinematical and assumes a great deal about instability in a time-dependent evolving flow field; apart from these difficulties, the physical origin of the counter-rotating vortex pairs was not explained.

A third type of vortex structure that has often been proposed as a basic feature in turbulent boundary-layer flows is the hairpin vortex. A variety of terms have been used to describe hairpin vortices; Head and Bandyopadhyay (1981) have pointed out that these terminologies really imply the same vortex structure but at different Reynolds numbers. The classification scheme taken from their paper is reproduced in Figure 1.3, which simply implies that

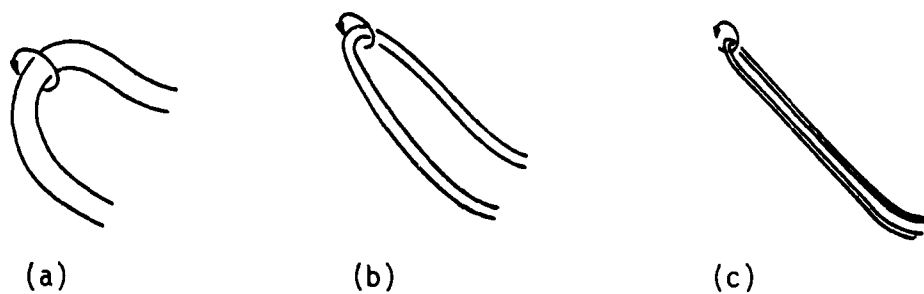


Figure 1.3 - Effect of Reynolds number on eddies
(a) very slow Re (vortex loops);
(b) low-moderate Re (horseshoes);
(c) moderate-high Re (hairpins).

at higher Reynolds numbers the vorticity tends to become more tightly concentrated in smaller and smaller core regions. Head and Bandyopadhyay (1981) carried out a series of wind tunnel flow visualization experiments using smoke; their results indicate that the turbulent boundary layer consists of a "forest" of hairpin vortices which continually stretch in shear and appear to be inclined at a characteristic angle of 45° to the wall. A similar picture has also been suggested by Perry and Chong (1982) who conjectured that the structure of the turbulent boundary layer is dominated by a systematic hierarchy of hairpin vortices. There are some appealing features about this conjectured type of structure but the physical picture appears incomplete. For example, there is no explanation concerning the processes leading to the production of new vorticity from the wall region; in addition the notion of a series of hairpin vortices which continually stretch and intertwine in shear does not appear to lead to a complete and an entirely satisfactory pattern of evolution.

Recently, Smith (1984) has proposed a conceptual model of the physical processes that occur near the wall in a turbulent boundary layer which was based upon extensive flow visualization experiments as well as a previous model by Offen and Kline (1975). In the latter study, it was suggested that lift-up of the low speed streaks (which appeared to be a precursor of the bursting process) was associated with the temporary imposition of an adverse pressure gradient on the

wall layer by a convected disturbance. Smith (1984) also adopts this view and suggests that the effect of the local adverse pressure gradient is to induce an inflectional behavior in the streamwise velocity profile near the interface of the streak and the high speed outer region fluid. The instantaneous inflectional profile is assumed to be unstable and to give rise to a series of roll-ups into a number of hairpin vortices. As the hairpin vortices are convected away from the surface, a strong vortex stretching process in the streamwise direction cause intensification in the legs of the hairpin vortices; thus, the counter-rotating legs of the hairpin vortices act to reinforce the streak, thus creating an appearance of streak persistence. The bursting process is suggested to be due to the breakup of the low-speed streak which is lifted by the counter-rotating legs of the hairpin; rapid ejection may be due to the viscous effects induced by the local streamwise adverse pressure associated with the moving head of the hairpin vortex.

In order to observe the motion of hairpin vortices in a controlled environment, Acarlar and Smith (1984, 1987a, 1987b) carried out a series of experiments where hairpin vortices were artificially generated in a laminar boundary-layer flow on a plane surface. The hairpin vortices were synthetically generated by shedding from a hemispherical protuberance on the plane wall. Flow visualization was carried out using hydrogen bubble wires and it was determined that convecting hairpin vortices produce flow patterns which are very

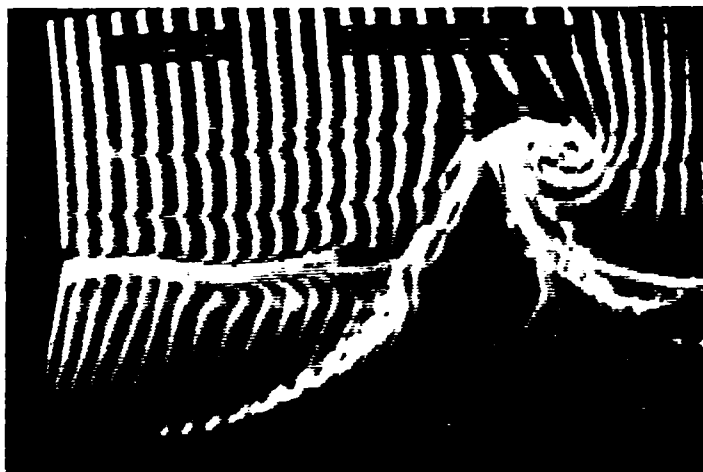
similar to those observed in the near-wall region of a turbulent boundary layer. In Figure 1.4, which is reproduced from Acarlar and Smith (1984, 1987a), the bubble line patterns generated from a bubble wire placed normal to the wall may be observed for (a) a convecting hairpin vortex in a laminar boundary-layer flow and (b) in a fully turbulent boundary layer. In Figure 1.4, the quantity $X/R = 20$ indicates that the flow pattern is at a streamwise distance equal to 20 radii downstream of the hemisphere; Re_θ is the Reynolds number of the turbulent boundary-layer flow based on momentum thickness. In Figure 1.5, the bubble wire was placed in an orientation across the span of the flow and close to the wall. It may be observed that the convecting hairpin vortices produce a "streaky" structure in the flow near the wall which is similar to the typical patterns observed in turbulent boundary layers. In addition to the flow visualization studies, Acarlar and Smith (1984, 1987a) also carried out quantitative measurements in the region downstream of the hemisphere; it was found that the measurements were very similar to those typically obtained in a fully turbulent boundary layer.

It is reasonable to conclude from the experimental evidence available that the hairpin vortex is a potentially important flow structure in turbulent flows near walls and worthy of further study.

1.3 Theoretical Background

1.3.1 Inviscid Vortex Dynamics

In recent times, there has been an increasing interest in the

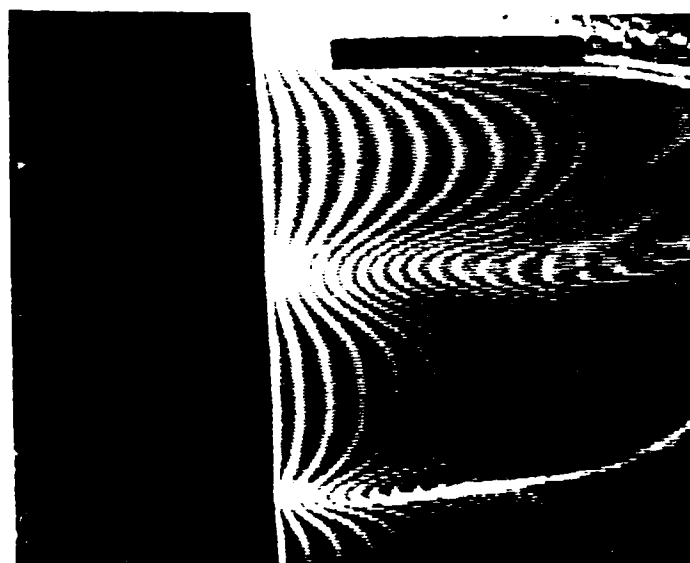


(a) Hairpin vortex, $X/R = 20$

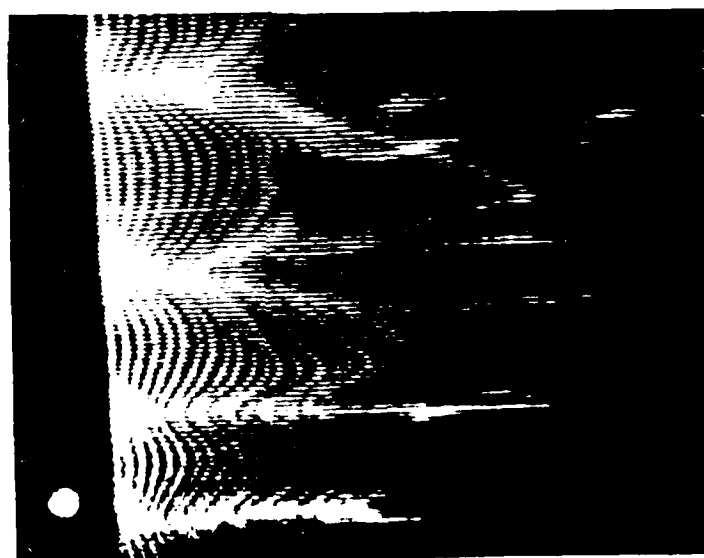


(b) Turbulent boundary layer, $Re = 2200$

Figure 1.4 - Side view comparison between hairpin vortex and turbulent boundary-layer patterns.



(a) Hairpin vortex, $X/R = 20$, $y_{\text{wire}}/R = 0.08$



(b) Turbulent boundary layer, $Re = 2200$, $y_{\text{wire}}^+ = 5$

Figure 1.5 - Top view comparison between hairpin vortex and turbulent boundary-layer patterns.

development of numerical algorithms to calculate three-dimensional vortex motion. The general approach may be described as follows. For a given vortex filament and a given initial configuration, a discretization is accomplished by placing a number of nodes on the filament; some approximation to the Biot-Savart integral (Batchelor, 1967) is then used to compute the local instantaneous velocity induced on a node by the other portions of the vortex. The motion of each node is then computed numerically thus giving the position of the vortex filament at the next time step. Such calculations are time consuming, notoriously unstable and difficult to carry out with good accuracy. One major difficulty is that a vortex filament having a core of zero cross-sectional area induces an infinite velocity on itself for any curved portion of the vortex; the infinitesimally thin vortex is therefore not a self-consistent dynamical model and in any computational algorithm it is necessary to take into account the fact that the vortex has a core of finite thickness. In addition it is, in principle, necessary to account for motions within the core and how such motions can influence the overall motion of the vortex.

The theoretical problem is immediately evident when the Biot-Savart integral over all space is replaced by a line integral along the instantaneous location of the vortex filament; a singularity occurs in the integrand at any point on the vortex filament where an evaluation of the velocity induced by the vortex is desired

(this location will be subsequently referred to as the field point). This singularity arises as a direct consequence of neglecting the thickness of the vortex core. Over the years, a variety of approaches have been proposed to deal with this difficulty and these will be discussed in more detail in Section 2.3; only a brief summary will be given here.

The first attempts at the calculation of vortex motion in three-dimensions were by Hama (1962) and Arms and Hama (1965). In their "localized induction concept", a Taylor series was used to represent the integrand near the field point; the integration was carried out only over a short portion of the filament and the contribution of the rest of the vortex was ignored. Crow (1970) introduced the "cut-off method" wherein a small piece of the Biot-Savart integral is omitted from the integration thereby bypassing the singularity. In subsequent studies, Bliss (1970) and Moore and Saffman (1972) put the "cut-off" procedure on a firmer basis by selecting the cut-off length so that the computational algorithm agreed with known exact results for a translating circular vortex ring. The "cut-off method" is somewhat inconvenient from a computational point of view and an alternative (and similar) approach was adopted by Moore (1972). In this technique, a small parameter is artificially introduced in the denominator of the integrand to remove the singularity; the small parameter is selected so that the procedure gives correct results for the circular vortex ring.

Another computational approach is due to Leonard (1975,1979) and Widnall, Bliss and Zelay (1971). In this technique, the self-induced velocity of a vortex filament is computed through numerical integration of the Biot-Savart integral except at the field point and the two adjacent nodal points on the vortex. The contribution due to these three points is estimated by fitting a vortex ring locally and by estimating the contribution to velocity due to the arc from known exact results for the vortex ring. Note however that Liu, Krause and Ting (1985) point out that this process does not necessarily give the correct direction of self-induced motion of the arc surrounding the field point.

In recent times, Callegari and Ting (1978) have used the method of matched expansions to investigate the dynamics of vortex motion in three dimensions in the limit of vanishing viscosity; (see also Bliss, 1970). These authors were able to determine the possible form of a viscous solution in the vortex core and to match this to an outer inviscid solution described by the solution of Biot-Savart integral. It was demonstrated that the apparent singularity in the Biot-Savart integral is removed by this procedure and a computational algorithm was developed to compute the evolution of vortex motion. Note, however, that the method at present is restricted to closed vortex loops.

1.3.2 Influence of Convecting Vortices on Viscous Flow Near Walls

As a vortex is convected over a wall, it induces an unsteady pressure gradient on the viscous flow near the wall. The effect of the vortex motion has been studied by Walker (1978), Doligalski et al (1980), Doligalski and Walker (1984), Ersoy and Walker (1985, 1986) and Walker et al (1987) for a variety of two- and three-dimensional boundary-layer flows. In general, these studies show that a moving vortex induces a region of adverse pressure gradient in the flow near the wall which in turn drives an unsteady boundary-layer separation effect. In the cited studies, it emerges that a wide variety of complex separation effects occur; however all situations have one feature in common. Eventually the boundary-layer flow near the wall develops strong outward local growth which ultimately leads to a strong inviscid-viscous interaction with the outer flow. Specific physical situations studied are as follows.

The unsteady boundary layer due to rectilinear vortex in an otherwise stagnant fluid above a plane wall was considered by Walker (1978). Inviscid theory predicts that the vortex will convect at constant height and speed in the velocity field of the image vortex. However, a short time after the initiation of the motion, a secondary eddy of opposite rotation to the parent vortex occurs in the unsteady boundary-layer flow near the wall. The numerical integrations show that strong and accelerating boundary-layer growth occurs near the secondary eddy and strongly suggest that the boundary-layer will erupt into the outer inviscid flow

region. The experiments of Harvey and Perry (1972) confirm that this is the case and show that the inviscid-viscous interaction consists of the ejection of the secondary eddy from the boundary layer.

The boundary layer due to a two-dimensional vortex convected in a uniform flow and a shear flow above a plane wall was considered by Doligalski and Walker (1984) and Doligalski et al (1980) respectively. At low convection speeds, the formation of a secondary eddy, of opposite rotation to the parent vortex, was observed in the boundary-layer flow along with explosive outward boundary-layer growth near the eddy. At higher convection speeds, secondary eddies did not occur but a narrow band of strong growth was observed in the calculations which was conjectured to ultimately give rise to an interaction with the outer flow. On the basis of these results Doligalski et al (1980) proposed a regenerative mechanism for turbulent flows near walls. According to this process, the viscous flow near the wall begins to respond to the motion of a convecting parent vortex above the wall giving rise to accelerating growth in a narrow band behind the moving parent vortex. As time increases, the upwelling fluid penetrates the inviscid flow region above the wall to an increasing extent; as the rising fluid penetrates the cross flow above the wall, it is ultimately overturned in a strong inviscid-viscous interaction leading to a roll-up into a secondary vortex.

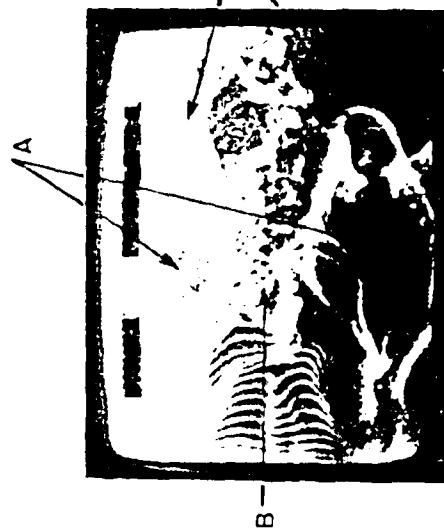
The wall-layer model of Blackwelder and Eckelmann (1979) is based on the assumption that counter-rotating vortex pairs play an important role in the dynamics of the near-wall flow. Ersoy and Walker (1985,1986) have computed the viscous flow development near a wall due to counter-rotating vortex pairs above the wall. A number of cases were considered and although a variety of unusual complex separation phenomena were observed, the boundary-layer flow evolved toward an eruptive state in all cases. When the sense of rotation of the vortices is such that the flow is away from the wall between the vortices, a boundary-layer eruption and local inviscid-viscous interaction is indicated in a streamwise region between the parent vortex centers; when the sense of rotation of the vortices is reversed, the interaction occurs outboard of the vortex centers.

One feature which is missing from the aforementioned studies and which is important in the three-dimensional flows observed in turbulent boundary layers is vortex stretching. The subsequent studies, Walker et al (1987) and Ersoy and Walker (1985) have examined the boundary layer induced by a vortex ring moving toward a wall and a vortex loop approaching a wall at angle of attack. Again strong boundary-layer growth was observed in the numerical calculations; vortex loops stretch as they approach the wall, and as the local vorticity levels increase, the eruptive response of the boundary-layer flow appears to intensify.

1.4 Summary and Overview

Current experimental research suggests that the motion of vortices, particularly hairpin vortices, plays an important part in the time-dependent dynamics of the turbulent boundary layer. The studies by Acarlar and Smith (1984,1987a,1987b) suggest that hairpin vortices are regenerative in at least two ways: (1) a hairpin in shear appears to be able to multiply itself to the side in the sense that secondary hairpin vortices are observed to form in the spanwise direction out board of the original hairpin vortex and (2) the creation of secondary hairpins through an inviscid-viscous interaction with the viscous flow near the wall was continually observed. In Figures 1.6(a) and 1.6(b) (Taken from Acarlar and Smith (1984)) both of these processes are depicted schematically. In the present study, the dynamics of hairpin vortices, with particular reference to the phenomena observed by Acarlar and Smith (1984), will be investigated on a theoretical basis.

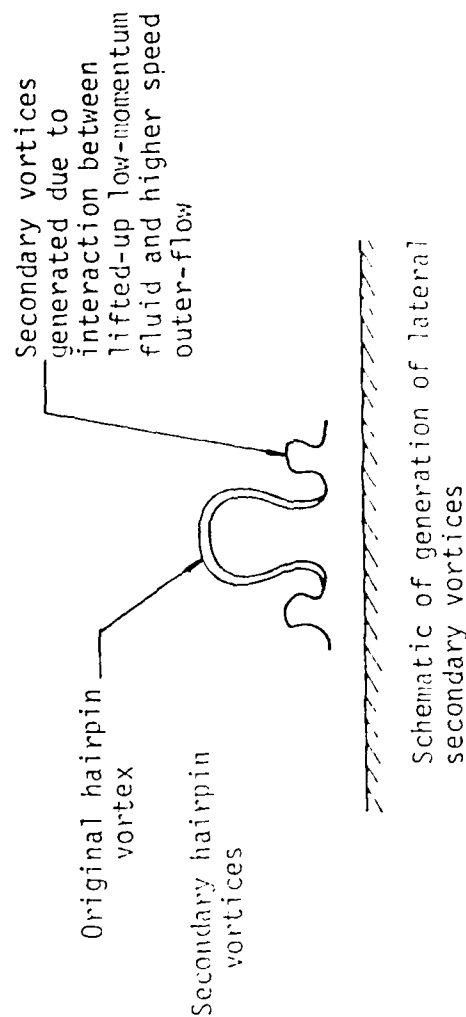
The plan of this study is as follows. In Chapter 2, a numerical method for computing the motion of a vortex filament which is based on a numerical approximation to the Biot-Savart integral will be given. It was determined that current numerical schemes for vortices having small core radii are highly unstable; previous numerical investigation of vortex motion (c.f. Dhanak and De Bernardinis, 1981) have been carried out for an unbounded fluid and have used relatively thick core sizes. In this type of situa-



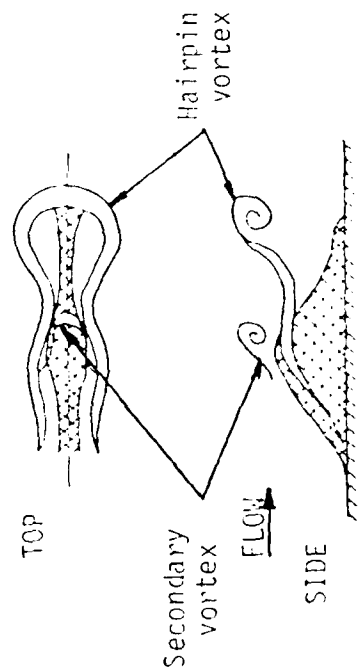
(a) Top-view, $y/R=0.465$, $x/R=7.5$



(b) Side view, $x/R=15$



Schematic of generation of lateral secondary vortices



Schematic of secondary vortex through interaction with flow near the wall lens

tion the numerical stability problem is not evident. In the present study, it was important to develop a reliable calculation method for vortices with small cores; this is because the main interest was in flows with walls and once the vortex core touches the wall, the Biot-Savart calculation must terminate.

In Chapter 3, the numerical algorithm is tested by computation of the trajectory of closed vortex loops near a wall. In addition, a series of calculations is performed to compute the trajectories of simulated "hydrogen bubble lines" in the flow as the vortex passes by. These computations show that a moving vortex loop causes the simulated "bubble lines" to form into a streaky type of structure near the wall. The indication of these results is that a convected vortex loop is a potential creator of wall-layer streaks in a turbulent boundary layer.

In Chapter 4, numerical solutions are carried out to show the evolution of a hairpin vortex in both a stagnant flow and a shear flow. The evolution of the vortex in a shear flow is consistent with the experimental results of Acarlar and Smith (1984). Simulations of hydrogen bubble lines also show that the hairpin vortex is a potential creator of wall-layer streaks. Finally, a numerical calculation is carried out to show the interaction that occurs between two hairpin vortices convecting in a shear flow.

In Chapter 5, a method is described which allows the determination of the viscous response of the boundary-layer flow near the wall

to the motion of the convected hairpin. The unsteady boundary-layer flow is three-dimensional and unsteady and the computation of this flow would require computer resources well beyond what was available in the course of this study. Consequently a method was devised which allows the calculation of the boundary-layer evolution along the symmetry plane of the hairpin vortex. The computed results are strongly suggestive that the moving hairpin vortex rapidly evokes an eruptive response in the viscous flow near the wall. Detailed conclusions are discussed in Chapter 6.

CHAPTER 2

THE VORTEX CALCULATION METHOD

2.1 Introduction

Three-dimensional vortex motions play an important role in a variety of practical situations involving fluid flow and consequently several computational methods have been developed over the past two decades to predict the evolution of three-dimensional vortex motion. In situations where the vorticity in the flow field is concentrated in thin vortex filaments which convect in an otherwise irrotational flow, calculation procedures are, in general, based on the Biot-Savart law and are Lagrangian in nature; the vortex filament is discretized at some initial time using a number of nodal points on the space curve defining the filament and the subsequent motion of the nodal points is evaluated as the filament distorts. In this chapter, a calculation method for the evolution of vortex filaments is developed. The general features of the Biot-Savart law are discussed in section 2.2 and some early calculation schemes are reviewed in section 2.3. In this study an adaptation of a procedure due to Moore (1972) was used to compute the evolution of vortices and in section 2.4, a basic numerical instability in this scheme is described. An improved calculation procedure is developed in section 2.5.

2.2 The Biot-Savart Law

Consider a Cartesian coordinate system (x,y,z) with origin at

0 and let the velocity vector at a point $P_0(x_0, y_0, z_0)$ be denoted by $\vec{u}(\vec{x}_0)$ where \vec{x}_0 is the vector from the origin to the point P_0 . In general (Batchelor, 1967), the velocity at P_0 is related to the vorticity distribution $\vec{\omega}$ throughout space by the Biot-Savart law which is given by,

$$\vec{u}(\vec{x}_0) = -\frac{1}{4\pi} \int_V \frac{(\vec{x}_0 - \vec{x}) \times \vec{\omega}}{|\vec{x}_0 - \vec{x}|^3} dV(\vec{x}) + \vec{u}_{\text{ext}}(\vec{x}_0) \quad (2.1)$$

In equation (2.1) the volume integral is carried out over all space where the vorticity is non-zero and \vec{u}_{ext} is an background external irrotational velocity field. The variable \vec{x} is an integration variable and the vector $\vec{x} - \vec{x}_0$ is directed from the field point P_0 to locations in the volume V as the integration in equation (2.1) is carried out.

Now consider the physical situation where the majority of the flow field is irrotational and the vorticity is concentrated in vortex tubes of small cross-section. For a single vortex tube, as the cross-sectional area of the tube approaches zero, the vortex approaches being a line filament defined by a space curve. The vorticity vector at any point on the curve may be written as,

$$\vec{\omega} = \Omega \hat{t} \quad , \quad (2.2)$$

where \hat{t} is the unit tangent to the curve (as indicated in Figure 2.1) and Ω is the local magnitude of the vorticity. Note that the direc-

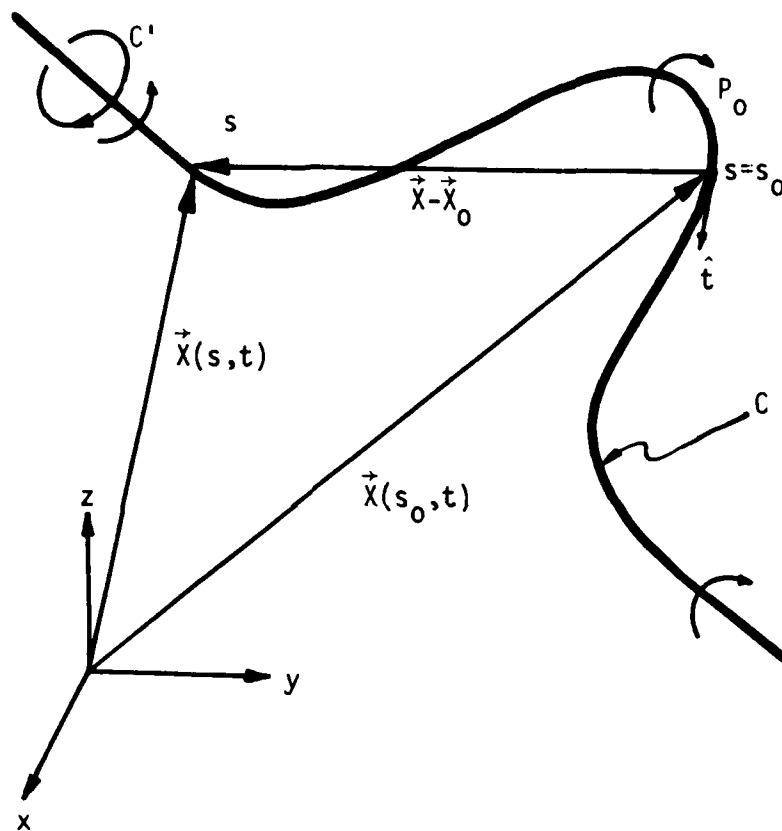


Figure 2.1 - A portion of a vortex filament
(Shown for $\Gamma < 0$).

tion of positive vorticity is determined by the right hand rule and for the situation in Figure 2.1, a vortex having the indicated sense of rotation has negative Ω . Since the vorticity is assumed to be non-zero only within the small vortex core, the integrand in equation (2.2) vanishes except within the core where the volume element may be written,

$$dV = dA_c d\ell . \quad (2.3)$$

Here $d\ell$ and dA_c are differential length and cross-sectional area elements along the core, respectively. The integral of the vorticity distribution over the cross-sectional area of the core may be related to the circulation about the core by Stokes' theorem and it is easily shown that

$$\int_{A_c} \Omega dA_c = \oint_C \vec{u} \cdot d\vec{s} = \Gamma . \quad (2.4)$$

Here C' is any closed contour surrounding the vortex core and ds is a length element on this path. According to Kelvin's theorem (Batchelor, 1967), the circulation Γ is constant in time and also constant along the length of the vortex filament. Consequently, the Biot-Savart law (2.1) becomes,

$$\vec{u}(\vec{x}_0) = - \frac{\Gamma}{4\pi} \int_C \frac{(\vec{x}_0 - \vec{x})}{|\vec{x}_0 - \vec{x}|^3} \times d\vec{x} + \vec{u}_{\text{ext}}(\vec{x}_0) , \quad (2.5)$$

where $d\vec{x}$ is a differential length element along the space curve C defining the current position of the vortex. Since $\vec{u}(\vec{x}_0) = \partial\vec{x}_0/\partial t$, equation (2.5) apparently defines a differential equation from which the evolution of each point along the vortex can be traced forward in time. The difficulty is that for \vec{x}_0 on the curve C , the integrand is singular and consequently the velocity field described by equation (2.5) must be interpreted as an outer inviscid solution which is not uniformly valid near the core of the vortex. To define a rational calculation procedure, it is in theory necessary to match any solution obtained from equation (2.5) with an inner solution in the vortex core and thereby take into account how the evolving flow in the vortex core influences the overall motion of the vortex. It emerges that this is a rather complex problem and although recent progress has been made (Callegari and Ting (1978)) in this area, a variety of approximate methods have been used over the years. Some of these techniques are discussed in detail by Ersoy and Walker (1985b) and only a brief summary is given here.

2.3 Previous Calculation Methods

For vortex motions in three-dimensions, there is one flow situation where the core solution can be determined and subsequently matched to the outer inviscid flow field described by the Biot-Savart integral; this is the problem of a circular vortex ring which propagates into an otherwise irrotational flow and has been considered by Tung and Ting (1967) and Saffman (1970). Consequently

there is one exact solution for three-dimensional flows and this solution has been used to structure a number of vortex calculation methods. In the early calculation methods of Widnall, Bliss and Zelay (1971) and Leonard (1975,1979) the curve defining the vortex filament was first discretized into a number of nodal points; as the vortex filament moves, the velocity induced by the filament at a particular nodal point was calculated by a numerical integration of the Biot-Savart law except over the segments of the vortex on either side of the nodal point in question. The contribution of the induced velocity due to the segments of the vortex adjacent to the nodal point was then estimated by fitting a vortex ring through the three adjacent points; the velocity induced by this arc at the nodal point is then estimated using the known results for a circular vortex ring. The approach has been termed a "patched" solution technique by Liu, Tavantzis and Ting (1984) and does not necessarily give the correct direction of the self-induced motion locally.

Another approach to the cut-off method originally described by Crow (1970) in his investigation of the stability of aircraft trailing vortices. In this method, a portion of the filament near the singularity at \vec{x}_0 is simply omitted in the Biot-Savart integral. Let s measure distance along the space curve defining the instantaneous vortex position and let s_0 denote the value of s corresponding to \vec{x}_0 ; in the cut off method, the approximation to the Biot-Savart integral is,

$$u(s_0, t) = \frac{\Gamma}{4\pi} \oint_{[\delta_c]} \frac{\partial \vec{X}}{\partial s} \times \frac{(\vec{X}_0 - \vec{X})}{|\vec{X}_0 - \vec{X}|^3} ds \quad . \quad (2.6)$$

The notation in equation (2.6) implies that an interval of length δ_c has been omitted in the integration on both sides of $s = s_0$; Crow (1970) determined a value for the cut-off length δ_c by comparing the result predicted by equation (2.6) when the vortex is a circular ring with the known exact solution. As a result of this comparison, a value of $\delta_c = 0.642 a$ was suggested by Crow (1970); here a denotes the small (not nonzero) radius of the vortex core. Moore and Saffman (1972) were subsequently able to give a formula for δ_c according to,

$$\log\left(\frac{\delta_c}{a}\right) = \frac{1}{2} - \frac{4\pi^2 a}{\Gamma^2} \int_0^a v'^2 r dr + \frac{8\pi^2 a}{\Gamma^2} \int_0^a w'^2 r dr \quad , \quad (2.7)$$

where r measures distance from the center of the vortex core and v' and w' denote the swirl and axial velocities in the core. The right side of equation (2.7) was obtained from detailed results for the flow in the core of a circular vortex ring; note that the result in equation (2.7) relates the cut-off length to quite general velocity distributions within the core but also that the validity of the cut off method is assumed.

From a computational standpoint, the cut-off method of Crow (1970) is normally not a convenient algorithm for the following reason. Calculations involving the Biot-Savart law are Lagrangian

in character; the space curve defining the vortex at some initial instant is discretized into a number of nodal points which then may be considered to be Lagrangian markers. The object of the numerical integration is to trace the path of these markers and thus determine the shape of the vortex filament at subsequent times. To use Crow's (1970) method, it is necessary to subtract a portion of the integration range near each point s_0 in equation (2.6); generally the cut-off length will not correspond to the mesh length and indeed will change with time in general. An alternative approach is due to Moore (1972) and has its origins in a study by Rosenhead (1930); in this technique, the singularity in the integrand is removed by artificially inserting a small parameter μ into the denominator and equation (2.5) is written according to,

$$\vec{u}(s_0, t) = \frac{\Gamma}{4\pi} \oint_C \frac{\partial \vec{X}}{\partial s} \times \frac{(\vec{X}_0 - \vec{X})}{\{|\vec{X}_0 - \vec{X}|^2 + \mu^2\}^{3/2}} ds + \vec{u}_{\text{ext}}(s_0) \quad (2.8)$$

Here s is a coordinate along the vortex and s_0 denotes a specific location on the vortex. The integral is now taken over the entire vortex and an expression for the small parameter μ is obtained by insisting that equation (2.8) give correct results for the circular vortex ring. The following expression is obtained for μ (Moore, 1972; Ersoy and Walker, 1985b).

$$\log\left(\frac{\mu}{a}\right) = -\frac{1}{2} - \frac{4\pi^2}{\Gamma^2} \int_0^a v'^2 r dr + \frac{8\pi^2}{\Gamma^2} \int_0^a w'^2 r dr \quad (2.9)$$

It may be observed from equations (2.8) and (2.9) that the internal structure of the vortex core flow influences the overall motion of the vortex only through the parameter μ in equation (2.8) which is calculated as an integrated effect over the core via equation (2.9).

It might be expected a priori that the core radius a could be a function of position s along the vortex as well as of t . However, Moore and Saffman (1972) have argued that the vortex core does not vary in the axial distance and is uniform at any instant in time; the physical reasoning is that any local non-uniformities in the vortex core will be rapidly smoothed out by travelling internal waves on a time scale which is much smaller than the time scale associated with the overall motion of the vortex itself. Thus the vortex core radius may be regarded as a function of time alone and Moore and Saffman (1972) also show that ,

$$L(t)a^2(t) = \text{constant} , \quad (2.10)$$

where $L(t)$ is the total arc length of the closed vortex filament at time t ; this result simply states conservation of volume of the vortex core. It follows from equation (2.10) that the core radius at any instant in the motion is described by,

$$a(t) = a_0 \left\{ \frac{1}{L_0} \oint_C \left| \frac{\partial \vec{X}}{\partial s} \right| ds \right\}^{-1/2} , \quad (2.11)$$

where a_0 and L_0 are the initial core radius and vortex length, respectively. It is worthwhile to note that these are rather strong results which have been confirmed by the asymptotic analysis of Callegari and Ting (1978). However the results apply only to a vortex filament which is closed and therefore of finite length. In addition, it appears that the theoretical description is incomplete since it does not account for situations where local variations in core size are observed before a phenomenon known as vortex break-down occurs.

Moore (1972) has used equation (2.8) to compute the motion of aircraft trailing vortices; the method was also subsequently used by Dhanak and De Bernardinis (1981) and by Dhanak (1981) to calculate the evolution of elliptic vortex rings and a vortex filament approaching a rigid sphere, respectively. In these calculations, typical values of the vortex core radius used were on the order of 0.2. Although the integrand in equation (2.8) is finite everywhere, it may become quite large near s_0 , particularly in situations where the vortex is undergoing stretching and a (and hence μ) decreases. To avoid potential inaccuracies in the numerical evaluation of the integral near s_0 , Moore (1972) obtains the leading term in an expansion around $s = s_0$ according to,

$$\frac{\partial \vec{X}}{\partial s} \times \frac{(\vec{X}_0 - \vec{X})}{(|\vec{X}_0 - \vec{X}|^2 + \mu^2)^{3/2}} \sim \left(\frac{\partial \vec{X}}{\partial s} \right)_0 \times \left(\frac{\partial^2 \vec{X}^2}{\partial s^2} \right)_0 P(s) , \quad (2.12)$$

where,

$$P(s) = \frac{\frac{1}{2}(s-s_0)^2}{\{(s-s_0)^2 (\frac{\partial \vec{X}}{\partial s})_0^2 + \mu^2\}^{3/2}}, \quad (2.13)$$

and the subscript 0 indicates that the partial derivatives are evaluated at $s = s_0$; the leading order form of the integrand near $s = s_0$ is added and subtracted to the integrand to obtain,

$$\begin{aligned} \vec{u}(s_0, t) = & \frac{\Gamma}{4\pi} \oint_C \left\{ \frac{\partial \vec{X}}{\partial s} \times \frac{(\vec{X}_0 - \vec{X})}{\{|\vec{X}_0 - \vec{X}|^2 + \mu^2\}^{3/2}} - \left(\frac{\partial \vec{X}}{\partial s}\right)_0 \times \left(\frac{\partial^2 \vec{X}}{\partial s^2}\right)_0 P(s) \right\} ds \\ & + \frac{\Gamma}{4\pi} \left(\frac{\partial \vec{X}}{\partial s}\right)_0 \times \left(\frac{\partial^2 \vec{X}}{\partial s^2}\right)_0 \oint_C P(s) ds \\ & - \frac{\Gamma}{4\pi} \oint_{\text{image}} \frac{\partial \vec{X}}{\partial s} \times \frac{(\vec{X}_0 - \vec{X})}{|\vec{X}_0 - \vec{X}|^3} ds + \vec{u}_{\text{ext}}. \end{aligned} \quad (2.14)$$

The apparent advantage of this procedure is that the integrand in the first integral is $O(1)$ everywhere while the second integral may be evaluated analytically. The method was used with good success by Moore (1972), Dhanak and De Bernardinis (1981) and Dhanak (1981); however, in all of these studies rather large values of the core radii ($a \sim 0.1-0.3$) were used. In the present study, one objective was to compute the evolution of hairpin vortices close to solid walls and to avoid situations where the vortex core impacted the wall at relatively early stages, it was considered desirable to be able to compute cases with very small vortex cores. It emerged that the method of Moore (1972) exhibited strong numerical instability for small values of a ; a modified formula based on equation

(2.8) which is suitable for small a was developed in this study and this will be discussed in section 2.5.

Another approach to the computation of vortex motion in three-dimensions was originally described by Arms and Hama (1965) and this is the "localized induction approximation". In this approach, it is assumed that the dominant contribution to the self-induced vortex velocity occurs locally; in this approach, the integrand in the Biot-Savart law is approximated everywhere by its asymptotic form near $s = s_0$ and it may be shown that,

$$\bar{u}(s_0) \sim \frac{\Gamma}{4\pi} \frac{\left(\frac{\partial \vec{X}}{\partial s}\right)_0 \times \left(\frac{\partial^2 \vec{X}}{\partial s^2}\right)_0}{\left|\left(\frac{\partial \vec{X}}{\partial s}\right)_0\right|^3} \log\left(\frac{1}{a}\right) + O(1) . \quad (2.15)$$

Note that this result may be obtained from equation (2.14) by ignoring the first integral and integrating $P(s)$ from $s = -\epsilon$ to $+\epsilon$ where ϵ is an $O(1)$ number; the integral over the image as well as the external field are also ignored. In equation (2.15), a is assumed to be small so that $-\log(a) \gg 1$ and the first term of equation (2.15) is presumed to describe the leading order behavior of the velocity field everywhere.

The "localized induction approximation" was used by Arms and Hama (1965) and more recently by Aref and Flinchem (1984) to obtain some interesting results. In the latter study, the term $\log(1/a)$ was regarded as a large but unknown quantity which could be absorbed in a time scale; results which bear a similarity to those obtained

in the present study were found for the propagation of a three-dimensional distortion on a two-dimensional vortex. However, it was evident at the outset that three-dimensional vortex motion involves some rather complex phenomena which often cannot be obtained through physical intuition; in addition, the effect of the wall was of prime concern. For these reasons, it was considered important to carry out numerical integrations of the full Biot-Savart law and to account for the presence of the image vortex.

One other approach should be noted. Recently Liu, Tavantzis and Ting (1984) have described a computational method for closed vortex loops which is potentially more general than some of the methods described here. The computational method is based on a previous analytical study by Callegari and Ting (1978) in which asymptotic methods were used to write the Biot-Savart integral in equation (2.1) as a part which is bounded everywhere (the finite part) plus a part which becomes singular as the curve defining the vortex core is approached; the analysis is valid for small vortex cores. Within the core, the flow is viscous and Callegari and Ting (1978) investigate possible unsteady solutions of the core equations; these are matched to the outer inviscid solution corresponding to the singular part of the Biot-Savart integral. Consequently, in this approach the evolving flow in the vortex core influences the overall motion of the vortex loop to an increasing extent as time passes. The details of the asymptotic analysis are complex and will not be summarized here. To date, the method has not been

extended to three-dimensional vortex filaments of infinite length, which are of principal interest in this study.

2.4 An Instability Associated With the Moore-Rosenhead Method

In the present study, the calculations of three-dimensional vortex motion were based on the Moore-Rosenhead model equations (2.8) and (2.9) for the Biot-Savart integral. The algorithm based on this model is convenient for computational purposes and is believed to realistically model the evolution of vortex motion. In order to avoid loss of accuracy in evaluation of the integrand, the procedure suggested by Moore (1972) given in equation (2.14) was used. However after running several test cases, it was determined that the scheme suffered from serious instabilities which generally became worse with either decreasing core size or an increased number of points on the vortex. To illustrate the problem, consider the case of a circular vortex ring which is moving on a normal trajectory toward a plane wall; the exact solution for the problem is known (Walker, Smith, Cerra and Doligalski, 1987) and it provides a convenient test case for the present calculation methods. Since,

$$\vec{u}(s_0, t) = \frac{\partial \vec{X}}{\partial t}(s_0, t) \quad , \quad (2.16)$$

equation (2.14) defines an initial value problem; for a specified number of mesh points along the vortex, equation (2.14) may be integrated forward in time to track the motion of each individual

point (denoted by s_0) on the vortex. The results of such a calculation are shown in Figure 2.2; here a vortex ring (of radius 1) has been started at a height 0.5 units away from the wall. The vortex core was assumed to be in solid body rotation with core radius $a = 0.005$ and with $v' = r/2\pi a^2$, $w' = 0$ it follows from equation (2.9) that,

$$\mu = a e^{-3/4} . \quad (2.17)$$

In the calculation depicted in Figure 2.2, there were 100 nodal points on the vortex and the time increment was $\Delta t = 0.005$. It may be observed that the ring proceeds smoothly toward the wall but that wiggles have developed in the ring by $t = 0.05$. Once "wiggles" develop in the ring shape the calculation rapidly breaks down and gives nonsensical results as indicated at $t = 0.055$. The onset of the appearance of the wiggles can be delayed somewhat by reducing the time step but the problem is made worse by using more mesh points to discretize the vortex.

The difficulty depicted in Figure 2.2 is due to a deficiency in Moore's (1972) method and has not been previously observed by Moore (1972), Dhanak and De Bernardinis (1981) and Dhanak (1981) because these authors have used relatively thick cores ($a \approx 0.1$ to 0.35). Here, because of the presence of the wall, it was considered desirable to be able to use very small cores and consequently it was necessary to find a resolution of the problem.

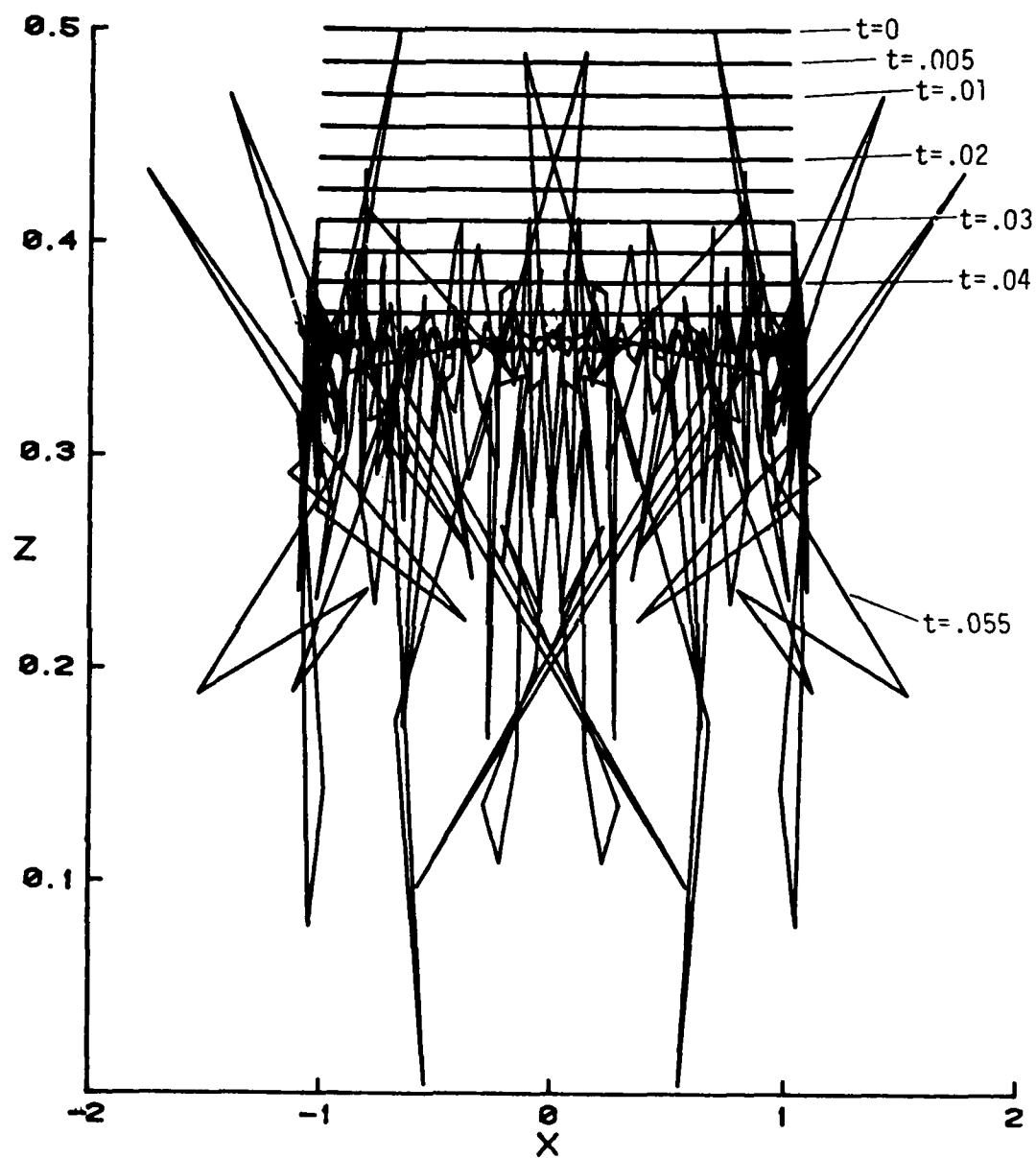


Figure 2.2 - Trajectory of a vortex ring (viewed from the side) approaching a wall; the results are computed using Moore's method (1972) and show the development of numerical instability.

The difficulty which gives rise to the instability is associated with the fact that for small values of a (and hence μ) the denominator in the first integrand in equation (2.14) is small near $s = s_0$ and hence inaccuracies in the derivative $\partial \vec{X} / \partial s$ are magnified. The integrand in the first integral in equation (2.14) is plotted in Figure 2.3(a) for a typical point s_0 at $t = 0.01$ for the calculation depicted in Figure 2.2. It may be observed that the integrand exhibits anomalous behavior near $s = s_0$; it does not tend smoothly to zero and shows two small negative spikes on either side of $s = s_0$. If the number of mesh points is increased to 200, the size of the spikes diminishes but the phenomena persists. With increasing mesh points on the vortex, the numerical evaluation of the gradients $\partial \vec{X} / \partial s$ is in general more accurate and this is reflected in the diminished levels of the spikes in Figures 2.3. In Appendix A, it is verified that the problem is due to an inaccurate evaluation of the first integrand in equation (2.14); a basic modification of the scheme is considered next.

2.5 The Present Method

The motivation behind the algorithm (2.14) described by Moore (1972) was to obtain an accurate evaluation of the integrand near $s = s_0$. However the results of the previous section and the discussion in Appendix A shows that there are still difficulties with the procedure for vortices with small cores. To eliminate these problems, the integrand in the first integral of equation

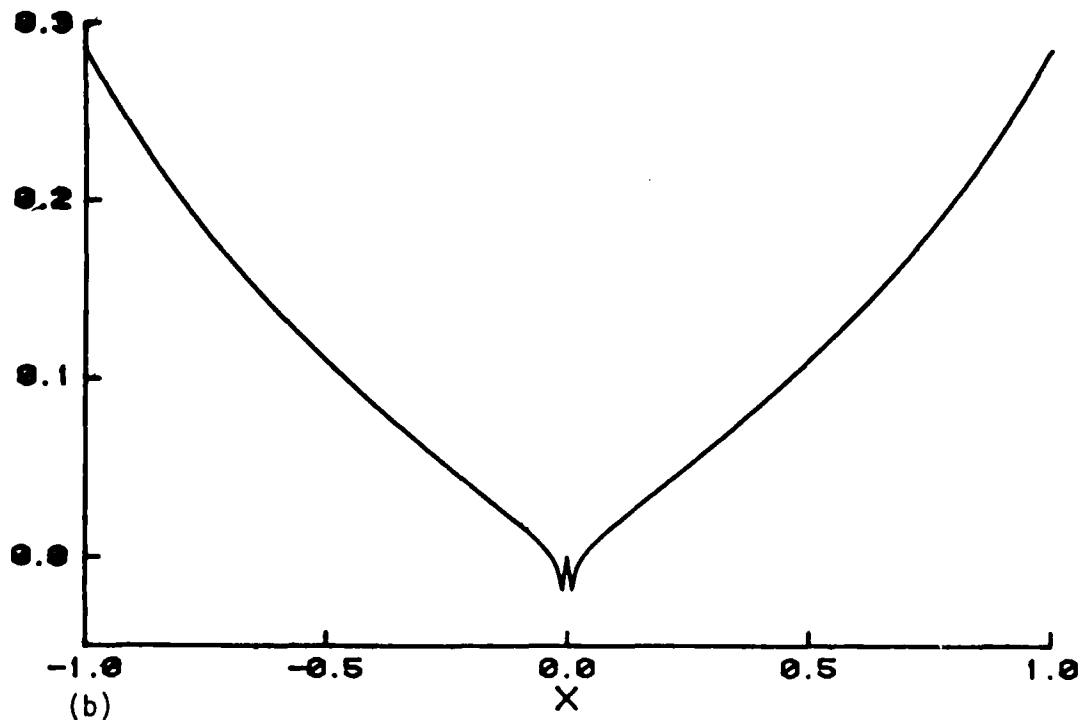
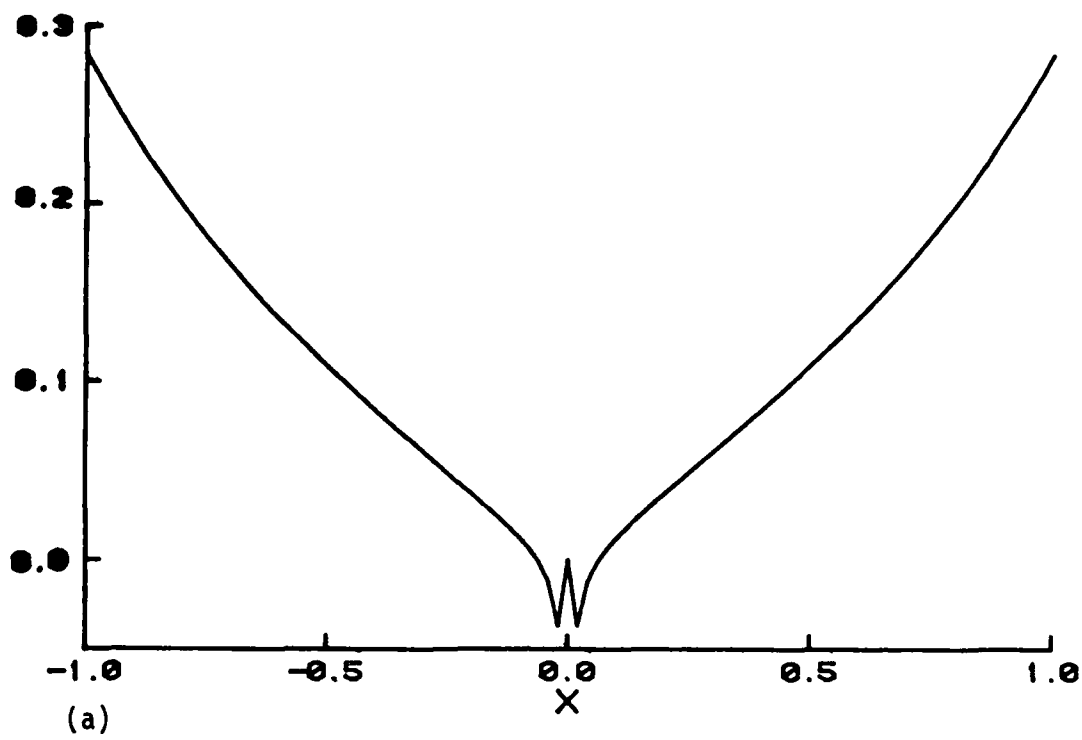


Figure 2.3 - Behavior of integrand in the first integral in equation (2.14) for (a) 100 and (b) 200 total points.

(2.14) was represented by higher order terms in an expansion about $s = s_0$; the details are described in Appendix B and if $R(s, s_0)$ denotes the integrand in equation (2.14) according to,

$$R(s, s_0) = \frac{\partial \vec{X}}{\partial s} \times \frac{(\vec{X}_0 - \vec{X})}{\{|\vec{X}_0 - \vec{X}|^{2+\mu^2}\}^{3/2}} - \left(\frac{\partial \vec{X}}{\partial s}\right)_0 \times \left(\frac{\partial^2 \vec{X}}{\partial s^2}\right)_0 P(s), \quad (2.18)$$

where $P(s)$ is defined by equation (2.13), it can be shown that

$$R(s, s_0) = \vec{D}_3(s-s_0)^3 + \vec{D}_4(s-s_0)^4 + \dots, \quad (2.19)$$

where \vec{D}_3 and \vec{D}_4 are vectors defined by equations (B.9) and (B.10) in Appendix B in terms of vector products of derivatives of \vec{X} evaluated at $s = s_0$.

In Figure 2.4, the exact value of the integrand $R(s, s_0)$ is plotted; here the expressions for a ring given in equations (A.2) and (A.3) in Appendix A have been used to evaluate the gradients in equation (2.18). The result for $R(s, s_0)$ using numerical differentiation to compute the gradients and the local approximation (2.19) is also plotted in Figure 2.4. It may be observed that the local approximation (2.19) represents R very well for small $(s-s_0)$ and that the behavior depicted in Figure 2.3 no longer occurs.

A calculation method for the vortex ring may now be structured as follows. In equation (2.14), the first integral is split into three parts and,

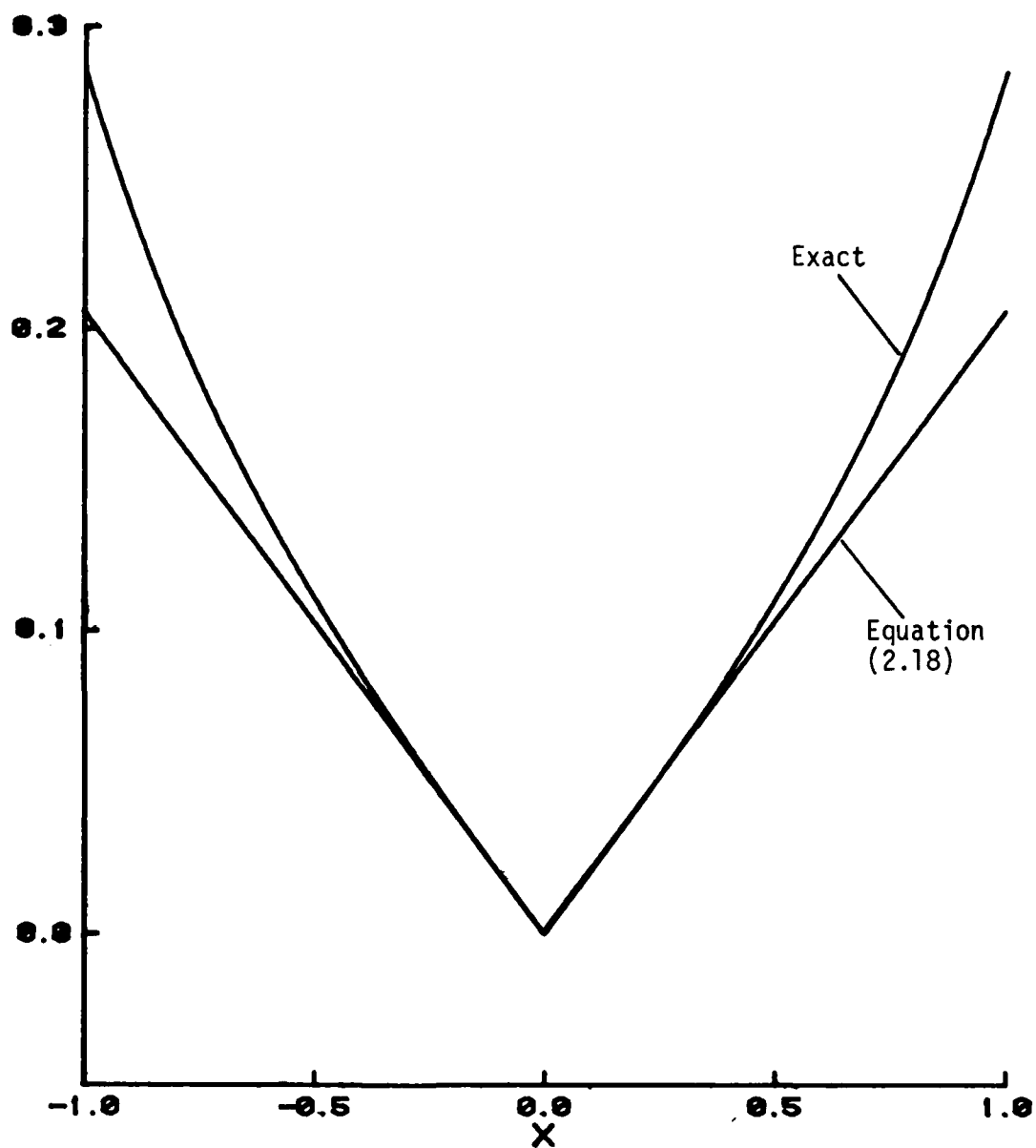


Figure 2.4 - Comparison of local approximation to the integrand $R(s, s_0)$ to the exact answer for a ring vortex.

$$\begin{aligned}
\frac{\partial \vec{X}}{\partial t}(s_0, t) = & \frac{\Gamma}{4\pi} \left\{ \left[\int_h^1 + \int_{-1}^{-h} \right] \left[\frac{\partial \vec{X}}{\partial s} \times \frac{(\vec{X}_0 - \vec{X})}{\{|\vec{X}_0 - \vec{X}|^2 + \mu^2\}^{3/2}} \right. \right. \\
& - \left. \left. \left(\frac{\partial \vec{X}}{\partial s} \right)_0 \times \left(\frac{\partial^2 \vec{X}}{\partial s^2} \right)_0 P(s) \right] ds \right. \\
& + \left. \int_{-h}^h R(s, s_0) ds \right\} + \frac{\Gamma}{4\pi} \left(\frac{\partial \vec{X}}{\partial s} \right)_0 \times \left(\frac{\partial^2 \vec{X}}{\partial s^2} \right)_0 \int_{-1}^1 P(s) ds \\
& - \frac{\Gamma}{4\pi} \int_{-1}^1 \frac{\partial \vec{X}}{\partial s} \times \frac{(\vec{X}_0 - \vec{X})}{|\vec{X}_0 - \vec{X}|^3} \Big|_{\text{image}} ds \quad (2.20)
\end{aligned}$$

In the ranges, $[1, h)$, $[-1, -h)$, the first integrand is evaluated as before while in the interval $[-h, h]$ surrounding the point $s = s_0$, the integrand is evaluated using the series representation (2.19). Calculations were once again carried out for the vortex ring moving toward the wall ($\Gamma < 0$) and the results are shown in Figure 2.5. Here a total of 100 mesh points were used on the ring with an initial vortex core radius of 0.005 and at time step of 0.002. It may be observed that the calculation proceeds without difficulty until the ring is quite close to the wall in contrast to the results of the computation depicted in Figure 2.2. Note that in equation (2.20), the value of h must be selected small enough so that the series in equation (2.19) is convergent; for the calculations depicted in Figure 2.5 $h = 3\Delta s$ and the integrals were evaluated by Simpson's rule.

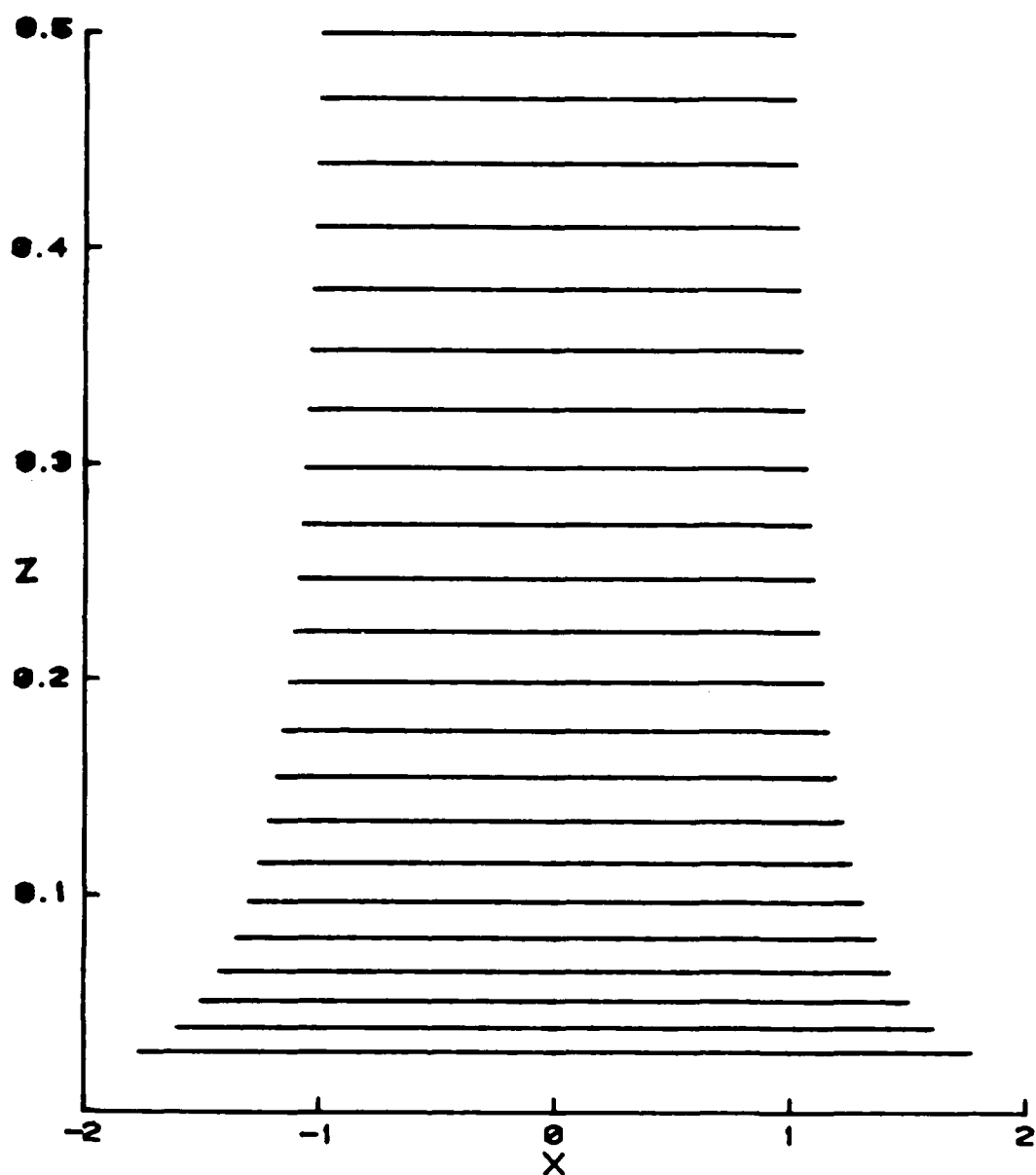
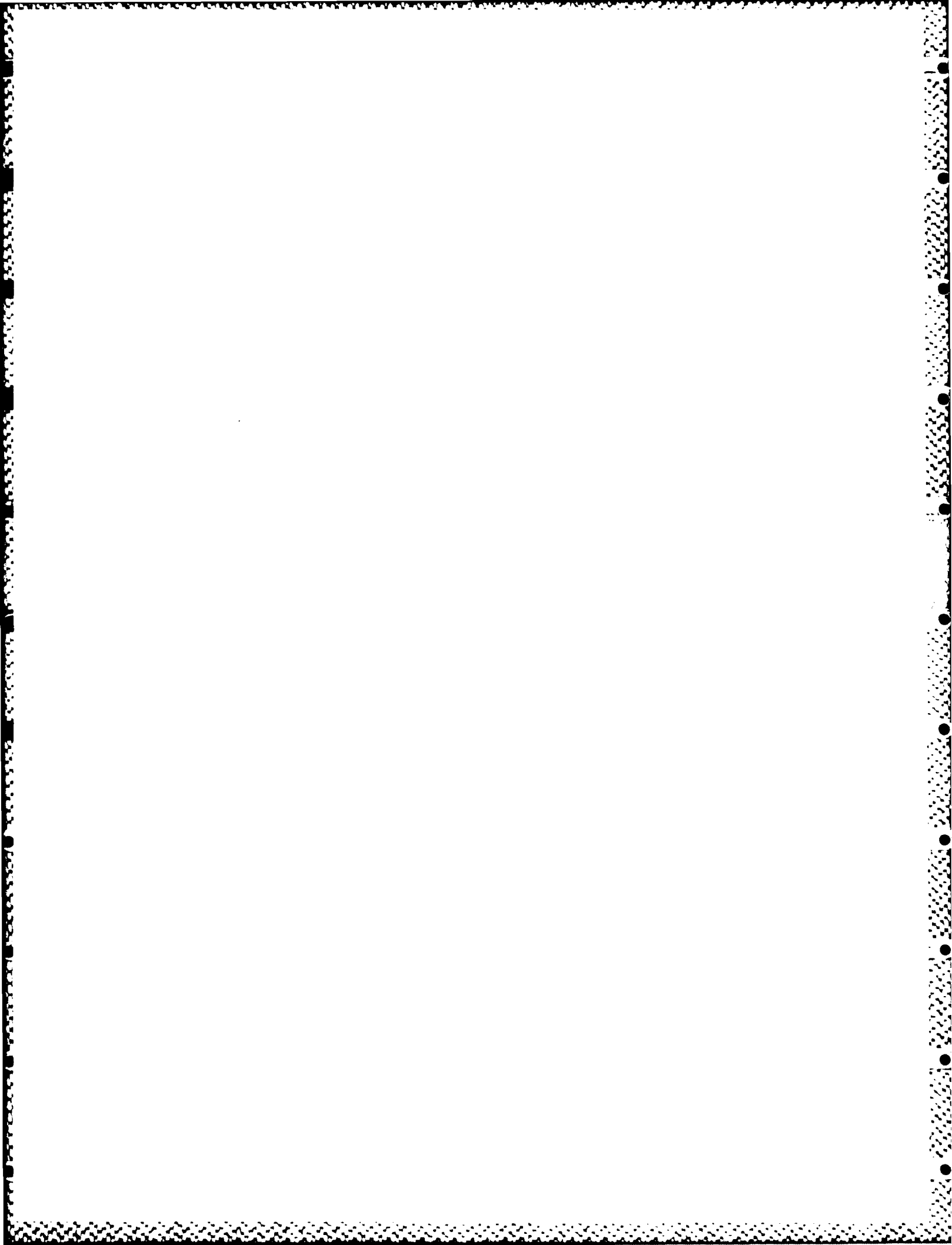


Figure 2.5 - Results for the trajectory of a vortex ring (viewed from the side) approaching a wall using the present method.

The numerical procedure described in this section was modified and used in this study to compute the evolution of hairpin vortices in shear; these results will be described in Chapter 4.



CHAPTER 3

THE INFLUENCE OF MOVING VORTEX LOOPS

3.1 Introduction

It is commonly believed that vortex motions play an important role in the dynamics of the turbulent boundary layer. Both closed loop vortices (rings) [Falco (1982,1983), Falco and Wiggert (1980)] and hairpin vortices [Acarlar and Smith (1984,1987a,1987b)] have been proposed as principal vortex structures in the outer region of the turbulent boundary layer. Wall-layer streaks are observed in the near-wall region of turbulent flows during the relatively long periods of time when the wall-layer flow is not strongly interacting with the essentially inviscid flow away from the wall; (Walker, Scharnhorst and Weigand, 1986). It is therefore of interest to understand the types of vortex motion which will induce a streaky structure in the flow near a wall. In this chapter, the effect of convecting vortex loops will be considered; the question of convecting hairpin vortices will be addressed in Chapter 4.

The numerical calculations that will be described here may be thought of as an inviscid simulation of the motion of hydrogen bubble lines. First the trajectory of a vortex ring was computed using the method developed in Chapter 2; for situations where the ring is initially inclined at an angle to the wall, the ring rapidly distorts into a vortex loop due to the effect of the wall. As the vortex loop convects above the wall, it is of interest to

understand the nature of the induced flow near the wall; in typical flow visualization experiments, hydrogen bubble lines are used to mark the flow and the nature of the flow is then inferred from the subsequent motion of the bubble lines. In the present study, the bubble lines were simulated by numerically tracking the motion of several initially straight lines near the wall as the vortex loop convected past. The objective of this simulation is to determine whether the convecting vortex will induce the marker lines to form a streaky structure.

3.2 The Trajectory of Vortex Loops

Consider a vortex ring having an initial radius R which is initially inclined at an angle α to the wall as indicated in Figure 3.1; here the α measures the angle between the normal to the plane of the ring and the wall. If $\alpha = \pi/2$, the ring will remain circular and either move toward or recede from the wall depending on the sense of the circulation; as the ring moves toward the wall, the ring radius will increase. If $\alpha \neq \pi/2$, the ring will immediately start to change into a "rubber-band" loop shape. In this section, the results for various vortex trajectories will be described.

In all cases described here, the initial ring radius R was used as a representative length and $4\pi R^2/|\Gamma|$ was used as a time scale to define dimensionless variables. Let s be a Lagrangian variable on the vortex loop which ranges from -1 to $+1$ with $s = \pm 1$

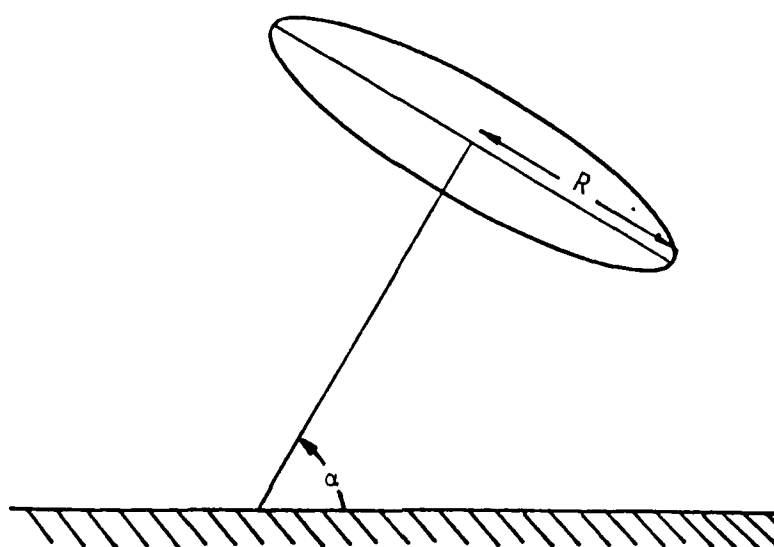


Figure 3.1 - Initial vortex ring configuration.

corresponding to the same point (initially opposite from $s = 0$ on the ring). In dimensionless form, equation (2.20) becomes

$$\begin{aligned}
\frac{\partial \vec{X}}{\partial t}(s_0, t) = & \text{sgn}(\Gamma) \left\{ \int_h^1 + \int_{-1}^{-h} \right\} \left\{ \frac{\partial \vec{X}}{\partial s} \times \frac{(\vec{X}_0 - \vec{X})}{\{|\vec{X}_0 - \vec{X}|^2 + \mu^2\}^{3/2}} \right. \\
& - \left. \left(\frac{\partial \vec{X}}{\partial s} \right)_0 \times \left(\frac{\partial^2 \vec{X}}{\partial s^2} \right)_0 P(s) \right\} ds + \text{sgn}(\Gamma) \int_{-h}^h R(s, s_0) ds \\
& + \text{sgn}(\Gamma) \left(\frac{\partial \vec{X}}{\partial s} \right)_0 \times \left(\frac{\partial^2 \vec{X}}{\partial s^2} \right)_0 \int_{-1}^1 P(s) ds \\
& - \text{sgn}(\Gamma) \int_{-1}^1 \frac{\partial \vec{X}}{\partial s} \times \frac{(\vec{X}_0 - \vec{X})}{|\vec{X}_0 - \vec{X}|^3} \bigg|_{\text{image}} ds . \quad (3.1)
\end{aligned}$$

For a closed vortex loop, it may be shown (Ersoy and Walker, 1985b) that

$$\begin{aligned}
\int_{-1}^1 P(s) ds = & - \frac{1}{A_0 \sqrt{A_0 + \mu^2}} + \frac{1}{2A_0^{3/2}} \log \left\{ \frac{2A_0}{\mu^2} + 1 \right. \\
& \left. + \frac{2}{\mu^2} \sqrt{A_0(A_0 + \mu^2)} \right\} , \quad (3.2)
\end{aligned}$$

where $A_0 = \vec{X}_0' \cdot \vec{X}_0'$. The parameter μ is related to the vortex core size through equation (2.17) and at any instant the core radius $a(t)$ may be computed from equation (2.11).

Starting from an initial ring configuration, the solution of equation (3.1) was advanced forward in time using a fourth-order

Runge-Kutta procedure. The spatial derivatives were computed at any instant using central differences and the numerical integrations were carried out using Simpson's rule.

Some typical results are shown in Figure 3.2 corresponding to a ring initially inclined at $\alpha \approx 135^\circ$ to the plane. For this calculation, $r < 0$ and so the vortex loop recedes from the wall; the initial core size was $a_0 = .005$ and the calculation was carried out with a time step $\Delta t = 0.005$ with 100 points on the vortex. The ring center was initially at $x = 0, y = 1.2$. As the vortex recedes from the wall, there is some contraction in the size of the loop until eventually the influence of the wall becomes negligible. Another case using the same numerical parameters is shown in Figure 3.3 for a ring which recedes from the wall on a normal trajectory; note that the ring radius decreases as the influence of the wall progressively diminishes.

3.3 Simulation of Hydrogen Bubble Lines

The vortex loop trajectories computed in the previous section are essentially unaltered if a uniform flow is superimposed in the positive x-direction, with the exception that the vortex loop is progressively convected to the right. In this section, the main interest is in determining the distortions that will occur in a pattern of simulated hydrogen bubble lines near the wall as the vortex convects over the bubble lines. Consider the schematic diagram in Figure 3.4; here a uniform flow of speed V is super-

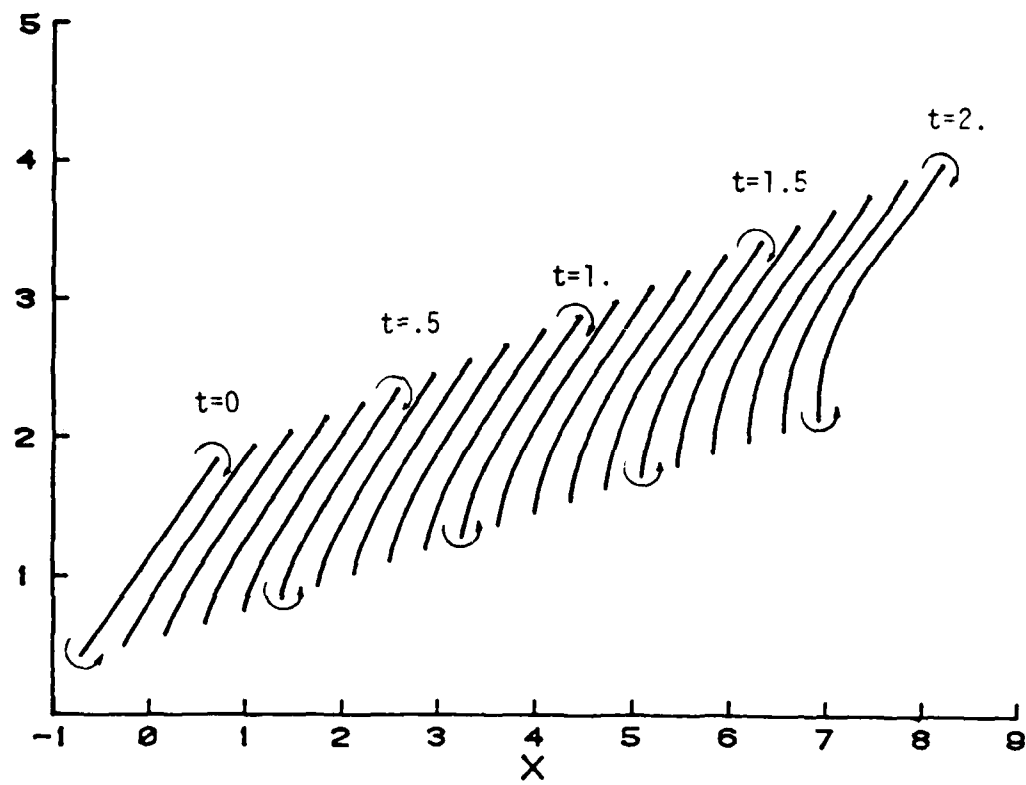
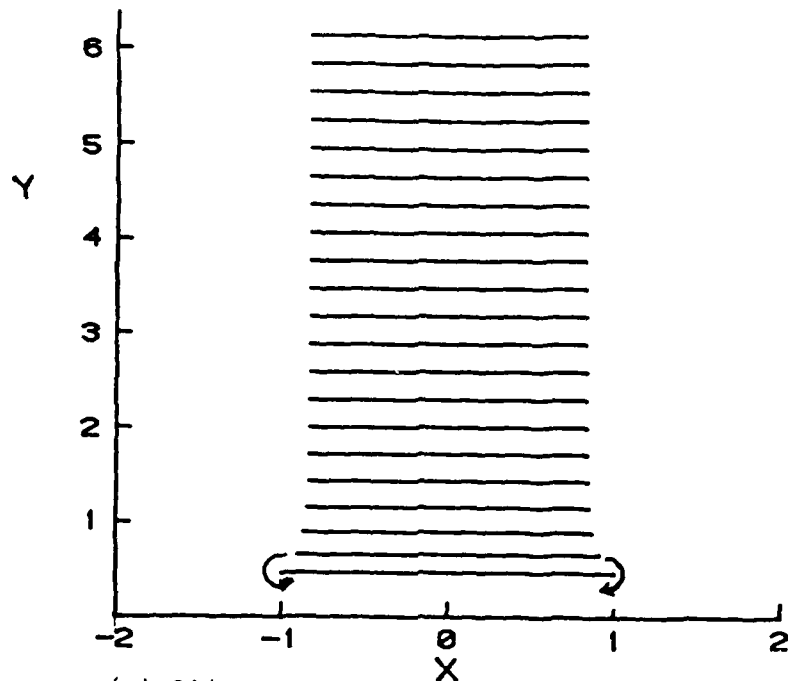
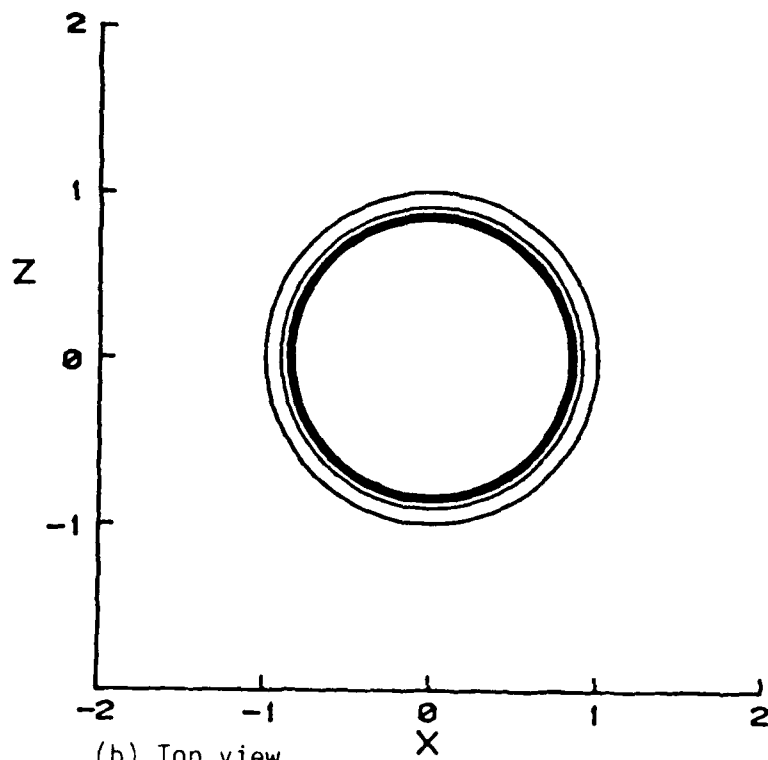


Figure 3.2 - Side view of the trajectory of vortex loop convected with speed $V = 5$ ($\alpha = 135^\circ$).

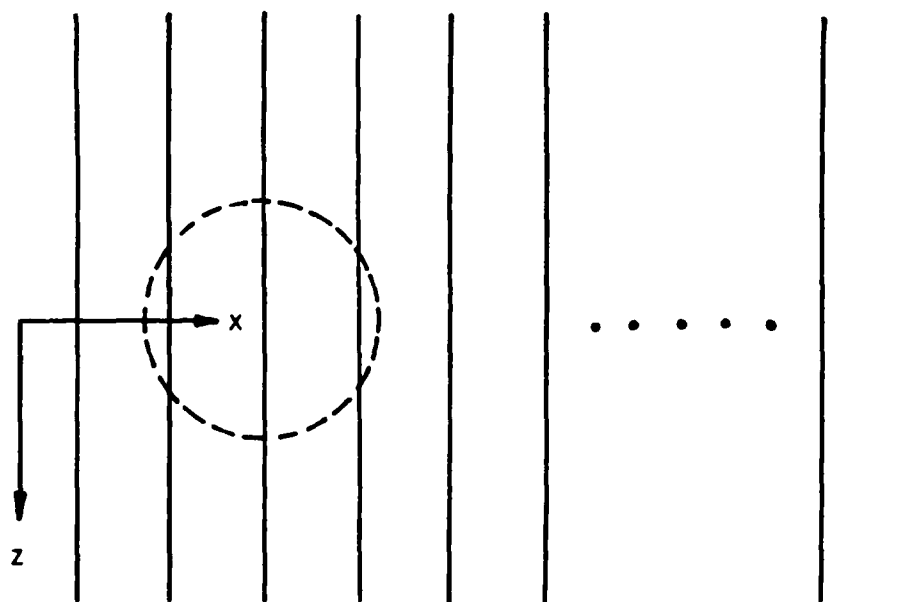
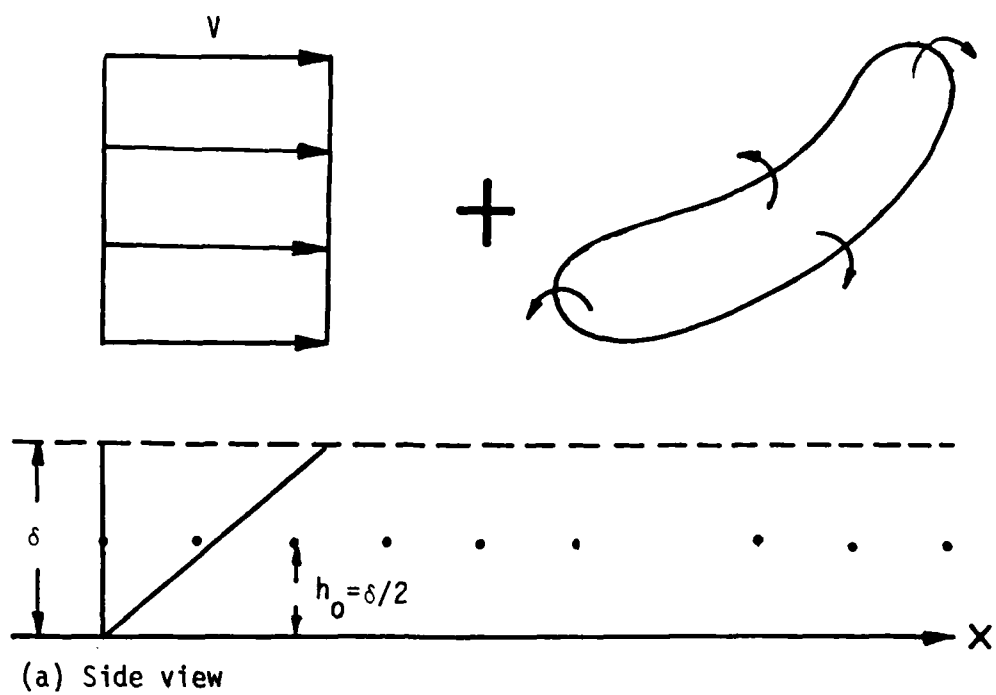


(a) Side view



(b) Top view

Figure 3.3 - Trajectory of a vortex ring moving normal to the wall.



(b) Top view

Figure 3.4 - Schematic diagram of hydrogen bubble line simulation.

imposed to the right so that the vortex loop is progressively convected to the right. To simulate a boundary-layer region with velocity gradients near the wall for $y < \delta$, the unsteady inviscid velocity distribution was multiplied by y/δ ; thus the velocity field for $y > 0$ is described by

$$\vec{V}(x,y,z,t) = \begin{cases} \vec{V}_{inv}(x,y,z,t) & y > \delta \\ \vec{V}_{inv}(x,y,z,t)(\frac{y}{\delta}) & y \leq \delta \end{cases} \quad (3.3)$$

A constant value of $\delta = 0.05$ was used in this simulation. It should be noted that this simulation is purely kinematical; a convected vortex will generally induce eruptive behavior in the viscous flow near the wall (Walker, 1978; Doligalski and Walker, 1984; Walker et al, 1987). The present simulation does not take account of this effect which will be addressed in Chapter 5.

Assume now that a hydrogen bubble wire is placed in the region of uniform shear near the wall at $y = h_0 = \delta/2$. When an electric current is passed through the wire, a line of hydrogen bubbles is produced in the water. In the absence of the vortex, these lines would convect downstream and remain straight lines; viewed from the side (Figure 3.4(a)). These lines would appear as a series of convecting points; the top view in the absence of the vortex is depicted in Figure 3.4(b). In the simulations that will be described, it was imagined that 17 equally spaced bubble lines were

placed in the flow near the wall; the vortex was then introduced into the flow and the subsequent trajectories of the bubble lines were computed numerically. Let \vec{H} denote the position vector to a point on a simulated bubble line; the trajectory of any point on the line may be computed from,

$$\frac{\partial \vec{H}}{\partial t} = \text{sgn}(r) \left\{ \int_{-1}^1 \frac{\partial \vec{X}}{\partial s} \times \frac{(\vec{H} - \vec{X})}{|\vec{H} - \vec{X}|^3} \Big|_{\text{vortex}} ds - \int_{-1}^1 \frac{\partial \vec{X}}{\partial s} \times \frac{(\vec{H} - \vec{X})}{|\vec{H} - \vec{X}|^3} \Big|_{\text{image}} ds \right\} f(y/\delta) , \quad (3.4)$$

where

$$f(y/\delta) = \begin{cases} V & y > \delta \\ \frac{Vy}{\delta} & y \leq \delta \end{cases} . \quad (3.5)$$

In the calculations that will be described 51 mesh points were used to discretize each of the simulated bubble lines. In the figures that will follow the projection of the convecting vortex loop in the xz plane will be shown as a broken line as indicated in Figure 3.4(b).

3.4 Calculated Results

Consider first the situation corresponding to a ring moving away from the wall on a normal trajectory ($\alpha = \pi/2$) with a uniform flow of speed $V = 6$ superimposed to the right. The trajectory is depicted in Figure 3.5 in side view. In Figure 3.6 the computed

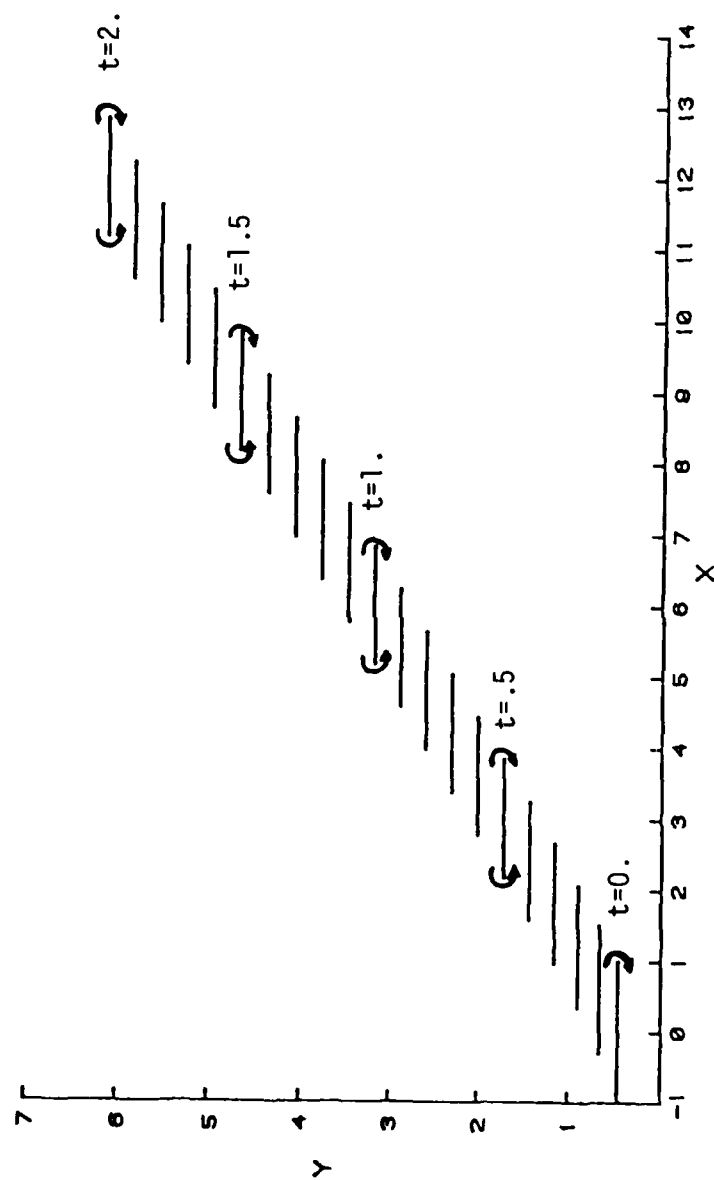
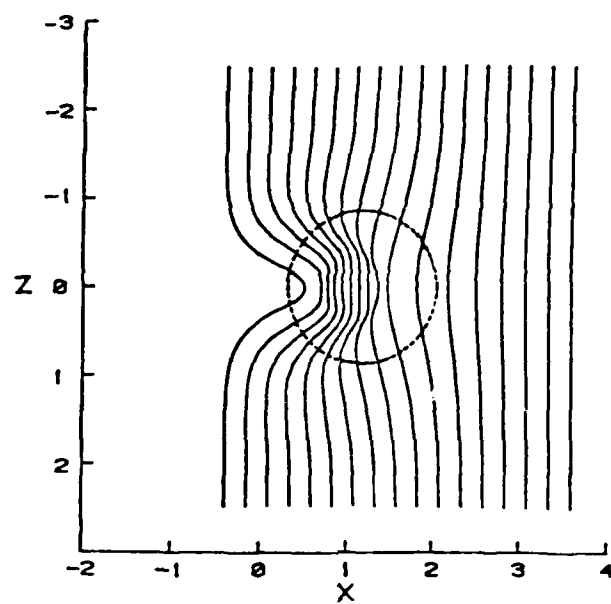
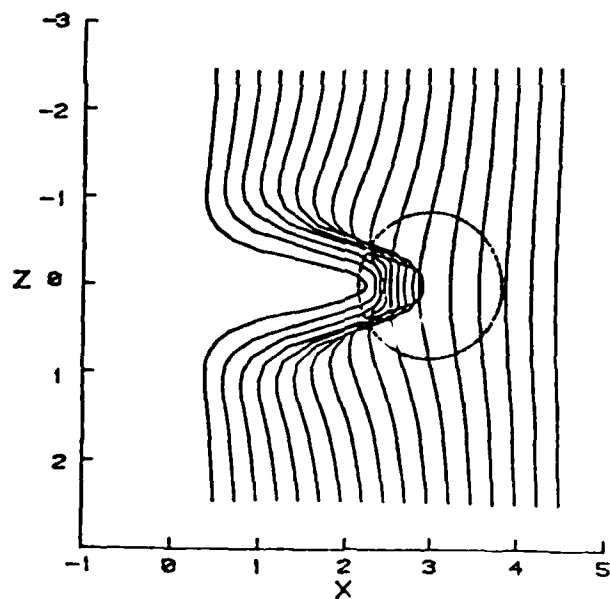


Figure 3.5 - Side view of the trajectory of a vortex ring convected with speed $V = 6$ ($\alpha=0^\circ$).

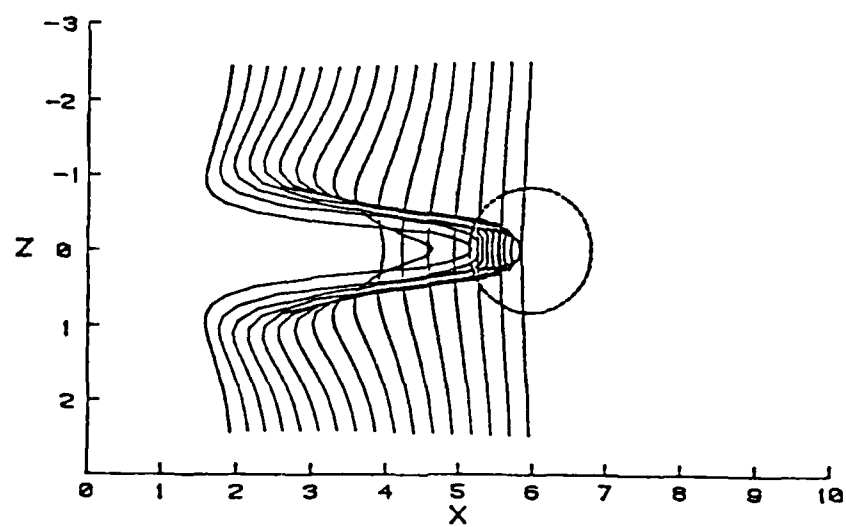


(a) $t=0.2$

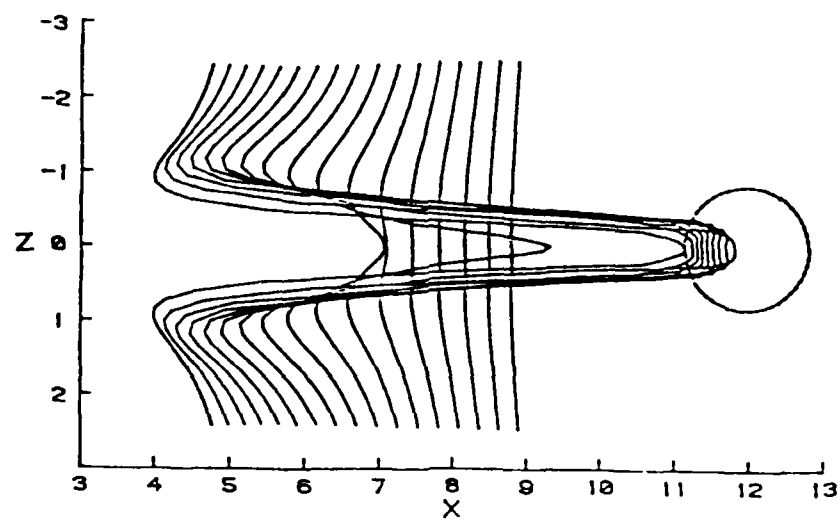


(b) $t=0.5$

Figure 3.6 - Temporal development of the simulated hydrogen bubble lines due to a convected ring ($V=6$).



(c) $t=1$.



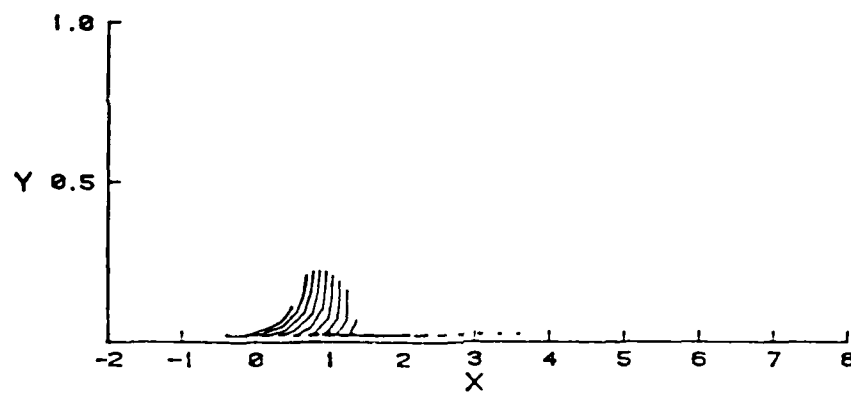
(d) $t=2$.

Figure 3.6 - Continued.

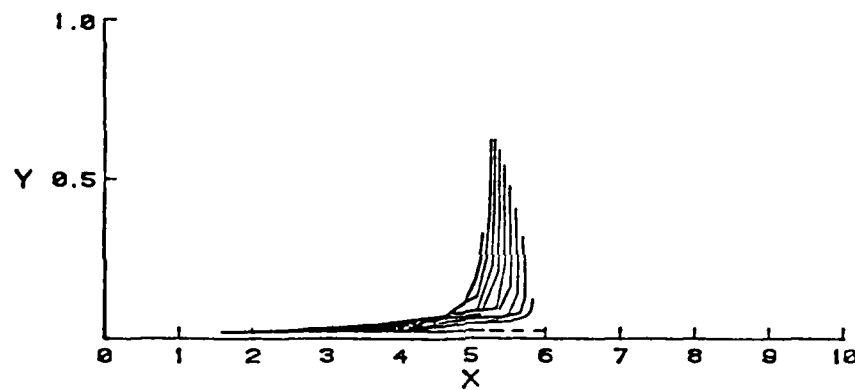
evolution of the simulated hydrogen bubble lines is shown at various stages of development. In Figures 3.7 and 3.8, the development is shown at various stages as viewed from the side and end on respectively; in these figures the dotted line represents the top of the simulated boundary-layer region at $y = \delta$. It may be observed, upon inspection of Figures 3.5, 3.6 and 3.7, that the motion induced by the convected ring vortex acts to concentrate the simulated hydrogen bubble lines into a "streaky" type of structure in the streamwise direction.

The second case detailed here corresponds to the same vortex configuration as in the first case but with the convection speed reduced 50% to $V = 3$. The vortex trajectory in side view is shown in Figure 3.9. The temporal development of the simulated hydrogen bubble lines for this case is shown in Figures 3.10, 3.11 and 3.12 in top, side and end views respectively. Again it may be observed that the effect of the convected ring is to draw the simulated flow markers into a "streaky" type of structure.

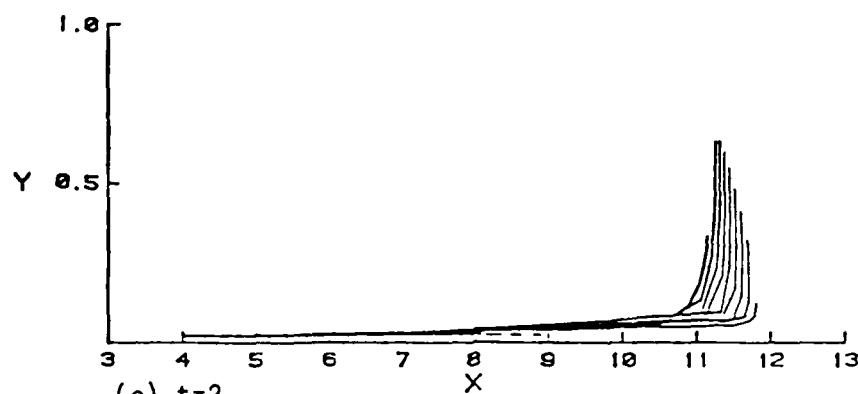
The last case considered here corresponds to a vortex ring which was initially started inclined at an angle of $\alpha = 135^\circ$ to the wall. In this case, the ring immediately starts to deform into a vortex loop shape; the trajectory is depicted in Figure 3.13 in a situation where the vortex is convected to the right with a speed of $V = 10$. Note that in this case the vortex stays closer to the wall than in the previous situations; as α is increased toward 180° , the



(a) $t=0.2$

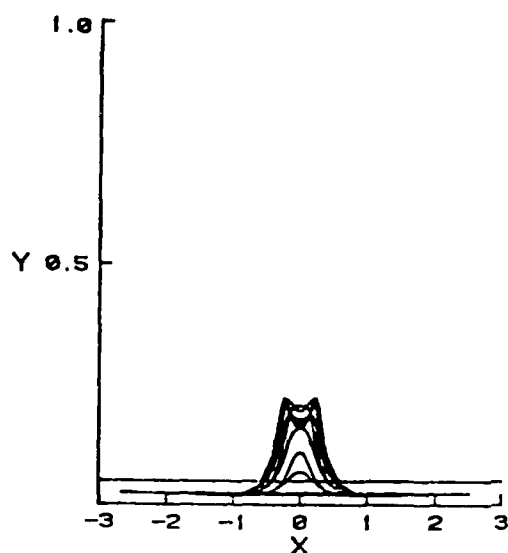


(b) $t=1$

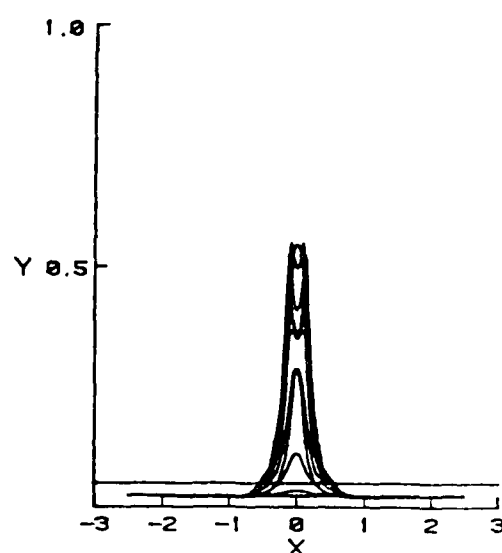


(c) $t=2$

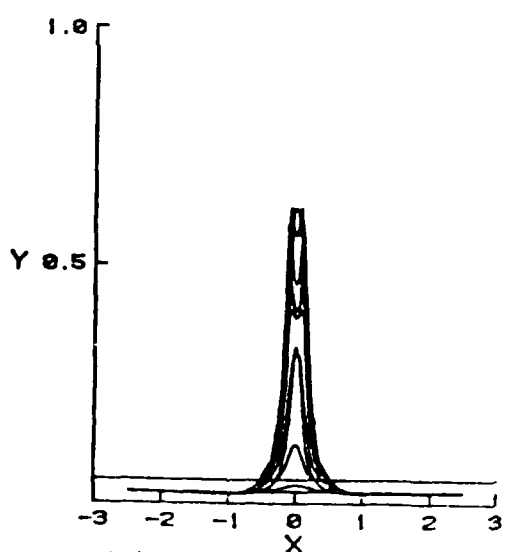
Figure 3.7 - Side view of the development of simulated hydrogen bubble lines due to a convected ring ($V=6$).



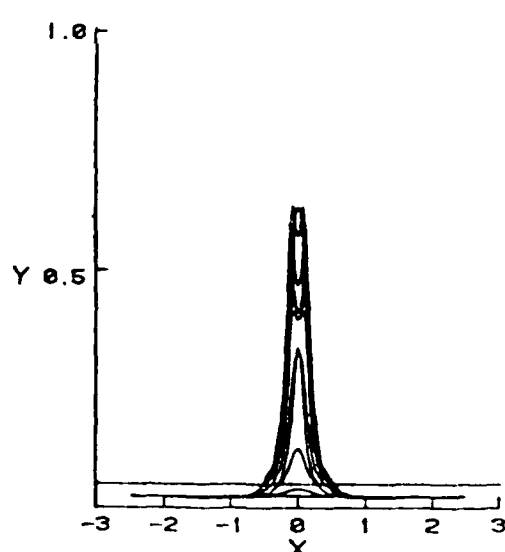
(a) $t=0.2$



(b) $t=0.5$



(c) $t=1$



(d) $t=2$

Figure 3.8 - End view of the development of simulated hydrogen bubble lines due to a convected ring ($V=6$).

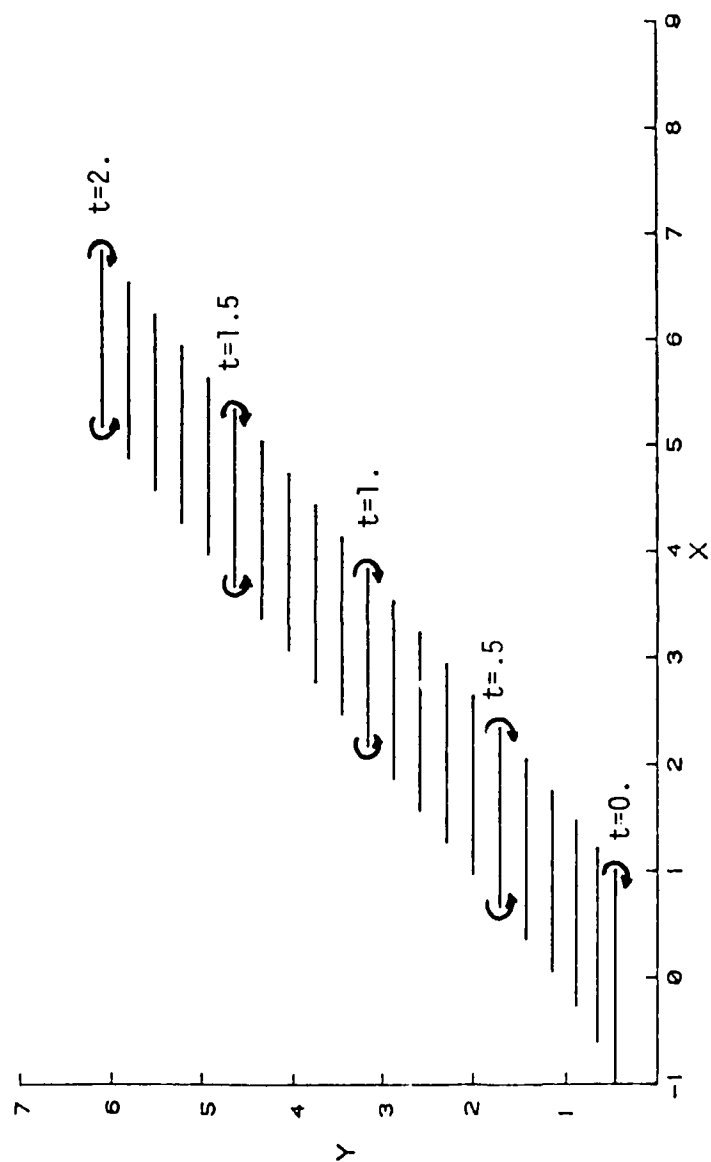
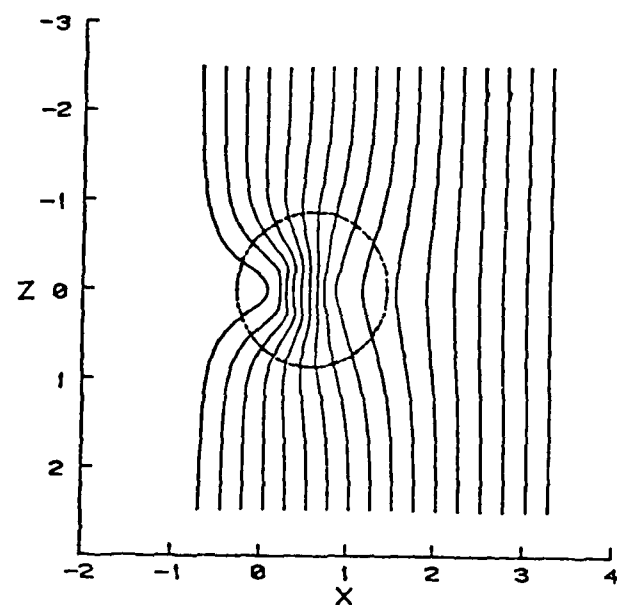
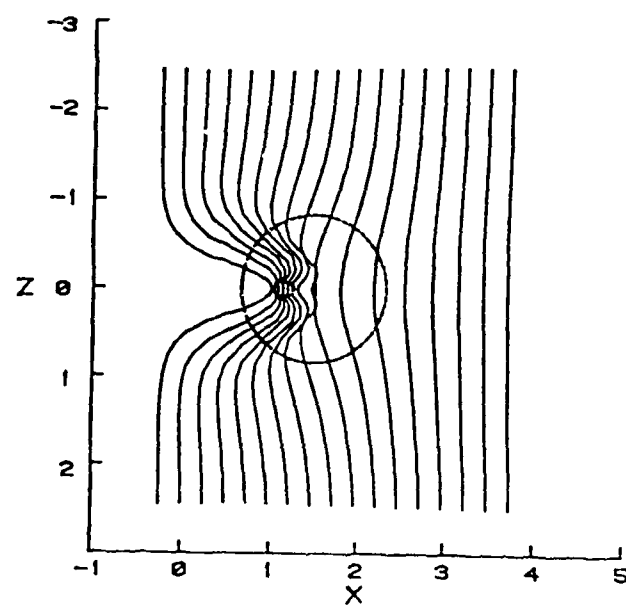


Figure 3.9 - Side view of the trajectory of a vortex ring convected with speed $V=3$.

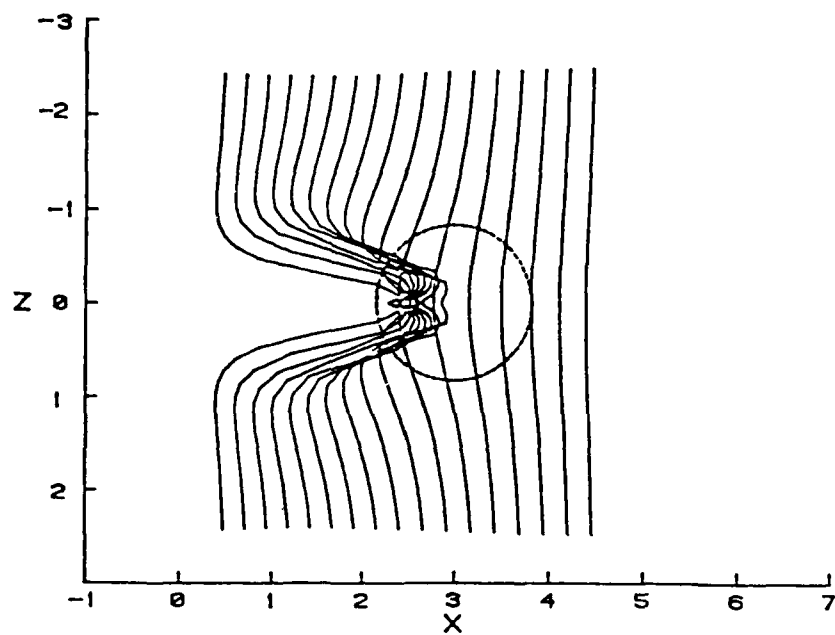


(a) $t=0.2$

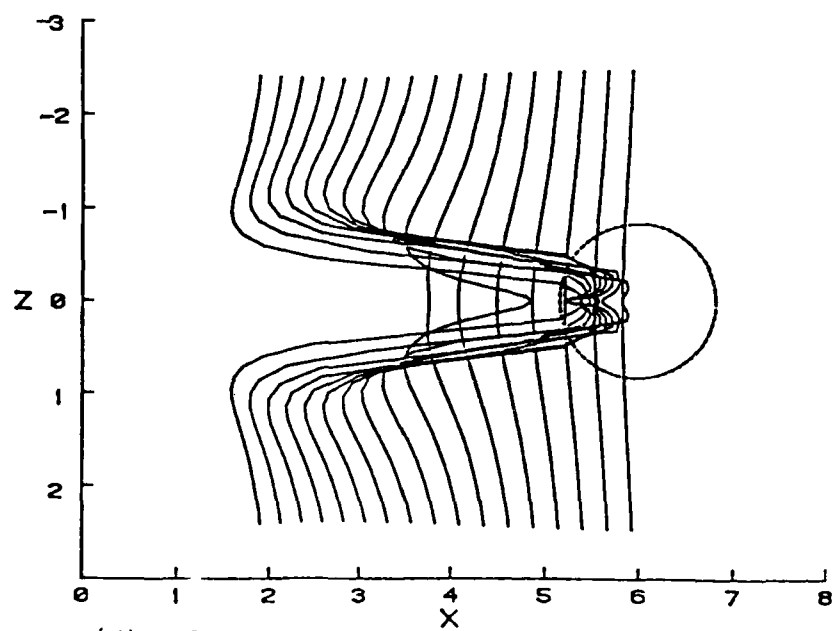


(b) $t=0.5$

Figure 3.10 - Temporal development of the simulated hydrogen bubble lines due to a convected ring ($V=3$).

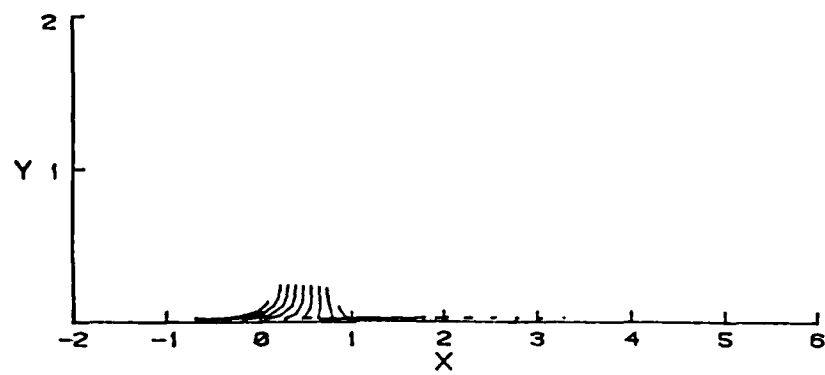


(c) $t=1$.

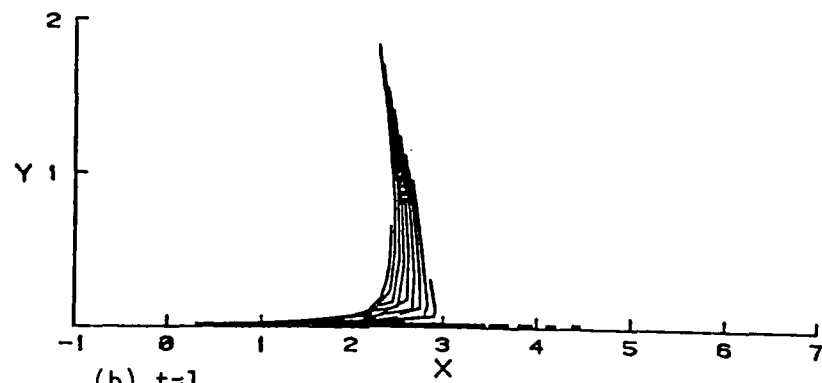


(d) $t=2$.

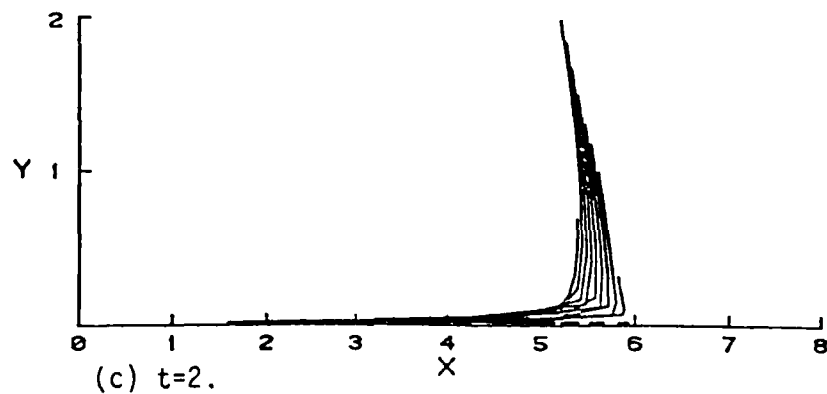
Figure 3.10 - Continued.



(a) $t=0.2$



(b) $t=1$.



(c) $t=2$.

Figure 3.11 - Side view of the development of simulated hydrogen bubble lines due to a convected ring ($V=3$).

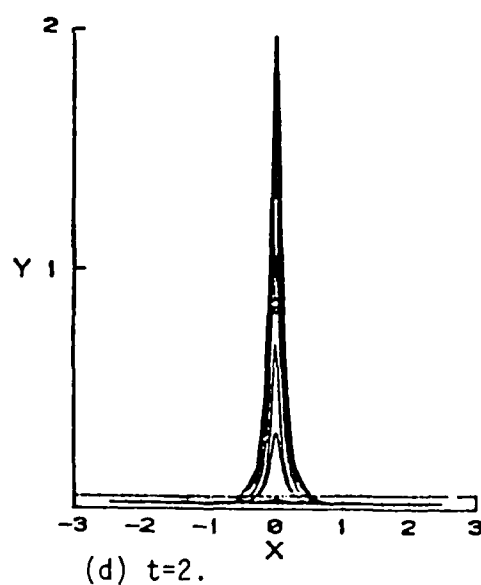
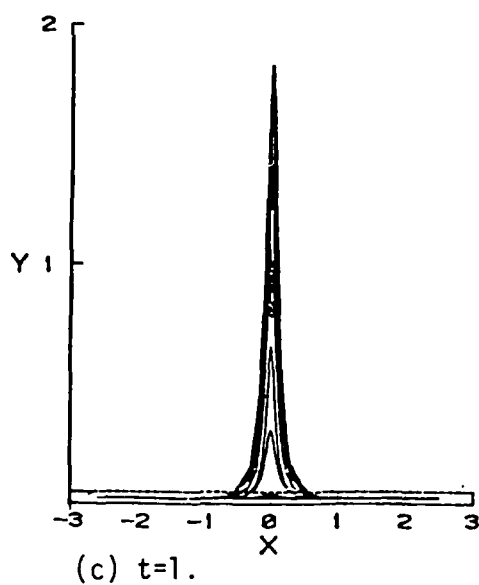
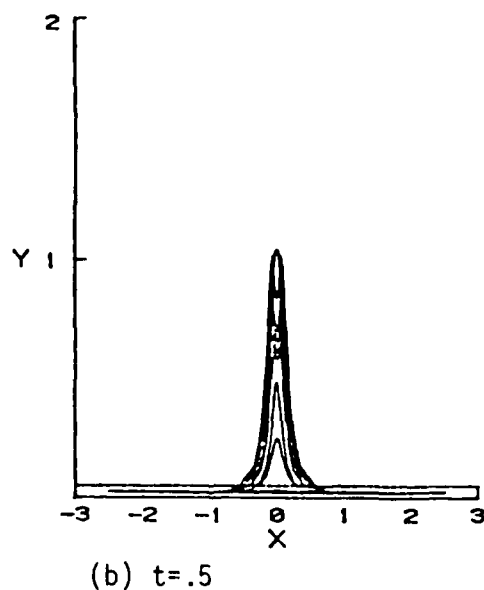
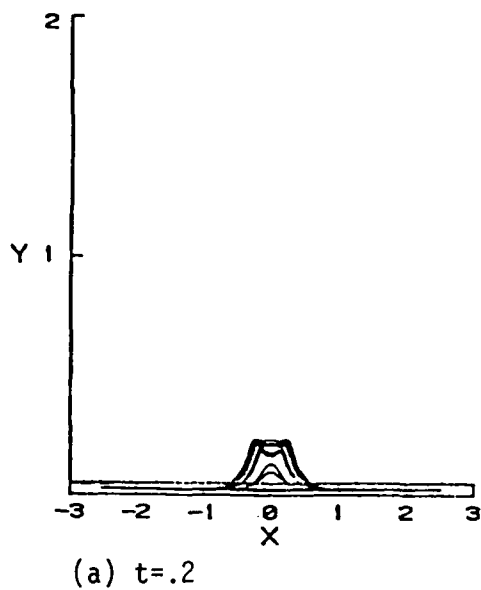


Figure 3.12 - End view of the development of simulated hydrogen bubble lines due to a convected ring ($V=3$).

trajectory of the vortex loop remains progressively closer to the wall. The deformation of the simulated hydrogen bubble lines in top, side and end views is shown in Figures 3.14, 3.15 and 3.16. Again it may be observed that the moving vortex collects the simulated flow markers into a streaky structure. The results obtained in this case are representative of all cases that were considered for $\alpha \neq 90^\circ$. For trajectories with α closer to 180° , the vortex remains closer to the wall; the simulated bubble lines are stretched to an increasing extent but also remain closer to the wall.

3.5 Conclusions

It may be concluded from the calculated results of this section that a convected vortex ring or vortex loop is one possible vortex motion which can give rise to a streaky structure in the flow near the wall. In Chapter 4, another type of vortex will be considered, namely the hairpin vortex, and it will be demonstrated that this type of vortex motion also gives rise to a "streaky" type of behavior.

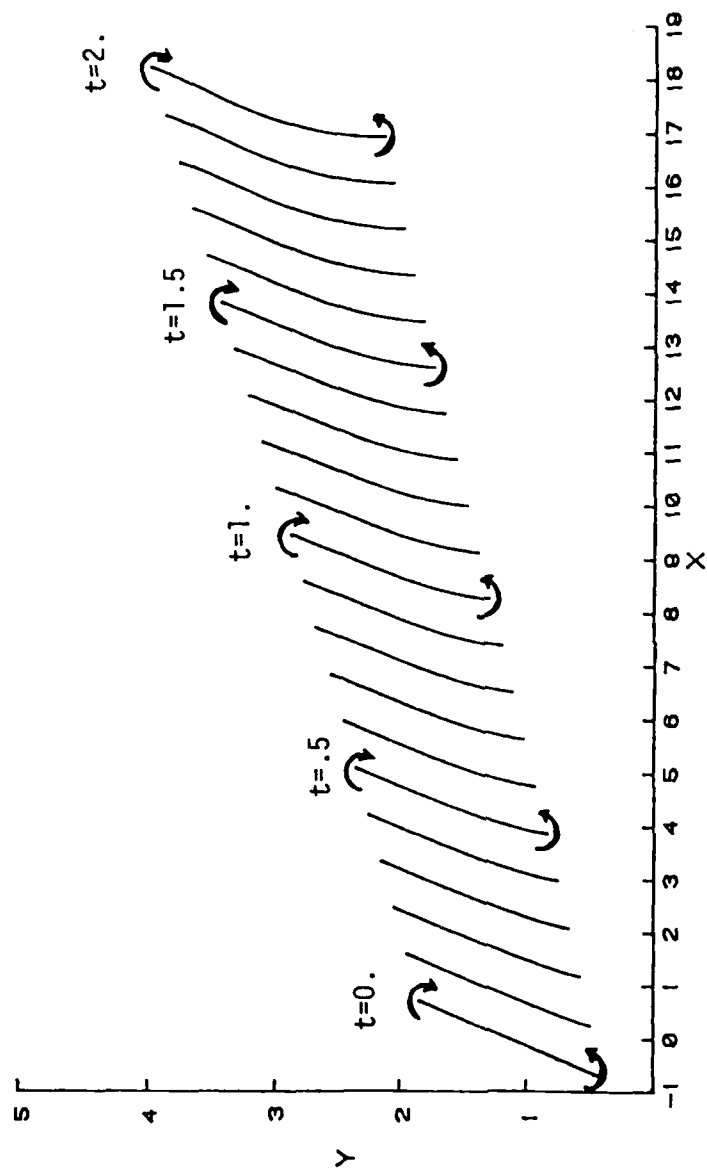
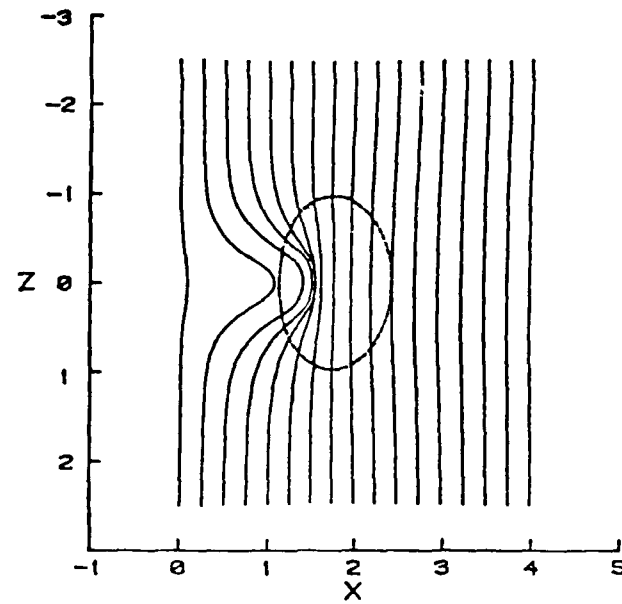
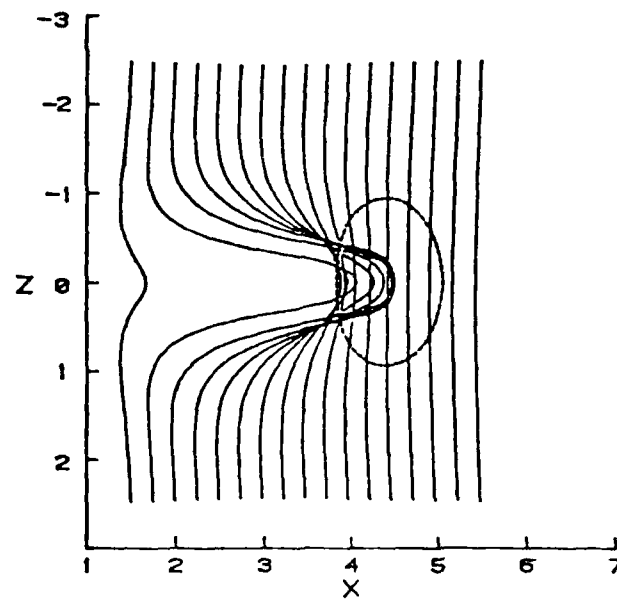


Figure 3.13 - Side view of the trajectory of a vortex loop convected with speed $V=10$ ($\alpha=135^\circ$).

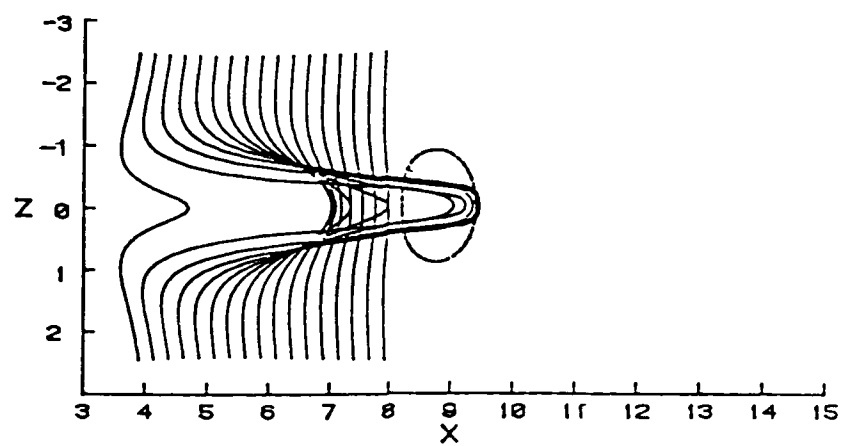


(a) $t=.2$

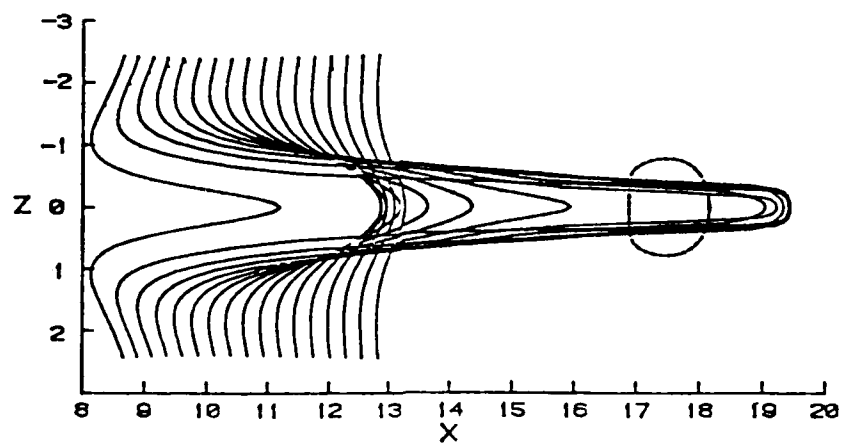


(b) $t=.5$

Figure 3.14 - Temporal development of the simulated hydrogen bubble lines due to a convected vortex loop ($V=10$).

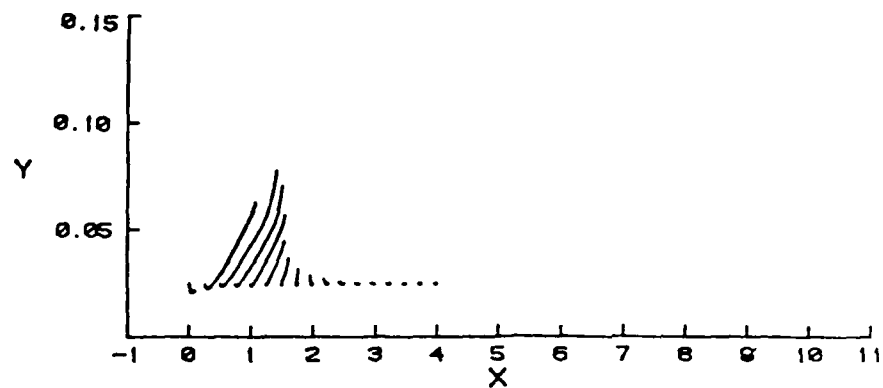


(c) $t=1$.

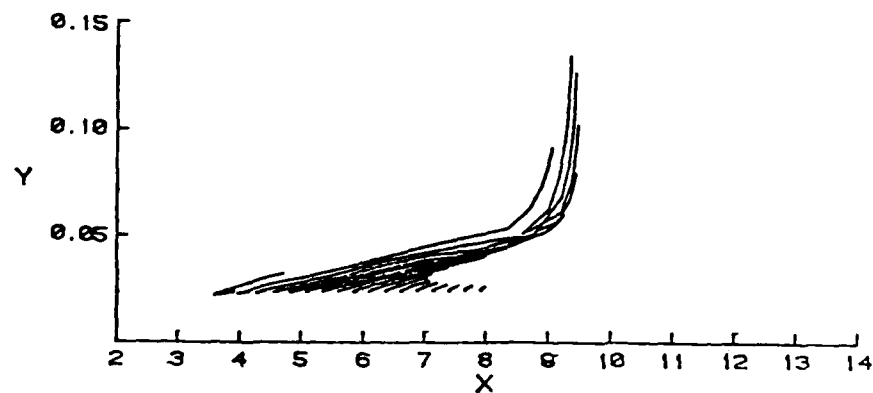


(d) $t=2$.

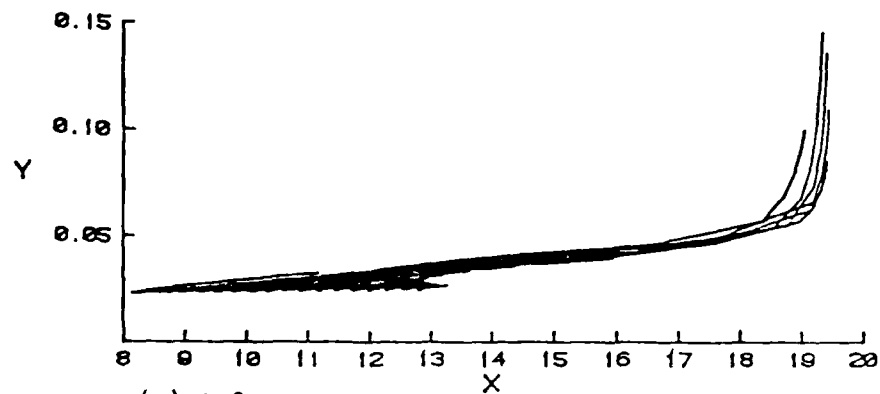
Figure 3.14 - Continued.



(a) $t=0.2$



(b) $t=1$



(c) $t=2$

Figure 3.15 - Side view of the development of simulated hydrogen bubble lines due to a convected vortex loop with speed $V=10$ ($\alpha=135^\circ$).

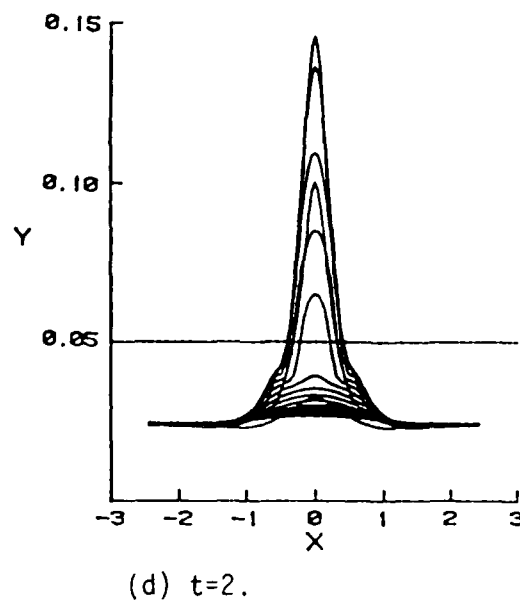
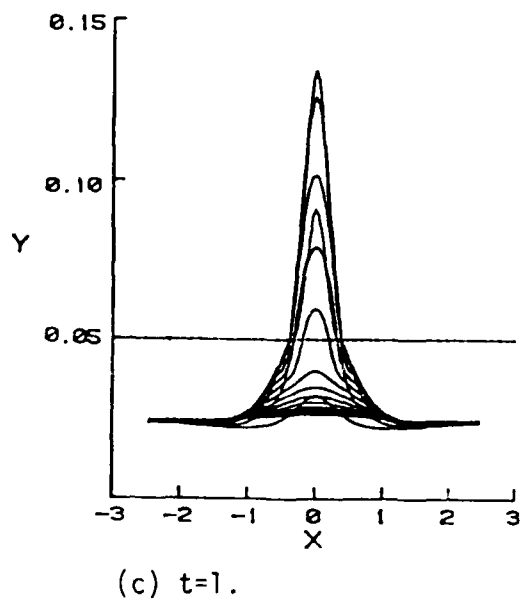
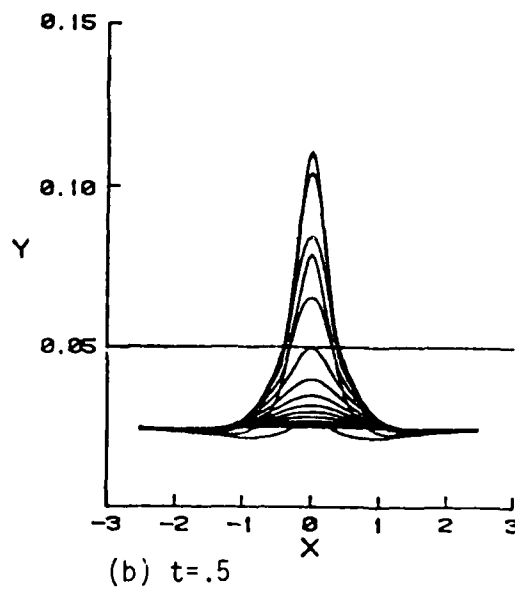
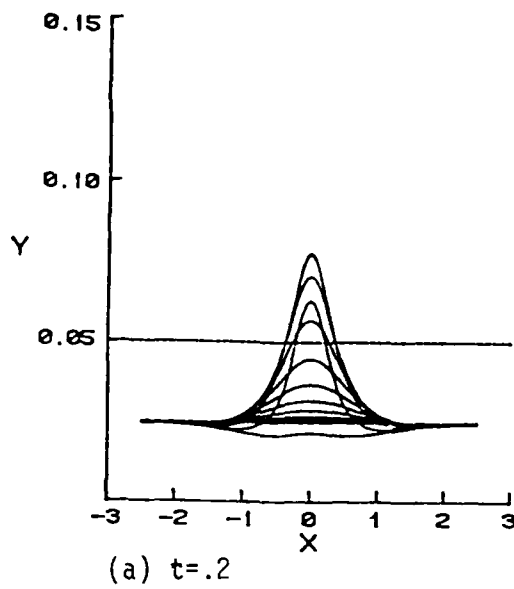
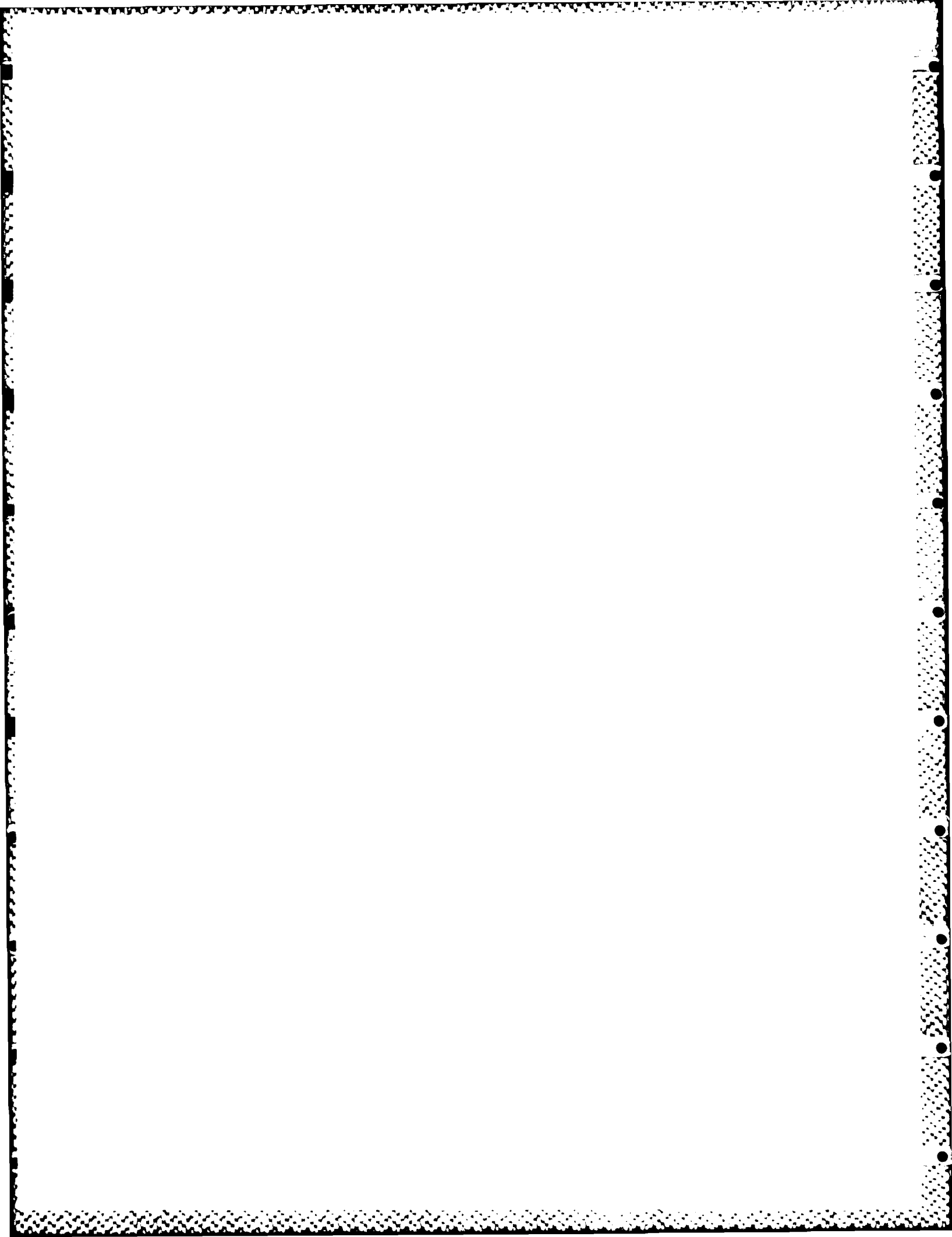


Figure 3.16 - End view of the development of simulated hydrogen bubble lines due to a convected vortex loop with speed $V=10$ ($\alpha=135^\circ$).



CHAPTER 4

THE EVOLUTION OF A HAIRPIN VORTEX

4.1 Introduction

In recent times it has become evident that the hairpin vortex may be a principal flow structure of the turbulent boundary layer. This viewpoint was expressed first in an early study by Theodorsen (1952) and a number of contemporary experimental studies have supported this idea (see for example Head and Bandyopadhyay, 1981; Perry and Chong, 1982 and Acarlar and Smith, 1984, 1987a, 1987b). In this chapter, the nature of the evolution of a hairpin vortex in a background flow is considered. The calculations described here are inviscid simulations which are based on an appropriate discretization of the Biot-Savart law. The plan of the chapter is as follows. In Section 4.2, the equations of motion governing the evolution of a three-dimensional distortion in an otherwise two-dimensional vortex are described; the numerical scheme used to compute the trajectory of the vortex is described in Section 4.3. Calculations for the evolution of a hairpin vortex in either a stagnant or uniform flow above a plane wall are described in Section 4.4. Computations for the development of a hairpin vortex in a shear flow above a wall are discussed in Section 4.5 and a discussion of results is given in Section 4.6. The effect of moving vortices is often observed experimentally using hydrogen bubble wires in water flows; in Section 4.7, the results of a numerical simulation are

described wherein the evolution of simulated hydrogen bubble lines was computed numerically as a hairpin vortex in a shear flow convected past. In Section 4.8, the nature of the streamwise velocity fluctuation induced by a moving hairpin vortex is described. Finally, calculations for the evolution of a pair of interacting hairpin vortices in a shear flow are described in Section 4.9.

4.2 Equation of Motion

It is convenient to develop the equations of motion in a dimensionless form and for the hairpin vortex motion of interest, it is necessary to define a velocity and length scale. Consider first the situation depicted in Figure 4.1(a) where a two-dimensional vortex of constant strength κ is located a distance d above a plane wall. For the sense of circulation indicated in Figure 4.1(a), inviscid theory predicts that the vortex will move to the left with speed,

$$U_0 = \frac{\kappa}{2d} , \quad (4.1)$$

and remain at constant height d above the wall as it convects in the velocity field of the image vortex below the plate. Now consider the more complex situation depicted in Figures 4.1(b) and 4.1(c) where a hairpin is in motion above a plane wall. In the present study, the hairpin was taken to evolve from a small local distortion in a two-dimensional vortex; at large distances from the hairpin the vortex will continue to behave like a two-dimensional vortex. For the present purposes, it is convenient to define dimensionless

NO-A187 261

AN ANALYSIS OF THE MOTION AND EFFECTS OF HAIRPIN
VORTICES(U) LEHIGH UNIV BETHLEHEM PA DEPT OF MECHANICAL
ENGINEERING AND M. T HON ET AL. JUN 87 FM-11

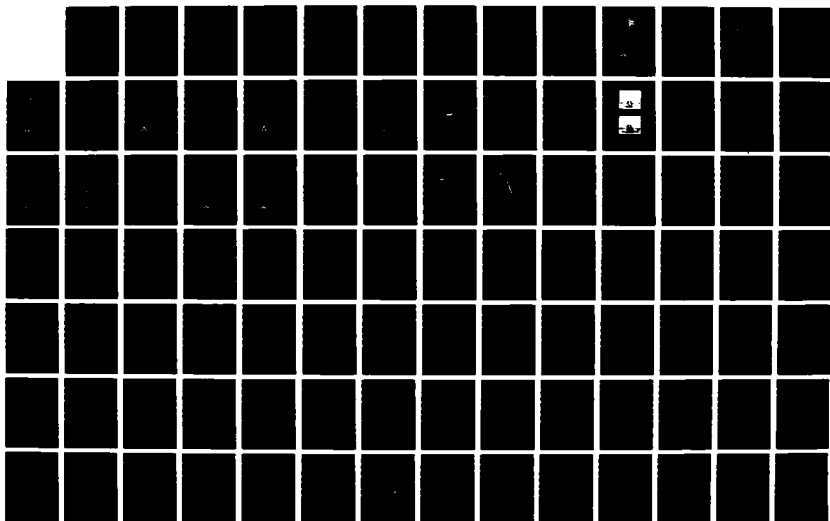
2/3

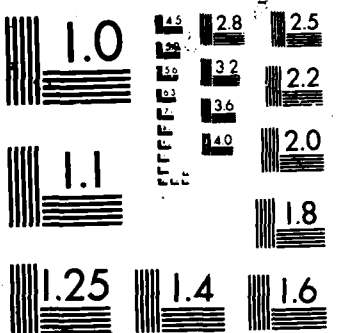
UNCLASSIFIED

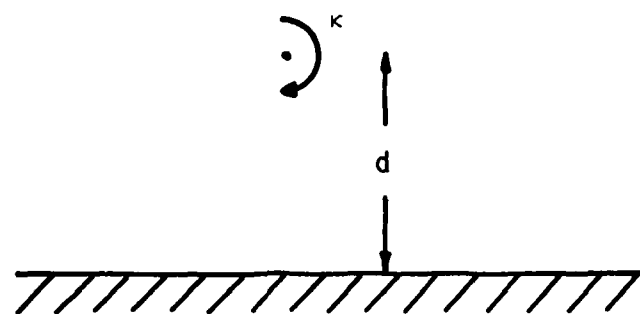
AFOSR-TR-87-1389 F49620-85-C-0100

F/G 20/4

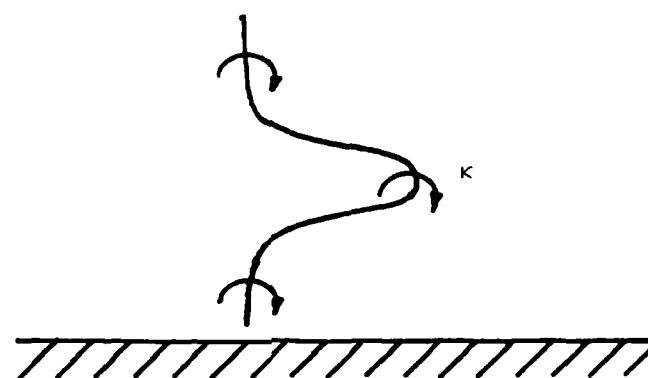
NL



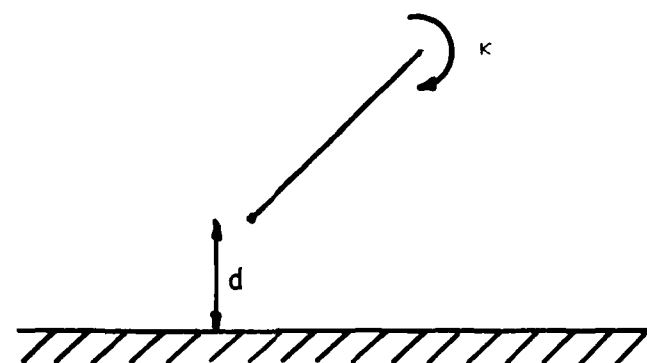




(a) Two-dimensional vortex (side view)



(b) Hairpin vortex (oblique view)



(c) Hairpin vortex (side view)

Figure 4.1 - Vortex motion above a wall.

variables in terms of d and the velocity defined by equation (4.1) according to

$$\vec{X} = \frac{\vec{X}^*}{d} , \quad t = \frac{t^* U_0}{d} = \frac{\kappa t^*}{2d^2} , \quad (4.2)$$

where the asterisks are used to denote a dimensional quantity. Note that the magnitude of the circulation $|\Gamma|$ is related to the vortex strength κ by,

$$|\Gamma| = 2\pi \kappa . \quad (4.3)$$

For situations of interest in the present study, $\Gamma < 0$ (c.f. Figure (4.1)) and the initial vortex configuration used is given by,

$$\vec{X}(s,t) = A\{\cos\alpha\hat{i} + \sin\alpha\hat{j}\}e^{-\beta s^2} + \hat{j} + s\hat{k} . \quad (4.4)$$

This configuration corresponds to a two-dimensional vortex located at a distance l from the wall with a symmetrical three-dimensional distortion centered at $s = 0$. Here A represents the amplitude of the distortion and α is the angle the plane of the distortion makes with the plane wall; in addition β is a (large) number whose value determines the width or spread of the distortion. The parameter s is a Lagrangian coordinate which ranges from $-\infty$ to $+\infty$ along the vortex.

The integrals involved in the Biot-Savart law are over infinite ranges. However it is not possible to carry out a numerical inte-

gration for infinite values of s and in practice, the computations must be carried out up to some large but finite value of s , say $s = \pm \ell$. For $|s| > \ell$, the vortex filament was assumed to remain as a straight line and

$$\vec{X}(s,t) = \hat{i} + \hat{j} + s\hat{k} \quad , \quad |s| > \ell \quad . \quad (4.5)$$

Note that ℓ must be selected large enough to ensure that there is no significant effect on the development of the hairpin vortex; as the hairpin vortex begins to spread in the spanwise direction, it was necessary to continually increase the value of ℓ .

In the present case, the generalization of equation (2.20) (in dimensionless variables) for a vortex filament of infinite length is

$$\frac{\partial \vec{X}}{\partial t}(s_0,t) = \sum_{j=1}^7 \vec{I}_j(s_0,t) + \vec{u}_{\text{ext}} \quad , \quad (4.6)$$

where the integrals \vec{I}_j are defined by the following expressions:

(1) The Integrals on the Main Part of the Vortex

$$\vec{I}_1 = \int_{-\ell}^{-h} \vec{Q}_v(s,s_0,t) ds \quad , \quad \vec{I}_2 = \int_h^{\ell} \vec{Q}_v(s,s_0,t) ds, \quad (4.7)$$

where

$$\vec{Q}_v = - \frac{\partial \vec{X}}{\partial s} \times \frac{(\vec{X}_0 - \vec{X})}{\{|\vec{X}_0 - \vec{X}|^{2+\mu^2}\}^{3/2}} + \left(\frac{\partial \vec{X}}{\partial s}\right)_0 \times \left(\frac{\partial^2 \vec{X}}{\partial s^2}\right)_0 P(s,s_0). \quad (4.8)$$

Here P is defined by equation (2.13), the variable s is a Lagrangian coordinate along the vortex and the subscript o implies that a quantity is evaluated at a specific point $s = s_o$ where the local velocity is being computed in equation (4.6). In addition, the quantity h denotes the half-interval removed from the conventional integration over the vortex; for $|s| < h$, the representation of the integrand is replaced by the series expansion given in Appendix B and there is

(2) The Integral Near the Field Point

$$\vec{I}_3 = \int_{-h}^h R(s, s_o, t) ds, \quad (4.9)$$

where \vec{R} is defined by equation (2.19) and corresponds to the detailed series expansions near $s = s_o$ given in equation (B.8) (Appendix B);

(3) The Integrals on the Straight Part of the Vortex

$$\vec{I}_4 = \int_{-\infty}^{-\ell} Q_{v\infty} ds + \int_{\ell}^{\infty} Q_{v\infty} ds, \quad (4.10)$$

where,

$$\vec{Q}_{v\infty} = - \frac{\partial \vec{X}}{\partial s} \times \frac{(\vec{X}_o - \vec{X})}{\{|\vec{X}_o - \vec{X}|^2 + \mu^2\}^{3/2}}; \quad (4.11)$$

(4) The Integral of the P function

$$\vec{I}_5 = \left(\frac{\partial \vec{X}}{\partial s} \right)_o \times \left(\frac{\partial^2 \vec{X}}{\partial s^2} \right)_o \int_{-\ell}^{\ell} P(s, s_o) ds, \quad (4.12)$$

where P is defined by equation (2.13);

(5) The Integral on the Main Part of the Image Vortex

$$\vec{I}_6 = \int_{-l}^l \vec{Q}_i ds, \quad (4.13)$$

where,

$$\vec{Q}_i = \frac{\partial \vec{X}}{\partial s} \times \frac{(\vec{X}_0 - \vec{X})}{|\vec{X}_0 - \vec{X}|^3}, \quad (4.14)$$

and finally,

(6) The Integrals on the Straight Part of the Image Vortex

$$\vec{I}_7 = \int_{-l}^{\infty} \vec{Q}_i ds + \int_l^{\infty} \vec{Q}_i ds, \quad (4.15)$$

where \vec{Q}_i is defined by equation (4.14).

The integrals (4.7), (4.9) and (4.13) were evaluated numerically using a procedure based on Simpson's rule; the remaining integrals were evaluated analytically. The integral appearing in equation (4.12) is,

$$\begin{aligned} \int_{-l}^l P(s, s_0) ds = \frac{1}{B_0} & \left\{ \frac{(s_0 - l)}{\{B_0(s_0 - l)^2 + \mu^2\}^{1/2}} - \frac{(s_0 + l)}{\{B_0(s_0 + l)^2 + \mu^2\}^{1/2}} \right. \\ & \left. + \frac{1}{B_0^{1/2}} \log \left[\frac{\{B_0(s_0 - l)^2 + \mu^2\}^{1/2} - B_0^{1/2}(s_0 - l)}{\{B_0(s_0 + l)^2 + \mu^2\}^{1/2} - B_0^{1/2}(s_0 + l)} \right] \right\}, \quad (4.16) \end{aligned}$$

where,

$$B_0 = \left(\frac{\partial \vec{X}}{\partial s} \right)_0 \cdot \left(\frac{\partial \vec{X}}{\partial s} \right)_0 \quad (4.17)$$

To evaluate the integrals in equation (4.10), it is first noted that along the straight portions of the vortex,

$$\vec{Q}_{v\infty} = \frac{(y_0 - y)\hat{i} - (x_0 - x)\hat{j}}{\{(x - x_0)^2 + (y_0 - y)^2 + (z_0 - s)^2 + \mu^2\}^{3/2}} \quad , \quad |s| \geq \ell \quad , \quad (4.18)$$

where (x_0, y_0, z_0) are the coordinates of the field point on the main part (the curved portion) of the vortex at $s = s_0$; $x(t)$ and $y(t)$ are the streamwise and normal coordinates of points on the straight part of the vortex. For fixed t , $x(t)$, $y(t)$ and (x_0, y_0, z_0) are fixed and upon taking the integrals indicated in equation (4.10) it is easily shown that,

$$I_4 = \left\{ \frac{(y_0 - y)\hat{i} - (x_0 - x)\hat{j}}{(x_0 - x)^2 + (y_0 - y)^2 + \mu^2} \right\} \left\{ 2 + \frac{(z_0 - \ell)}{\{(x_0 - x)^2 + (y_0 - y)^2 + (z_0 - \ell)^2 + \mu^2\}^{3/2}} - \frac{(z_0 + \ell)}{\{(x_0 - x)^2 + (y_0 - y)^2 + (z_0 + \ell)^2 + \mu^2\}^{3/2}} \right\} \quad (4.19)$$

In a similar manner, the corresponding integrals in equation (4.15) may be evaluated along the straight part of the image vortex with the result that,

$$\vec{I}_7 = - \left\{ \frac{(y_0 + y)\hat{i} - (x_0 - x)\hat{j}}{(x_0 - x)^2 + (y_0 + y)^2} \right\} \left\{ 2 + \frac{(z_0 - \ell)}{\{(x_0 - x)^2 + (y_0 + y)^2 + (z_0 - \ell)^2\}^{3/2}} - \frac{(z_0 + \ell)}{\{(x_0 - x)^2 + (y_0 + y)^2 + (z_0 + \ell)^2\}^{3/2}} \right\} \quad (4.20)$$

4.3 Numerical Methods

Starting from the initial vortex configuration described by equation (4.4), the subsequent shape of the vortex was tracked forward in time using the standard fourth-order Runge-Kutta algorithm. The initial vortex was split into a number of equal increments in the variable s and the subsequent motion of each point corresponding to a fixed value of s was tracked forward in time. The spatial gradients in equations (4.8), (4.12) and (4.14) were evaluated using three-point central difference formulae and the integrations in equations (4.7), (4.9) and (4.10) were carried out (at fixed t) using Simpson's rule. After some experimentation, the value of h (in equations (4.7) and (4.9)) used corresponded to one mesh length in s .

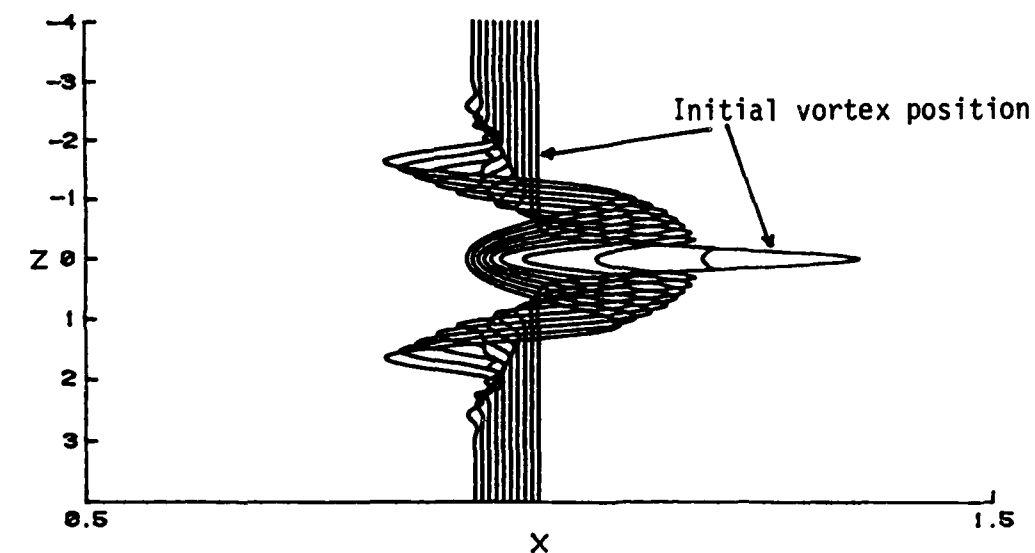
4.4 The Evolution of a Hairpin Vortex in Stagnant Flow

In the cases discussed in this section, the vortex was assumed to have the initial configuration given by equation (4.4) and to be in an otherwise stagnant flow above the wall ($\vec{u}_{\text{ext}} = 0$ in equation (4.6)). Note however that the subsequent development of the vortex in this case is identical to that for a vortex in a uniform flow ($\vec{u}_{\text{ext}} = U_0 \hat{i}$) with the exception that the vortex would be convected to the right (for $U_0 > 0$). In all cases considered the vortex was assumed to have a small core radius $a = 0.02$ which was held constant during the integration. Note that this may be approximation; the theory of Moore and Saffman (1972) applies only to closed filaments

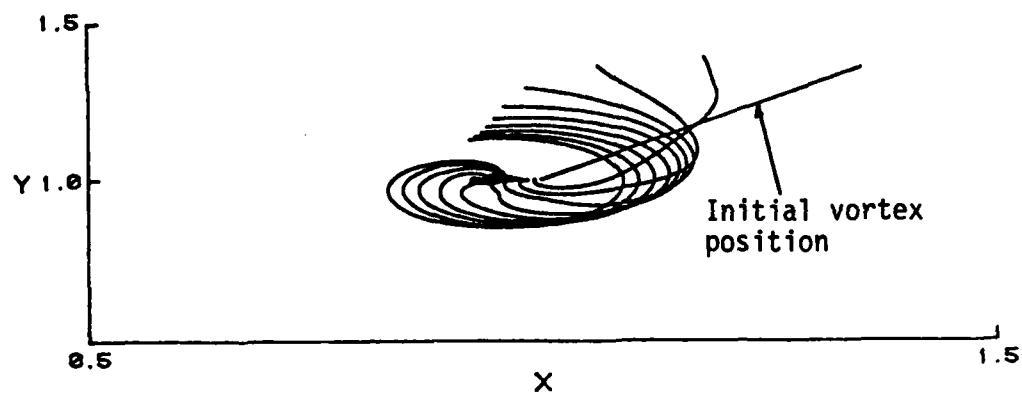
and a relationship like equation (2.10) cannot be used since a discontinuity in core size would ultimately develop at $s = \pm \ell$. The more recent theory of Callegari and Ting (1978) also applies only to closed loop vortices.

In the first case considered, the hairpin vortex was assumed to have an initial amplitude of $A = 0.5$ and angle of inclination of $\alpha = 45^\circ$ in equation (4.4); the value of the spread parameter β used was 20. It emerges that the self-induced velocities predicted by the Biot-Savart law are rather large, particularly near $s = 0$ where the curvature of the vortex is initially largest. Consequently it was necessary to take rather small time steps in order to avoid the occurrence of "wiggles" or sharp corners in the vortex shape; once such anomalies appear, the numerical scheme rapidly breaks down. A time step of $\Delta t = 0.0002$ was used in the integrations. For the first case, a uniform mesh size of $\Delta s = 0.005$ was used and initially the value of ℓ employed was $\ell = 2$. Therefore in the initial phases of the integration, there were 800 points along the vortex from $(-\ell, \ell)$. As t increased and the hairpin began to spread to the side, the value of ℓ was increased to $\ell = 3$ at $t = 0.03$ and then to $\ell = 4$ at $t = 0.06$. The calculations are very time consuming and were stopped at $t = .072$ when the general trends were evident.

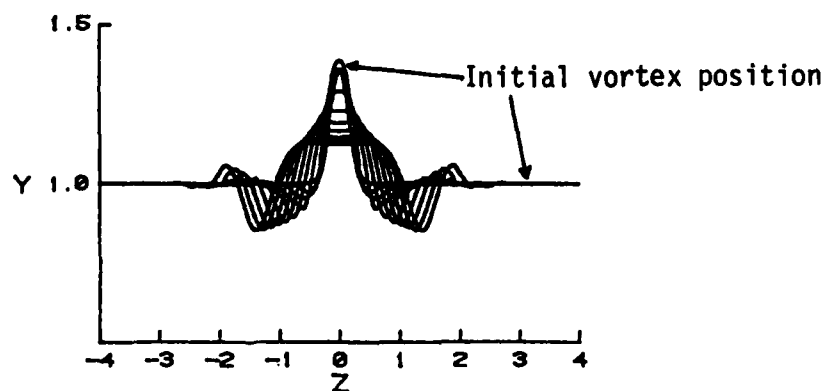
In Figures 4.2(a), 4.2(b) and 4.2(c), the evolution of the hairpin is plotted for case 1 in top, side and end views respectively; the vortex is drawn at intervals corresponding to every 40 time steps.



(a) Top view



(b) Side view

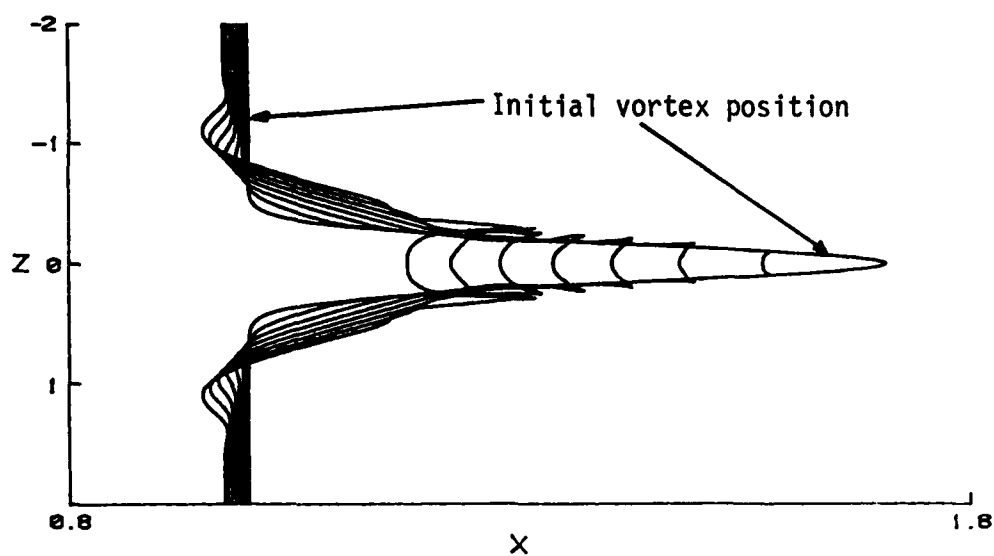


(c) End view

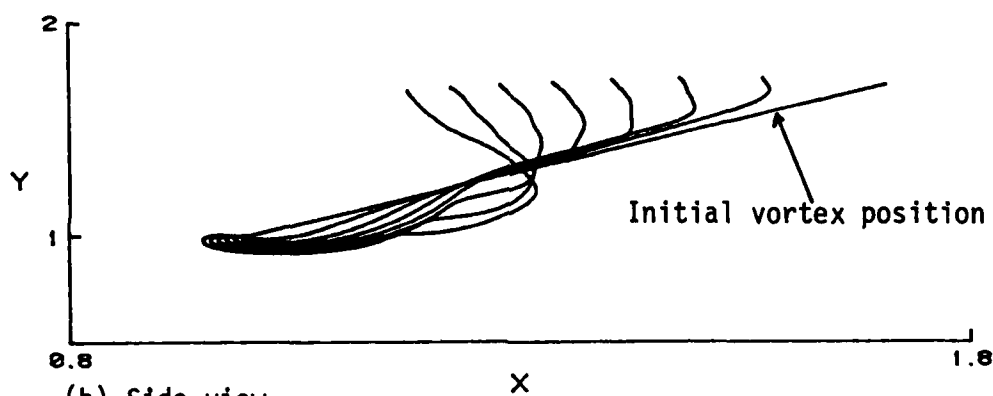
Figure 4.2 - Temporal development for a hairpin vortex in a stagnant flow. Case 1 ($\alpha=45^\circ$, $A=0.5$, $\beta=20$); the vortex position is plotted every 40 time steps ($\Delta t=0.0002$).

It may be observed that the head of the vortex (corresponding to the tip of the distortion) moves rapidly backward and after a brief interval starts to move downward toward the wall. The rate of movement of the head should be contrasted with the relatively slow backward movement of the straight portions of the vortex; for $|z| > 3$, the vortex moves basically in the velocity field of its image and advances slowly upstream. It is evident that on the curved portion of the filament, the vortex evolves in such a manner so that high local curvature is rapidly diminished. As the head bends back, the legs of the vortex curl backward in a counter-clockwise direction; the disturbance moves down toward the wall and spreads to both sides. With the evolution of the legs, new secondary hairpin heads evolve to the side of the main disturbance. The calculation was terminated at $t = .072$ since the general trend of the disturbance is reasonably well established at this point; the disturbance is expected to continue to propagate to the side as the vortex evolves into a "cork-screw" shape.

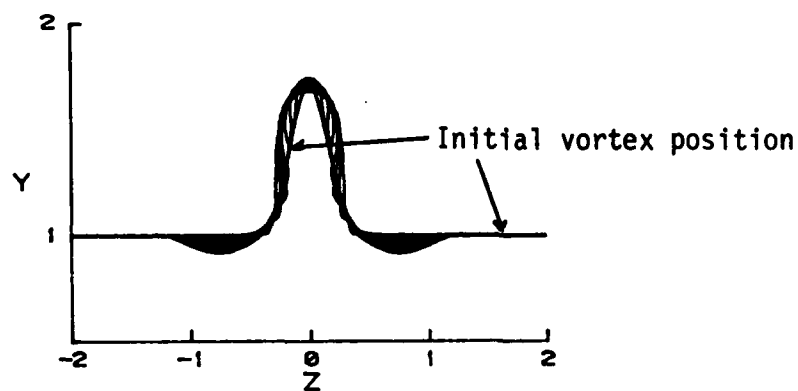
In the second case considered, the same geometrical parameters were used as in Case 1 with the exception that the amplitude of the disturbance was doubled to $A = 1.0$ and the mesh size used was $\Delta s = 0.01$. The basic development of the vortex is similar to Case 1 and is shown in Figures 4.3 at every 20th time step. It may be observed in Figures 4.3(a) and 4.3(b) that the head of the vortex pulls rapidly backward and the vortex begins to evolve into the same type of "corkscrew" configuration observed in Case 1. The calcula-



(a) Top view



(b) Side view



(c) End view

Figure 4.3 - Temporal development for a hairpin vortex in a stagnant flow. Case 2 ($\alpha=45^\circ$, $A=1.$, $\beta=20$); the vortex position is plotted every 20 time steps ($\Delta t=0.0002$).

tion was terminated at $t = 0.028$ since the evolution of the filament was judged to be similar to Case 1.

In the final case considered, the effect of the initial angle of the disturbance was considered by calculating a case where the initial angle $\alpha = 0^\circ$. The results are shown in Figures 4.4. Again the vortex head bends abruptly back and the evolution of the vortex becomes similar to the previous cases. Consequently in all cases, the initial distortion in the two-dimensional vortex was observed to evolve into a "corkscrew" type of motion and the disturbance spreads outward along the vortex. While the calculations were carried out for a vortex in a stagnant flow, the same vortex evolution would be observed in a uniform flow; if a uniform flow is superimposed from left to right, the only difference in the evolution depicted in Figures 4.2-4.4 would be that the vortex would convect progressively to the right.

4.5 The Evolution of A Hairpin Vortex in Shear

In the previous section, the development of a hairpin vortex in either a stagnant or uniform flow was considered; in this section, the evolution of a hairpin vortex in a shear flow will be addressed. The following background flow for these calculations was assumed:

$$\vec{u}_{\text{ext}} = \begin{cases} \frac{yV}{y_s} \hat{i} & y \leq y_s \\ V \hat{i} & y > y_s \end{cases} \quad (4.21)$$

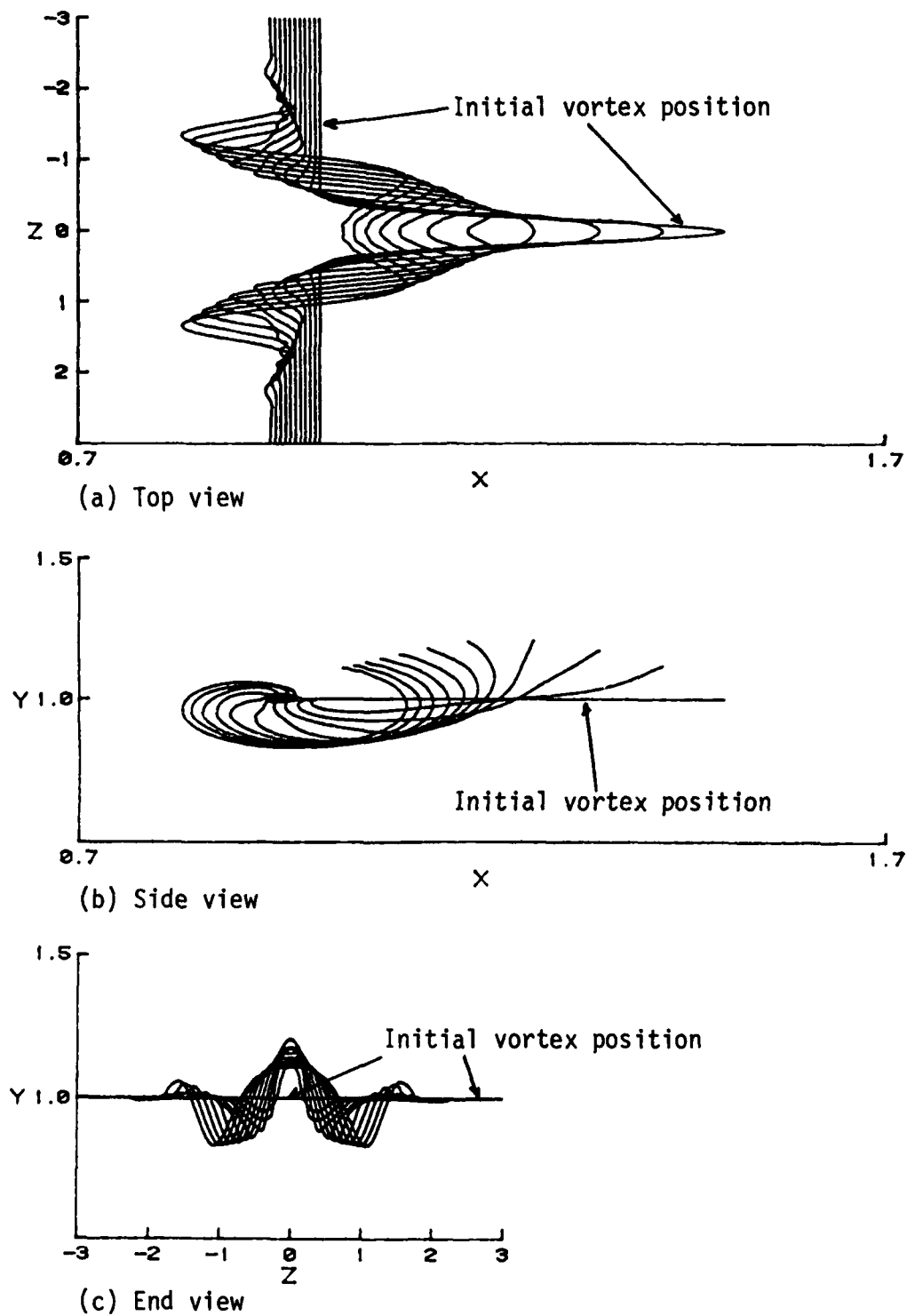


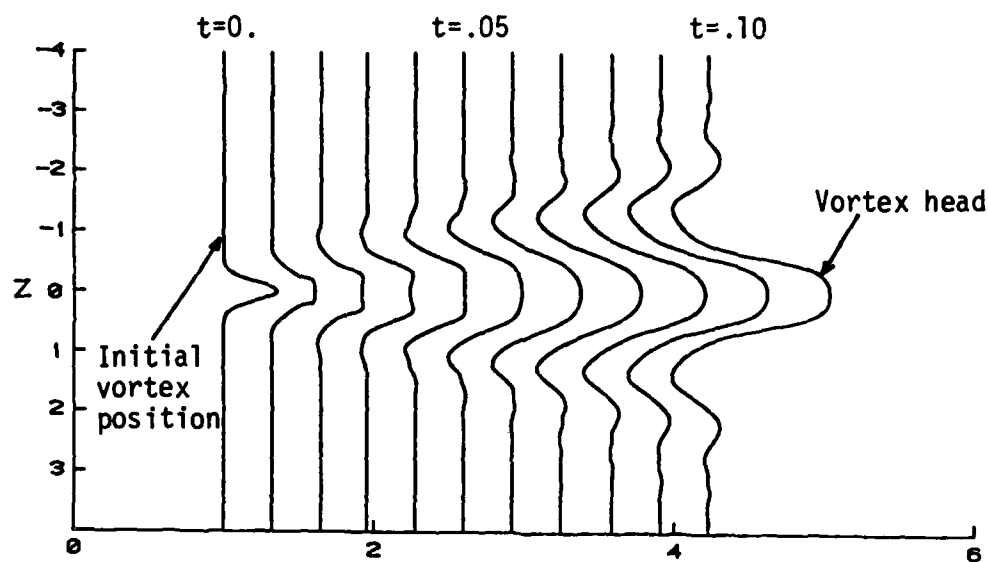
Figure 4.4 - Temporal development for a hairpin vortex in a stagnant flow. Case 3 ($\alpha=0^\circ$, $A=0.5$, $\beta=20$); the vortex position is plotted every 30 time steps ($\Delta t=0.0002$).

Here V is the (dimensionless) uniform flow speed at large distances from the wall and y_s is the height of shear flow.

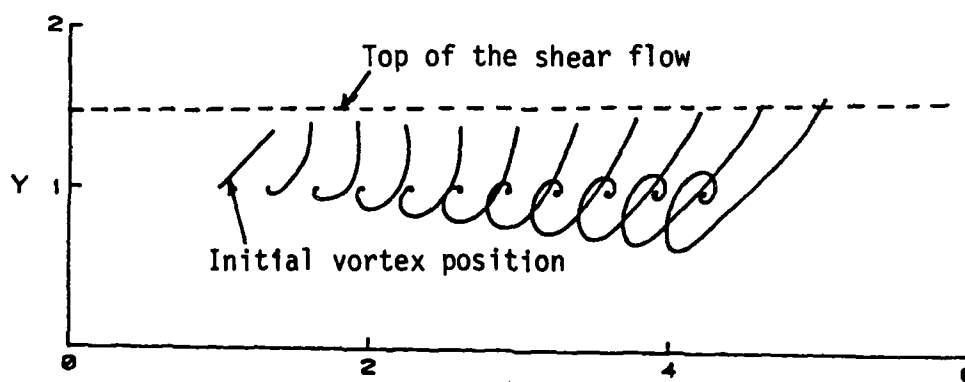
A series of these calculations were carried out using the initial vortex configuration given by equation (4.4) with $A = 0.5$, $\alpha = 45^\circ$ and $\beta = 20$; the vortex core radius was $a = 0.02$. The evolution of the vortex was tracked by computing the solution of equation (4.6) numerically using equation (4.21). In all cases, the dimensionless height of the shear flow was taken to be $y_s = 1.5$; the mesh size along the vortex was $\Delta s = 0.01$. Initially the spanwise extent of s was taken to be at $s = \ell = 2$ and consequently there were 400 points on the vortex; as the hairpin vortex began to evolve in the spanwise direction the value of ℓ was progressively increased to $\ell = 3$ and then $\ell = 4$.

The first case for a vortex in shear will be denoted here as Case 4 and for this situation, a uniform flow velocity (at large distances from the wall) of $V = 50$ (to the right) was used; note that the velocities near the head are about 25 units to the left (for the initial configuration in equation (4.4)). The value of V selected in this case is thus about twice the initial maximum self-induced velocity. Results for Case 4 are plotted in Figures 4.5 every 20 time steps; the time step used was $\Delta t = 0.0005$.

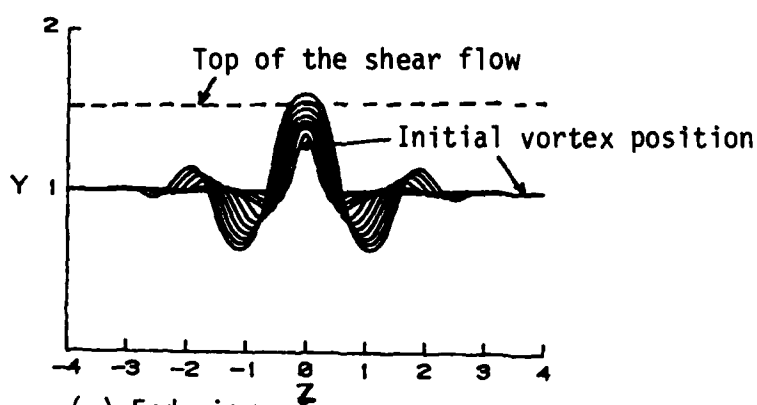
It may be observed in Figures 4.5 that the distortion in the initial hairpin vortex grows as the vortex convects downstream in the shear flow. The vortex head lifts away from the wall and eventually rises into the uniform flow region. It may also be observed that the



(a) Top view



(b) Side view



(c) End view

Figure 4.5- Temporal development for a hairpin vortex in a shear flow ($V=50$). Case 4 ($\alpha=45^\circ$, $A=0.5$, $\beta=20$); the vortex position is plotted every 20 time steps ($\Delta t=0.0005$).

vortex legs move progressively toward the wall and that new hairpin disturbances form outboard of the primary disturbance. It is apparent that the shear flow has the effect of amplifying the initial distortion as well as giving rise to additional hairpin vortices on the initially undisturbed portions of the vortex. Calculations of this nature are rather time consuming and were terminated at $t = 0.1$ for Case 4 since the general trends of the vortex evolution were evident at this point.

In Case 5, the effect of increasing the shear rate was studied by taking $V = 150$; the background flow (given by equation (4.21)) is now at higher speed and it was necessary to decrease the time step to $\Delta t = 0.0003$ to obtain smooth development in the vortex trajectory. The results are plotted in Figures 4.6. It may be observed by comparison of Figures 4.5 and 4.6 that one effect of the increased level of shear is to increase the rate of amplification of the original disturbance as well as the evolution of secondary hairpin vortices. The trend for the vortex head to lift out of the shear flow (and then bend back) is evident in Figure 4.6(b) both for the primary vortex head and the secondary hairpin vortex heads. The tendency for the hairpin legs to move toward the surface may also be seen in Figures 4.6(b) and 4.6(c). It is also clear from Figure 4.6(a) that the increased level of shear gives rise to an increased level of stretching along the vortex legs.

The last case considered corresponds to an even higher level of

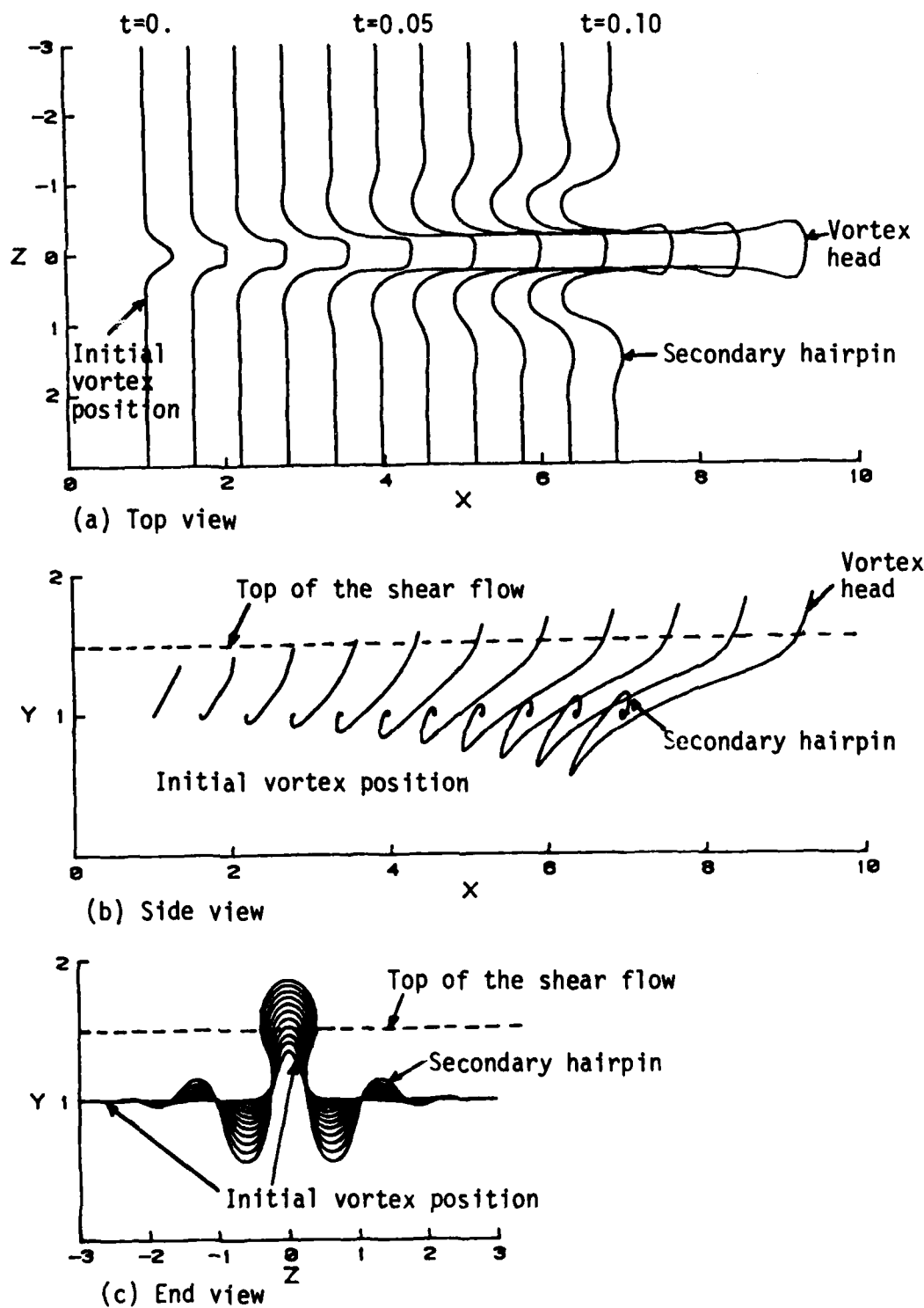


Figure 4.6 - Temporal development for a hairpin vortex in a shear flow ($V=150$). Case 5 ($\alpha=45^\circ$, $A=0.5$, $\beta=20$); the vortex position is plotted every 20 time steps ($\Delta t=0.0003$).

shear with $V = 250$ and is denoted as Case 6; in this case, it was necessary to reduce the time step to $\Delta t = 0.0002$ in order to obtain smooth results. Calculated results for the initial development are depicted in Figures 4.7. It may be observed that the development is similar to Case 5 but that the deformation of the vortex takes place at a much faster rate. At $t = 0.06$, two secondary hairpins have developed outboard of the primary disturbance, the legs of the vortex move progressively toward the wall (Figure 4.7(c)) and are relatively close to the wall at $t = 0.06$. In order to extend the calculation to larger times, it was necessary to extend the computational domain from $s = \ell = 3$ to $\ell = 4$; a continuation of the sequence for Case 6 is shown in Figures 4.8. It may be observed that the bending back of the primary vortex head is now quite pronounced. In addition, the vortex legs have moved very close to the wall; when the integration was carried forward beyond the last stage depicted in Figures 4.8, the vortex legs touch the wall after a few time steps and the numerical algorithm terminated.

4.6 Discussion

The present results provide a detailed time history of the evolution of a hairpin vortex both in an irrotational flow as well as a shear flow. Some of the features of the flow development are similar to those obtained by previous investigators. Perry and Chong (1982), in an attempt to describe the mechanisms of wall layer turbulence, have described the evolution of " Λ -vortices"; such vortices are meant to be a crude representation of hairpin vortices

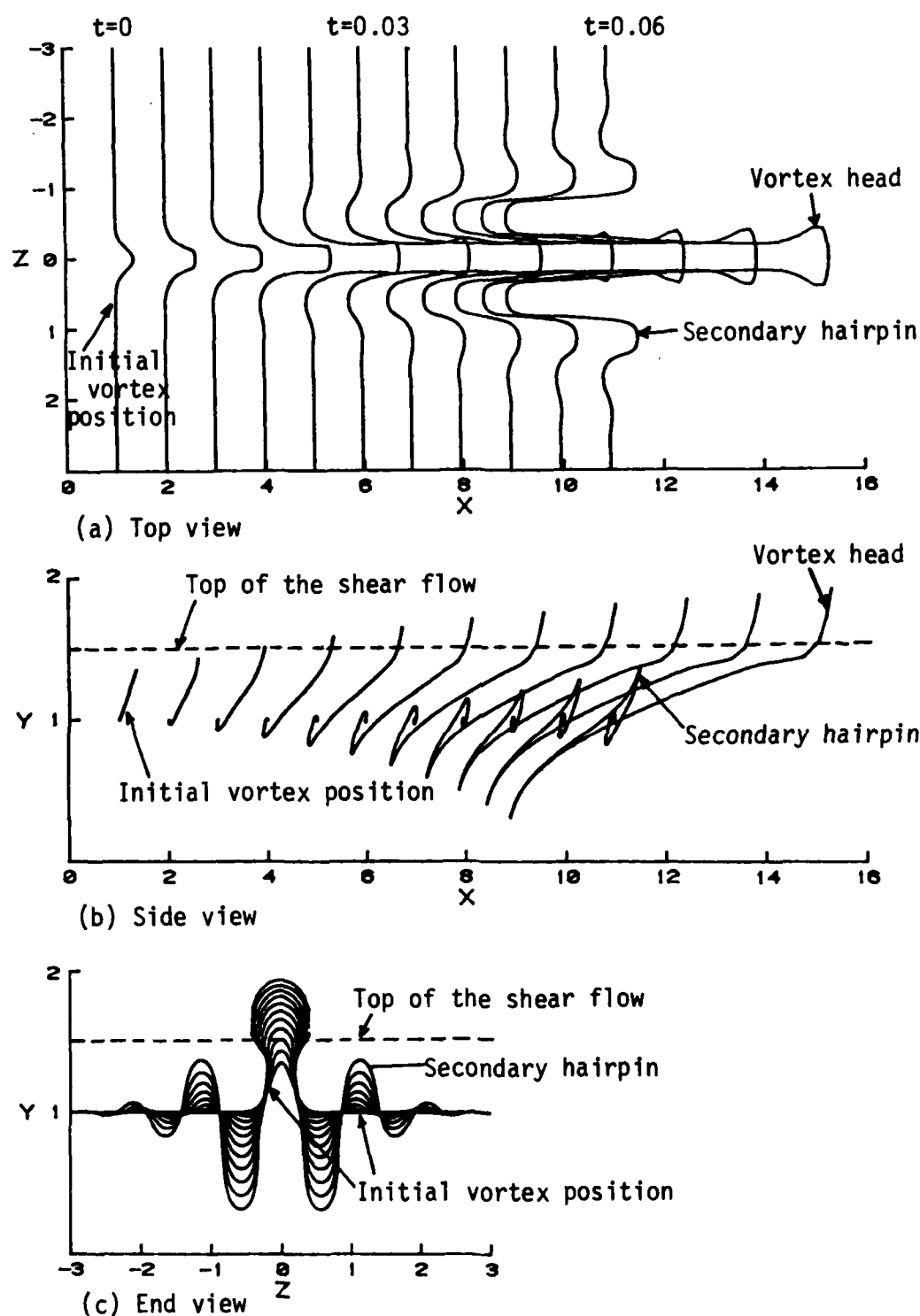
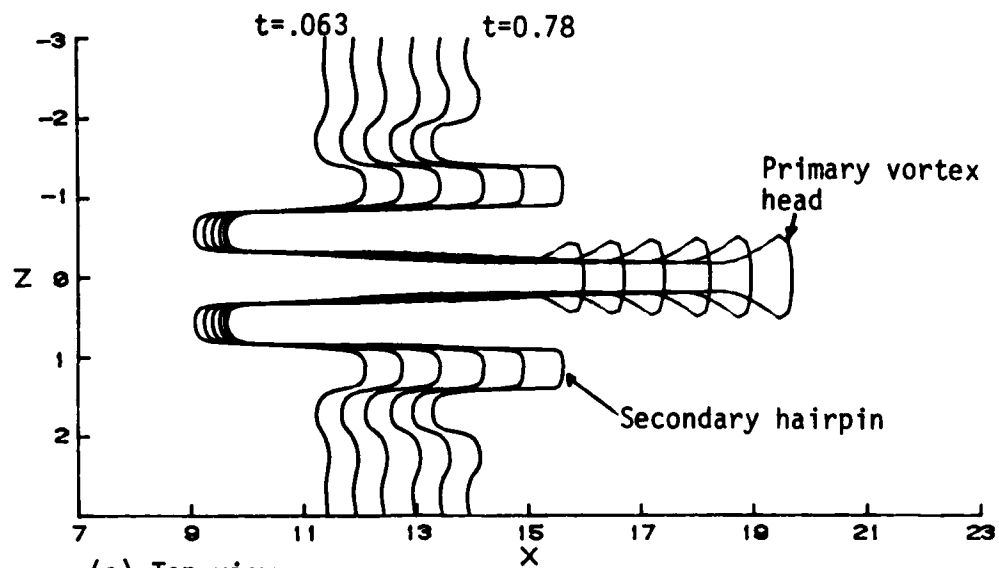
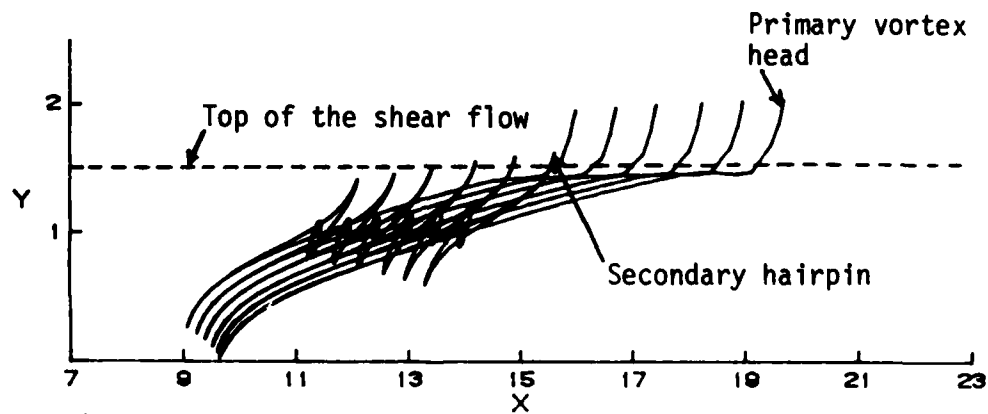


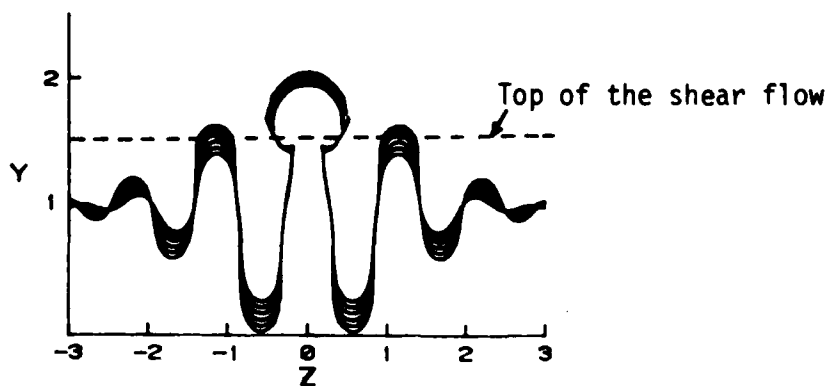
Figure 4.7 - Temporal development for a hairpin vortex in a shear flow ($V=250$). Case 6 ($\alpha=45^\circ$, $A=0.5$, $\beta=20$); the vortex position is plotted every 30 time steps ($\Delta t=0.0002$).



(a) Top view



(b) Side view



(c) End view

Figure 4.8 - Continuation of integration for Case 6; the vortex position is plotted every 15 time steps ($\Delta t = 0.0002$).

and consisted of two finite-length straight vortex filaments forming an inverted V shape above the wall. A numerical integration based on the Biot-Savart law was carried out for such "vortices" in a stagnant flow. Although this is a rather crude and questionable representation of a hairpin vortex, the results of Perry and Chong (1982) do show features similar to the detailed integrations depicted in Figures 4.2 to 4.4; the tip of the Λ -vortex was observed to bend backward and the Λ was observed to flatten and spread in the spanwise direction. The present integrations are based on the full Biot-Savart law with a self-consistent representation of the vortex core flow and provide a detailed record of the hairpin development.

Aref and Flinchem (1984) have considered the evolution of a hairpin vortex in a shear flow near a wall using the localized induction method due to Hama (1962). In this approach, the effect of the image vortex below the plate was ignored and the self-induced velocity at a point was computed from the contribution due to a small arc of the vortex near the point; the effect of portions of the vortex remote from the field point is neglected in the "localized induction approximation". Despite these deficiencies, the calculated results of Aref and Flinchem (1984) do show an evolution of a hairpin vortex in shear which shows some qualitative similarities to the development depicted in Figures 4.5 to 4.8.

Recently, Moin, Leonard and Kim (1986) have computed the evolution of a curved vortex using the Biot-Savart law; the vortex core

was accounted for using an ad hoc model described by Leonard (1985). Their calculations were carried out with relatively coarse mesh sizes but do show some features that bear a similarity to some of the detailed results obtained here.

The present results may be compared with experimental results of Acarlar and Smith (1984, 1981a, 1987b); in these experiments, hairpin vortices were created in a sub-critical laminar boundary layer and the effects and motion of the vortices were observed as the hairpins convected downstream. The vortex trajectories that have been computed in this study are in broad agreement with the behavior observed in the experiments of Acarlar and Smith (1984). The heads of the hairpins were invariably observed to lift upward and ultimately bend backwards. The evolution of secondary hairpin vortices outboard of the original hairpin was clearly observed in the experiments in agreement with the evolution shown in Figures 4.5-4.8. Figure 4.9 is reproduced from the study of Acarlar and Smith (1984); in this sequence the hairpin vortex is moving toward the observer and as it passes a hydrogen bubble wire was pulsed to produce a line of bubbles within the flow. In this sequence, the movement of the hairpin legs toward the surface may be observed which is in qualitative agreement with the evolution shown in Figures 4.5-4.8.

4.7 Influence of a Hairpin Vortex on Dye Markers

A common method of flow visualization is to introduce a

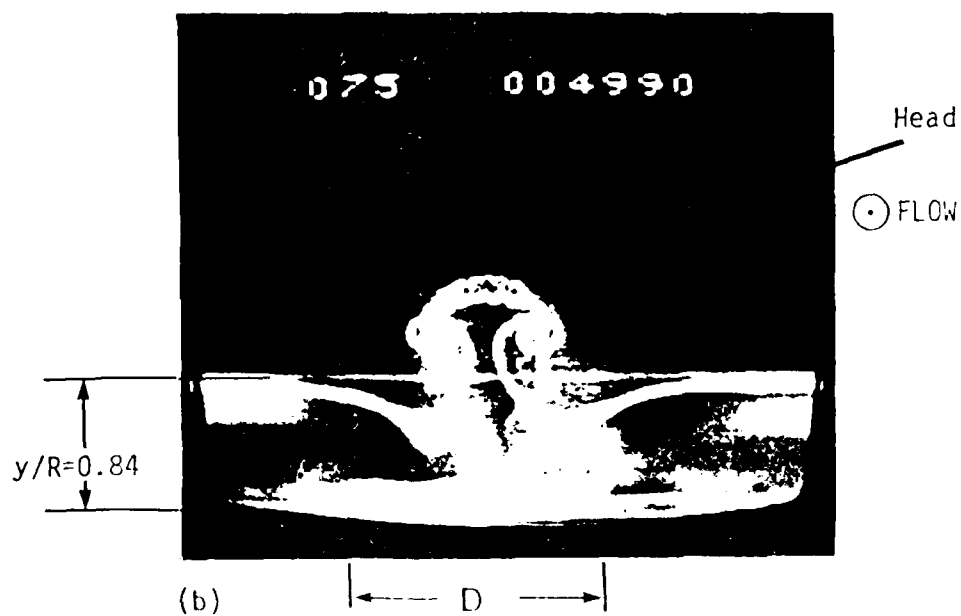
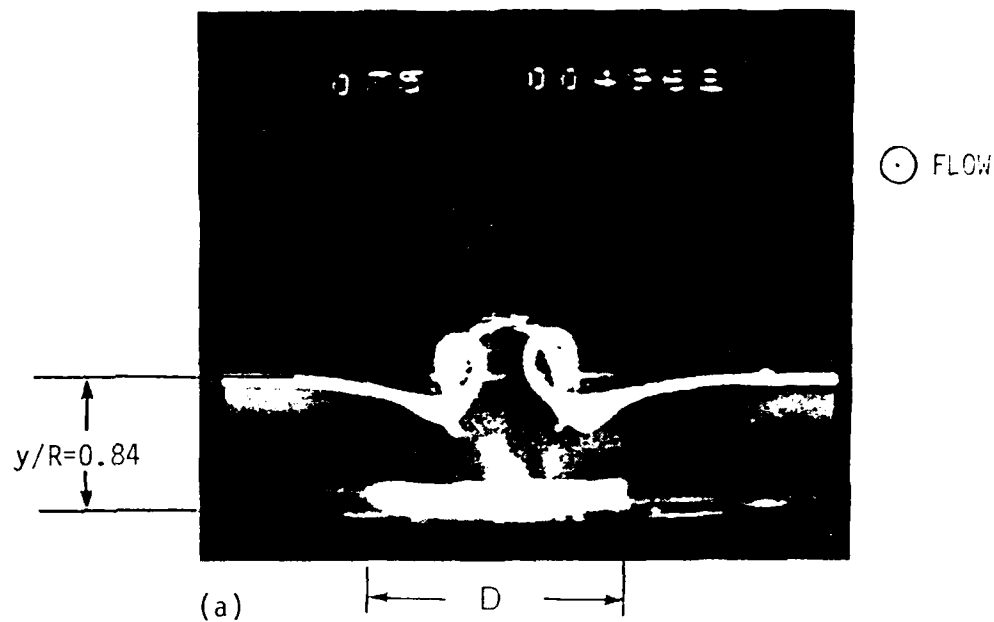


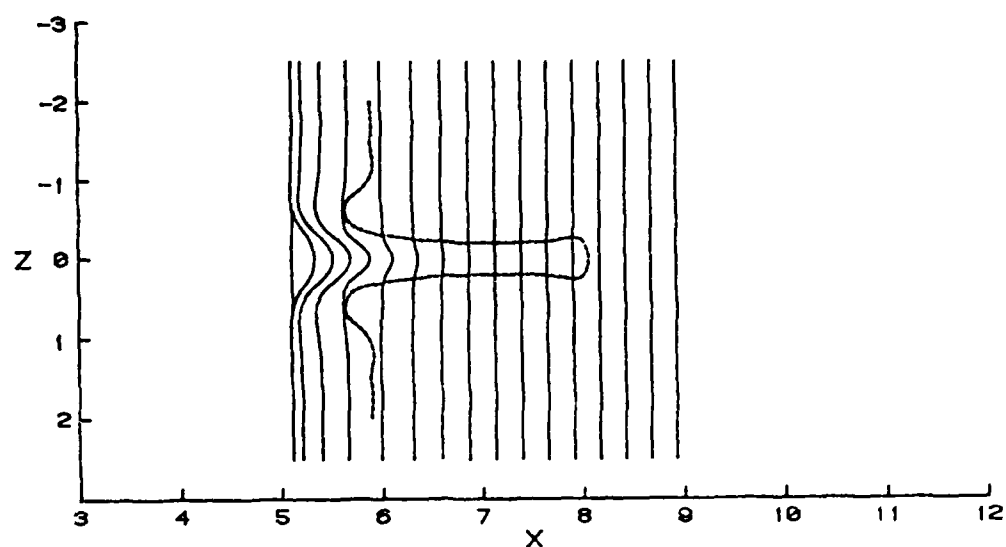
Figure 4.9 - Flow visualization sequence reproduced from Acalar and Smith (1984) showing a hairpin vortex moving toward the observer; the visualization is accomplished with a hydrogen bubble wire.

sequence of hydrogen bubble lines into the flow (in water) and to observe their subsequent deformation. The wall-layer streaks in a turbulent boundary layer are often considered to be the signature of a moving hairpin vortex; this view is strongly supported by the experimental studies of Acarlar and Smith (1984, 1987a, 1987b). In the present study, the evolution of a hairpin vortex in a shear flow has been calculated and in this section, the influence of the moving hairpin vortex on simulated hydrogen bubble lines in the flow will be evaluated.

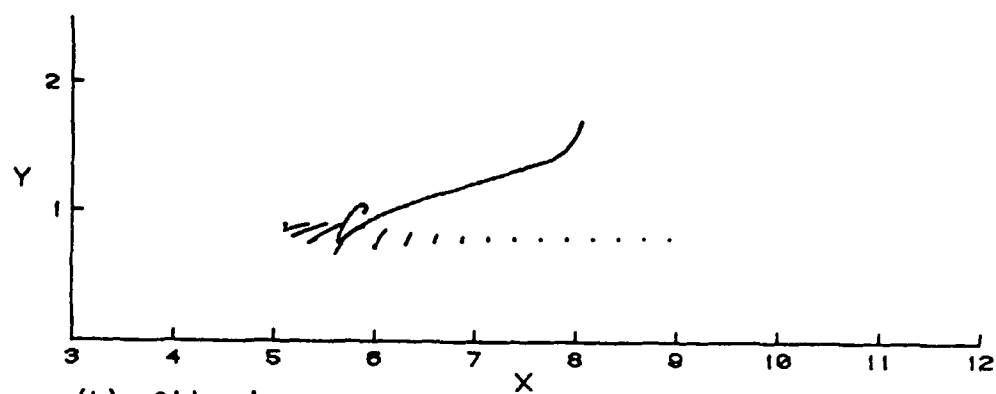
To carry out the numerical calculations, a total of 17 equally spaced lines were inserted in the flow field at the initial instant for the vortex development of Case 6 depicted in Figure 4.7. A total of 51 mesh points were used on each half of each line. In the first case considered, the lines were all at an initial constant height of $y_0 = 0.8$ and were separated by a streamwise distance of 0.25 units in the streamwise direction. As the hairpin vortex evolved in the shear flow according to the development depicted in Figure 4.7, the trajectories of the "bubble lines", were computed numerically. A series of trajectories is shown in Figures 4.10 to 4.12 in top, side and end views; the current vortex position is shown as a dotted line. It may be observed that the simulated bubble lines are collected into two nearly parallel strips of concentration; this behavior is closely consistent with the observed results of Acarlar and Smith (1984) (c.f. Figures 3.21 and 3.25

of that study) where horizontal lines of hydrogen bubble were introduced at different levels above the wall to detect the typical "footprint" of a moving hairpin vortex.

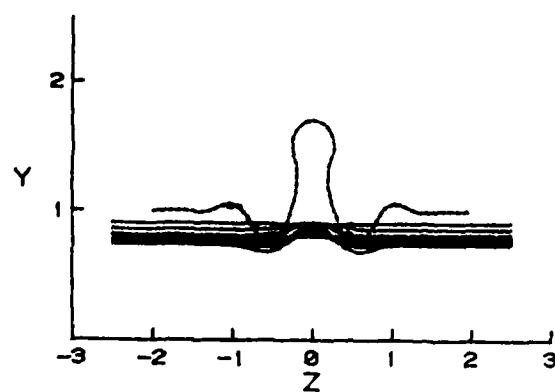
A similar sequence is shown in Figures 4.13 to 4.15 for the "bubble lines" located initially lower at $y_0 = 0.7$. A similar type of development may be observed.



(a) Top view

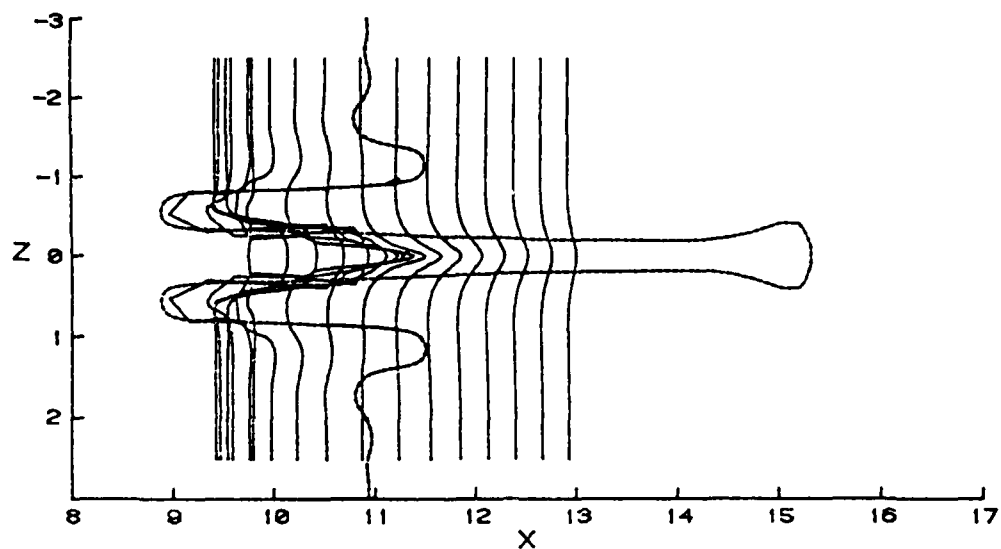


(b) Side view

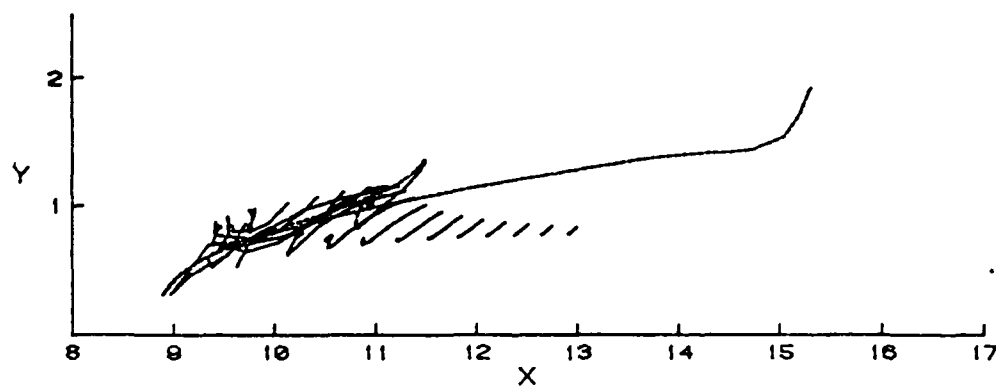


(c) End view

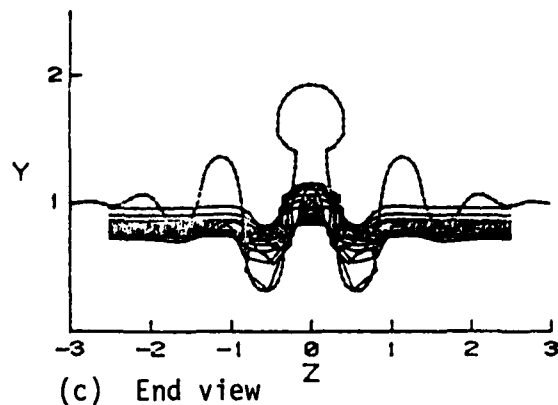
Figure 4.10 - The simulated hydrogen bubble lines due to a convected hairpin vortex (Case 6) at $t = .03$; initial bubble lines were located at $y = .8$.



(a) Top view

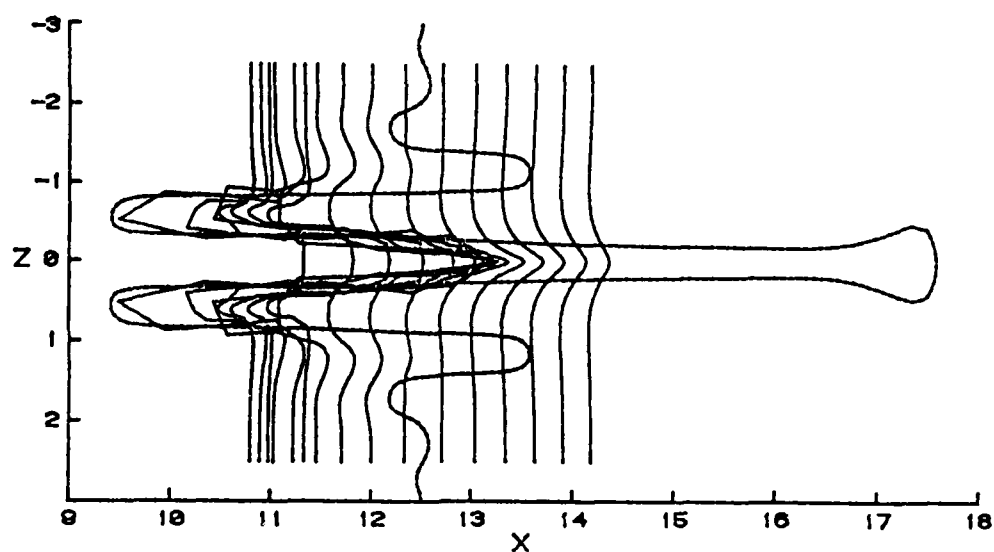


(b) Side view

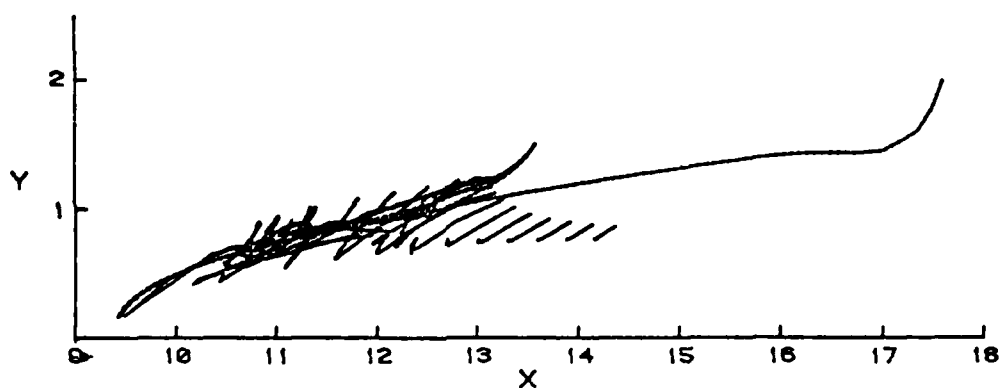


(c) End view

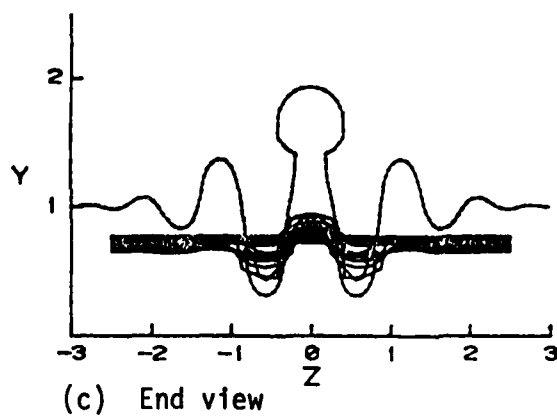
Figure 4.11 - The simulated hydrogen bubble lines due to a convected hairpin vortex (Case 6) at $t = .06$; initial bubble lines were located at $y = .8$.



(a) Top view

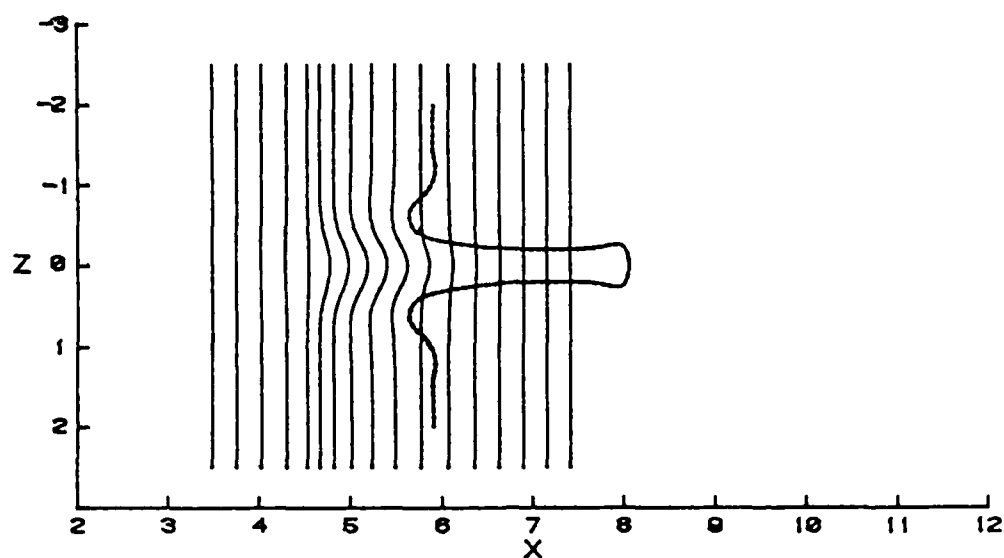


(b) Side view

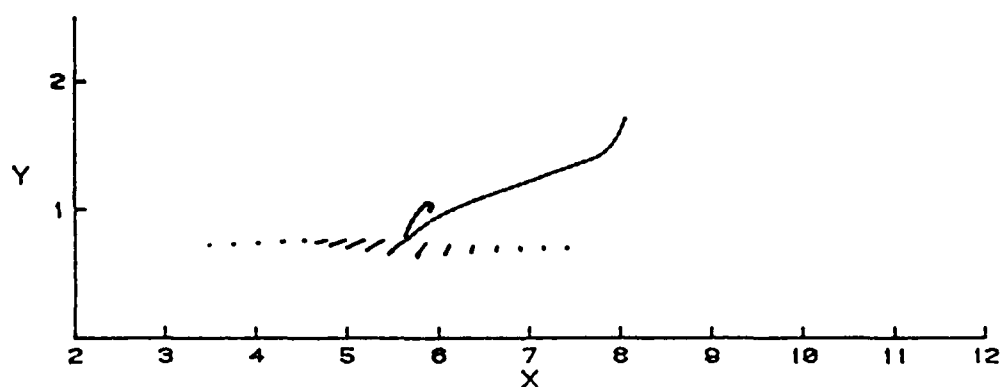


(c) End view

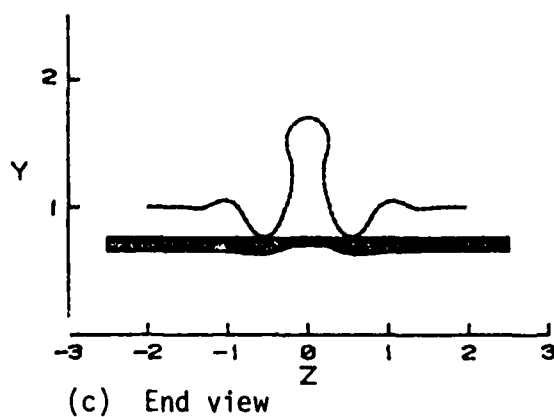
Figure 4.12 - The simulated hydrogen bubble lines due to a convected hairpin vortex (Case 6) at $t = .07$; initial bubble lines were located at $y = .8$.



(a) Top view

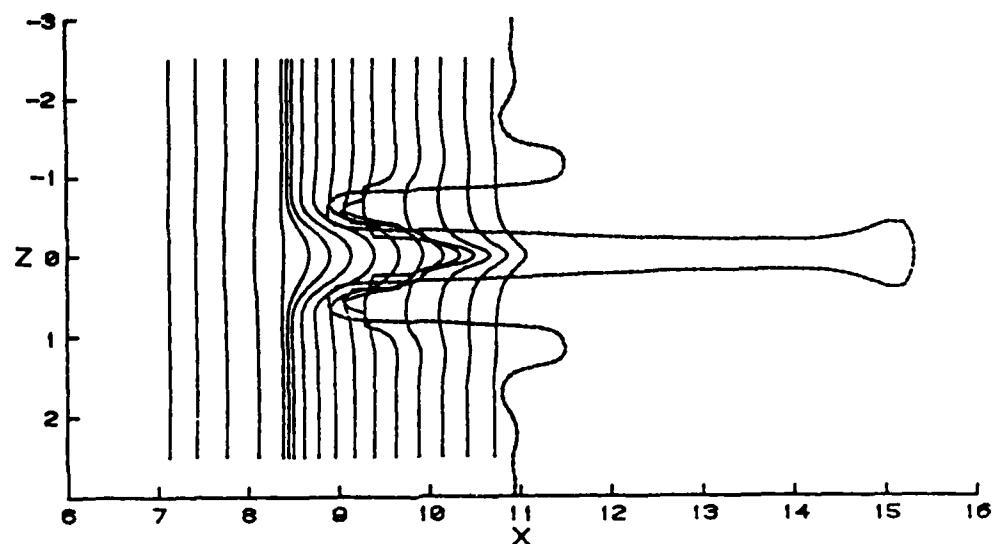


(b) Side view

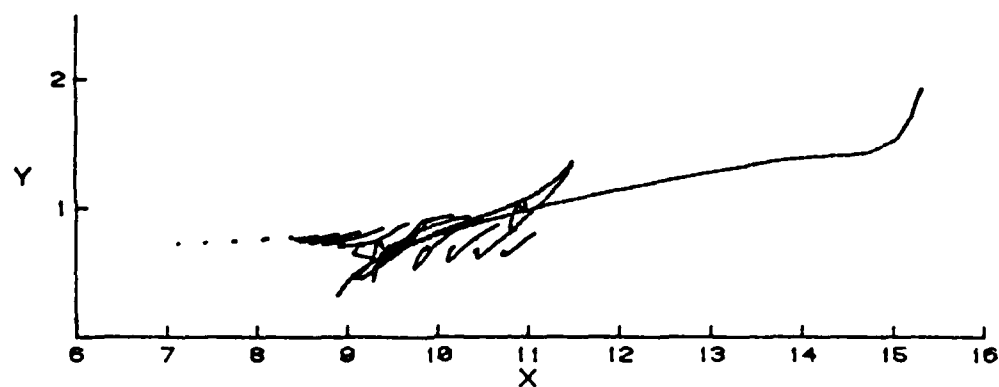


(c) End view

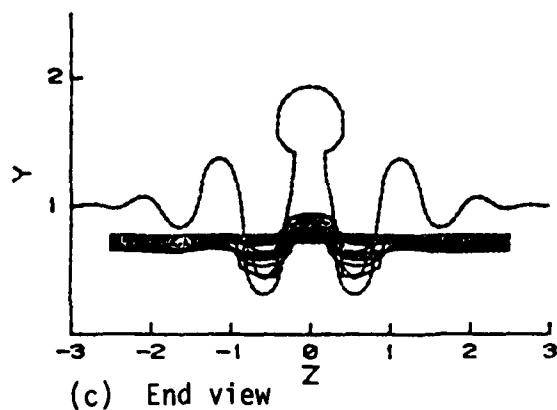
Figure 4.13 - The simulated hydrogen bubble lines due to a convected hairpin vortex (Case 6) at $t = .03$; initial bubble lines were located at $y = .7$.



(a) Top view

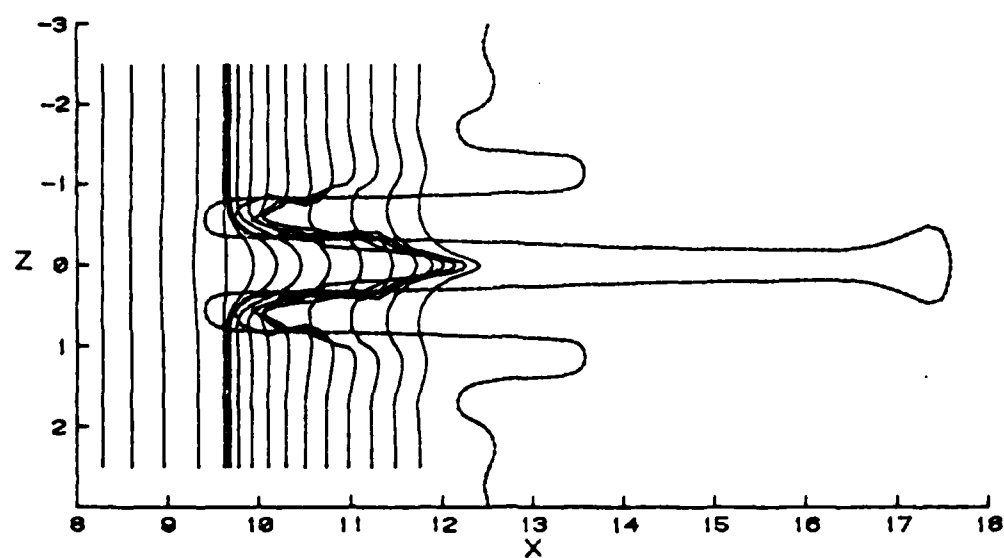


(b) Side view

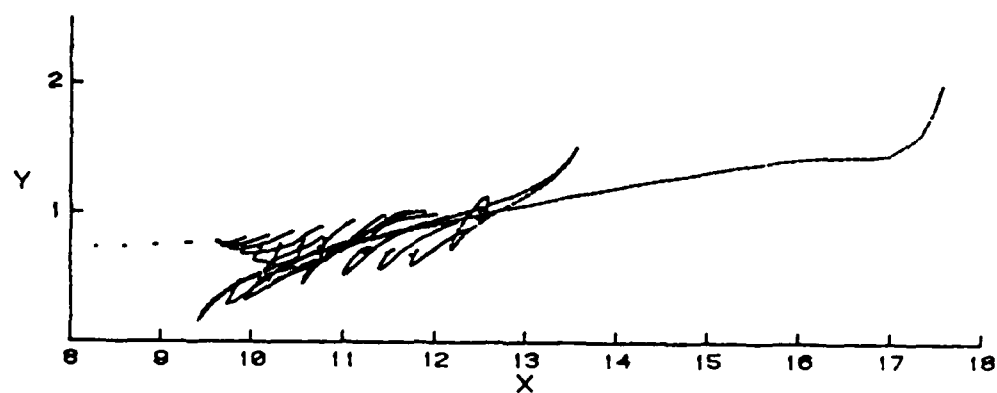


(c) End view

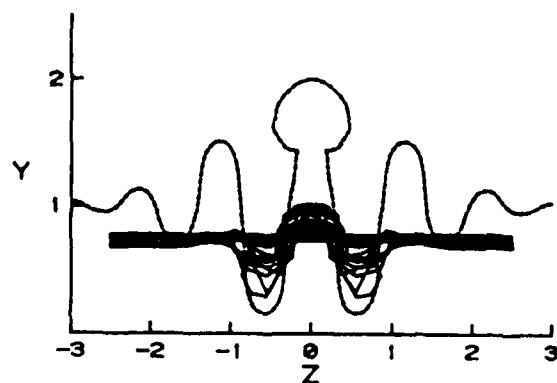
Figure 4.14 - The simulated hydrogen bubble lines due to a convected hairpin vortex (Case 6) at $t = .06$; initial bubble lines were located at $y = .7$.



(a) Top view



(b) Side view



(c) End view

Figure 4.15 - The simulated hydrogen bubble lines due to a convected hairpin vortex (Case 6) at $t = .07$; initial bubble lines were located at $y = .7$.

4.8 The Velocity Signature of a Hairpin Vortex

As a moving hairpin vortex convects in a shear flow, it induces distortions in the streamwise velocity profiles and in this section, the nature of the induced flow will be considered briefly. Consider first the situation corresponding to Case 4 of Section 4.5 and select a particular vortex configuration at $t = 0.1$; the side view of the vortex at this stage of development is shown in Figure 4.16(a). At the eleven streamwise locations indicated in Figure 4.16(a), the instantaneous velocity fluctuation profiles are depicted in Figure 4.16(b); these profiles represent the instantaneous velocity fluctuations due to the hairpin vortex and were computed using the Biot-Savart law. It may be observed in Figure 4.16(b) that the velocity profile labeled 8 displays the largest negative velocity fluctuation at about $y = 1.5$; as y decreases, the magnitude of the fluctuation decreases. On the other hand, the velocity fluctuation above $y = 1.5$ is positive and peaks near 1.75. The abrupt and relatively large reversals in velocity fluctuations are indicative of the presence of the vortex head. The actual instantaneous velocity profiles at each station are shown in Figure 4.16(c).

Another perspective on the nature of the streamwise velocity induced by a moving hairpin vortex is shown in Figure 4.17 for Case 4. In this illustration, the instantaneous velocity fluctuations were computed at a fixed streamwise location (at $x = 4.29$), in the time interval $t = 0.07$ to $t = 0.12$ as the vortex convected past the measuring station. The vortex positions at various times are shown

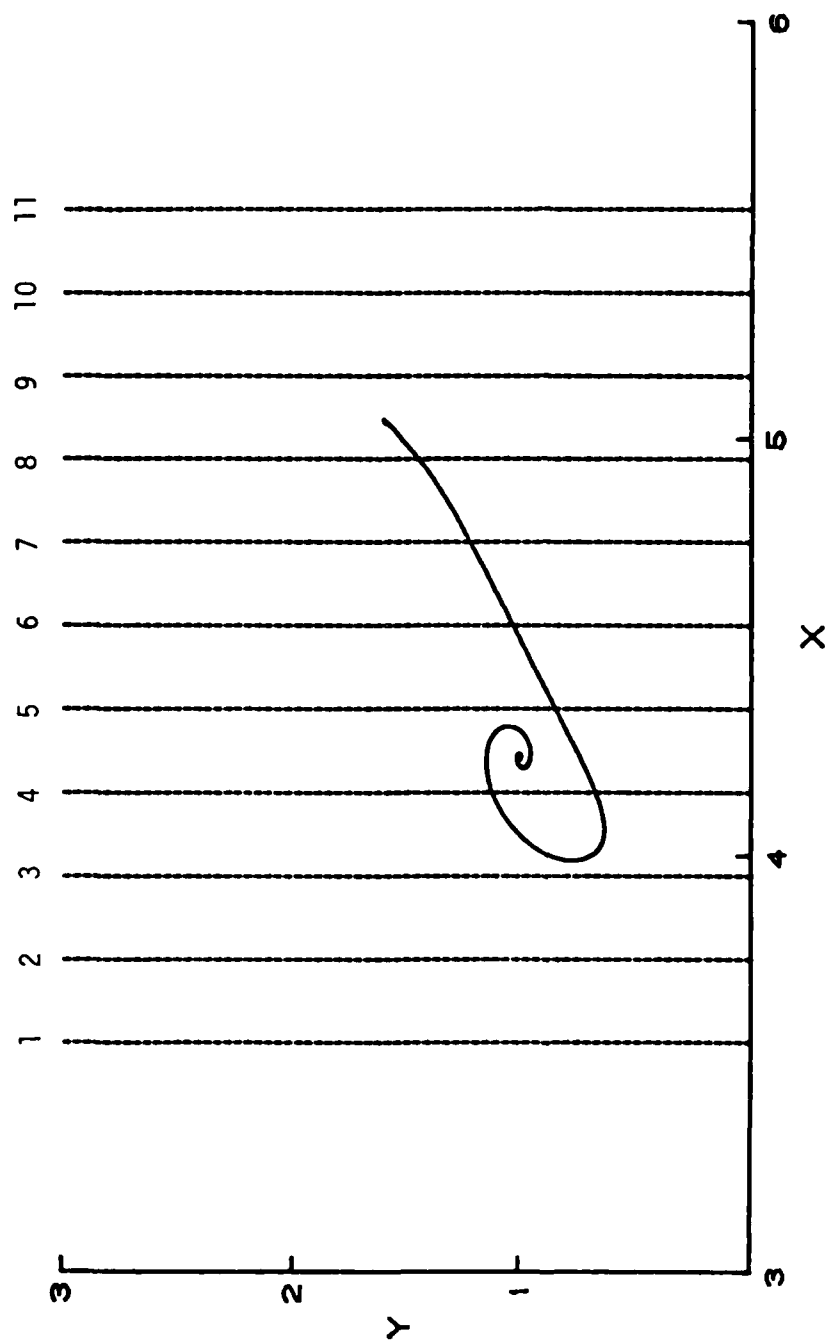


Figure 4.16(a) - Side view of hairpin vortex (at $t = 0.1$ for Case 4 of Section 4.5) and instantaneous streamwise measuring locations

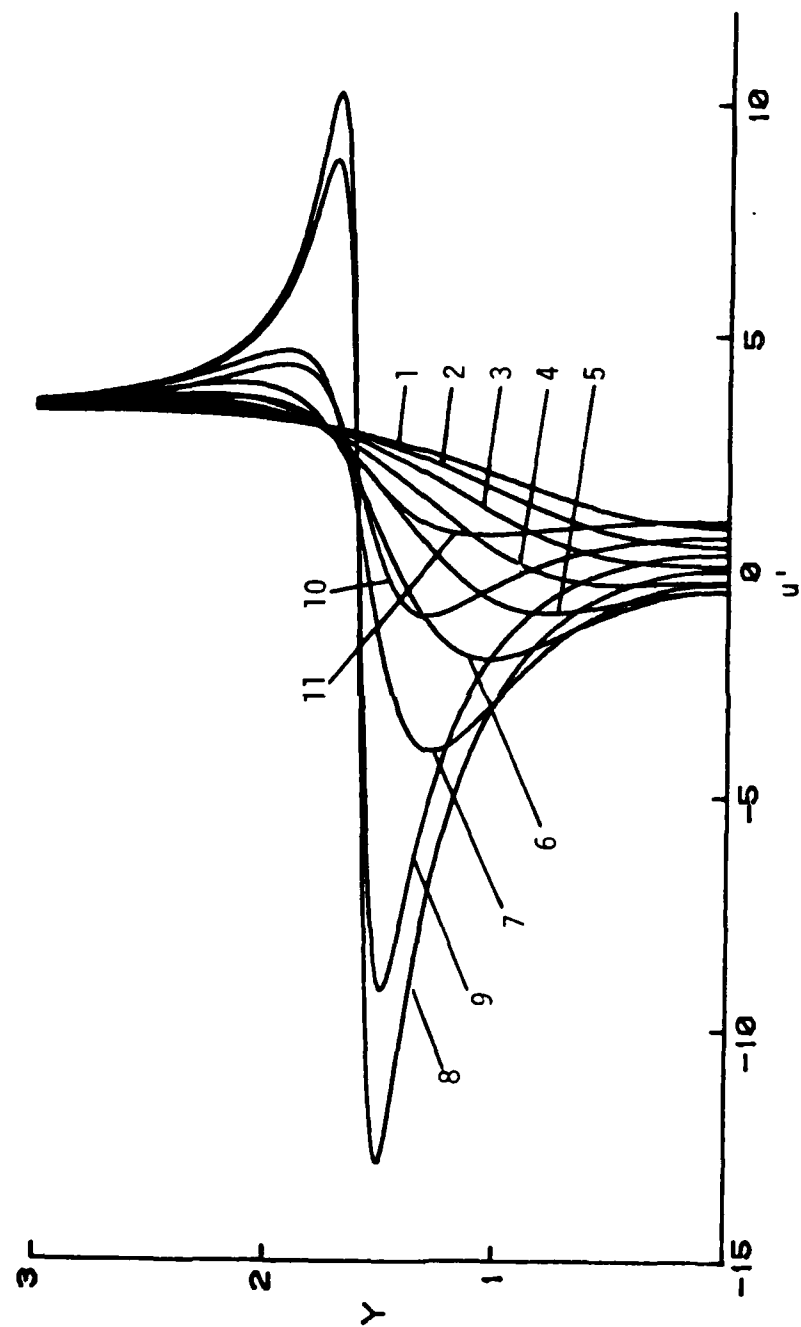


Figure 4.16(b) - Instantaneous streamwise velocity fluctuations at stations indicated in Figure 4.16(a).

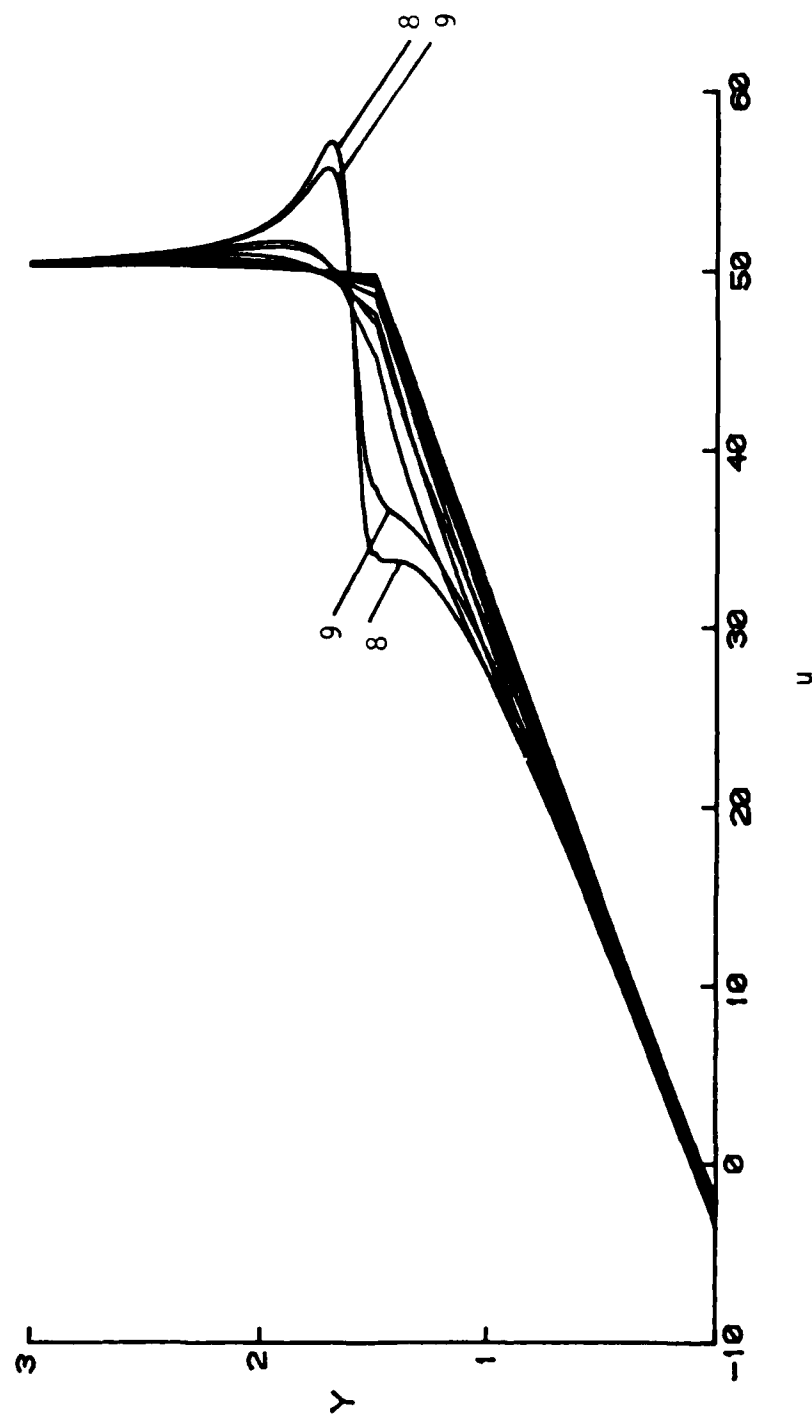


Figure 4.16(c) - Instantaneous streamwise velocity profiles at stations indicated in Figure 4.16(a).

in Figure 4.17(a) in side view and the instantaneous velocity fluctuations are depicted in Figure 4.17(b) at time intervals of $\Delta t = 0.005$. The corresponding velocity profiles are indicated in Figure 4.17(c). It may be observed from Figure 4.17(b) that a rather large velocity fluctuation occurs as the head convects past the measuring station. As the hairpin head moves downstream there is a negative velocity fluctuation near the wall at subsequent times which gradually diminishes with increasing time.

A set of instantaneous velocity profiles for Case 6 of Section 4.5 at fixed value of t are shown in Figures 4.18; this case corresponds to the largest shear rate considered and the instantaneous shape of the vortex in side view is plotted in Figure 4.18(a) at $t = 0.078$. Again the abrupt reversal in sign and the relatively large values of fluctuating velocity are an indication of the presence of the head at station 11. Note that in this case the vortex legs have moved relatively close to the wall at this stage and induce a relatively large negative velocity at the wall (profile 1 in Figure 4.18(b)). In Figures 4.19, the velocity fluctuation due to the moving hairpin vortex are shown as the vortex convects past a fixed measuring station at $x = 9.2$; the fluctuations are plotted in the interval $t = 0.03$ to $t = 0.075$ in Figure 4.19(b). Again the strong sign reversal in the velocity fluctuation may be observed as the hairpin head passes the measuring station. As time increases, a negative velocity fluctuation is observed with a peak that moves gradually toward the wall. At $t = 0.065$, the trailing portion of the

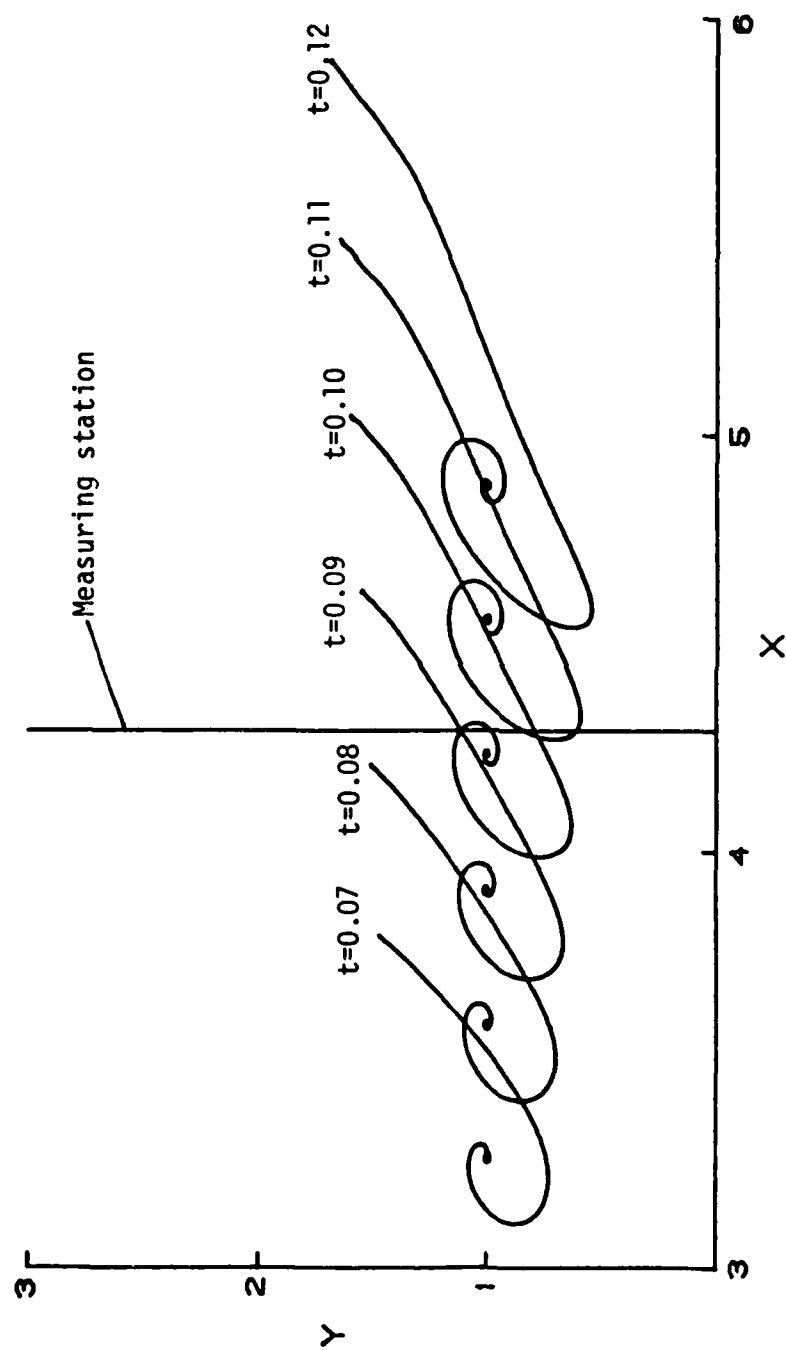


Figure 4.17(a) - Side view of the developing hairpin vortex for Case 4 at various times.

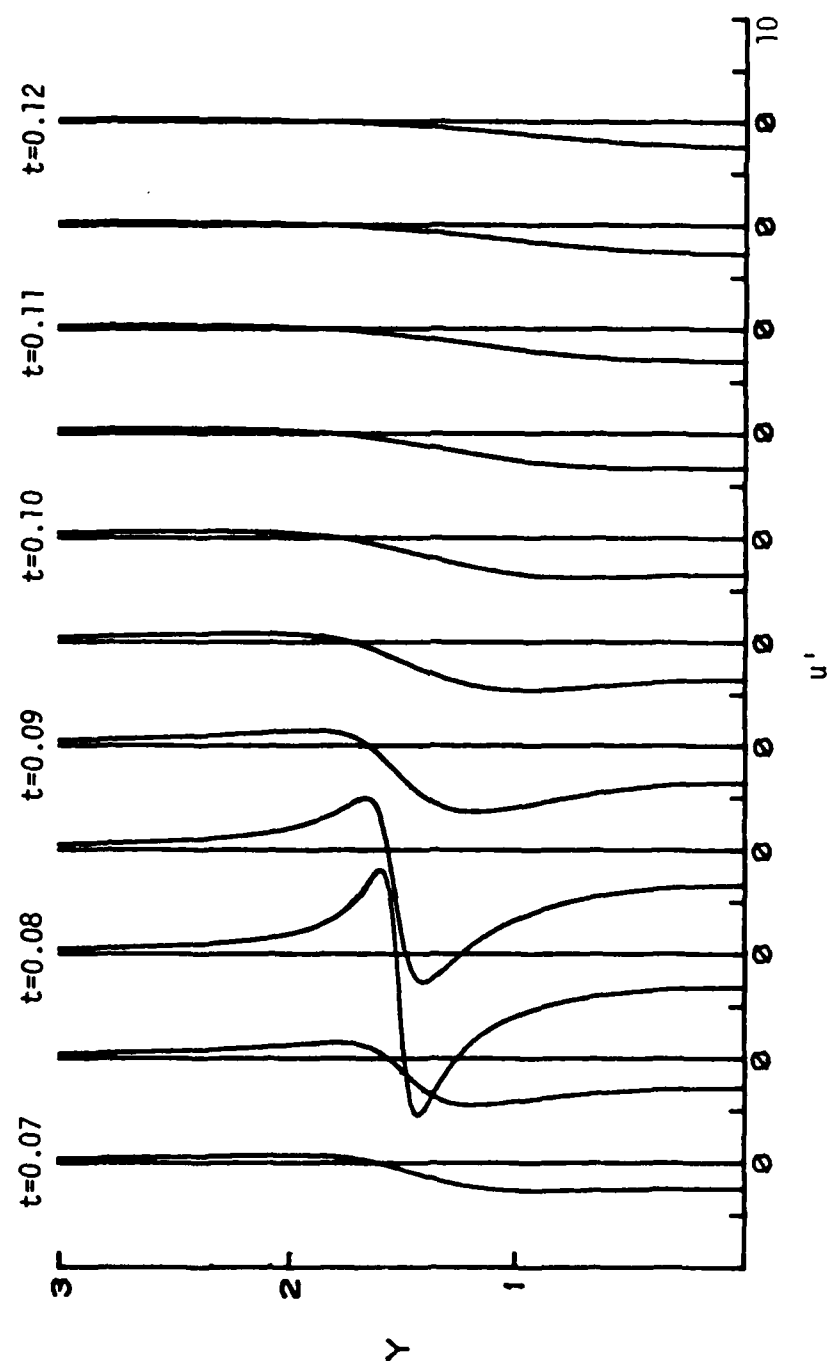


Figure 4.17(b) - Instantaneous velocity fluctuations of the measuring station indicated in Figure 4.17(a); note the shifted origins.

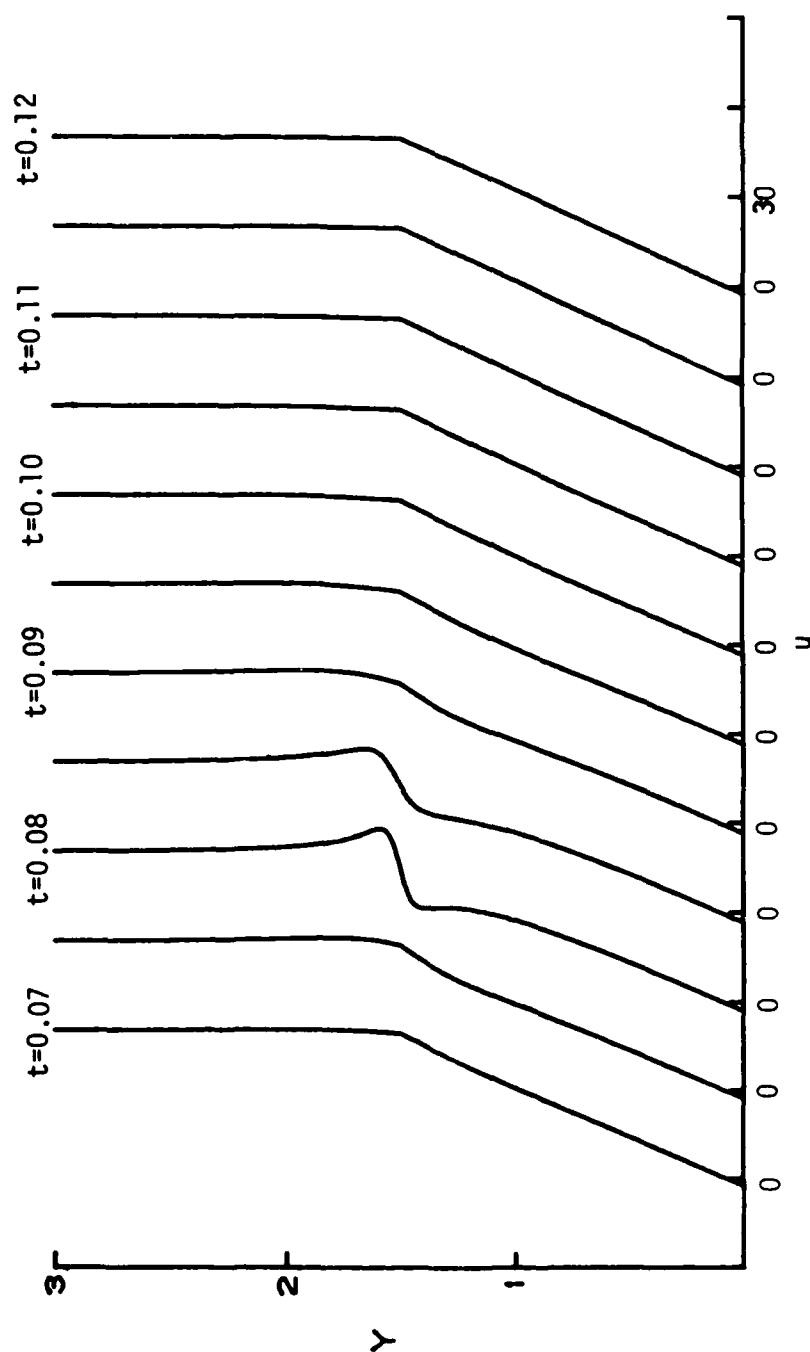


Figure 4.17(c) - Instantaneous velocity profiles at the measuring station indicated in Figure 4.17(a).

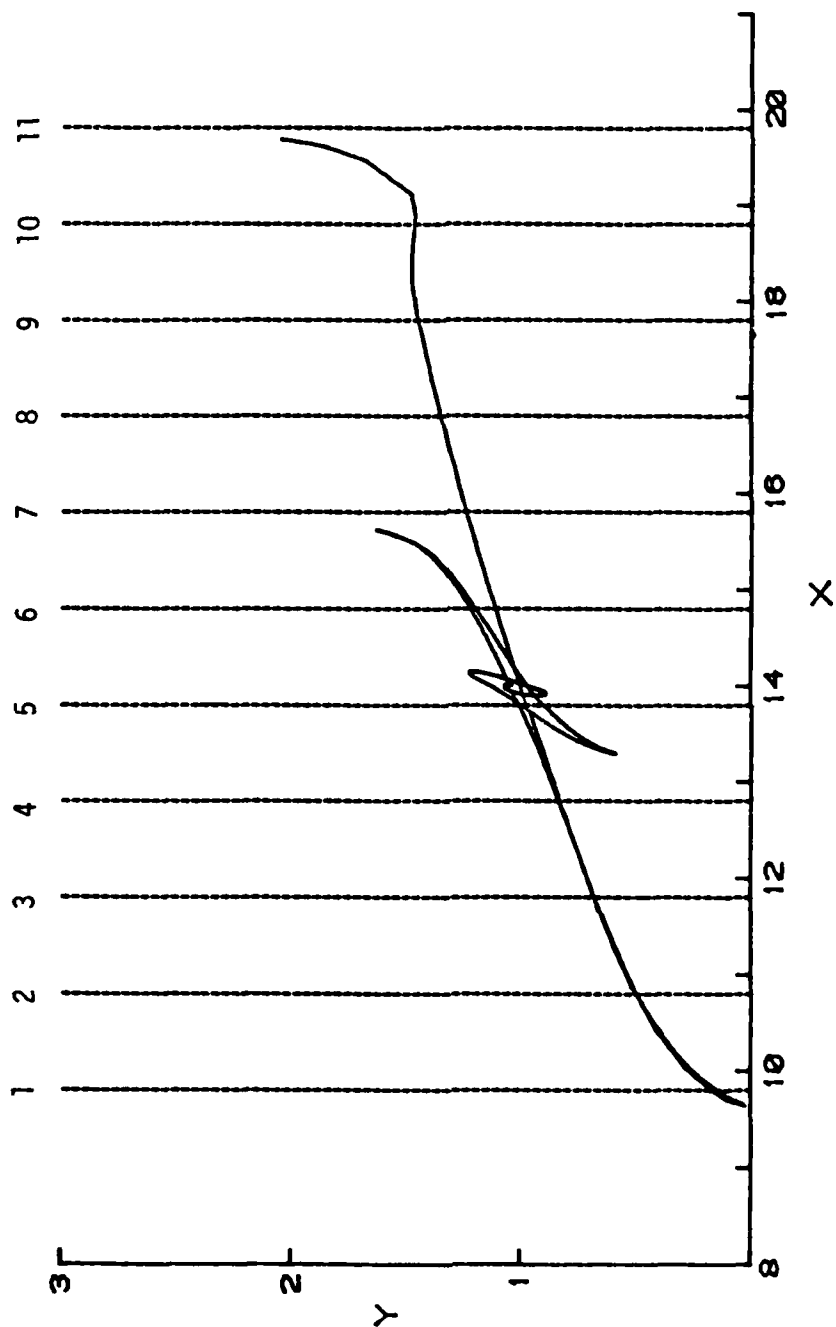


Figure 4.18(a) - Side view of hairpin vortex (at $t = 0.78$ for Case 6 of Section 4.5) and instantaneous streamwise measuring locations.

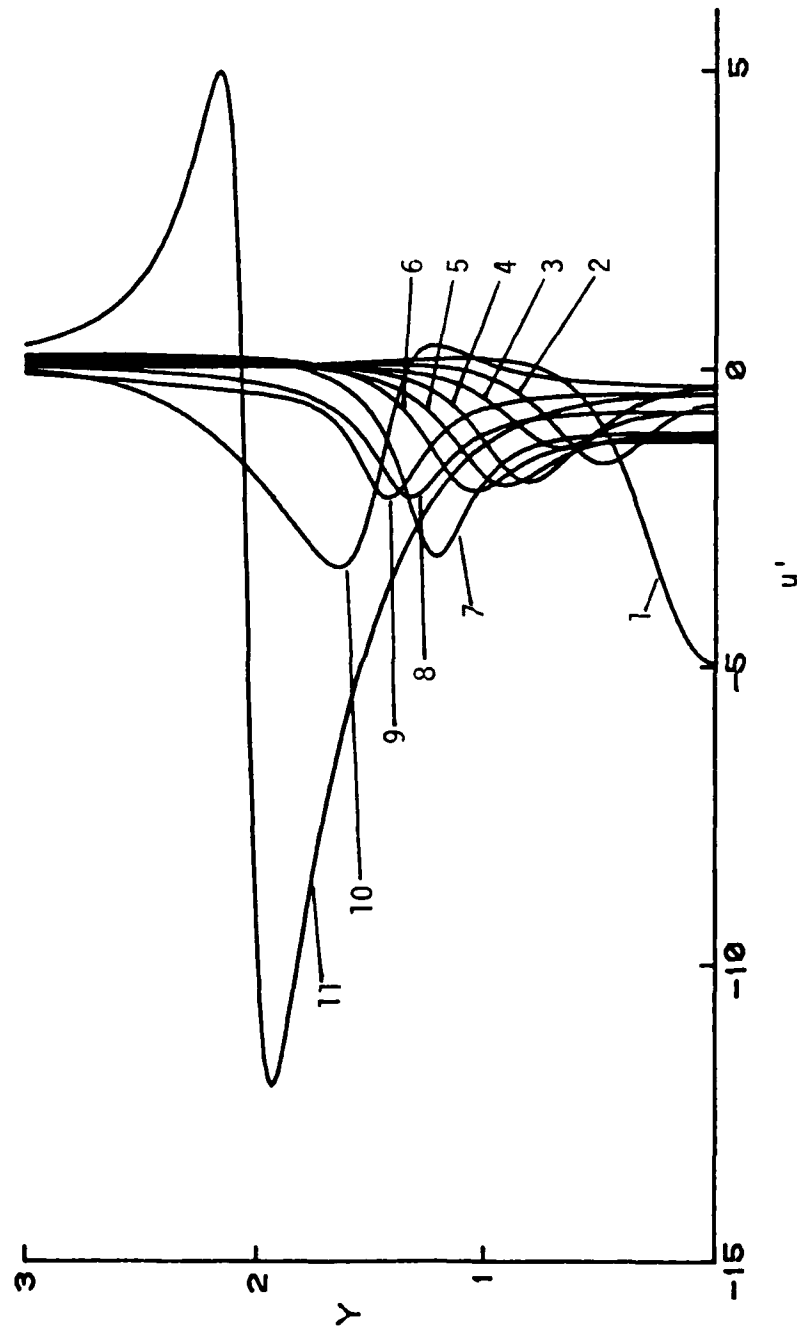


Figure 4.18(b) - Instantaneous streamwise velocity fluctuations at stations indicated in Figure 4.18(a).

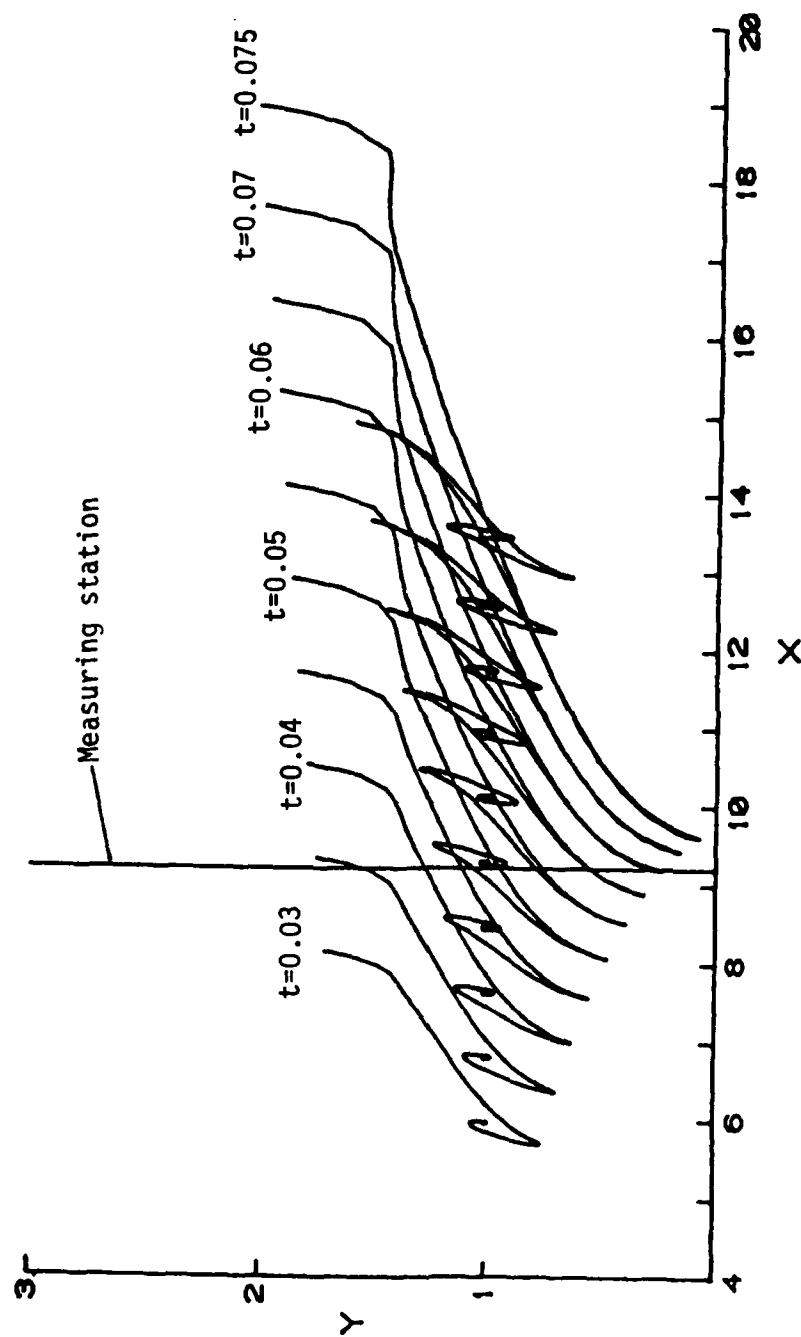


Figure 4.19(a) - Side view of the developing hairpin vortex for Case 6 at various times.

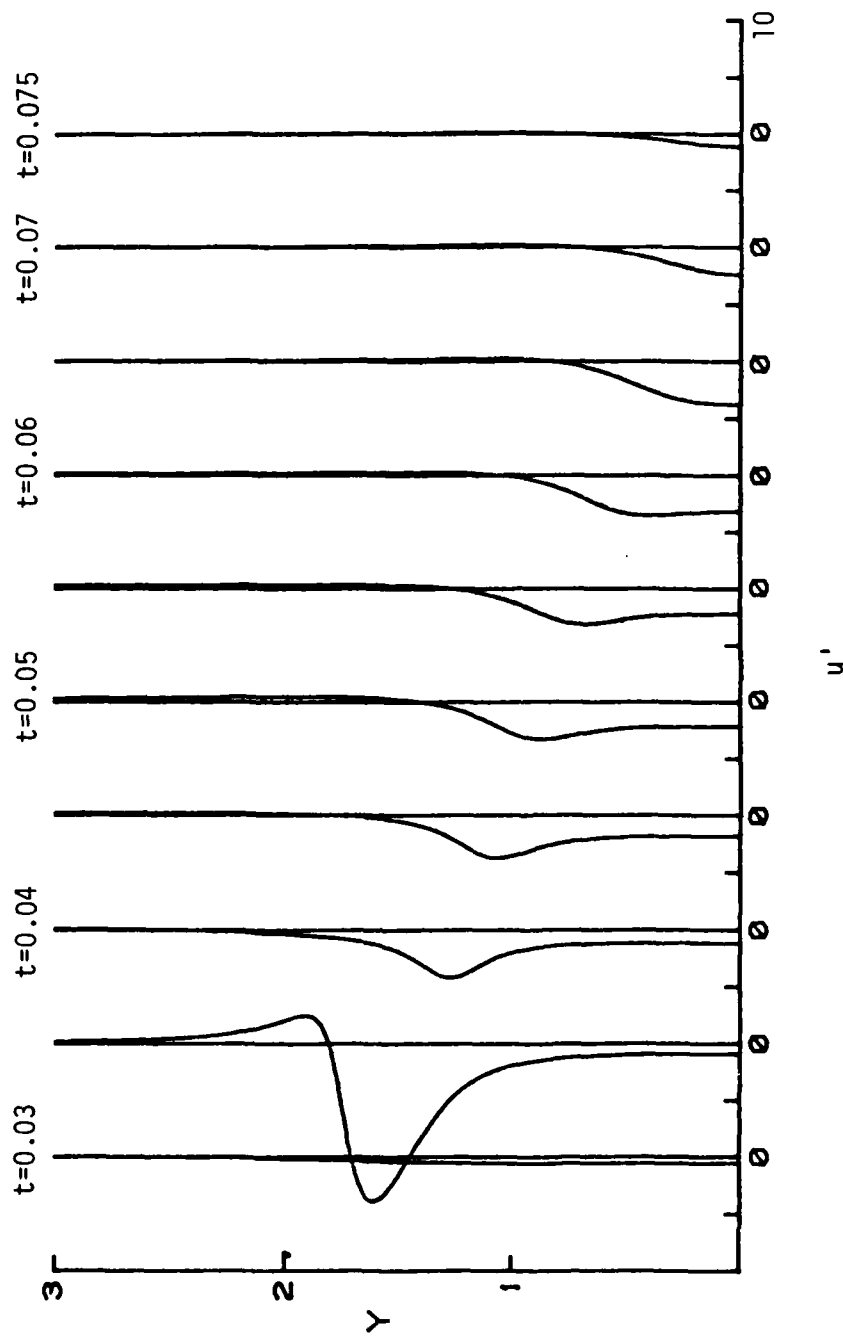


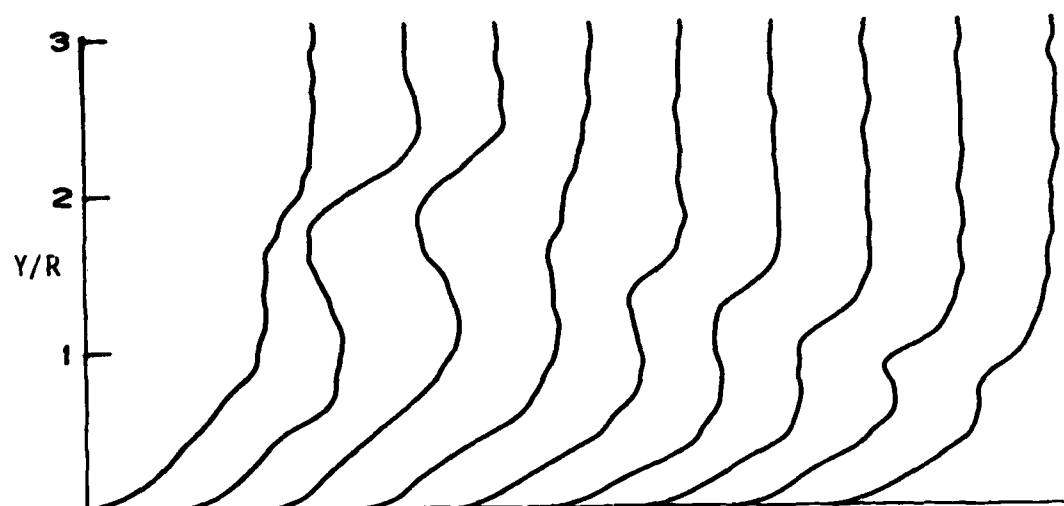
Figure 4.19(b) - Instantaneous velocity fluctuations at the measuring station indicated in Figure 4.19(a); note the shifted origins.

legs are near the measuring station and the negative fluctuation is at a maximum near the wall. With the passage of the hairpin vortex, the velocity fluctuation at the wall decreases.

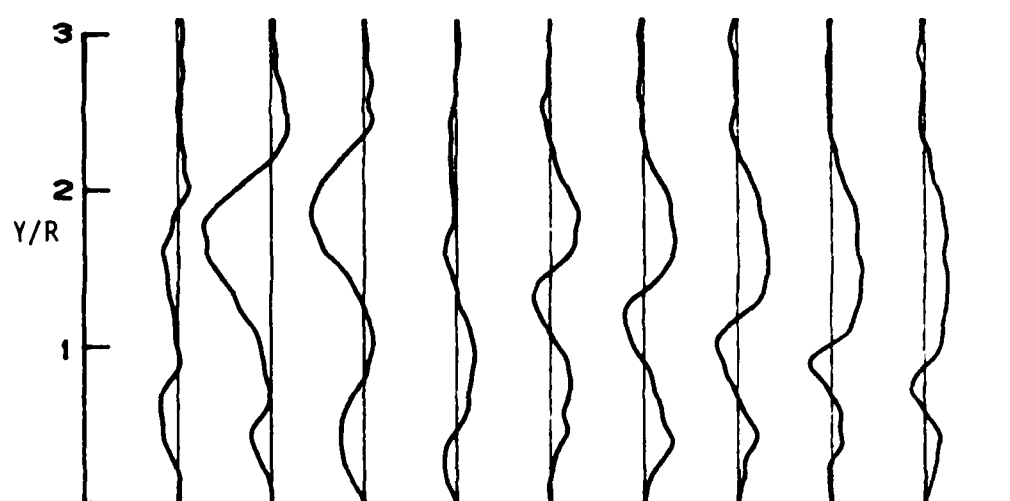
The velocity distribution due to a hairpin vortex moving in a shear flow close to a wall has been determined recently through use of image processing techniques (Lu, 1987). In this approach, the velocity profile and streamwise velocity fluctuations were obtained at a single measuring station by digitizing the high-speed video sequences of the hydrogen bubble-line patterns released by a bubble wire oriented normal to the wall. By comparing the results from successive video frames, it is possible to determine the instantaneous streamwise velocity distribution at the bubble wire (Lu and Smith, 1985). In the experiments of Lu (1987), this process was applied to hairpin vortices shed from a hemispherical protuberance in a subcritical laminar boundary-layer flow on an otherwise smooth wall. Some results from Lu (1987) are shown in Figure 4.20 for the streamwise velocity and streamwise velocity fluctuations which were recorded as a hairpin vortex passed by the hydrogen bubble wire. The sequences shown in Figure 4.20 shown successive profiles with time increasing from left to right. The trends in these results are qualitatively similar to that shown in Figures 4.17(b), (4.17(c) and 4.19(b).

4.9 Interaction of two Hairpin Vortices

In the previous section, the motion of a single hairpin vortex



(a) Velocity profiles



(b) Velocity fluctuations

Figure 4.20 - Profiles of (a) velocity and (b) velocity fluctuation of hairpin vortex over a cycle as obtained from hydrogen bubble flow visualization pictures on plane of symmetry of the hairpin vortex.

above a plane wall was considered. In this section the evolution of two interacting hairpin vortices is addressed.

For two hairpin vortices above a plane wall, the generalization of equation (4.6) is,

$$\frac{\partial \vec{\chi}_k}{\partial t}(s_0, t) = \sum_{j=1}^9 I_j(s_0, t) + \vec{u}_{\text{ext}}. \quad (4.22)$$

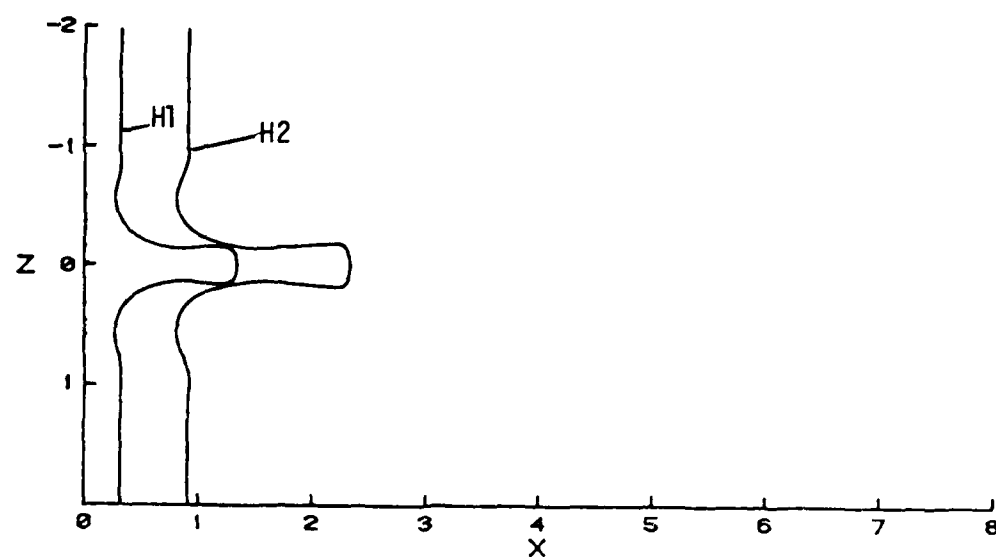
Here $k = 1, 2$ since there are now two hairpin vortices; s_0 denotes a point on vortex k and the I_j for $j = 1, 7$ are given by equations (4.7) through (4.20) for integrations along vortex k . In addition, the background flow \vec{u}_{ext} is given by the shear flow in equation (4.21). The two additional terms in equation (4.22) represent the integrations along the second vortex and are given by,

$$\begin{aligned} \vec{I}_8 &= - \int_{-\infty}^{\infty} \frac{\partial \vec{\chi}_{k'}}{\partial s} \times \frac{\vec{\chi}_k - \vec{\chi}_{k'}}{|\vec{\chi}_k - \vec{\chi}_{k'}|^3} ds, \\ \vec{I}_9 &= \int_{-\infty}^{\infty} \frac{\partial \vec{\chi}_{k'}}{\partial s} \times \frac{\vec{\chi}_k - \vec{\chi}_{k'}}{|\vec{\chi}_k - \vec{\chi}_{k'}|^3} \bigg|_{\text{image}} ds. \end{aligned} \quad (4.23)$$

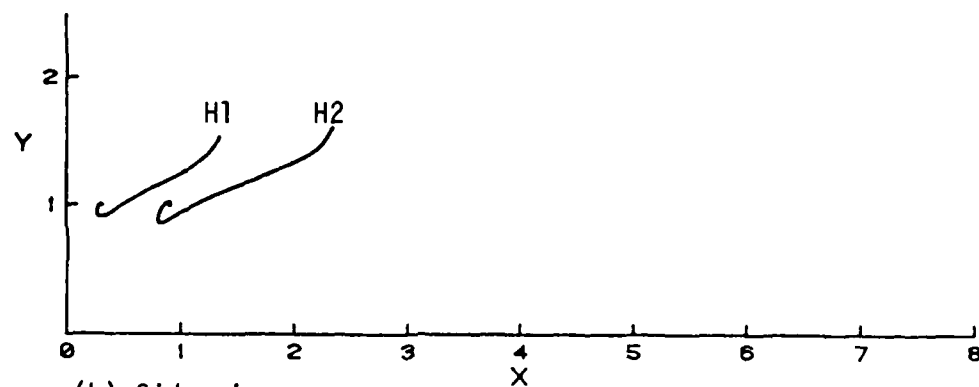
Here k' denotes the second vortex and the second integrand in equations (4.23) is evaluated along the image of vortex k' .

The numerical method used is similar to that described for the single hairpin vortex. At each stage in the 4th order Runge-Kutta method, the intermediate location of each hairpin was computed; the calculation then passed on to the next sub-step and the process was continued until a complete time step had been taken. Note that the computing time for two hairpin vortices is approximately four times as great as for a single hairpin vortex. Because of the relatively long computing times, calculations were carried out for only one case. The two hairpin vortices were selected from two locations computed in Case 6 (c.f. Section 4.5) with the second vortex positioned slightly ahead of the first. The initial configuration is shown in Figure 4.21; the first vortex is labeled H1 and is initially located slightly behind the vortex labeled H2. The evolution of these two vortices was then computed numerically; there were 600 nodal points on each vortex and the time step used was $\Delta t = 0.0001$.

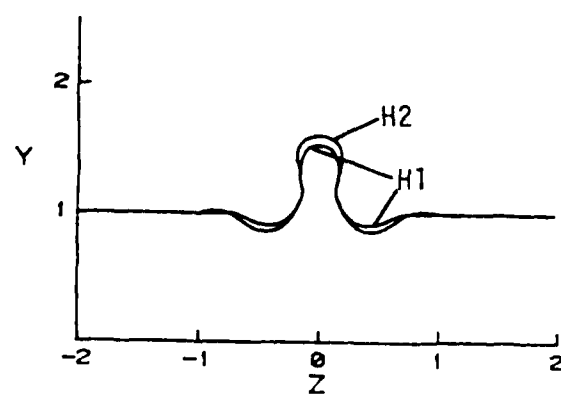
The development of the hairpins is shown in Figure 4.22 after 100 time steps at $t = 0.01$. It is evident that both vortices have been stretched in the shear flow; however, the legs of the leading hairpin H2 have moved closer together under the action of the hairpin H1 as well as being lifted (Figure 4.22(b)). The next stage of development is shown in Figure 4.23 where it may be observed that the interaction of the two vortices has continued. The trailing



(a) Top view

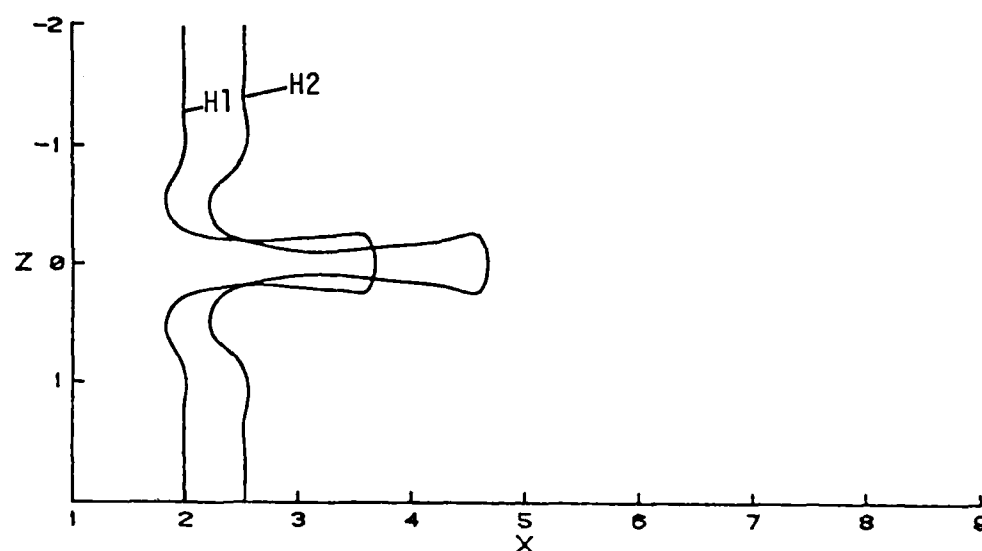


(b) Side view

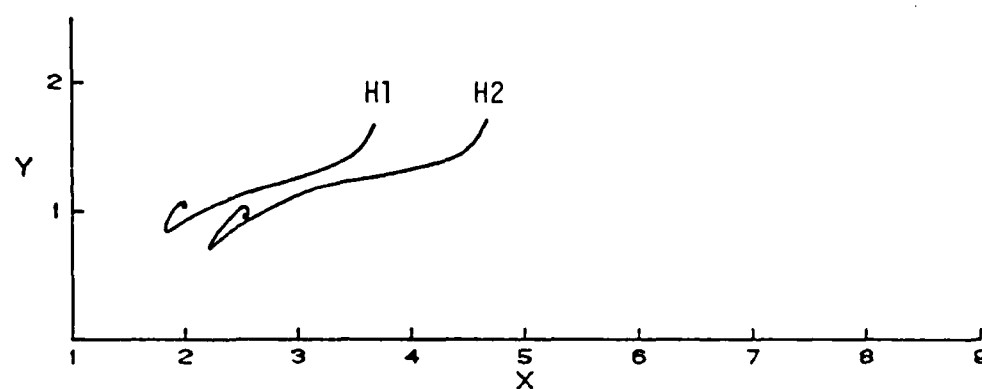


(c) End view

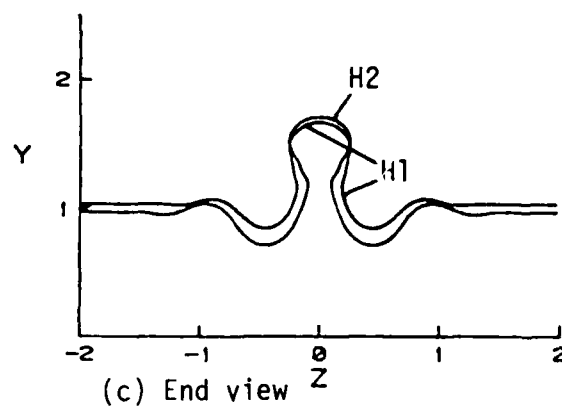
Figure 4.21 - Initial configuration for two hairpin vortices in shear.



(a) Top view

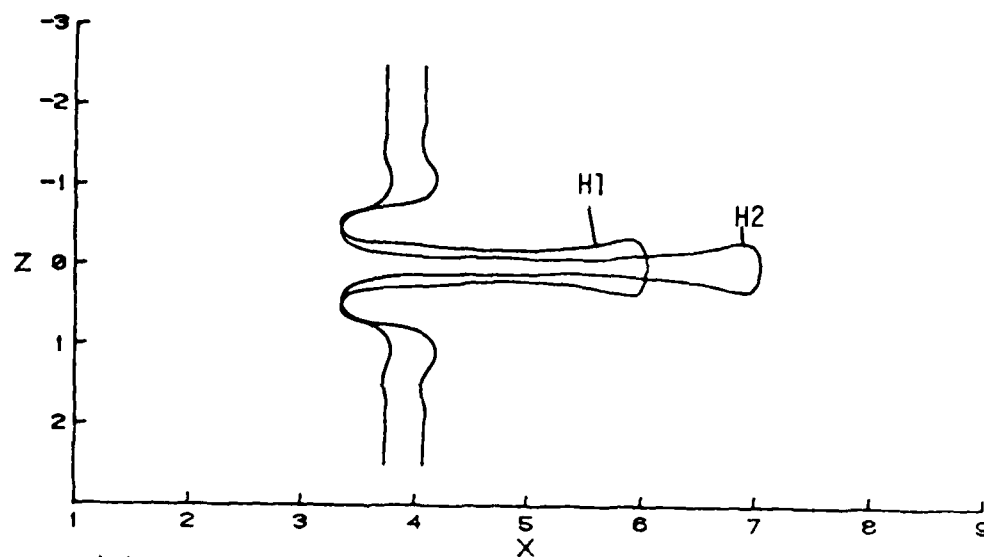


(b) Side view

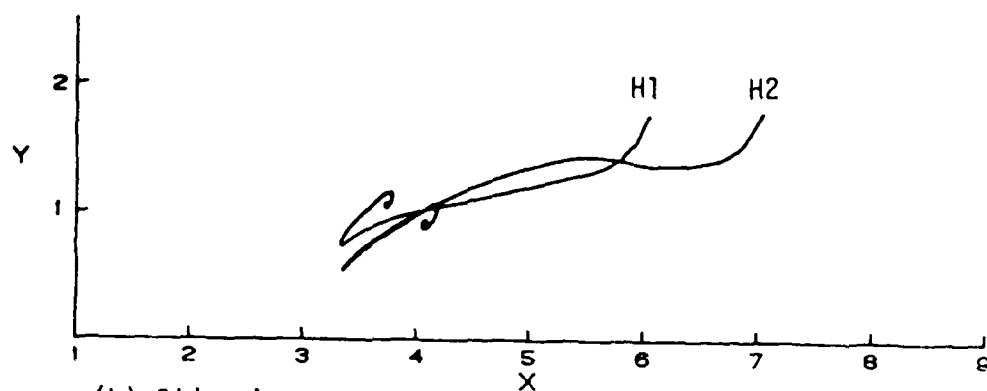


(c) End view

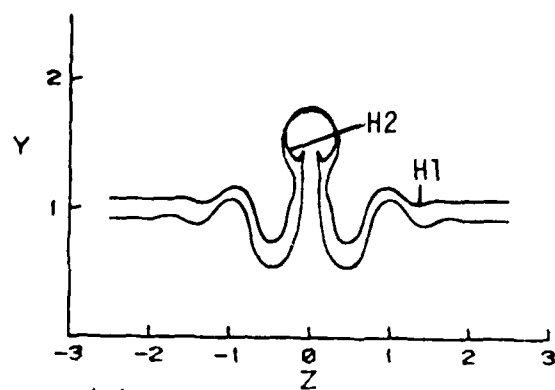
Figure 4.22 - Development of the two hairpin vortices at $t=.01$.



(a) Top view



(b) Side view



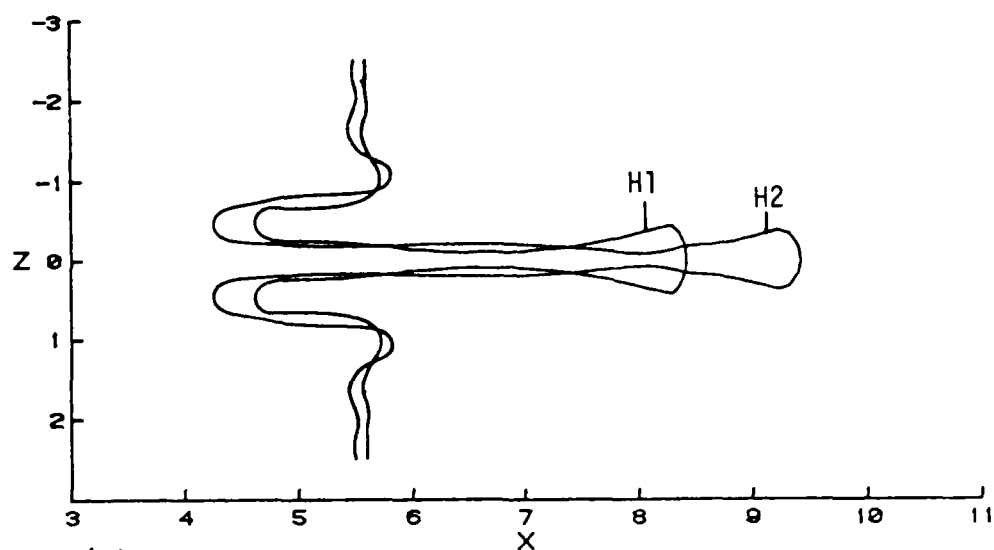
(c) End view

Figure 4.23 - Development of the two hairpin vortices at $t=.02$.

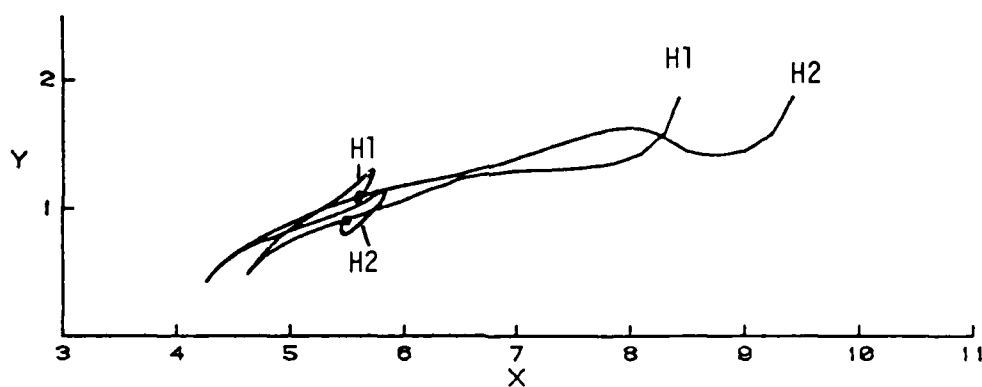
legs of H2 have now passed underneath the trailing part of H1; the middle portion of the legs of H2 have passed upward between the legs of vortex H1 (Figure 4.23(b)). The continuation of the interaction may be observed at the 300th time step at $t = 0.03$ in Figures 4.24 and then at $t = 0.4$ at the 400 time step in Figures 4.25; the calculations were terminated at the 480 time step and the vortex configurations are shown at this stage in Figures 4.26. It may be observed from these figures that the vortices tend to intertwine and then reinforce one another, particularly along the vortex legs. At the stage shown in Figure 4.26, the two vortices are relatively close to one another and the calculation failed shortly thereafter. The reason for this is believed to be due to the fact that the vortices were so close that the vortex cores were touching. Once two vortex cores approach this closely, it is necessary to consider a local interaction region where viscous effects are important and where the flow development is described by the full Navier-Stokes equations. Such a calculation has recently been carried out by Weston, Ting and Liu (1986) and by Liu, Ting and Weston (1986) for merging vortex rings. This type of calculation is extremely complicated and is beyond the scope of the present study. However it is worthwhile to note that when the interaction on merging of vortices occurs, the vortices merge in interaction zone and then recombine and break apart. The processes involved are clearly complex and not well understood.

The interaction of a pair of hairpin vortices has been observed experimentally by Acarlar and Smith (1984, 1987a, 1987b).

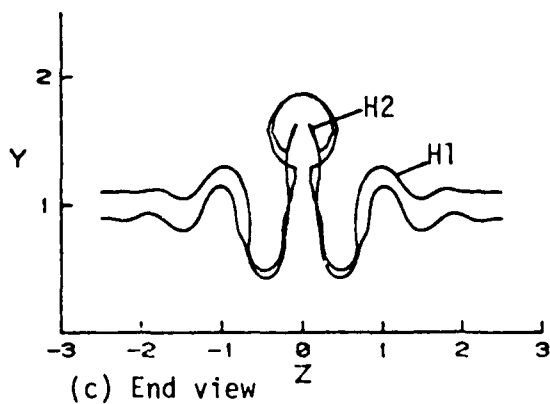
Hairpin vortices which were shed from a hemispherical protuberance located on the wall in a subcritical laminar boundary layer were marked with dye and the evolution of the vortices was observed as the vortices convected downstream. A development similar to that depicted in Figures 4.21-4.26 was clearly observed in the experiments. The legs of the older leading vortex were observed to stretch in the shear flow but then to move together under the influence of the trailing younger vortex and subsequently lift through the legs of the younger vortex. The process of vortex intertwining was clearly discernible in the experiments (c.f. Figures 3.19 and 3.20 of Acarlar and Smith, 1984).



(a) Top view

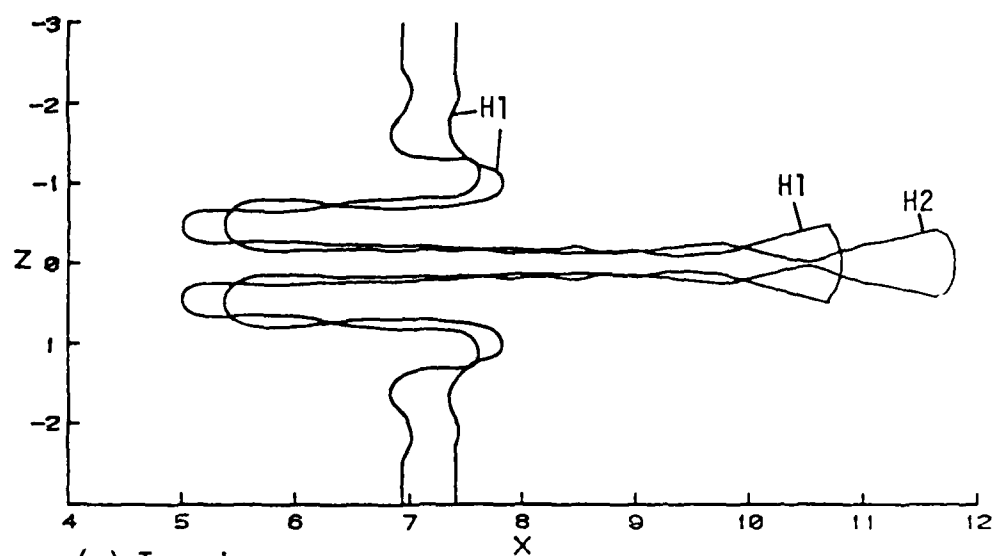


(b) Side view

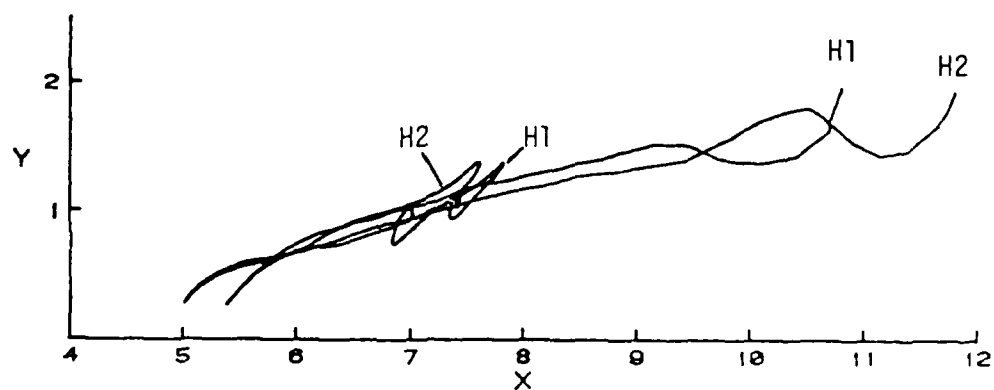


(c) End view

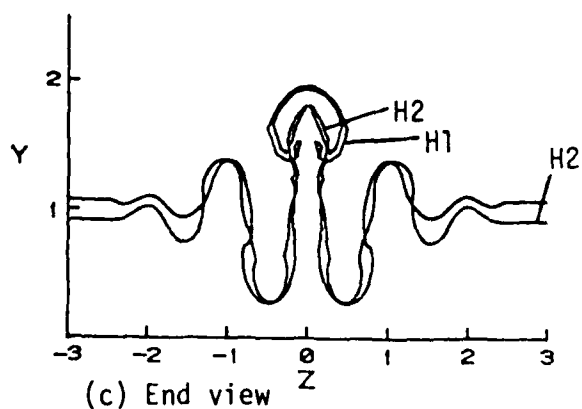
Figure 4.24 - Development of the two hairpin vortices at $t=0.03$.



(a) Top view



(b) Side view



(c) End view

Figure 4.25 - Development of the two hairpin vortices at $t=.04$.

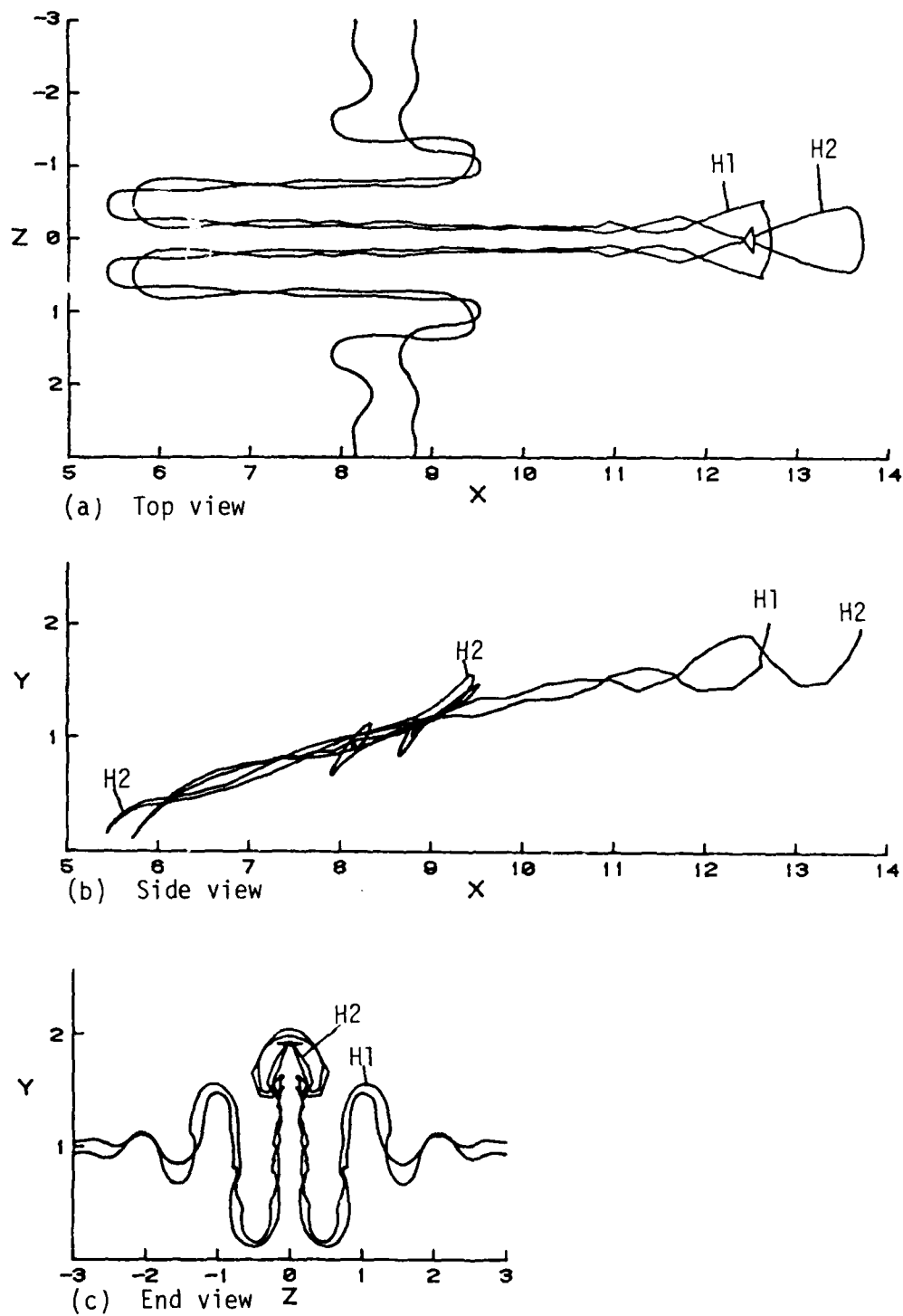
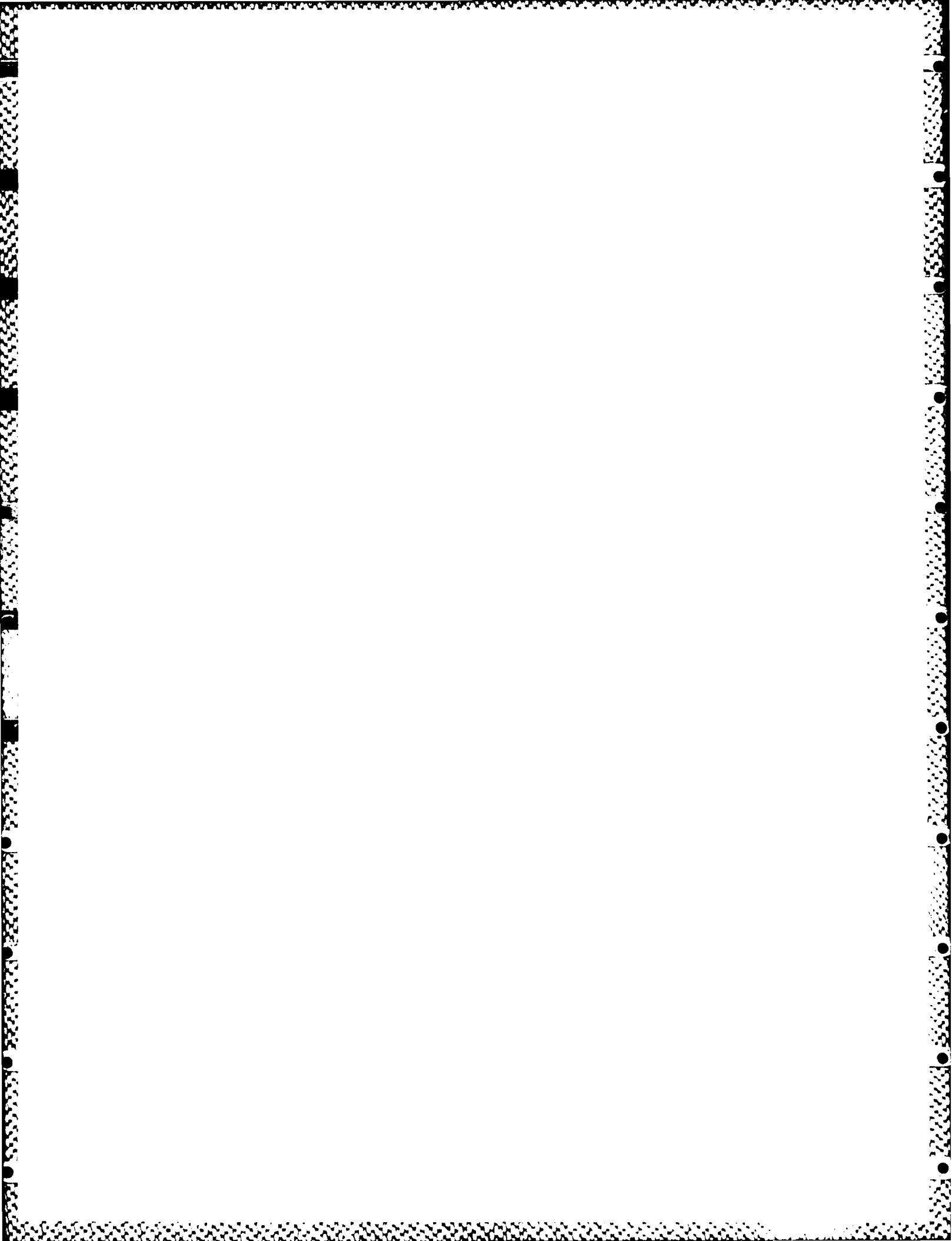


Figure 4.26 - Development of the two hairpin vortices at $t=0.048$.



CHAPTER 5

THE BOUNDARY LAYER INDUCED BY A MOVING HAIRPIN VORTEX

5.1 Introduction

In Chapter 4, the trajectories of hairpin vortices were calculated for situations where the hairpin was convected in both a uniform flow and a shear flow above a wall. In this chapter the nature of the unsteady viscous flow induced at the wall by the moving hairpin vortex will be considered. The motion of the hairpin vortex gives rise to an inviscid velocity distribution near the wall which varies in the streamwise and spanwise direction and which changes with time; near the wall, a three-dimensional unsteady boundary-layer flow develops with time. The full three-dimensional boundary-layer problem is complex and a successful treatment of such problems would require computational resources far beyond what was available in the course of the present investigation. Consequently a method was developed to study the boundary-layer development but only on the plane of symmetry of the moving hairpin vortex.

The plan of this chapter is as follows. In Section 5.2 the nature of the inviscid velocity distributions due to the moving hairpin vortex on the symmetry plane is examined. The boundary-layer problem is formulated in Section 5.3 and a set of transformations for the boundary-layer problem is described in Section 5.4. A discussion of the numerical methods used is given in Section 5.5 and calculated results for one case are described in Section 5.6.

5.2 The Inviscid Velocity Distribution

In Chapter 4, the three-dimensional evolution of hairpin vortices was computed through a numerical integration of the Biot-Savart law. At any instant, the inviscid velocity induced by the hairpin vortex is given by,

$$\begin{aligned} \vec{u}(\vec{X}_0, t) = \text{sgn}(\Gamma) \left[\int_{-\infty}^{\infty} \frac{\partial \vec{X}_h}{\partial s} \times \frac{(\vec{X}_0 - \vec{X}_h)}{|\vec{X}_0 - \vec{X}_h|^3} ds \right. \\ \left. - \int_{-\infty}^{\infty} \frac{\partial \vec{X}_i}{\partial s} \times \frac{(\vec{X}_0 - \vec{X}_i)}{|\vec{X}_0 - \vec{X}_i|^3} ds \right] . \end{aligned} \quad (5.1)$$

Here \vec{X}_0 is a vector to any location within the flow which is not located on the hairpin vortex. The vector,

$$\vec{X}_h = x_h \hat{i} + y_h \hat{j} + z_h \hat{k} , \quad (5.2)$$

is to an arbitrary point on the hairpin vortex while the vector

$$\vec{X}_i = x_h \hat{i} - y_h \hat{j} + z_h \hat{k} , \quad (5.3)$$

is to the corresponding point on the image vortex. In equation (5.1), the first and second integrals are the contributions of the hairpin and its image respectively to the induced velocity field at \vec{X}_0 .

Now consider the inviscid flow distribution near the wall which corresponds to taking the limit $y \rightarrow 0$ in equation (5.1); near the wall the position vector is,

$$\vec{\chi}_w = x\hat{i} + z\hat{k} \quad , \quad (5.4)$$

and if the inviscid velocity distribution at the wall is denoted by,

$$\vec{u}_w = U_w(x,z,t)\hat{i} + W_w(x,z,t)\hat{k} \quad , \quad (5.5)$$

it may readily be shown that,

$$U_w(x,z,t) = 2\text{sgn}(\Gamma) \int_{-\infty}^{\infty} \frac{\{(z-z_h)\frac{\partial y_h}{\partial s} + y_h \frac{\partial z_h}{\partial s}\}}{\{(x-x_h)^2 + y_h^2 + (z-z_h)^2\}^{3/2}} ds \quad , \quad (5.6)$$

$$W_w(x,z,t) = -2\text{sgn}(\Gamma) \int_{-\infty}^{\infty} \frac{\{(x-x_h)\frac{\partial y_h}{\partial s} + y_h \frac{\partial x_h}{\partial s}\}}{\{(x-x_h)^2 + y_h^2 + (z-z_h)^2\}^{3/2}} ds \quad . \quad (5.7)$$

The form of the velocity components near the symmetry plane is obtained by taking the limit $z \rightarrow 0$ in equations (5.6) and (5.7); the quantities x_h , y_h and $\partial z_h/\partial s$ are even functions of s while z_h , $\partial x_h/\partial s$ and $\partial y_h/\partial s$ are odd functions of s . Denoting the limit of U_w as $z \rightarrow 0$ by $U_\infty(x,t)$, it is easily shown from equation (5.6) that

$$U_\infty(x,t) = 4\text{sgn}(\Gamma) \int_0^{\infty} \frac{\{y_h \frac{\partial z_h}{\partial s} - z_h \frac{\partial y_h}{\partial s}\}}{\{(x-x_h)^2 + y_h^2 + z_h^2\}^{3/2}} ds \quad . \quad (5.8)$$

As $z \rightarrow 0$, $W_w \rightarrow 0$ but $\partial W_w/\partial z$ is nonzero; defining $\theta_\infty(x,t)$ by,

$$\theta_\infty(x,t) = \lim_{z \rightarrow 0} \frac{\partial W_w}{\partial z} \quad , \quad (5.9)$$

so that,

$$W_w \sim z\theta_\infty(x,t) + \text{---- as } z \rightarrow 0, \quad (5.10)$$

it may be shown using equation (5.7) that,

$$\theta_\infty(x,t) = -12\text{sgn}(\Gamma) \int_0^\infty \frac{\{y_h \frac{\partial x_h}{\partial s} + (x-x_h) \frac{\partial y_h}{\partial s}\}}{\{(x-x_h)^2 + y_h^2 + z_h^2\}^{5/2}} z_h ds. \quad (5.11)$$

It is evident that distributions of $U_\infty(x,t)$ and $\theta_\infty(x,t)$ may be evaluated at any instant by carrying out the indicated integrations in equations (5.8) and (5.11) for several values of x . This was accomplished as follows. For a fixed value of x , the integrations in equations (5.8) and (5.11) were carried out for $|s| < \ell$ using a numerical integration based on Simpson's rule. For $|s| > \ell$, the vortex was assumed to be a straight line filament and thus,

$$\frac{\partial x_h}{\partial s} = \frac{\partial y_h}{\partial s} = 0, \quad \frac{\partial z_h}{\partial s} = 1. \quad (5.12)$$

The portion of the integral in equation (5.8) for $s > \ell$ may be evaluated by exact integration using,

$$\int_\ell^\infty \frac{y_h}{\{(x-x_h)^2 + y_h^2 + z_h^2\}^{3/2}} ds = \frac{y_h}{(x-x_h)^2 + y_h^2} \left\{ 1 - \frac{z_h}{\{(x-x_h)^2 + y_h^2 + z_h^2\}^{1/2}} \right\}, \quad (5.13)$$

while the integrand for $s > \ell$ in equation (5.11) vanishes.

As examples of the nature of the U_∞ and θ_∞ distributions, two extreme cases are considered here. The first was denoted as Case 6 in Chapter 4 and corresponds to a hairpin vortex embedded in a strong shear flow; the temporal development of the vortex shape was given in Figure 4.7. In Figure 5.1, the distribution of $U_\infty(x,t)$ is depicted at various stages during the evolution of the vortex. At $t = 0$, the streamwise velocity distribution shows a region of strong deceleration and then acceleration near the wall; in this case, all values of U_∞ are negative. Note that for the case considered in Figure 5.1, the basic shear flow is zero at the wall; if the shear flow were such that the inviscid flow is reduced (through a region of uniform shear) to a finite but non-zero velocity at the wall (say U_0), then the only difference in Figure 5.1 would be that all distributions are relative to U_0 rather than 0.

As time increases, the vortex head moves progressively away from the wall and the maximum inviscid speed near the wall induced by the hairpin diminishes slightly. At a later stage ($t = 0.04$), the hairpin head has moved further from the wall but has also moved further downstream as the vortex is stretched out in the shear flow; the influence of the hairpin head at $t = 0.04$ may be seen in Figure 5.1 where a distortion has developed in the velocity distribution near $x = 11$. For increasing t , this distortion amplifies as may be observed at $t = 0.05$ near $x = 14$, at $t = 0.06$ near $x = 15$ and then near $x = 18$ at $t = 0.07$; this effect is directly associated

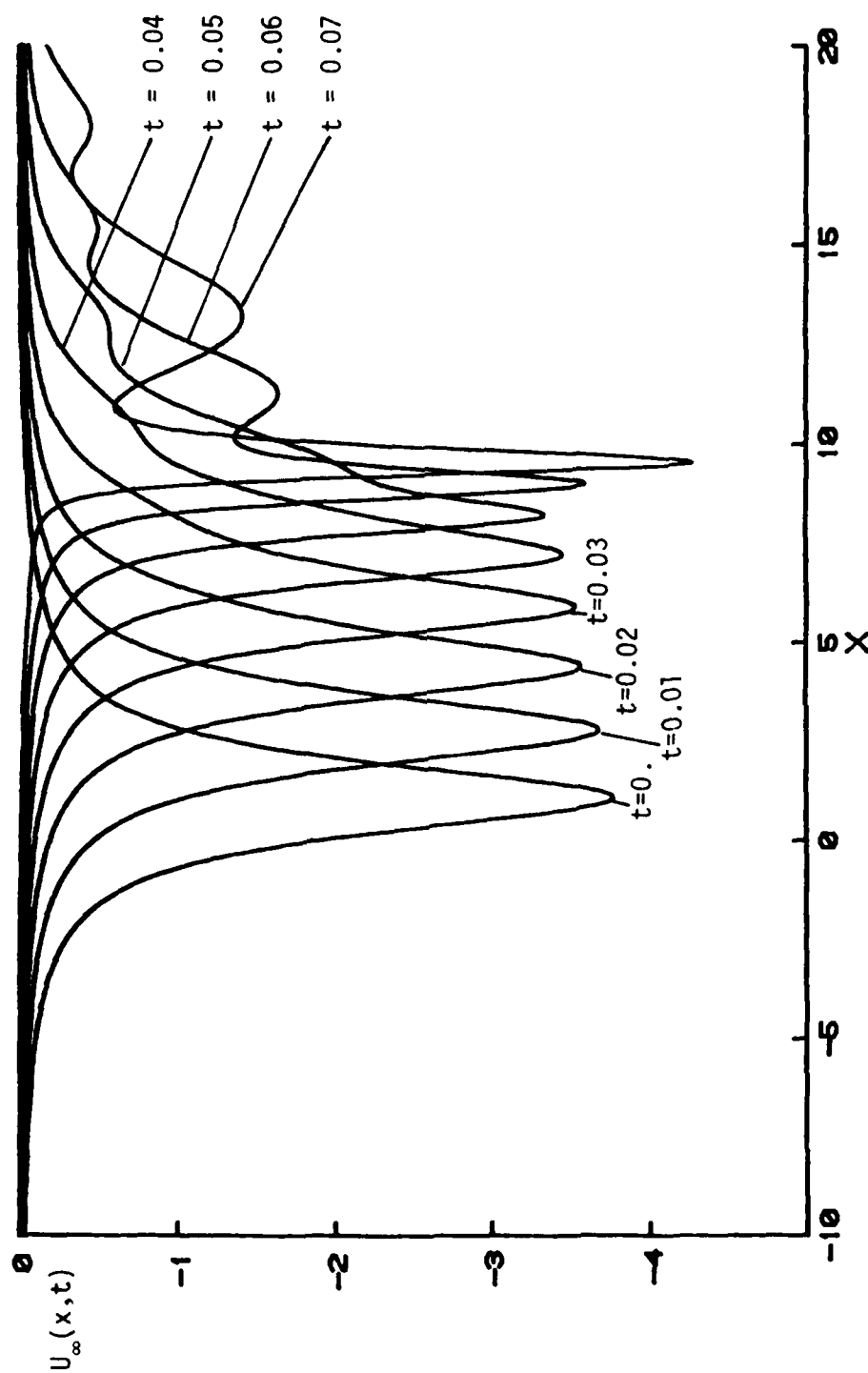


Figure 5.1 - Inviscid streamwise velocity on the symmetry plane near the wall induced by a moving hairpin vortex in shear.

with the moving vortex head and this may be confirmed by comparing Figures 5.1 and 4.7. At the later stages depicted in Figure 5.1, additional distentions develop in the inviscid velocity distributions and the origin of these can be understood from Figure 5.2. As the vortex begins to develop secondary (and then tertiary) heads which are then convected downstream, local minima will develop in the streamwise velocity distribution; for example the local minimum near $x = 12$ at $t = 0.06$ (and near $x = 13$ at $t = 0.07$) is associated with the instantaneous location of the secondary head. One final feature of the distribution in Figure 5.1 is worthy of note; at $t = 0.06$ and then at $t = 0.07$, the maximum inviscid speed has increased. This is believed to be due to the influence of the primary leg (see Figure 5.2) as it moves closer to the wall (c.f. Figures 4.7).

The evolution of the spanwise velocity is depicted in Figure 5.3 where $\theta_{\infty}(x,t)$ is plotted at various stages during the process. It may be observed that, as the hairpin is stretched in the shear and convects downstream, there is a spanwise inflow toward the symmetry plane of increasing magnitude ($\theta_{\infty} < 0$). Essentially this behavior is due to the movement of the legs toward the wall. It may be observed that the θ_{∞} distribution is developing a complicated form by $t = 0.06$. It is worthwhile to note that the θ_{∞} distribution is not entirely negative and changes sign (even at early times) at an x -location to the left of the minimum. One other feature of interest is that by $t = 0.06$ the region over which a significant θ_{∞} occurs has expanded in the streamwise direction considerably as the vortex stretches out

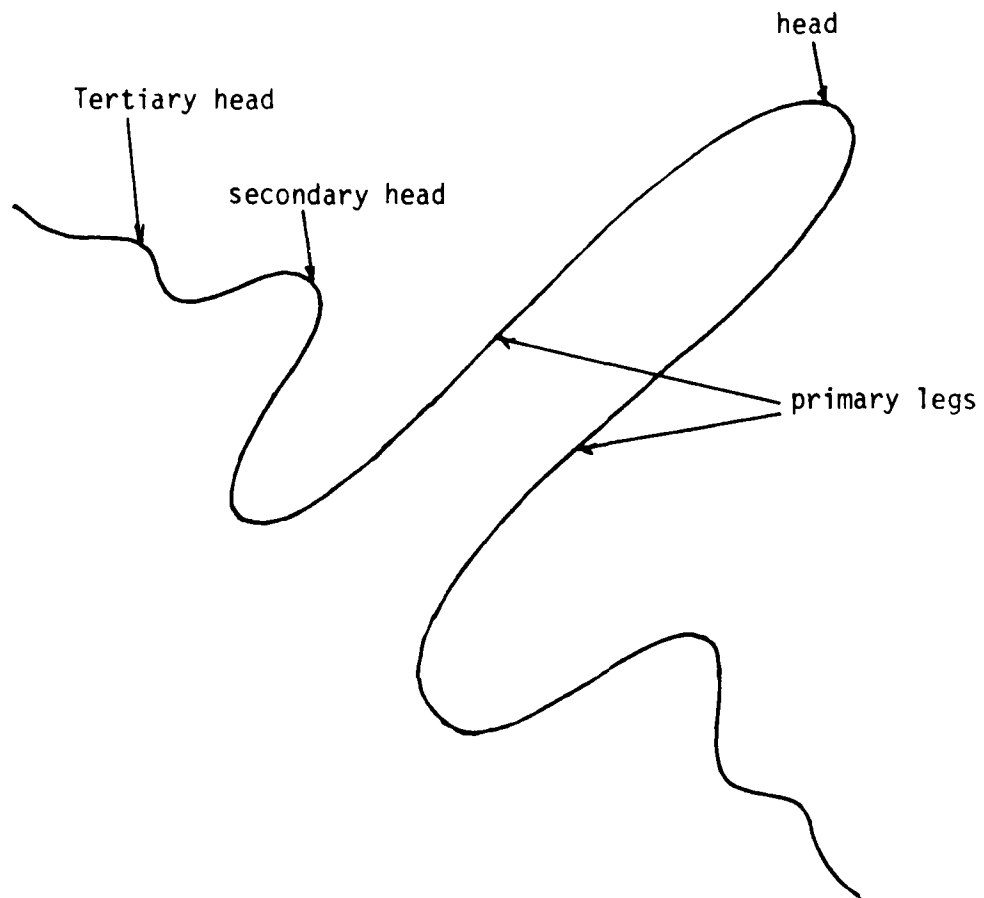


Figure 5.2 - Schematic sketch of a hairpin vortex after deformation in a shear flow.

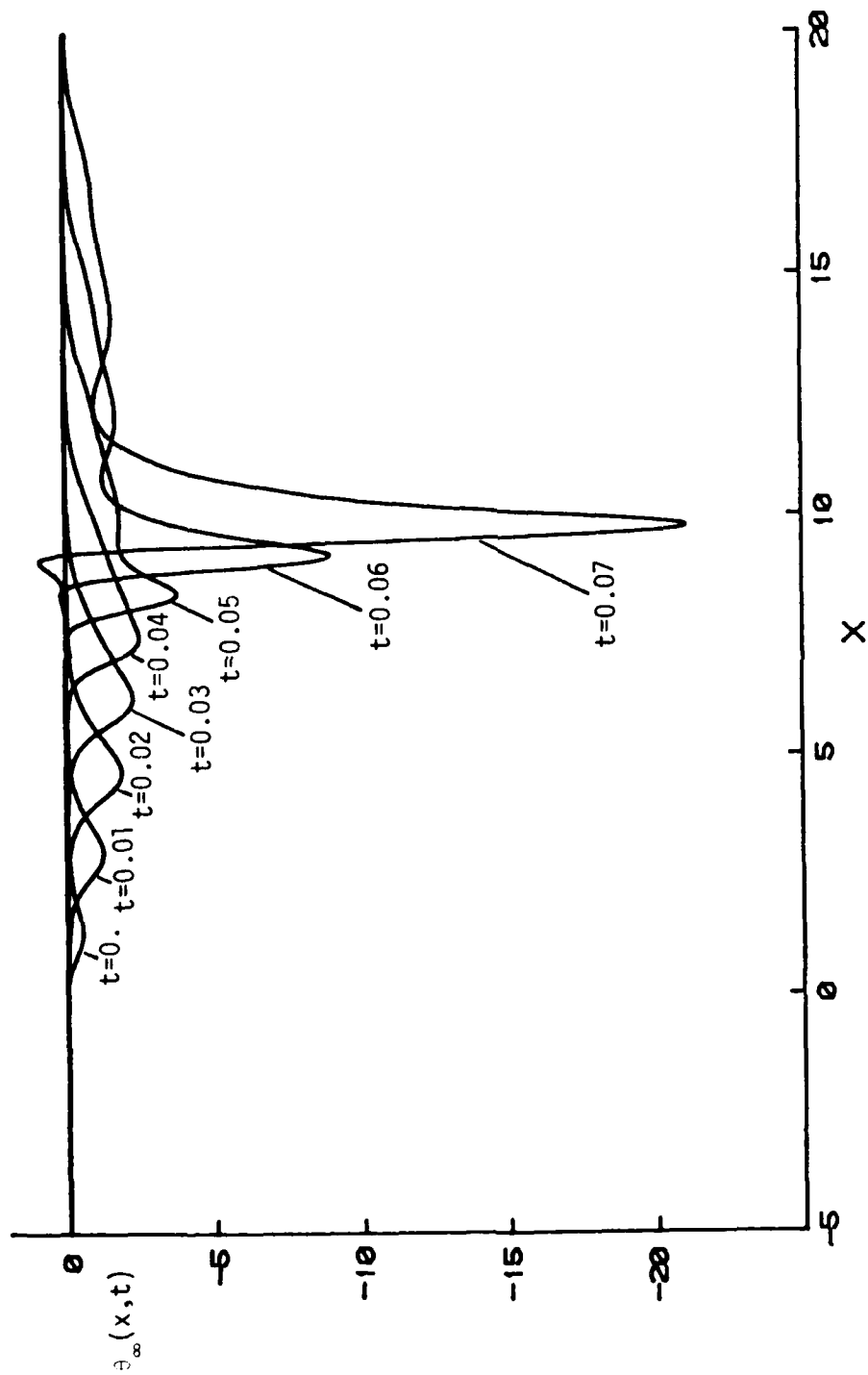


Figure 5.3 - Temporal development of the spanwise velocity distribution near the symmetry plane induced by the moving hairpin vortex in shear.

in the shear flow; at this stage, there is a significant θ_∞ in the range $9 \leq x \leq 18$ and to some extent, the spanwise flow is similar to that induced by a pair of counter-rotating streamwise vortices.

The second case considered here corresponds to the hairpin vortex evolving in an otherwise stagnant flow above a plane wall; the trajectories of the vortex for this case were plotted in Figure 4.2. The temporal evolution of $U_\infty(x,t)$ and $\theta_\infty(x,t)$ are plotted in Figures 5.4 and 5.5. Note that the changes in these distributions are rather less dramatic compared to the situation when the hairpin vortex is in shear. For a purely two-dimensional vortex, the absolute minimum in U_∞ would be at -4 and thus the effect of the three-dimensionality of the vortex is to slightly weaken the U_∞ distribution. If the same hairpin vortex were placed in an otherwise uniform flow above the wall, the only change from Figures 5.4 and 5.5 would be that the distributions would be convected to the right.

5.3 The Boundary-Layer Problem

The boundary layer that develops near the wall below the moving hairpin vortex is unsteady and fully three-dimensional. Let a representative length be d (the distance of the undisturbed straight line vortex from the wall) and take the representative velocity to be $V_c = \kappa/2d$ corresponding to self-induced convection speed of the straight part of the vortex at large distances from the hairpin. The Reynolds number for the vortex flow is defined by,

$$Re = \kappa/2\nu \quad . \quad (5.14)$$

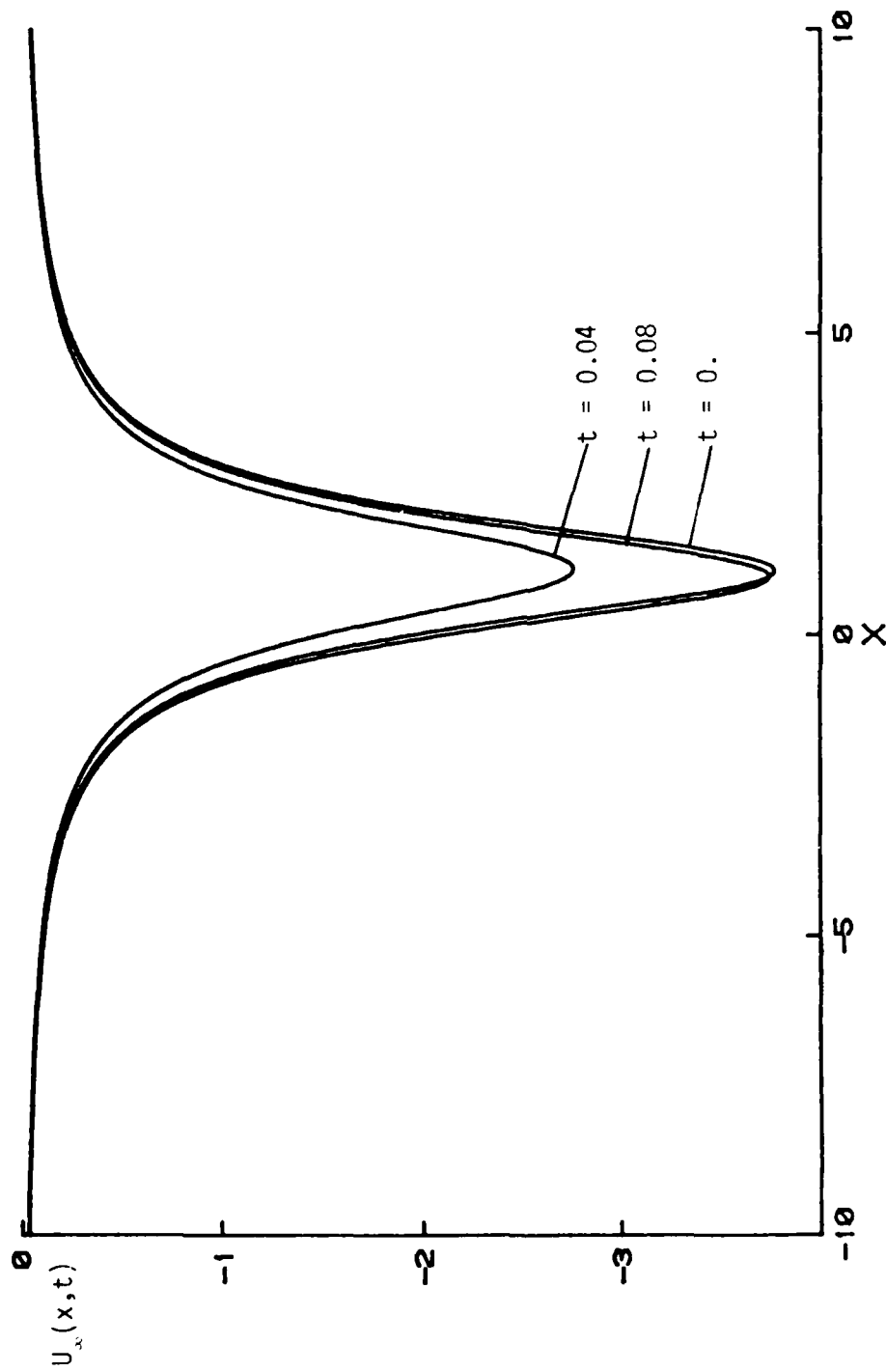


Figure 5.4 - Inviscid streamwise velocity distribution on the symmetry plane near the wall induced by a moving hairpin vortex in a stagnant flow.

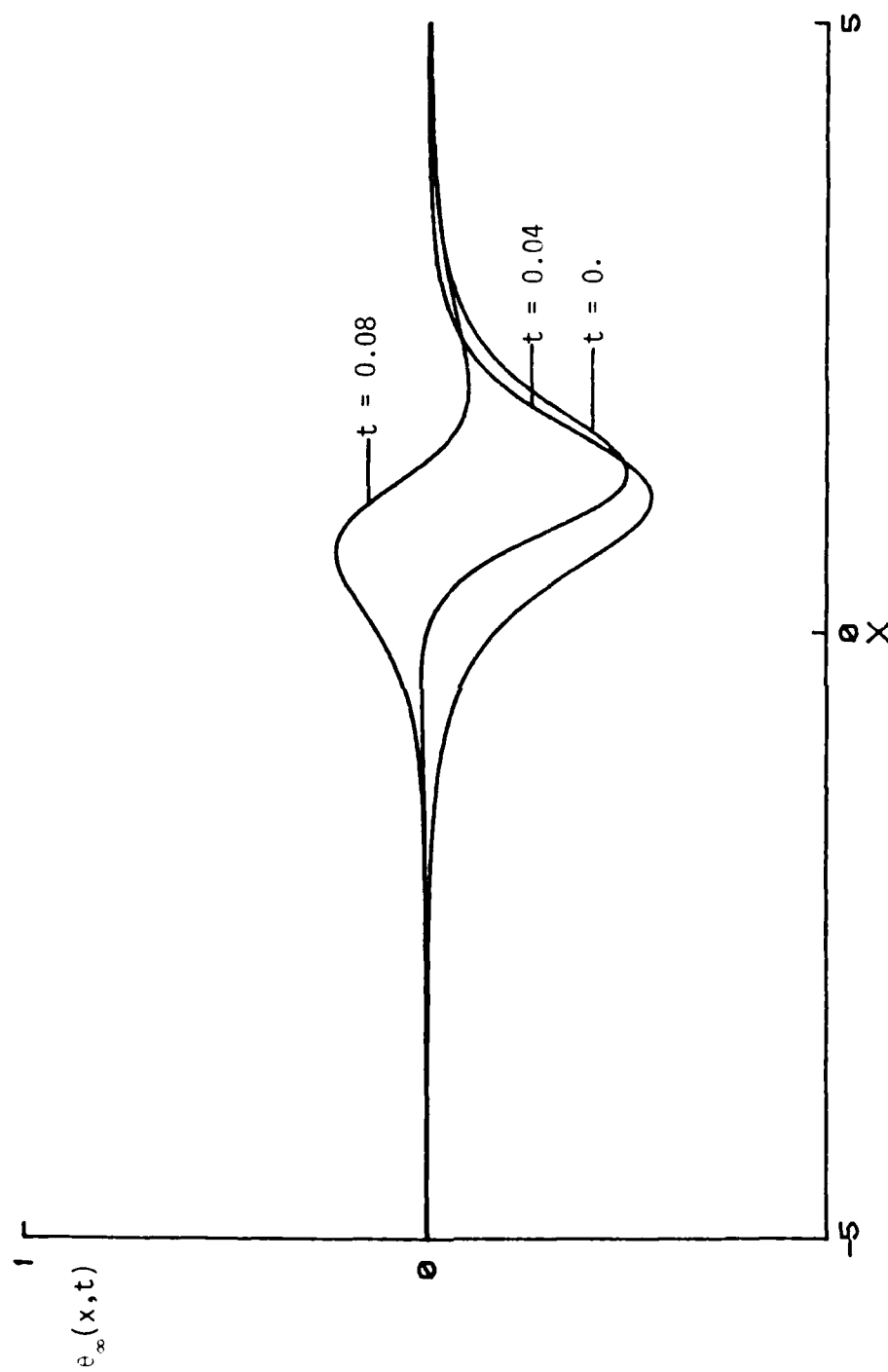


Figure 5.5 - Temporal development of the spanwise velocity distribution near the symmetry plane induced by a moving hairpin vortex in a stagnant flow.

If (x,y,z) are dimensionless Cartesian coordinates with corresponding velocity components (u,v,w) , a scaled normal coordinate and velocity in the boundary layer are defined by,

$$y' = yRe^{1/2} \quad , \quad v' = vRe^{1/2} \quad , \quad (5.15)$$

and the three-dimensional unsteady boundary-layer equations become,

$$\frac{\partial u}{\partial t} + u \frac{\partial u}{\partial x} + v' \frac{\partial u}{\partial y'} + w \frac{\partial u}{\partial z} = \frac{\partial U_w}{\partial t} + U_w \frac{\partial U_w}{\partial x} + W_w \frac{\partial U_w}{\partial z} + \frac{\partial^2 u}{\partial y'^2} \quad , \quad (5.16)$$

$$\frac{\partial w}{\partial t} + u \frac{\partial w}{\partial x} + v' \frac{\partial w}{\partial y'} + w \frac{\partial w}{\partial z} = \frac{\partial W_w}{\partial t} + U_w \frac{\partial W_w}{\partial x} + W_w \frac{\partial W_w}{\partial z} + \frac{\partial^2 w}{\partial y'^2} \quad , \quad (5.17)$$

$$\frac{\partial u}{\partial x} + \frac{\partial v'}{\partial y'} + \frac{\partial w}{\partial z} = 0 \quad , \quad (5.18)$$

where U_w and W_w are the inviscid velocities defined in equations (5.6) and (5.7).

The numerical problem associated with the full three-dimensional boundary-layer flow is very complex and would require computer resources which were not available in the present study. However the boundary-layer flow on the symmetry plane $z = 0$ develops independently of the rest of the boundary layer. The flow near the symmetry plane gives some insight into the nature of flow near the wall and consequently is of interest here. Both u and v are symmetric about $z = 0$ while w is an odd function of z ; specifically,

$$w \sim z\theta(x,y,t) + \dots \quad \text{as } z \rightarrow 0 \quad , \quad (5.19)$$

where θ is a function to be determined. Substituting equation (5.19) into equations (5.16) - (5.18) and taking the limit $z \rightarrow 0$, leads to the special form of the boundary-layer equations on the symmetry plane, viz.

$$\frac{\partial u}{\partial t} + u \frac{\partial u}{\partial x} + v' \frac{\partial u}{\partial y'} = \frac{\partial U_\infty}{\partial t} + U_\infty \frac{\partial U_\infty}{\partial x} + \frac{\partial^2 u}{\partial y'^2} , \quad (5.20)$$

$$\frac{\partial \theta}{\partial t} + u \frac{\partial \theta}{\partial x} + v' \frac{\partial \theta}{\partial y'} + \theta^2 = \frac{\partial \theta_\infty}{\partial t} + U_\infty \frac{\partial \theta_\infty}{\partial x} + \theta_\infty^2 + \frac{\partial^2 \theta}{\partial y'^2} , \quad (5.21)$$

$$\frac{\partial u}{\partial x} + \frac{\partial v'}{\partial y'} + \theta = 0 . \quad (5.22)$$

In normal circumstances it is convenient in a numerical solution of unsteady boundary-layer equations to write the streamwise velocity for example, in the form

$$u = U_\infty(x,t) F(x,y,t) . \quad (5.23)$$

The function F is then a normalized velocity which varies from zero at the wall to one at the boundary-layer edge; the procedure is successful when U_∞ is such that there are no zeros in U_∞ for all x and t . It was mentioned in Section 5.2, that U_∞ is negative for all x and t ; this may be confirmed with reference to Figure 5.1. The distribution of θ_∞ however is somewhat more complex; it may be observed in Figure 5.3 that θ_∞ is predominantly negative but eventually develops a region of positive values (and two zeros) as the

legs of the hairpin approach the wall. It is convenient to obtain a decomposition of θ_∞ of the form,

$$\theta_\infty(x,t) = \theta_1(x,t) + \theta_2(x,t) , \quad (5.24)$$

which is such the θ_1 and θ_2 do not have zeros for all x and t .

Presumably there are a variety of such decompositions; however due to the complex nature of the evolution of θ_∞ (c.f. Figure 5.3) it proved difficult to find a suitable decomposition which was valid for all t of interest. The following decomposition was obtained by trial and error:

$$\theta_1(x,t) = \int_0^\infty \frac{\{(x-x_\ell)^2+3\}^{1/2}}{\{(x-x_h)^2+y_h^2+z_h^2\}^{5/2}} e^{-s} ds , \quad (5.25)$$

$$\theta_2(x,t) = \theta_\infty(x,t) - \theta_1(x,t) . \quad (5.26)$$

Here the subscript h denotes coordinates along the hairpin and $x_\ell(t)$ is the instantaneous location of the undisturbed two dimensional portion of the vortex (at large distances from the hairpin disturbance). The temporal evolution of θ_1 and θ_2 are depicted in Figure 5.6 when it may be observed that θ_1 is positive for all (x,t) while θ_2 is always negative.

Returning now to the boundary-layer equations on the symmetry plane, it is convenient to introduce a functions $\phi(x,y,t)$ and $\psi(x,y,t)$ defined by,

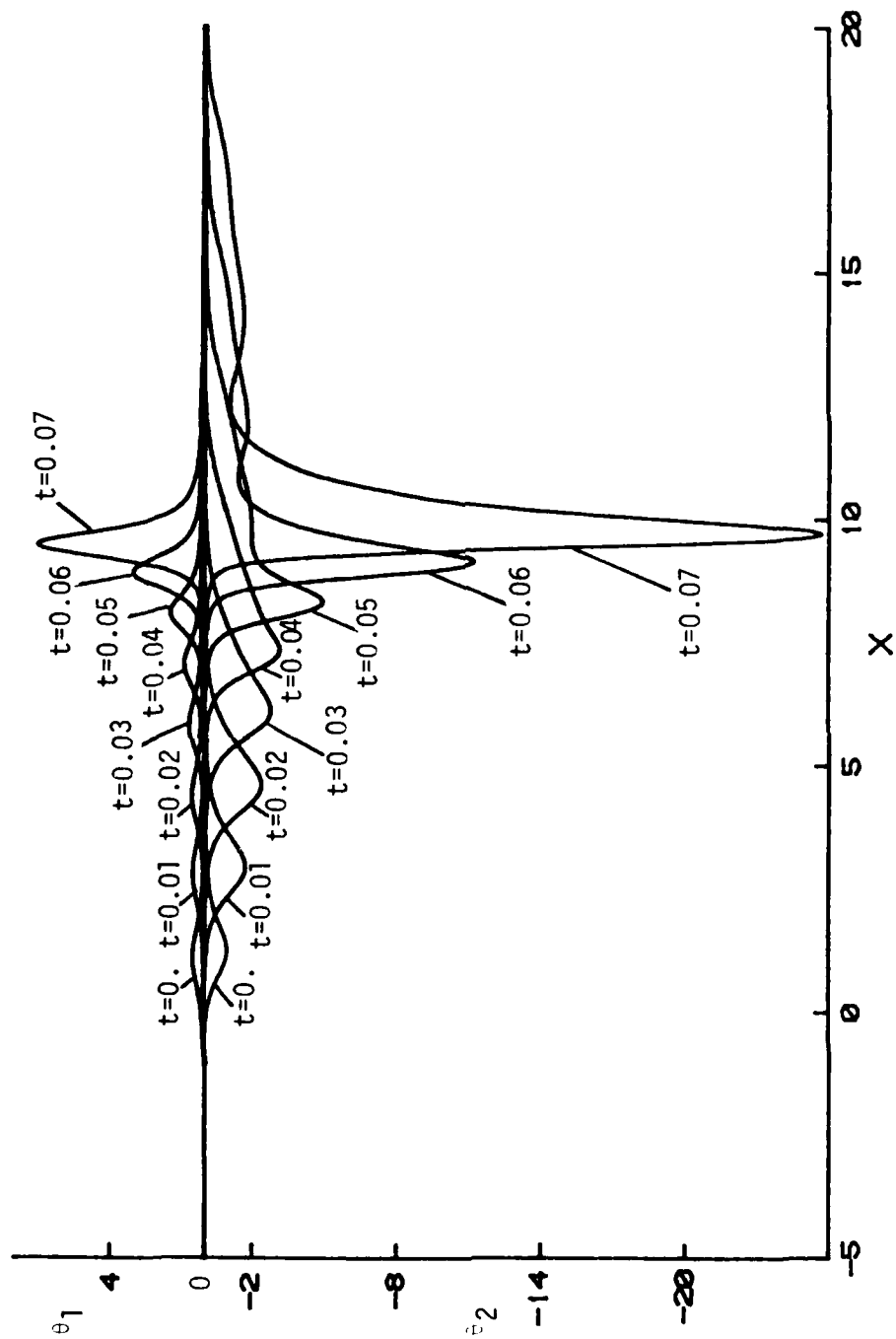


Figure 5.6 - Temporal evolution of θ_1 and θ_2 , the decomposition of ψ_a .

$$\theta = \frac{\partial \phi}{\partial y} , \quad \phi(x,0,t) = 0 , \quad (5.27)$$

and

$$u = \frac{\partial \psi}{\partial y} , \quad v = - \frac{\partial \psi}{\partial x} - \phi , \quad \psi(x,0,t) = 0 . \quad (5.28)$$

The continuity equation (5.22) is identically satisfied using these variables; note however that $\psi(x,y,t)$ is not a streamfunction and that it is not possible to define a streamfunction in a three-dimensional flow.

5.4 The Transformed Boundary-Layer Problem

The streamwise coordinate x ranges from $-\infty$ to ∞ and it is convenient to transform to a new variable ξ defined by

$$\xi = \frac{2}{\pi} \tan^{-1} \left\{ \frac{x - x_\ell(t) + \pi}{\pi} \right\} , \quad (5.29)$$

Here $x_\ell(t)$ represents the instantaneous streamwise location of the undisturbed two-dimensional portion of the vortex; this transformation is one-to-one and transforms the doubly infinite range in x to the range $(-1,1)$ in ξ . The factors of π in equation (5.29) were chosen for convenience with the objective of transforming the streamwise position of the trailing legs of the hairpin vortex to near $\xi = 1/2$. Generally one objective of a transformation like equation (5.29) is to expand or magnify regions where the streamwise velocity distribution is undergoing severe variations. In the present problem,

this is difficult to accomplish, as may be inferred from Figure 5.1, since the locations of severe variation are constantly shifting in time. The transformation in equation (5.29) is tied to the moving two-dimensional part of the vortex but as the hairpin legs begin to move near the surface, a region of intense streamwise velocity develops at values of x increasingly less than $x = x_\ell$. The transformation (5.29) does a reasonable job of keeping this range near $\xi = 1/2$ in the latter stages of the integrations. It was found by trial and error that the form of the transformation (5.29) was very important; furthermore unless particular care was taken to properly expand the regions of intense variation in U_∞ and θ_∞ , significant inaccuracies occurred in the numerical boundary-layer solutions.

In the calculations that will be reported here it was assumed that the effects of viscosity become important near the wall abruptly at $t = 0$; for all $t > 0$, a thin unsteady boundary-layer flow develops near the wall as the hairpin vortex evolves in the shear flow above the wall. In view of this "impulsive start" condition, it is necessary to define a new scaled normal coordinate by

$$\eta = \frac{y}{2\sqrt{t}} \quad , \quad (5.30)$$

which takes into account the fact that the boundary layer initially thickens proportional to $t^{1/2}$. In addition, the streamwise velocity and spanwise velocity gradient in the boundary layer are written according to,

$$u = U_{\infty} \frac{\partial \Psi}{\partial \eta} , \quad \theta = \theta_1 \operatorname{erf} \eta + \theta_2 \frac{\partial \Phi}{\partial \eta} . \quad (5.31)$$

Here the functions Ψ and Φ are related to the original functions ψ and ϕ by,

$$\psi = 2\sqrt{\epsilon} U_{\infty} \Psi , \quad \phi = 2\sqrt{\epsilon} \{ \theta_1 I(\eta) + \theta_2 \Phi \} , \quad (5.32)$$

and $I(\eta)$ is the integral of the error function given by,

$$I(\eta) = \int_0^{\eta} \operatorname{erf} \eta d\eta = \eta \operatorname{erf} \eta + \frac{1}{\sqrt{\pi}} (e^{-\eta^2} - 1) . \quad (5.33)$$

The vertical velocity v may be obtained by substitution of equations (5.32) into the second of equations (5.28) and,

$$v = -2\sqrt{\epsilon} \left\{ \theta_1 I(\eta) + \theta_2 \Phi + \frac{\partial \xi}{\partial x} \left\{ \frac{\partial U_{\infty}}{\partial \xi} \Psi + U_{\infty} \frac{\partial \Psi}{\partial \xi} \right\} \right\} . \quad (5.34)$$

The functions Ψ and Φ are subject to the boundary conditions,

$$\Psi = \frac{\partial \Psi}{\partial \eta} = \Phi = \frac{\partial \Phi}{\partial \eta} = 0 \quad \text{at} \quad \eta = 0 , \quad (5.35)$$

for all (ξ, t) at the wall and at the boundary-layer edge,

$$\lim_{\eta \rightarrow \infty} \frac{\partial \Psi}{\partial \eta} = \lim_{\eta \rightarrow \infty} \frac{\partial \Phi}{\partial \eta} = 1 , \quad (5.36)$$

for all (ξ, t) .

Under these transformations, the streamwise momentum equation along the symmetry plane becomes,

$$4t \frac{\partial U}{\partial t} = \frac{\partial^2 U}{\partial \eta^2} + P_x \frac{\partial U}{\partial \eta} + R_x U + Q_x \frac{\partial U}{\partial \xi} + G_x, \quad (5.37)$$

where,

$$U = \frac{\partial \Psi}{\partial \eta}, \quad (5.38)$$

and the coefficients in equation (5.37) are given by,

$$\left. \begin{aligned} P_x &= 2\eta + 4tV, \\ R_x &= -\frac{4t}{U_\infty(x,t)} \left\{ \frac{\partial U_\infty}{\partial t} + \frac{\partial U_\infty}{\partial \xi} \frac{\partial \xi}{\partial t} + U_\infty \frac{\partial U_\infty}{\partial \xi} \frac{\partial \xi}{\partial x} \right\}, \\ Q_x &= -4t \left\{ \frac{\partial \xi}{\partial t} + U_\infty \frac{\partial \xi}{\partial x} \right\}, \\ G_x &= \frac{4t}{U_\infty(x,t)} \left\{ \frac{\partial U_\infty}{\partial \xi} \frac{\partial \xi}{\partial t} + \frac{\partial U_\infty}{\partial t} + U_\infty \frac{\partial U_\infty}{\partial \xi} \frac{\partial \xi}{\partial x} \right\}. \end{aligned} \right\} \quad (5.39)$$

Here V is given by,

$$V = \theta_1 I(\eta) + \theta_2 \phi + \frac{\partial U_\infty}{\partial \xi} \frac{\partial \xi}{\partial x} \Psi + U_\infty \frac{\partial \Psi}{\partial \xi} \frac{\partial \xi}{\partial x}. \quad (5.40)$$

The spanwise momentum equation assumes a similar form with,

$$4t \frac{\partial T}{\partial t} = \frac{\partial^2 T}{\partial \eta^2} + P_z \frac{\partial T}{\partial \eta} + R_z T + Q_z \frac{\partial T}{\partial \xi} + G_z, \quad (5.41)$$

where,

$$T = \frac{\partial \Phi}{\partial \eta}, \quad (5.42)$$

and the coefficients in equation (5.41) are given by,

$$\begin{aligned}
 P_z &= 2\eta + 4Vt, \\
 R_z &= \frac{4t}{\theta_2} \left\{ \frac{\partial \theta_2}{\partial t} + \frac{\partial \theta_2}{\partial \xi} \frac{\partial \xi}{\partial t} + U_\infty U \frac{\partial \theta_2}{\partial \xi} \frac{\partial \xi}{\partial x} + 2\theta_1 \theta_2 \operatorname{erf} \eta + \theta_2^2 \right\}, \\
 Q_z &= -4t \left\{ \frac{\partial \xi}{\partial t} + U_\infty U \frac{\partial \xi}{\partial x} \right\}, \\
 G_z &= -\frac{4t}{\theta_2^2} \left\{ \frac{\partial \theta_1}{\partial t} \operatorname{erf} \eta + \frac{\partial \theta_1}{\partial \xi} \frac{\partial \xi}{\partial t} \operatorname{erf} \eta + U_\infty U \frac{\partial \theta_1}{\partial \xi} \frac{\partial \xi}{\partial x} \operatorname{erf} \eta \right. \\
 &\quad - \frac{2}{\sqrt{\pi}} V \theta_1 e^{-\eta^2} + \theta_1^2 \operatorname{erf}^2 \eta - \frac{\partial \theta_1}{\partial t} - \frac{\partial \theta_2}{\partial t} \\
 &\quad \left. - \left(\frac{\partial \theta_1}{\partial \xi} + \frac{\partial \theta_2}{\partial \xi} \right) \frac{\partial \xi}{\partial t} - (\theta_1 + \theta_2)^2 - U_\infty \left(\frac{\partial \theta_1}{\partial \xi} + \frac{\partial \theta_2}{\partial \xi} \right) \frac{\partial \xi}{\partial x} \right\}.
 \end{aligned} \tag{5.43}$$

Note that U_∞ , θ_1 and θ_2 in equations (5.37) through (5.43) as well as their derivatives with respect to ξ and t , are to be regarded as known functions of ξ and t which may be evaluated from equations (5.8), (5.25) and (5.26); in addition, the terms $\partial \xi / \partial x$ and $\partial \xi / \partial t$ may be evaluated by differentiation of equation (5.29), viz.

$$\frac{\partial \xi}{\partial x} = \frac{2}{\pi^2 + (x - x_\ell + \pi)^2}, \quad \frac{\partial \xi}{\partial t} = -\frac{2dx_\ell/dt}{\pi^2 + (x - x_\ell + \pi)^2}, \tag{5.44}$$

where dx_ℓ/dt is the speed (in the $+x$ direction) of the two-dimensional part of the vortex. For a given value of ξ and location $x_\ell(t)$, equation (5.29) may be solved for x and the derivatives in equation (5.44) may be computed.

The boundary conditions for equations (5.37) and (5.41) are

$$\begin{aligned} U = \psi = \tau = \eta = 0 \quad \text{at} \quad \eta = 0, \\ U, \tau \rightarrow 1 \quad \text{as} \quad \eta \rightarrow \infty. \end{aligned} \quad (5.45)$$

In addition, as $x \rightarrow \pm \infty$ ($\xi \rightarrow \pm 1$), the solution of the boundary-layer equations develops independently of the solution for $|x| < \infty$ ($|\xi| < 1$). It may be verified from equations (5.8), (5.11), (5.25) and (5.26) that U_∞ , θ_1 and θ_2 are all $O(x^{-3})$ as $|x| \rightarrow \infty$; it also follows from equations (5.44) that the gradients $\partial \xi / \partial x$ and $\partial \xi / \partial t$ are $O(x^{-2})$ as $|x| \rightarrow \infty$. Consequently it is easily confirmed that the limiting values of the coefficients in equations (5.39) and (5.43) are,

$$\left. \begin{aligned} P_{x^\infty} = P_{z^\infty} = 2\eta, \quad Q_{x^\infty} = Q_{z^\infty} = 0, \\ G_{x^\infty} = R_{x^\infty} = 4tA_1(t), \quad G_{z^\infty} = -R_{z^\infty} = 4tB_1(t), \end{aligned} \right\} \quad (5.46)$$

where $A_1(t)$ and $B_1(t)$ are defined by,

$$\left. \begin{aligned} A_1(t) &= \lim_{|x| \rightarrow \infty} \frac{1}{x} \frac{d\alpha}{dt}, \quad \alpha = \int_0^\infty \left(y_h \frac{\partial z_h}{\partial s} - z_h \frac{\partial y_h}{\partial s} \right) ds, \\ B_1(t) &= \lim_{|x| \rightarrow \infty} \frac{1}{x} \frac{d\beta}{dt}, \quad \beta = \int_0^\infty \frac{\partial y_h}{\partial s} z_h ds. \end{aligned} \right\} \quad (5.47)$$

Therefore if the solution for $U(\xi, \eta, t)$ and $\tau(\xi, \eta, t)$ at $\xi = \pm 1$ ($x \rightarrow \pm \infty$) is denoted by \bar{U} and $\bar{\tau}$, then these functions satisfy the equations

$$\left. \begin{aligned} 4t \frac{\partial \bar{U}}{\partial t} &= \frac{\partial^2 \bar{U}}{\partial \eta^2} + 2\eta \frac{\partial \bar{U}}{\partial \eta} - 4tA_1(t)\bar{U} + 4tA_1(t), \\ 4t \frac{\partial \bar{\tau}}{\partial t} &= \frac{\partial^2 \bar{\tau}}{\partial \eta^2} + 2\eta \frac{\partial \bar{\tau}}{\partial \eta} - 4tB_1(t)\bar{\tau} + 4tB_1(t), \end{aligned} \right\} \quad (5.48)$$

and the boundary conditions (5.45)

The boundary-layer flow was assumed to develop abruptly from rest corresponding to the insertion of the hairpin vortex in the shear flow at $t = 0$. As $t \rightarrow 0^+$, the limiting form of equations (5.37), (5.41) and (5.43) is,

$$\left. \begin{aligned} 4t \frac{\partial U}{\partial t} &= \frac{\partial^2 U}{\partial n^2} + 2n \frac{\partial U}{\partial n} \\ 4t \frac{\partial T}{\partial t} &= \frac{\partial^2 T}{\partial n^2} + 2n \frac{\partial T}{\partial n} \end{aligned} \right\}, \quad (5.49)$$

and the solution of these equations satisfying conditions (5.45) is,

$$U = T = \operatorname{erf} n. \quad (5.50)$$

5.5 Numerical Methods

The numerical methods used in this study are similar to those described by Ersoy and Walker (1985b). Starting from an initial location, the evolution of the hairpin vortex was computed using the methods outlined in Chapter 4; the results of this calculation were stored on disk and a boundary-layer integration using a Crank-Nicolson method (Ersoy and Walker, 1985b) was initiated. The initial boundary-layer flow is described by equations (5.50) and to advance the solution in time the following procedure was used. The solution at $\xi = +1$ was first advanced one time step by advancing the solution of equations (5.48); with the solution at $\xi = +1$ known for a given value of t , the solution of equations (5.37) and (5.41) was then

advanced one time step. Central difference approximations were used for the spatial derivatives and the method is second order accurate both in space and time. The numerical method for the interior calculation ($-1 < \xi < 1$) is implicit and at a given time step iteration is required; typically 15 to 20 sweeps of the mesh were needed at each time step to obtain convergence which was deemed to have occurred when two successive iterates for U and T agreed to within four significant figures at each mesh point. A typical time step used was $\Delta t = 0.0002$ and typical spatial mesh sizes were $h_1 = 0.01$ in the ξ direction and $h_2 = 0.05$ in the η direction. The last of conditions (5.45) were applied at a value of $\eta_{\omega} = \lambda = 6$ as an approximation and this was believed to be large enough to ensure that there would be no significant change in the solution with a larger value of λ . Consequently in a typical calculation there were 201 mesh points in the ξ direction and 121 in the direction normal to the wall; these mesh sizes are believed to be small enough to ensure good accuracy.

The results of the computations are subsequently depicted through three types of plots, namely: (a) instantaneous streamline plots in the $x\eta$ plane, (b) plots of lines of constant ψ in the $x\eta$ plane and (c) limiting surface streamlines in the xz plane near the symmetry plane of the hairpin vortex at $z = 0$. The methods used to plot these results are described in detail by Ersoy and Walker (1985b) but will be discussed briefly here.

As a result of a completed boundary-layer integration, values of u and v are known at each time step at each point in a rectangular

mesh covering the xr plane. In general, the equations of an instantaneous streamline are given by,

$$\frac{dx}{u} = \frac{dy}{v} = \frac{dz}{w} = d\tau, \quad (5.51)$$

where τ is a parameter measuring distance along a given streamline. A numerical approximation to the first of equations (5.51) is

$$x - x_0 = u_0 \Delta\tau, \quad r - r_0 = \frac{v_0}{2\sqrt{t}} \Delta\tau, \quad (5.52)$$

where (u_0, v_0) are the instantaneous velocities at an arbitrary initial point (x_0, r_0) at fixed time t . By selecting a step $\Delta\tau$, the streamline through the initial point may be traced in the xr plane at time t ; since the spatial mesh sizes h_1 and h_2 are small it is possible to compute accurate values of u and v at any point in the plane using two-dimensional linear interpolation. In order to ensure a smooth tracing, the step length $\Delta\tau$ was selected so that (Ersoy and Walker, (1985b),

$$(u^2 + v^2) \Delta\tau = 0.005, \quad (5.53)$$

at any stage.

The lines of constant θ were obtained in a standard way. The third type of plot which will be described are limiting surface streamlines in the xz plane; at locations close to the symmetry plane, the u and w velocity components are given by,

$$u = u(x,y,t) + O(z^2) \quad , \quad w = z\theta(x,y,t) + O(z^3), \quad (5.54)$$

where the right sides of equations (5.54) are the symmetry plane quantities computed in this study. For small z , equations (5.54) provide a reasonable description of the flow field near the symmetry plane. Near the surface, v is $O(y^2)$ while u and w are $O(y)$; thus for small y the streamlines are described approximately by,

$$\frac{dz}{z\theta} = \frac{dx}{u} = d\tau' \quad , \quad y \ll 1 \quad , \quad (5.55)$$

where τ' is a variable measuring distance along a streamline. In the present study, the limiting streamlines were plotted using values of u and θ at $y = h_2 = 0.05$, which is one mesh length off the surface. Note that it is not possible to clearly delineate a specific range of values of z for which equations (5.54) give a good representation of the velocity components; the maximum value of z used here was $z = 0.1$. It is also worthwhile to mention that an alternate representation of the limiting surface streamlines is to formally take the limit as $y \rightarrow 0$ in equation (5.55) to obtain,

$$\frac{dz}{dx} = z \lim_{y \rightarrow 0} \frac{\theta(x,y,t)}{u(x,y,t)} = z f(x,t) \quad , \quad (5.56)$$

where

$$f(x,t) = \left. \frac{\partial \theta / \partial y}{\partial u / \partial y} \right|_{y=0} \quad . \quad (5.57)$$

Integration of equation (5.56) yields,

$$z = z_0 \exp \left\{ \int_{x_0}^x f(\xi, t) d\xi \right\} , \quad (5.58)$$

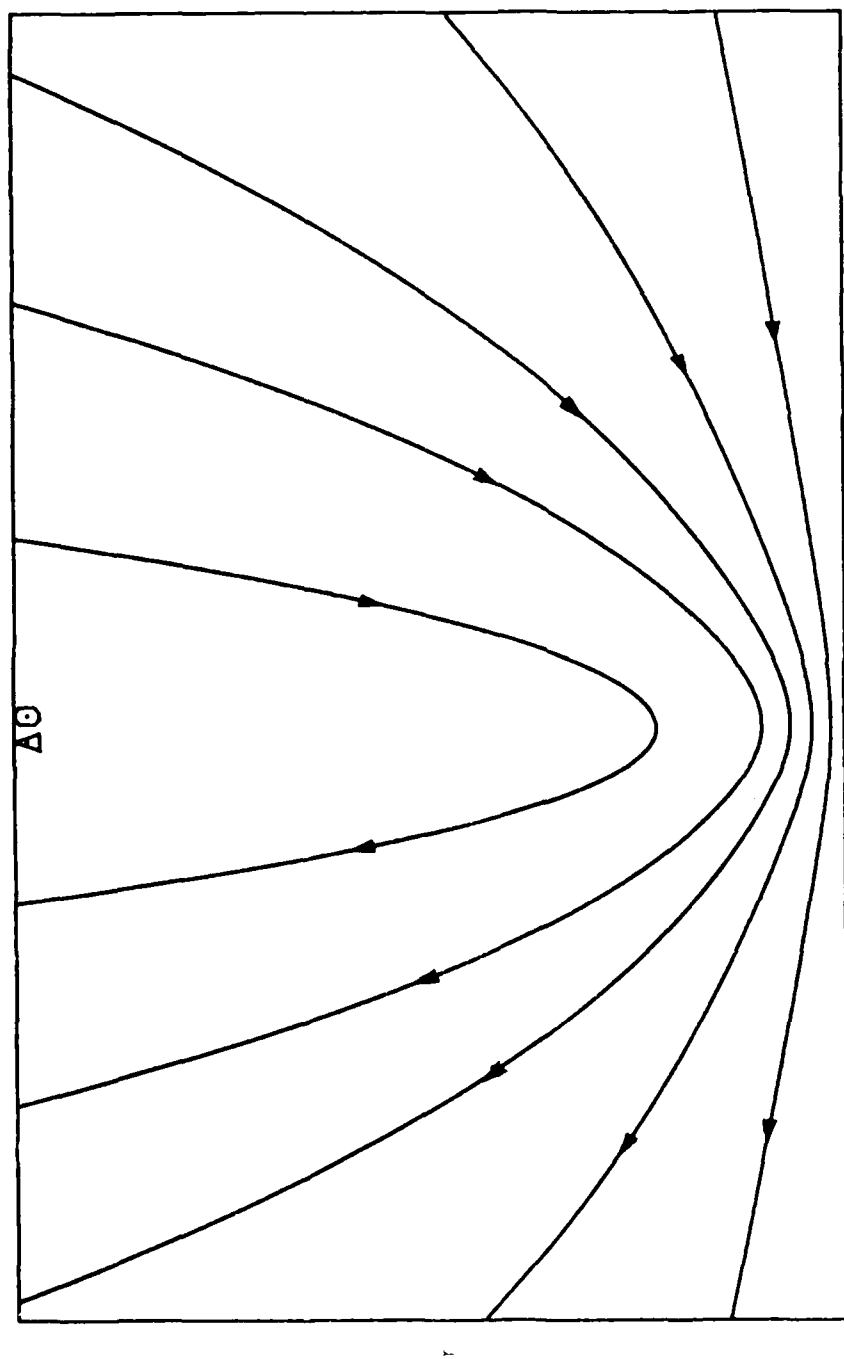
where x_0 and z_0 are constants. In principle the limiting surface streamlines may be plotted using equation (5.58); in the present study, it was convenient to use the same methods that were used to plot the streamlines on the symmetry plane to plot the limiting surface streamlines (using equations (5.55)).

5.6 Calculated Results

The computation of the developing boundary-layer flow on the symmetry plane is very time consuming and each case involved on the order of several days on a VAX 8300. The problem is complicated by the fact that as the hairpin moves, the regions of intense variation in the θ_∞ and U_∞ distributions constantly shift with time and considerable effort had to be expended in finding a suitable transformation of the form (5.29) which would reflect the vortex behavior in a specific case. In the calculations that will be reported, there were 201 mesh points in the ξ direction ($h_1 = 0.01$) and 121 points in the η direction ($h_2 = 0.05$). Even with the large number of points in the ξ direction, it was determined that unless the transformation (5.29) was adjusted to a specific case, that "wiggles" would develop in the computed results as the vortex began to severely deform in the shear flow; these "wiggles" were thought to be a clear indication of an inadequate streamwise mesh spacing in particular regions of the flow. Due to the considerable difficulties that were experienced in

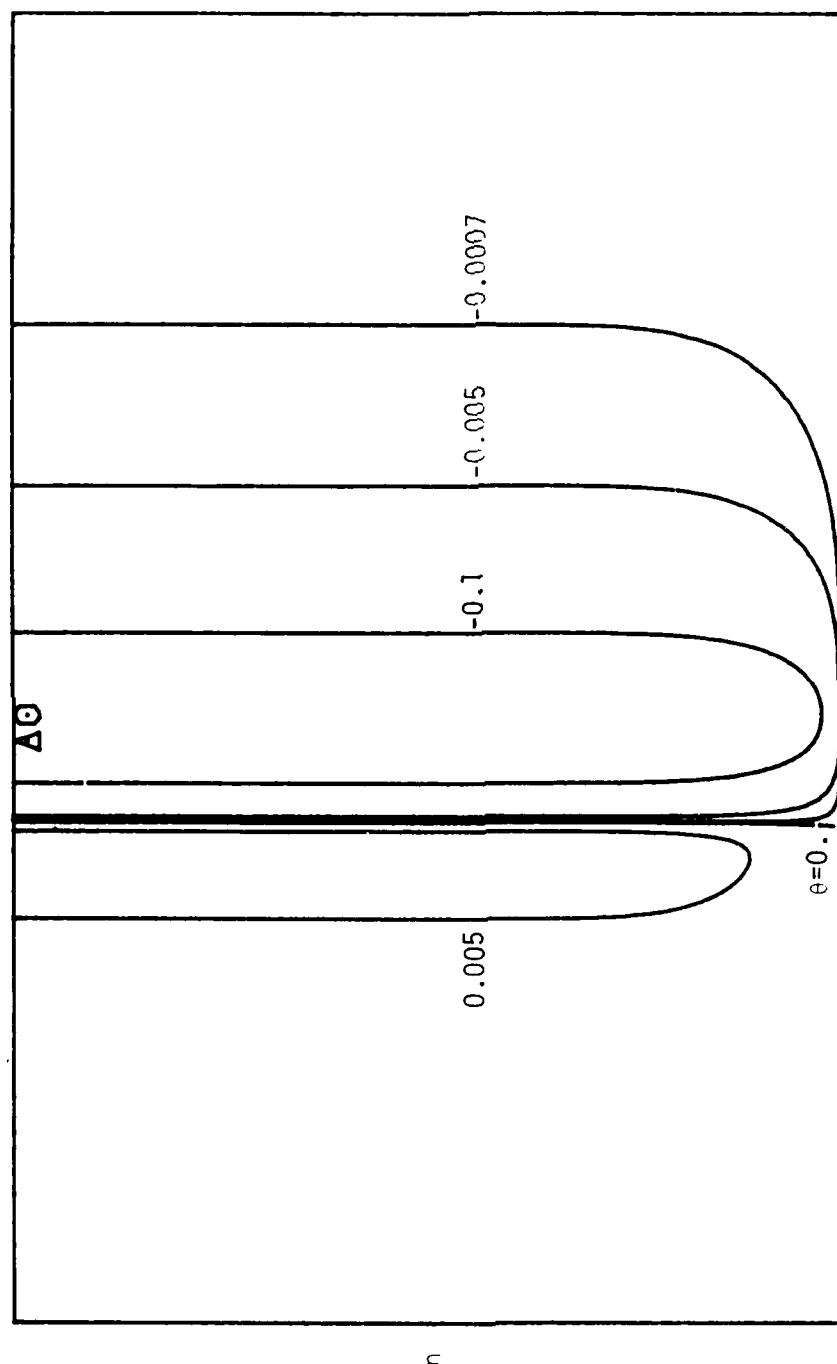
calculating the boundary-layer evolution, a limited number of reliable results were obtained in the computational time available and results will be reported here for only one case. This situation corresponds to Case 6 of Section 4.5 and consists of a hairpin vortex convected in a shear flow above a boundary-layer flow near a wall. The cases involving a vortex deforming in an irrotational flow were not considered interesting and most of the effort here was directed toward the situations involving vortices in shear. The time-step used in this calculation was $\Delta t = 0.0002$. In the early stages of the integration, the difference equations were solved with successive-over-relaxation iterative methods; at later times, it was found that under-relaxation was more effective in obtaining a converged solution of the difference equations at each time step.

The flow development at $t = 0.001$ is depicted in Figures 5.7. In these graphs (and all subsequent graphs) the polygonal symbol at the top of the graph denotes the instantaneous streamwise location of the hairpin head on the symmetry plane; the triangle denotes the streamwise location of the undisturbed two-dimensional vortex. In Figure 5.7(a) the arrows denote the instantaneous direction of flow in the symmetry plane where it may be observed that the flow is initially almost symmetric. In Figure 5.7(b) the contours of constant θ are plotted; positive values of θ mean that the local spanwise flow is away from the symmetry plane while negative values of θ show that the vortex is inducing a fairly strong inflow toward the symmetry plane. The limiting surface streamlines in the xz plane

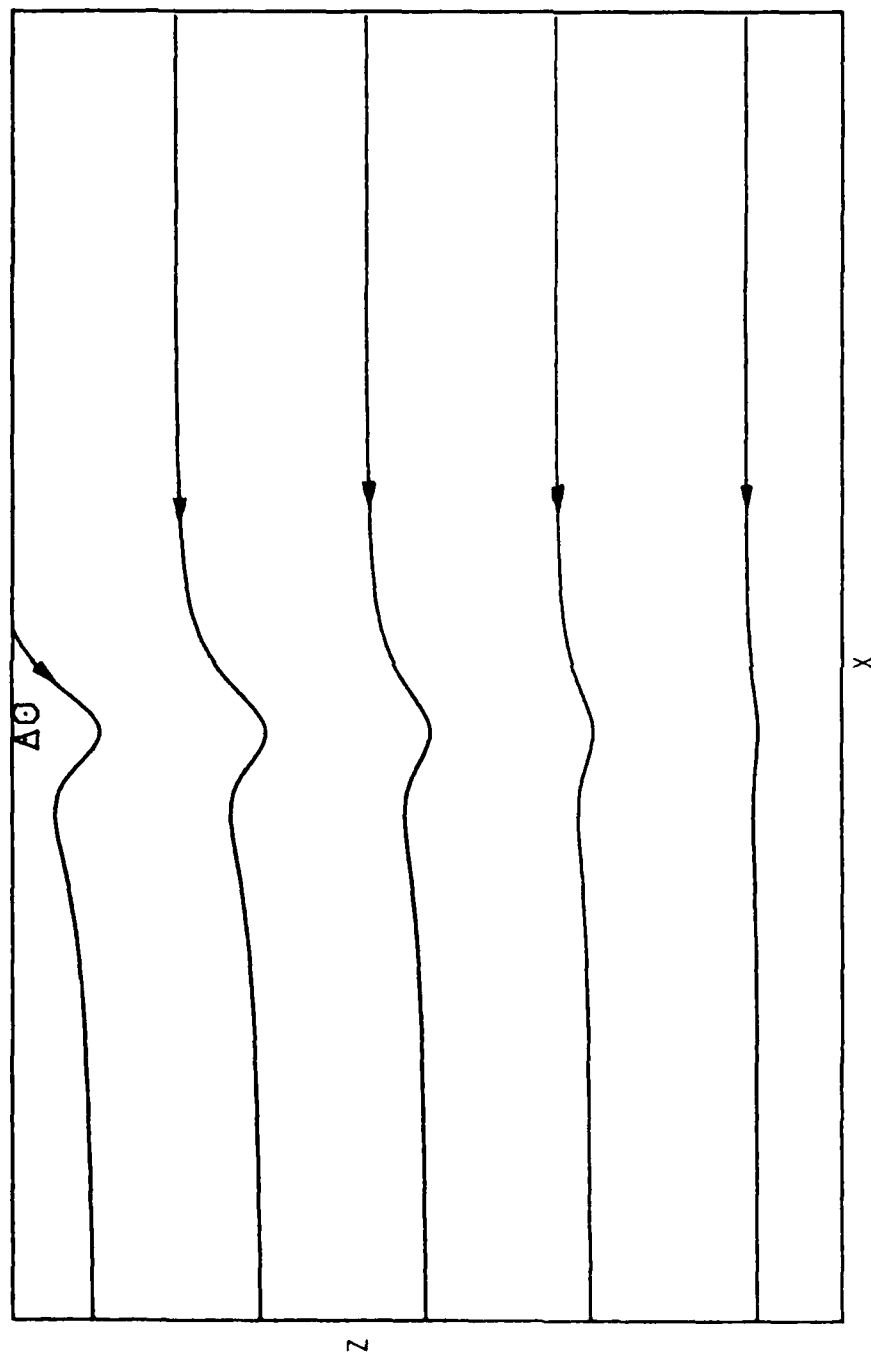


x

5.7(a) - Streamlines in the symmetry plane at $t = 0.001$.



5.7(b) - Lines of constant θ at $t = 0.001$.



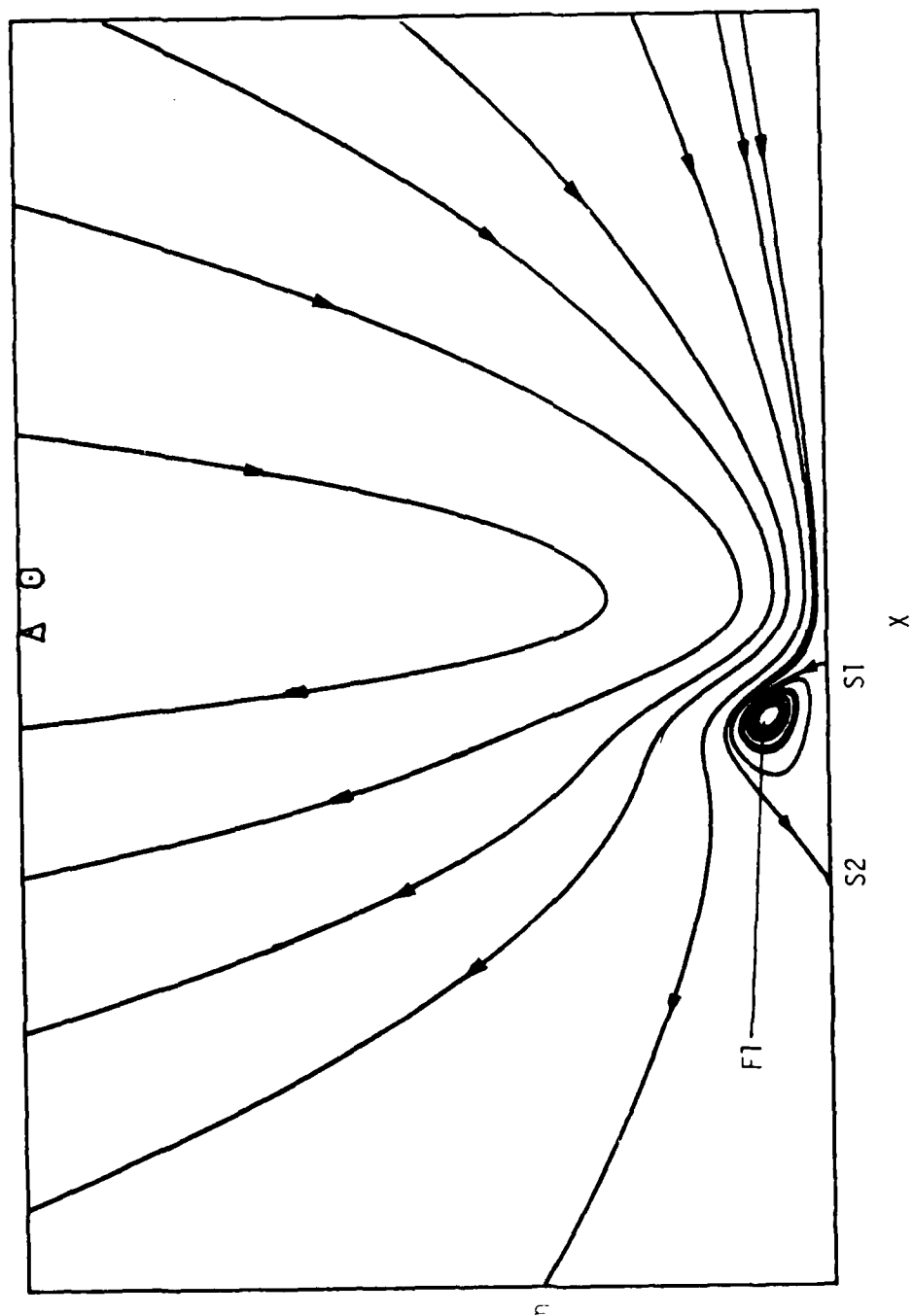
5.7(c) - Limiting surface streamlines in the xz plane at $t = 0.001$

Figure 5.7 - Streamlines in the symmetry plane, constant θ contours and surface streamlines on the wall at $t = 0.001$.

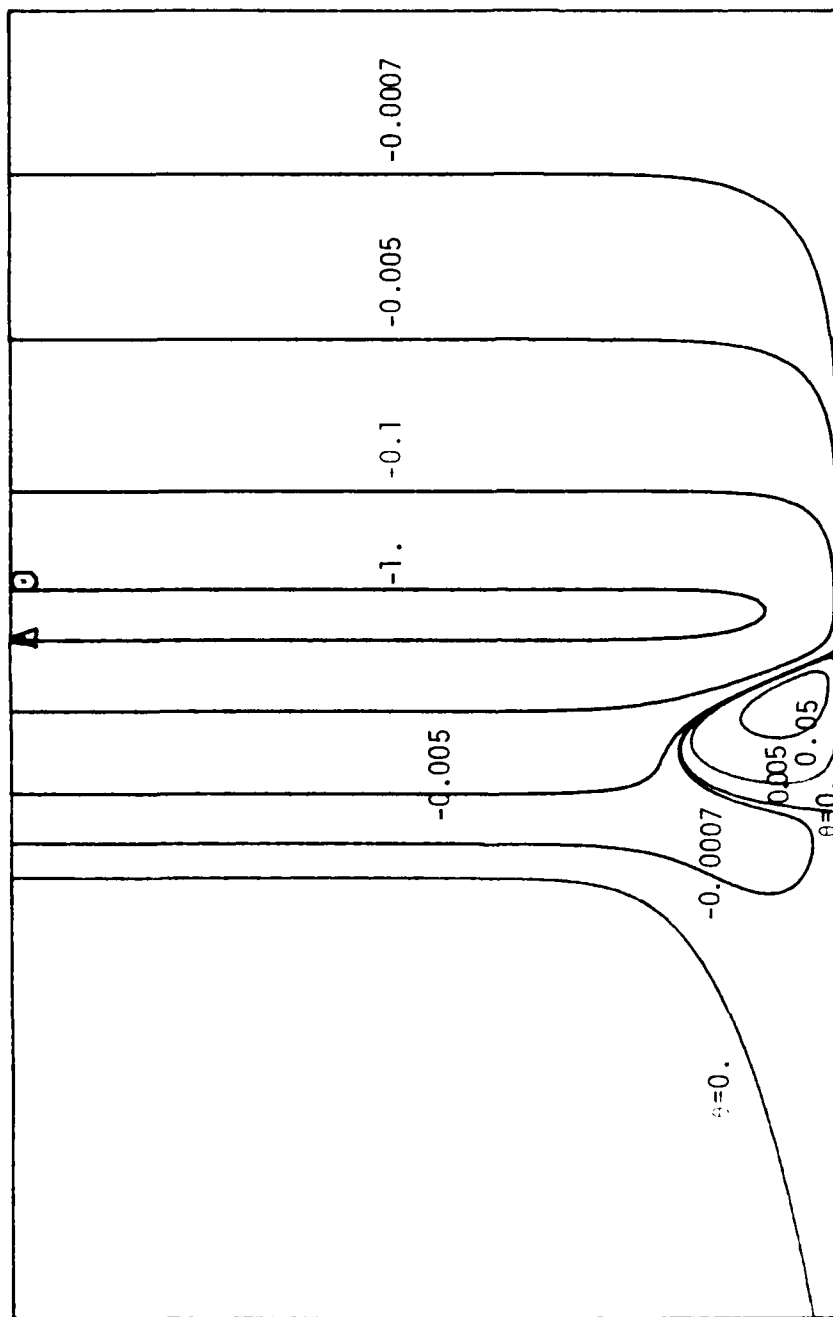
are shown in Figure 5.7(c) where again, the flow direction is indicated by arrows.

A further stage of development is shown in Figures 5.8 at $t = 0.01$. It may be observed that a region of three-dimensional flow separation is now present; there are two stagnation points, labelled S1 and S2, associated with this region. Fluid particles in the region bounded by the limiting streamlines through S1 and S2 spiral toward a focus at F1 where the instantaneous flow is leaving the symmetry plane. In Figure 5.8(b), it may be observed that a new feature in the constant θ contours has developed in the form of a pocket of positive θ near the wall. The increasingly positive values of θ near the center of this region indicate increasingly strengthening outflows from the symmetry plane; the center of this region is close to the focus F1 in Figure 5.8(a). The limiting surface streamlines at $t = 0.01$ are shown in Figure 5.8(c) where it may be observed that limiting streamlines through S1 and S2 divide the plot into three regions. In the right of S1, the flow first moves toward the symmetry plane but is then deflected away toward the limiting streamline through S1. To the left of S2 the flow is toward the symmetry plane while between S2 and S1 the surface flow reverses direction.

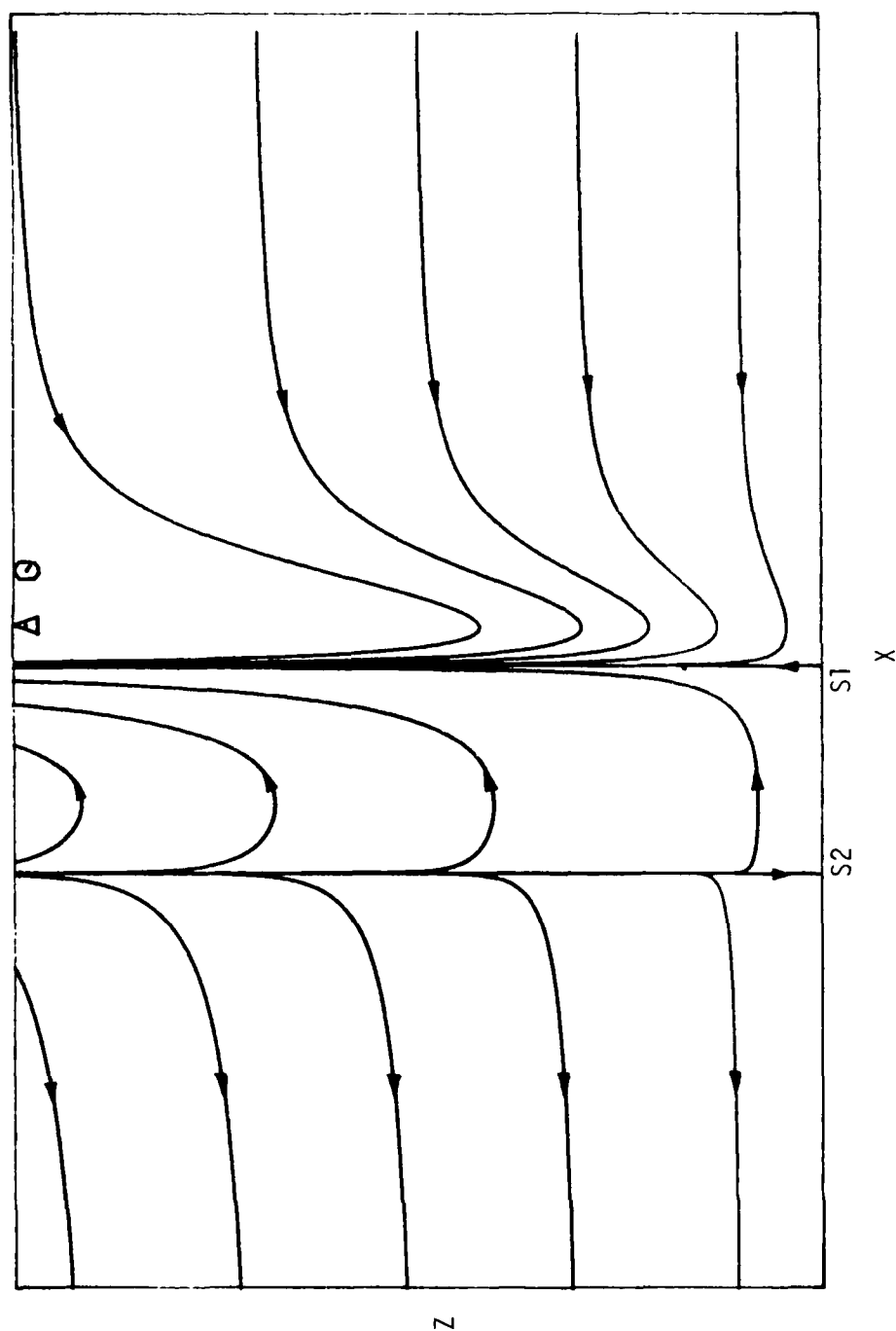
As time increases the region of three-dimensional separation increases in extent in the streamwise direction as may be seen in Figure 5.9(a) at $t = 0.02$; the stagnation point S1 remains almost fixed relative to the moving hairpin vortex while the stagnation



5.8(a) - Streamlines in the symmetry plane at $t = 0.01$.



5.8(b) - Lines of constant θ at $t = 0.01$.



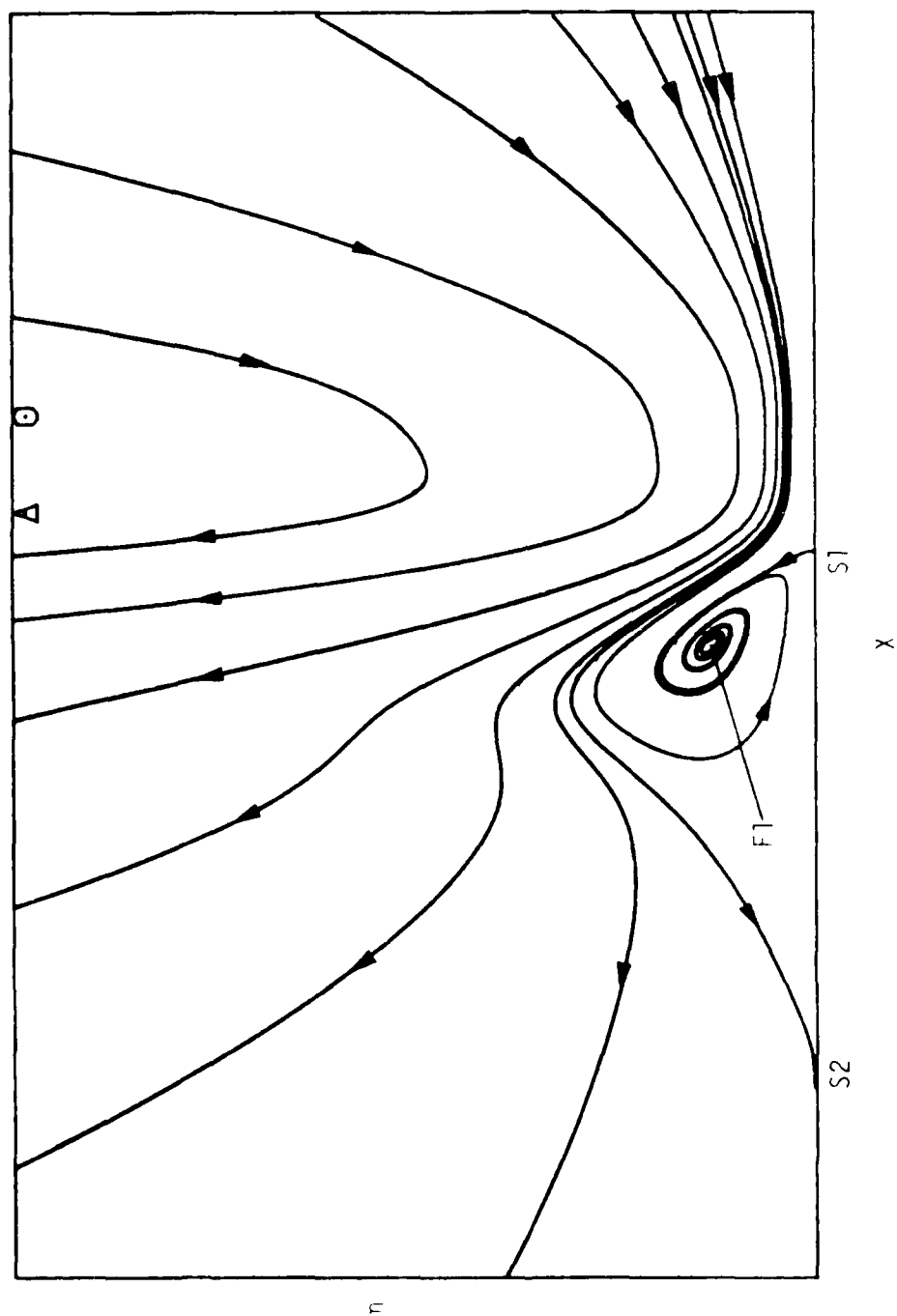
5.8(c) - Limiting surface streamlines in the xz plane at $t = 0.01$.

Figure 5.8 - Streamlines in the symmetry plane, constant θ contours and surface streamlines on the wall at $t = 0.01$.

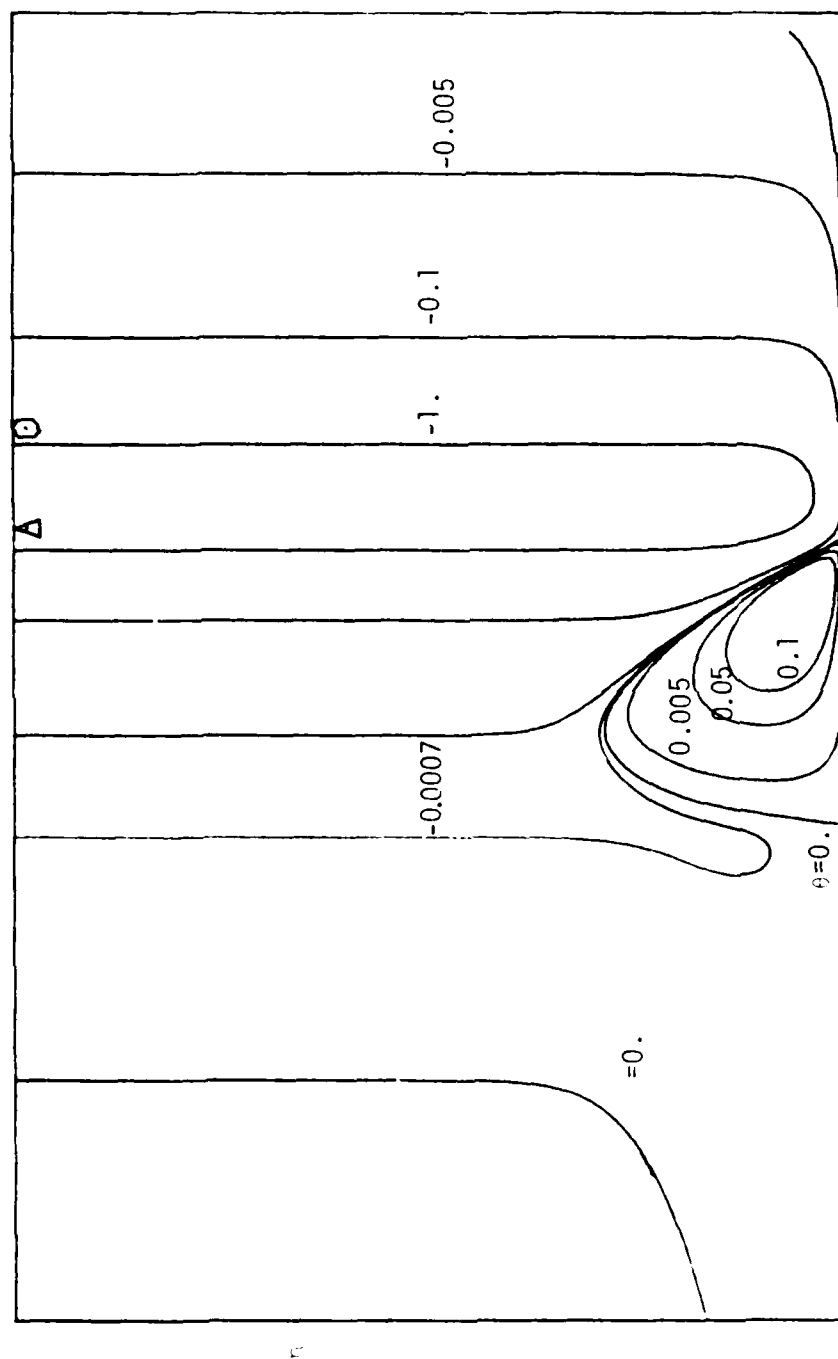
point S2 moves progressively downstream to the left. It may also be observed (in Figure 5.9(b)) that the region of positive outflow from the symmetry plane near the wall is expanding. The expanding region of recirculating flow is also apparent from the relative position of the stagnation points in the surface streamlines at $t = 0.02$ in Figure 5.9(c).

The continuation of the trends observed in connection with Figures 5.9 may be observed in Figures 5.10 at $t = 0.03$. Note that an intense variation in the velocity field is beginning to develop to the right of the region of separation (Figure 5.10(a)) and also that the streamlines to the right of S1 are beginning to lift away from the wall (in response to the development of the secondary hairpin heads in the spanwise direction). The next stage of development at $t = 0.04$ is shown in Figures 5.11; with the arrival of the trailing legs of the hairpin, the streamlines that were observed to have been lifting in Figure 5.10(a) are now seen to be accelerated in Figure 5.11(a) to the right of S1. Note that the region of recirculating flow has expanded to the extent that the stagnation point S2 has now moved out of the picture to the left in Figures 5.11(a) and 5.11(c). In addition the surface streamlines near S1 are essentially tangential to the symmetry plane.

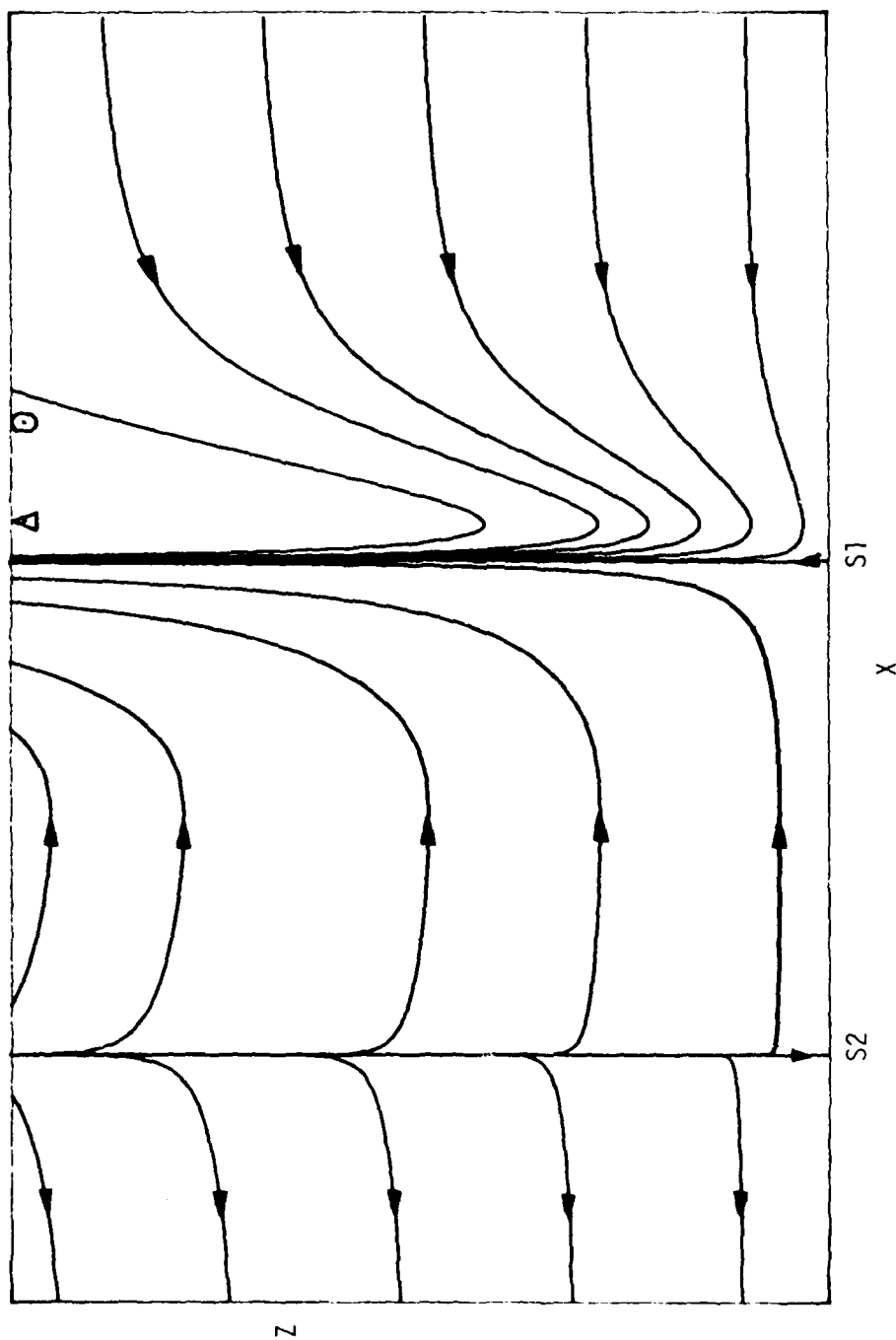
The flow development at $t = 0.05$ is depicted in Figures 5.12; the region of recirculation, depicted in Figure 5.12(a), has continued to expand and has grown substantially in the direction normal to the wall. The intense variation in the flow field to the



5.9(a) - Streamlines in the symmetry plane at $t = 0.02$.



5.9(b) - Lines of constant θ at $t = 0.02$.



5.9(c) - Limiting surface streamlines in the xz plane at $t = 0.002$.

Figure 5.9 - Streamlines in the symmetry plane, constant θ contours and surface streamlines on the wall at $t = 0.02$.

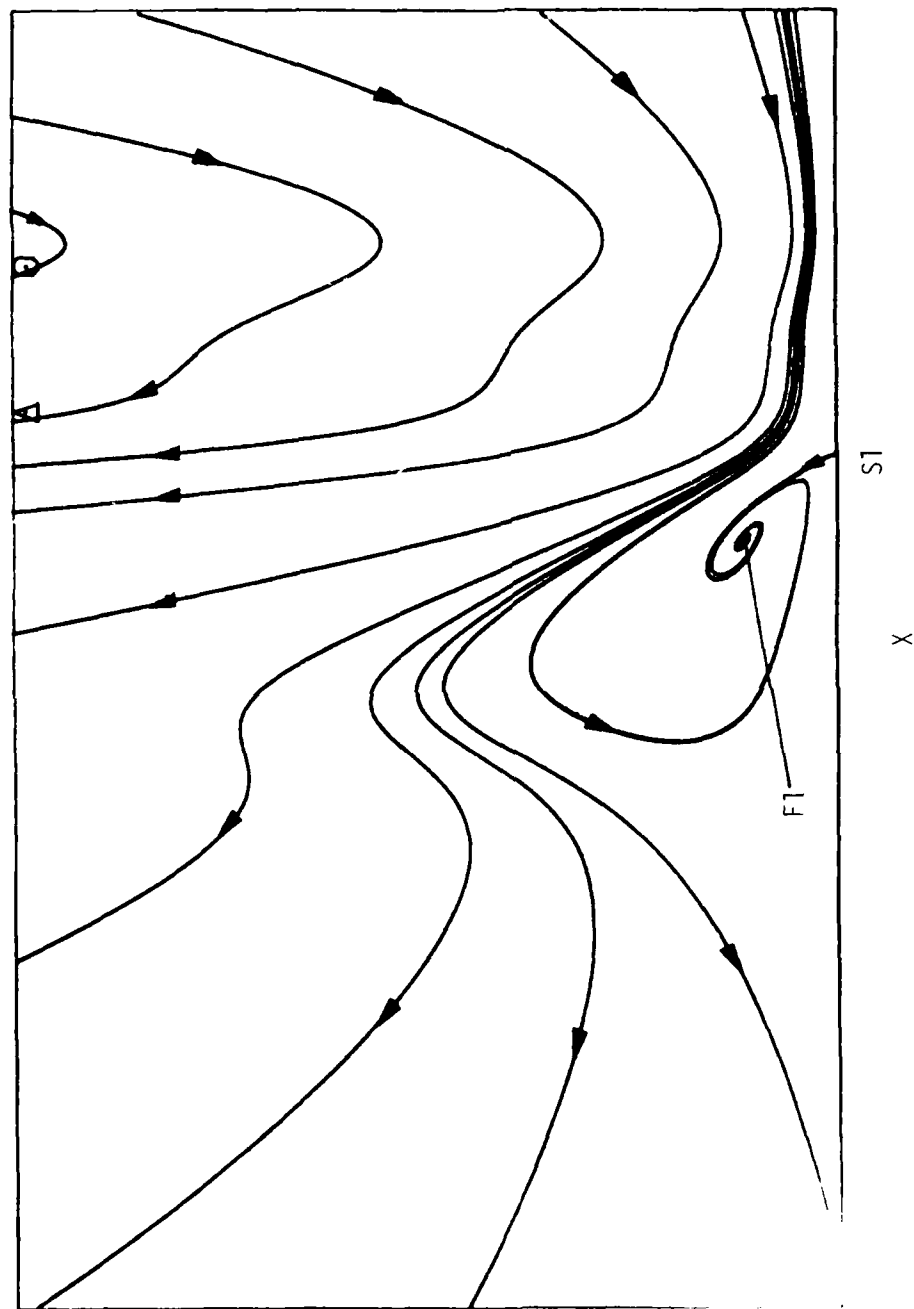


Figure 1(a) - Streamlines in the symmetry plane at $t = 0.03$.

AD-A187 261

AN ANALYSIS OF THE MOTION AND EFFECTS OF HAIRPIN
VORTICES(U) LEHIGH UNIV BETHLEHEM PA DEPT OF MECHANICAL
ENGINEERING AND M. T HON ET AL. JUN 87 FH-11

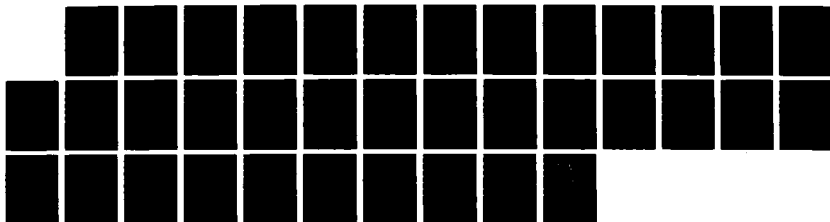
3/3

UNCLASSIFIED

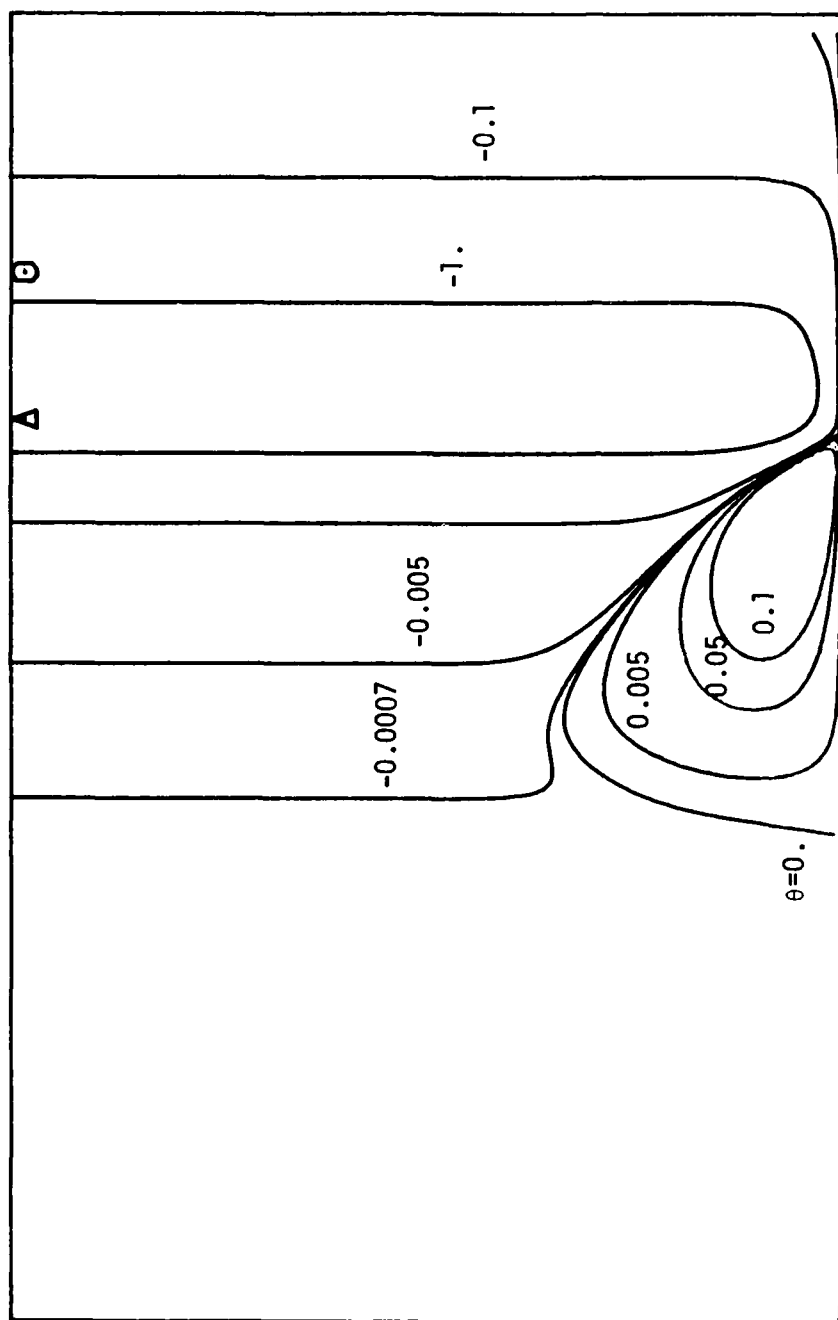
AFOSR-TR-87-1389 F49620-85-C-0100

F/G 20/4

NL

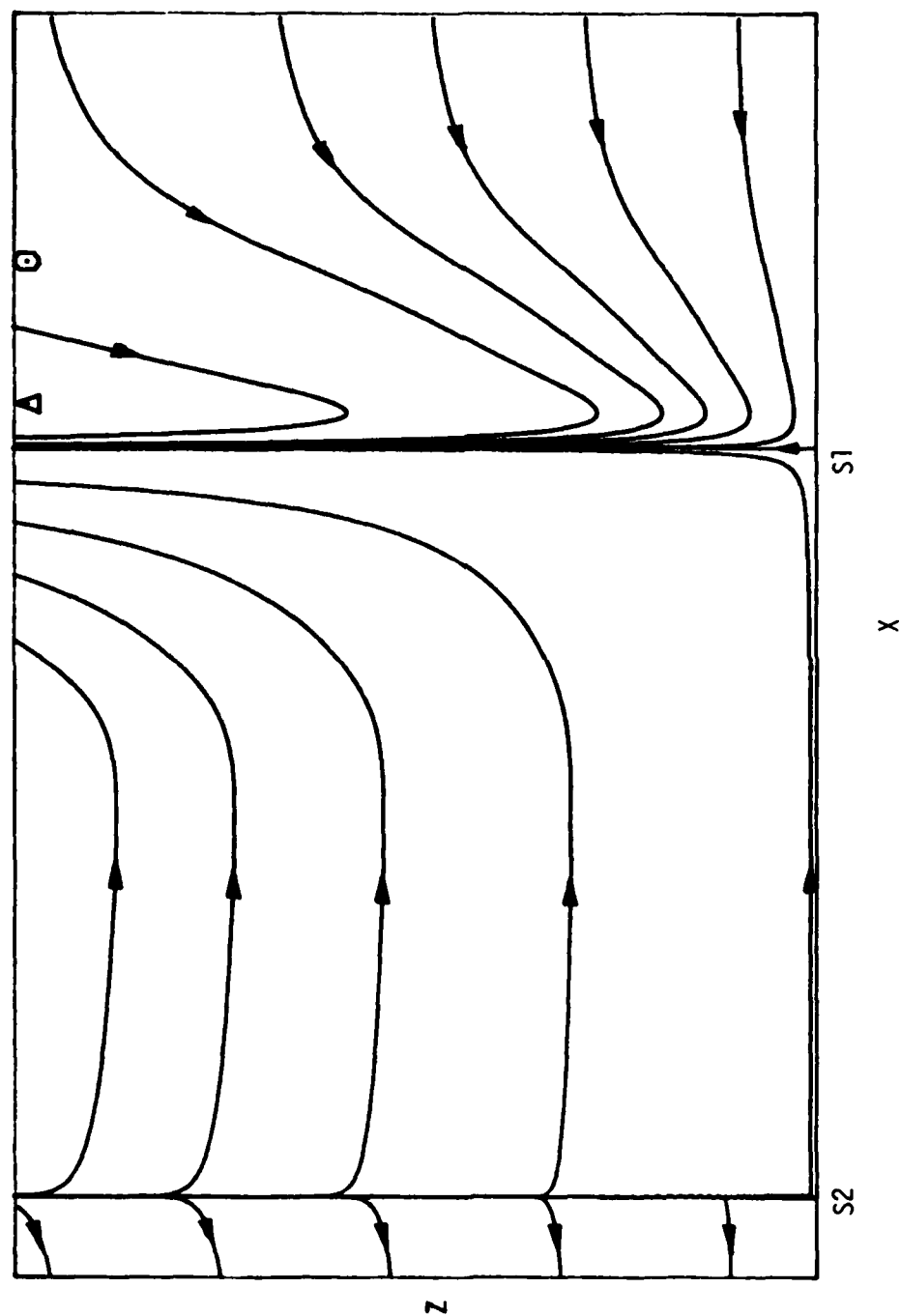






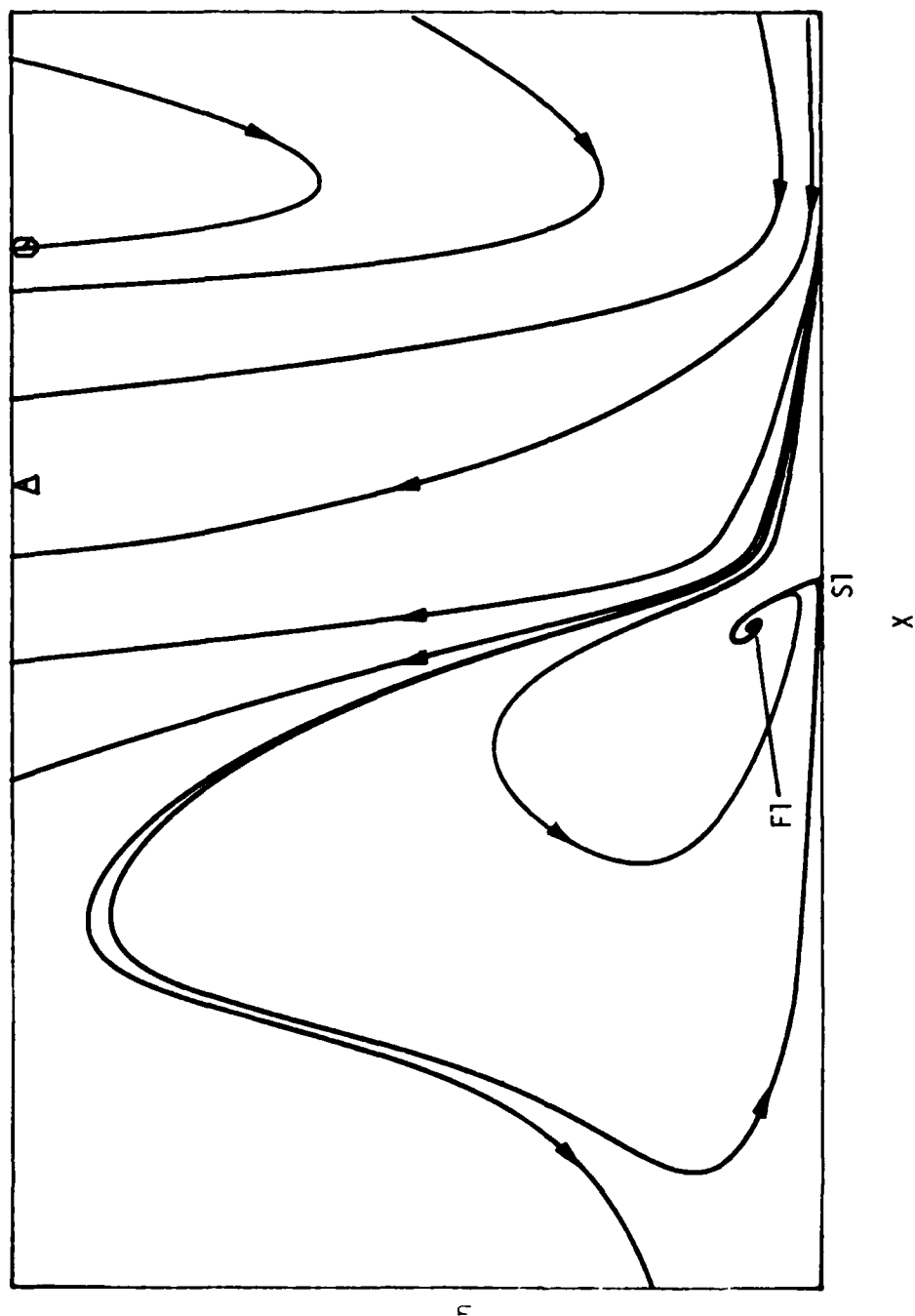
x

5.10(b) - Lines of constant θ at $t = 0.03$.

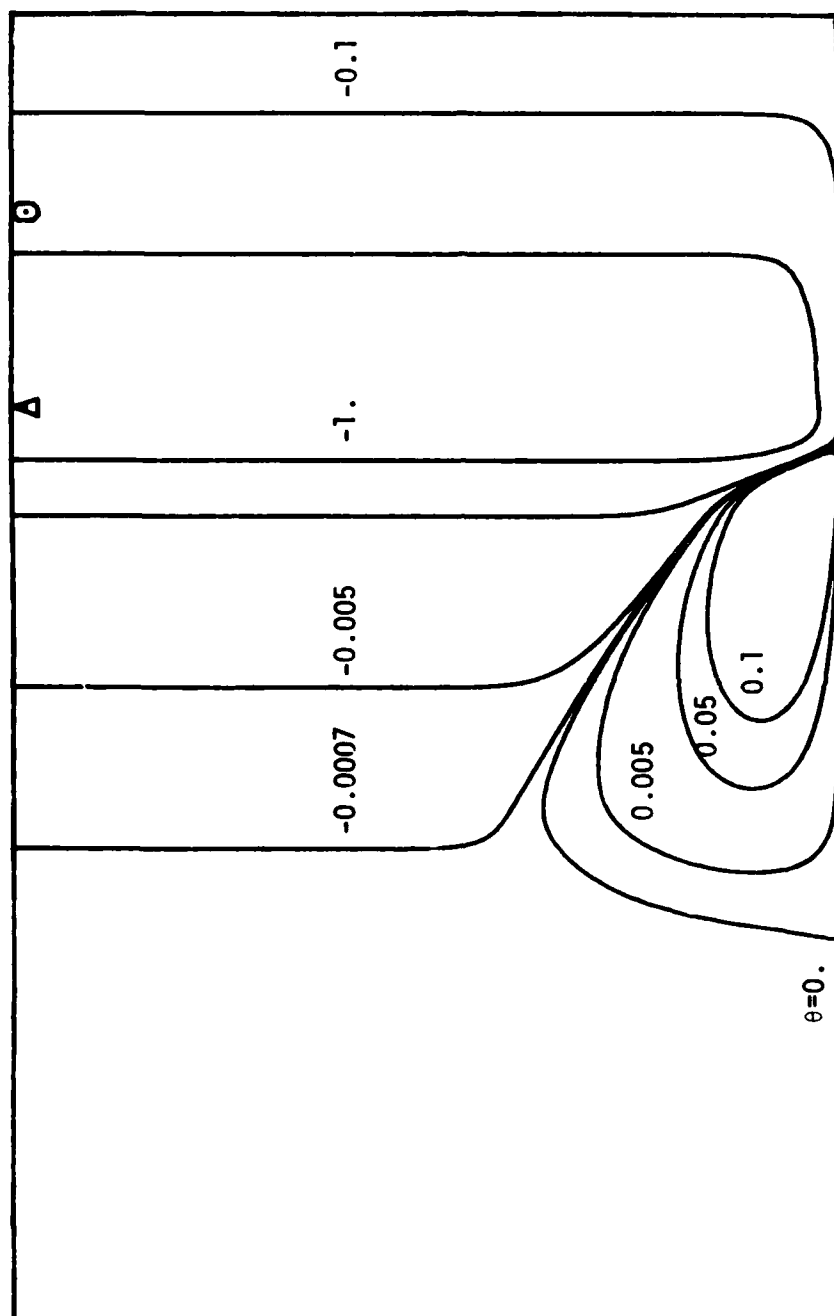


5.10(c) - Limiting surface streamlines in the xz plane at $t = 0.03$.

Figure 5.10 - Streamlines in the symmetry plane, constant θ contours and surface streamlines on the wall at $t = 0.03$.

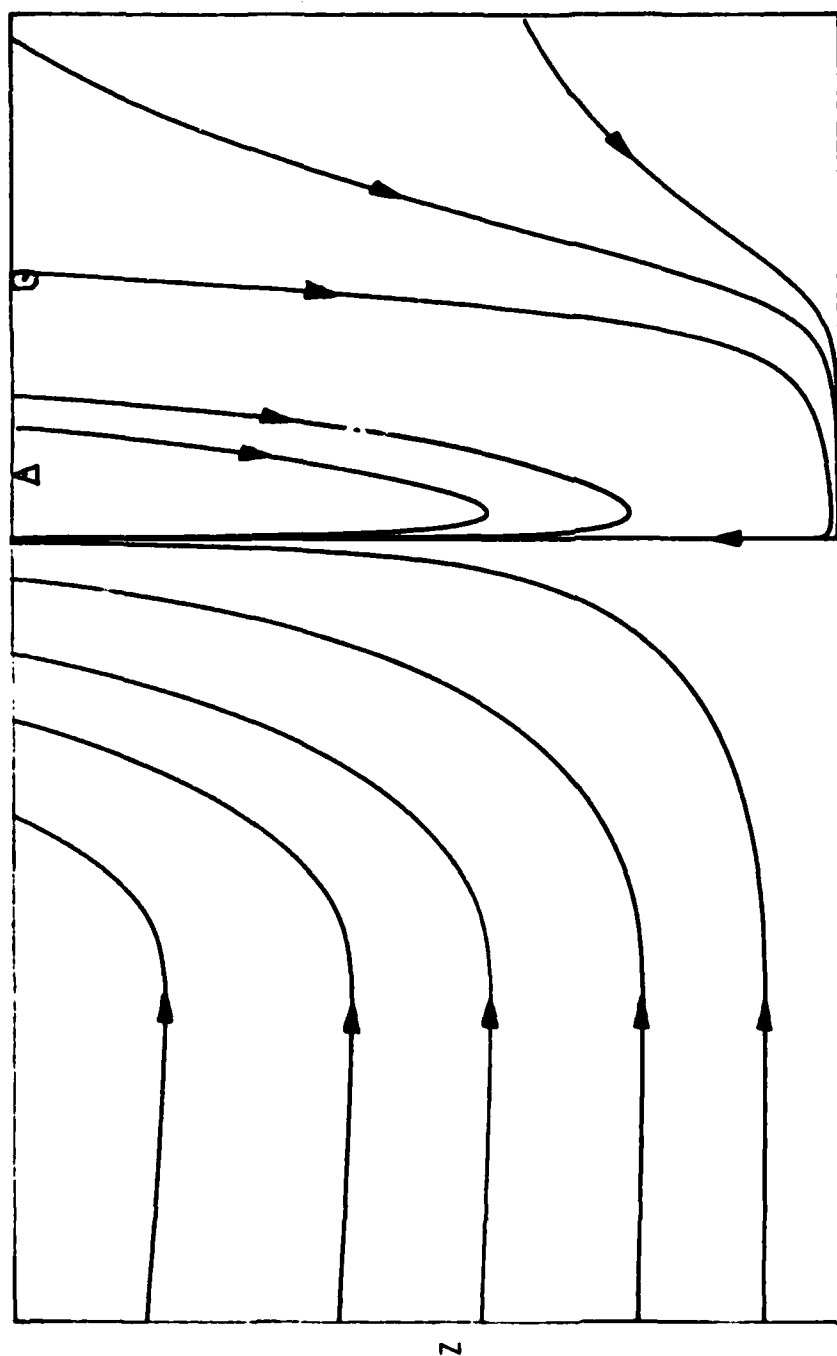


5.11(a) - Streamlines in the symmetry plane at $t = 0.04$.



x

5.11(b) - Lines of constant θ at $t = 0.04$.



x

5.11(c) - Limiting surface streamlines in the xz plane at $t = 0.04$.

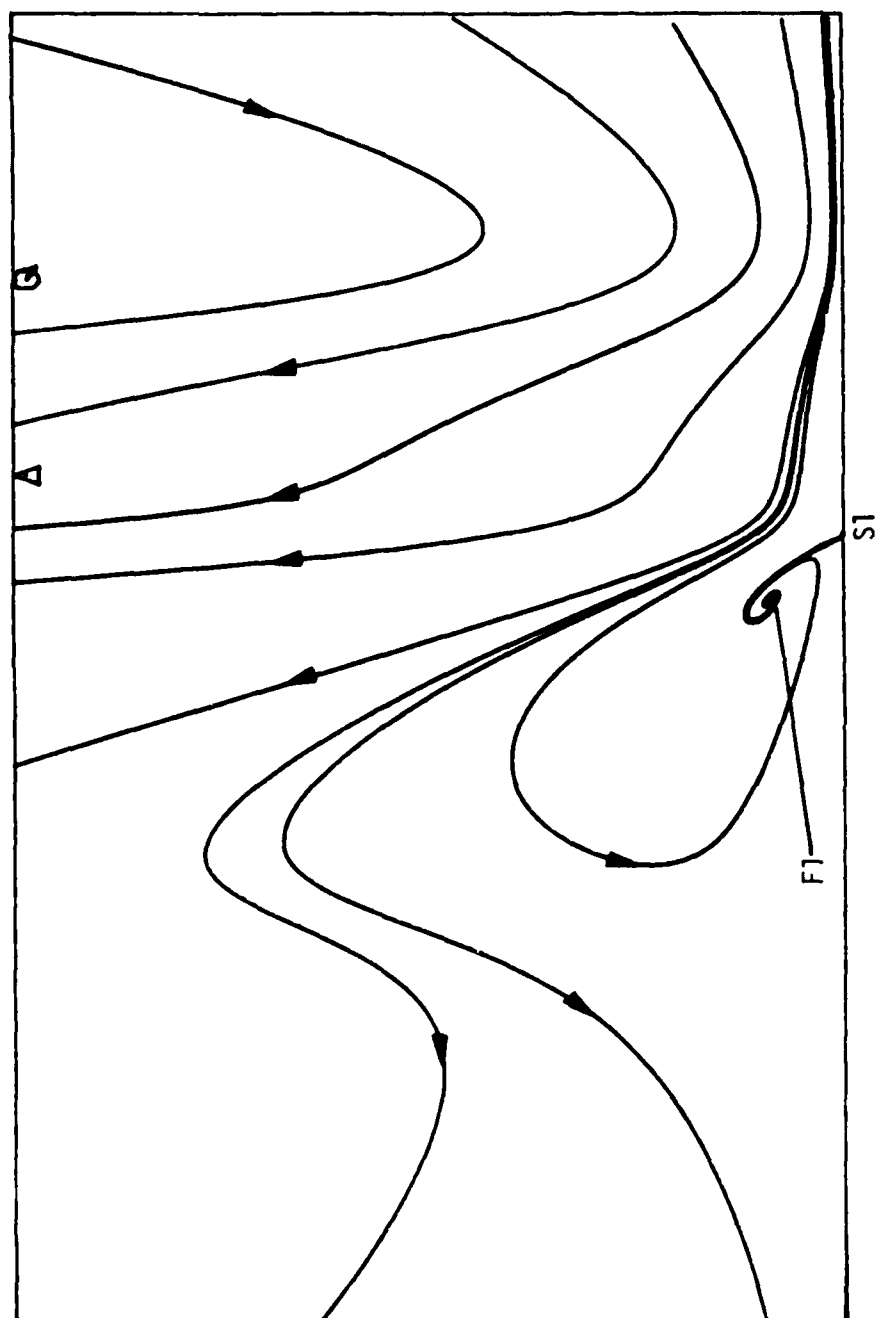
Figure 5.11 - Streamlines in the symmetry plane, constant θ contours and surface streamlines on the wall at $t = 0.04$.

right of S1 is evident from the relative closeness of the streamlines there. It may also be observed in Figure 5.12(b) that a pronounced hump has developed in the constant θ contours to the left of S1; an additional lifting in these contours may be observed to the right of S1.

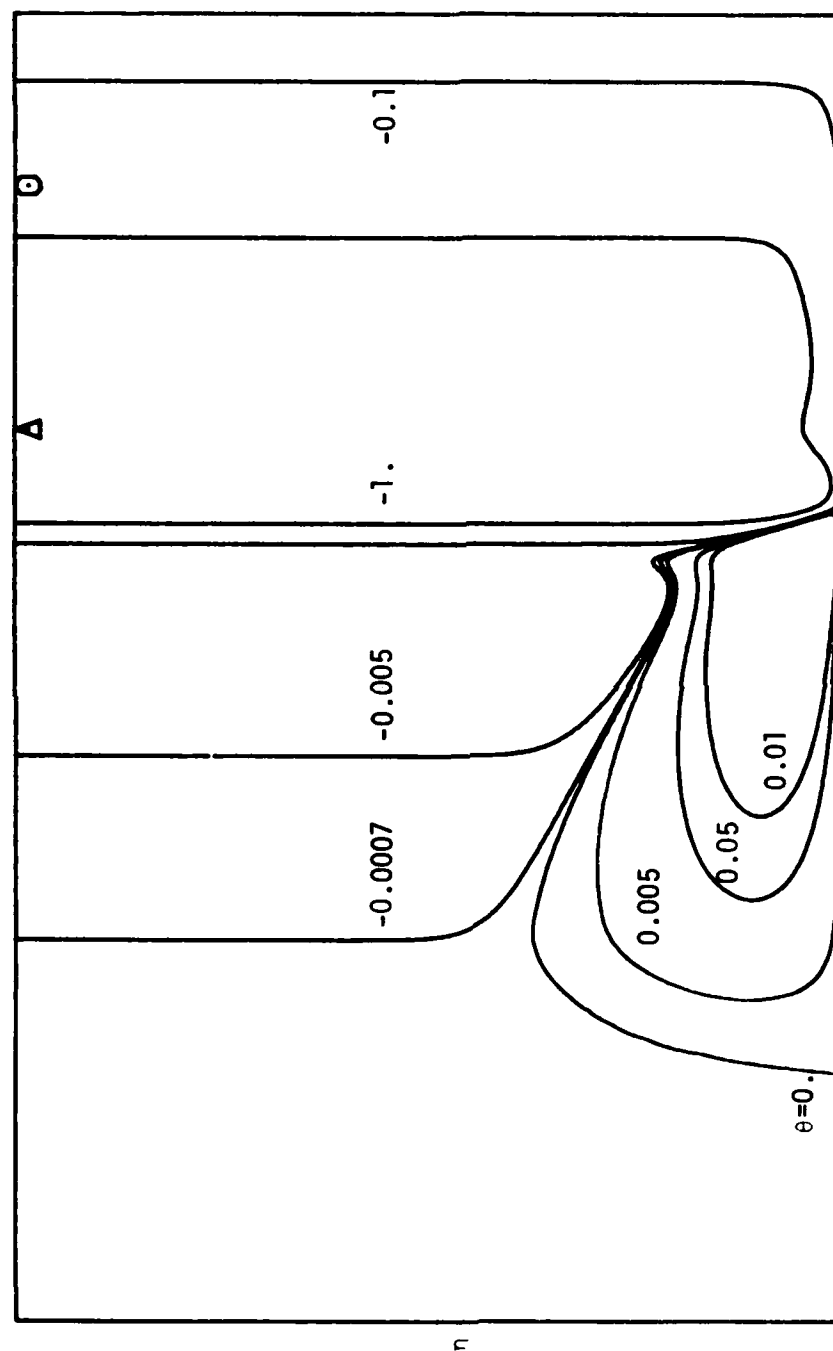
The development at $t = 0.06$ is plotted in Figures 5.13. It may be observed in Figure 5.13(a) that the recirculating region has extended out of the plot window in a direction normal to the wall. The streamlines to the right of S1 are very close to the wall and it may be observed from Figure 5.13(c) that at this stage (at least) there are no stagnation points to the right of S1. It may also be seen that the kink in the constant θ contours which was noted in Figure 5.12(b) has now extended all the way across the boundary layer. Consequently there is a narrow band of outflow from the symmetry plane which extends all the way to the inviscid region and which forms in response to the development of a small region of positive θ_∞ (c.f. Figure 5.3).

The last stage of the present calculations is shown in Figures 5.14 at $t = 0.07$. At this point, there are now two additional stagnation points S3 and S4 which may be observed in Figures 5.14(a) and 5.14(c). The limiting streamlines through S3 and S4 bound a region of strong outflow from the wall which is fed by spanwise flow toward the symmetry plane. Note that an additional small region of positive θ may be observed to the right of S1 in Figure 5.14(b).

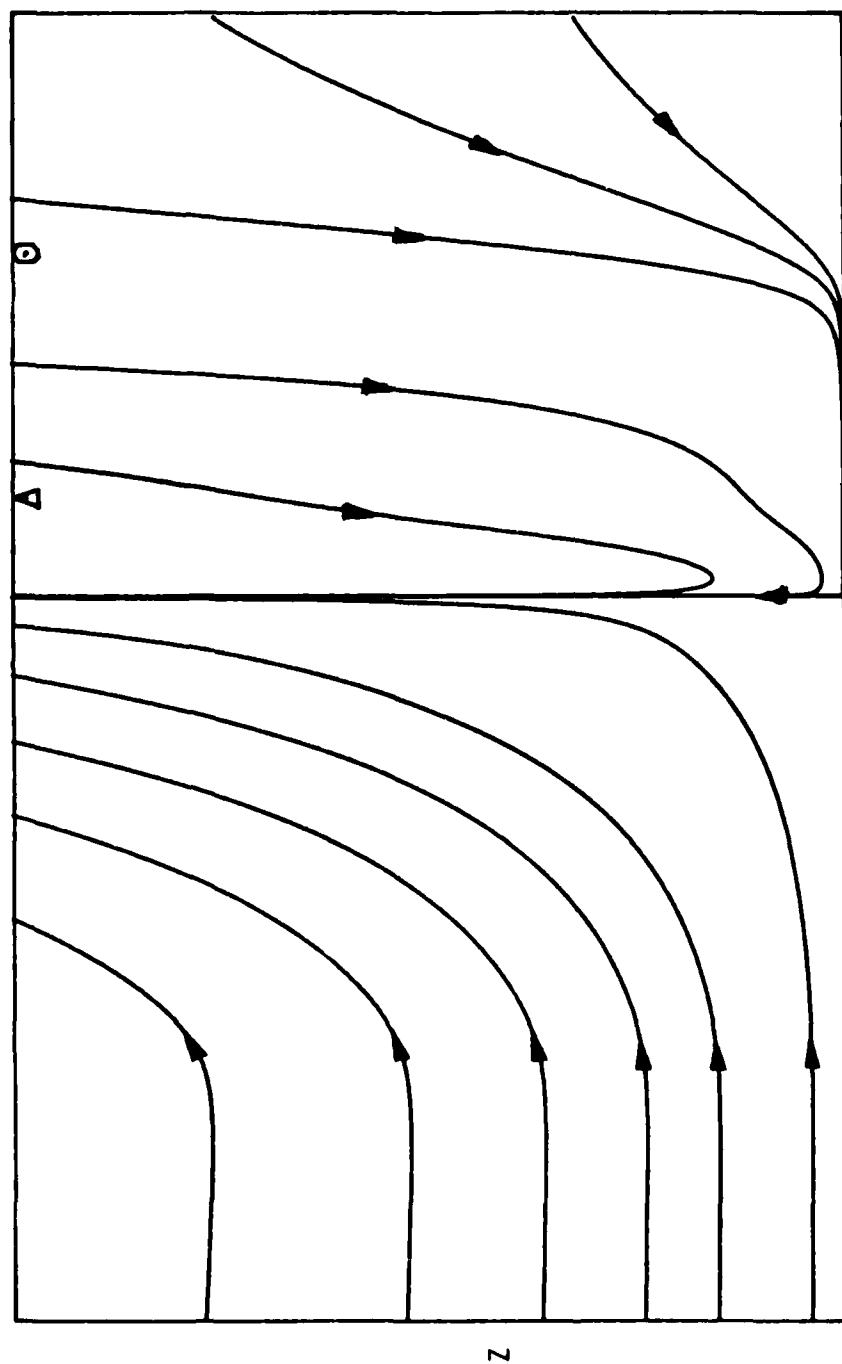
It may be observed in Figure 5.14(b) that "wiggles" are starting



5.12(a) - Streamlines in the symmetry plane at $t = 0.05$.



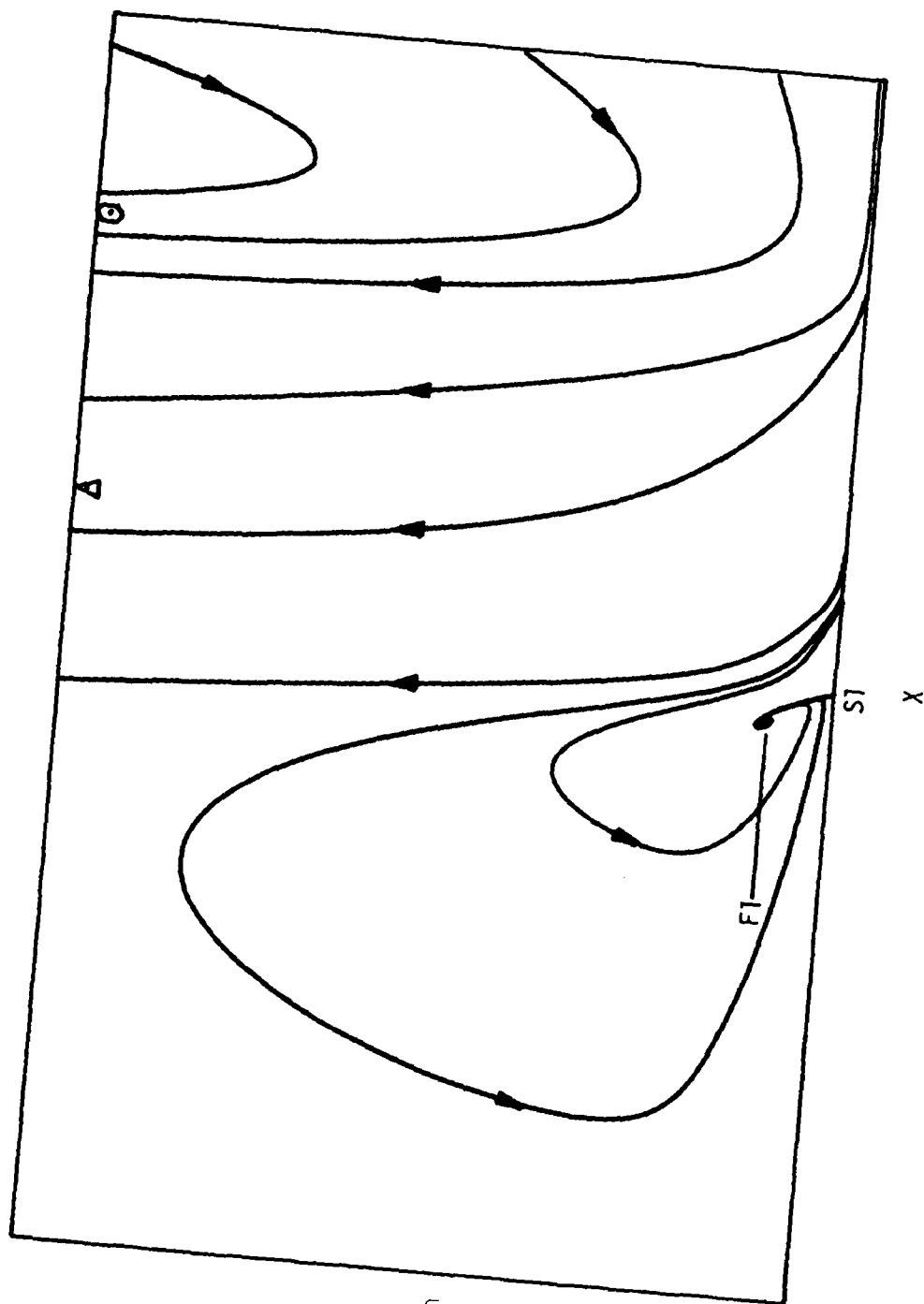
5.12(b) - Lines of constant θ at $t = 0.05$.



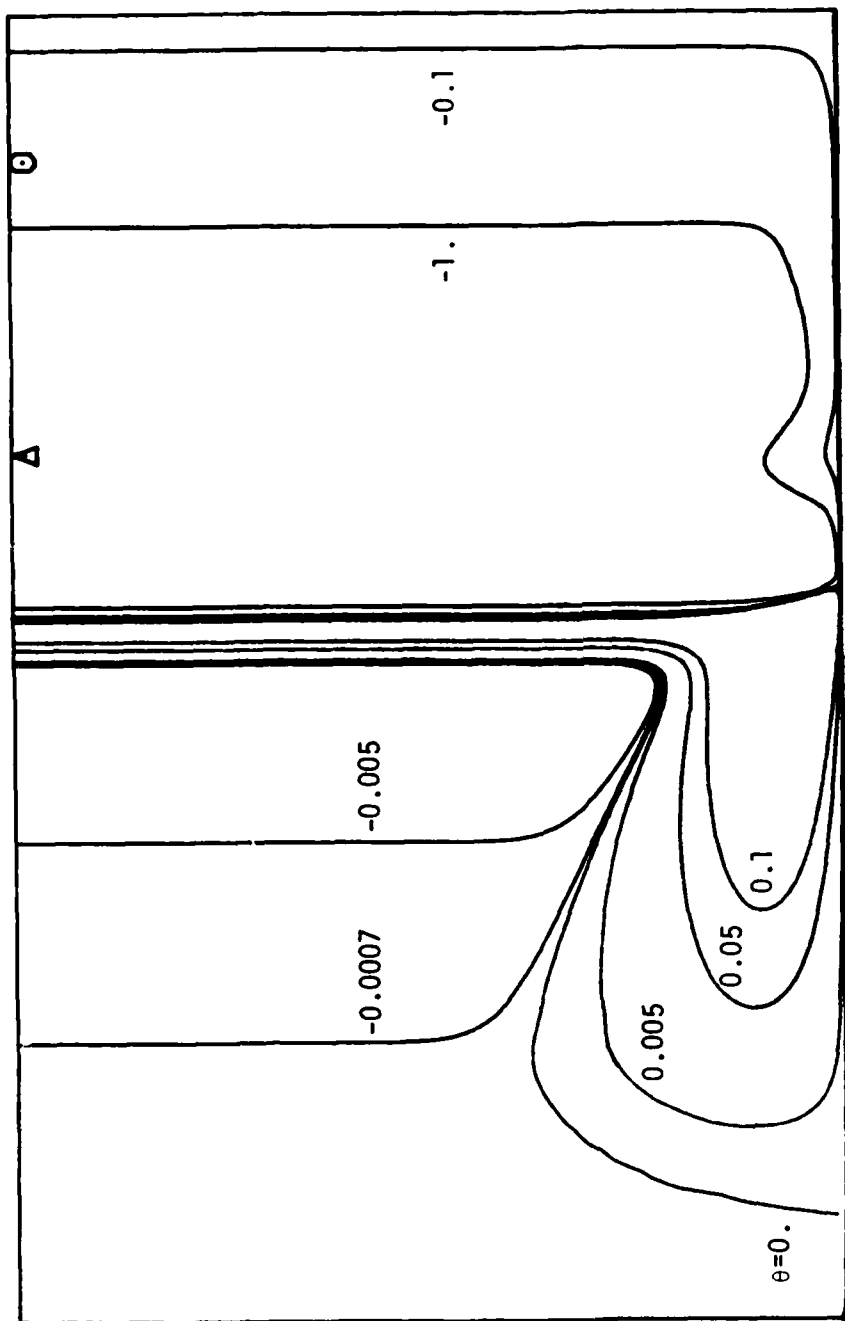
x

5.12(c) - Limiting surface streamlines in the xz plane at $t = 0.05$.

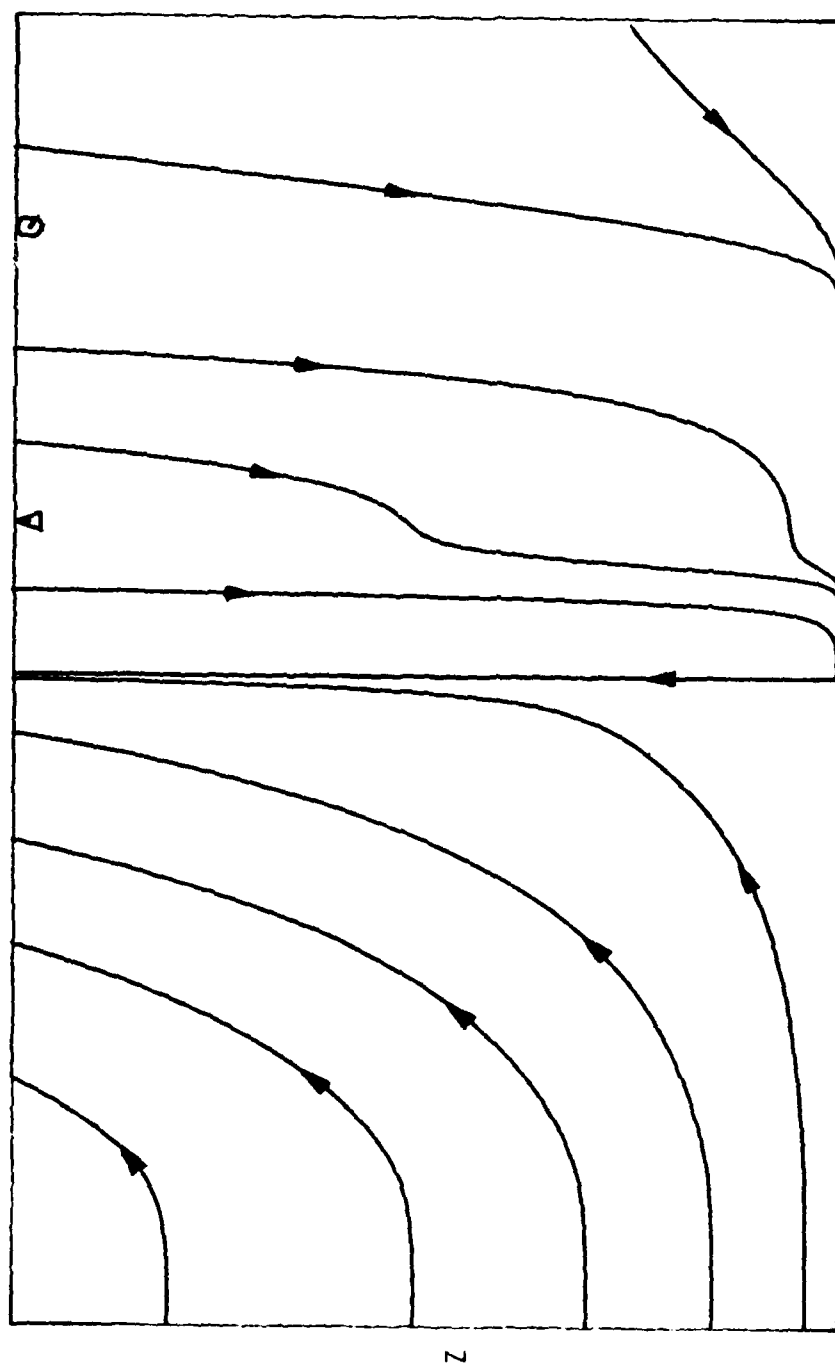
Figure 5.12 - Streamlines in the symmetry plane, constant θ contours and surface streamlines on the wall at $t = 0.05$.



5.13(a) - Streamlines in the symmetry plane at $t = 0.06$.



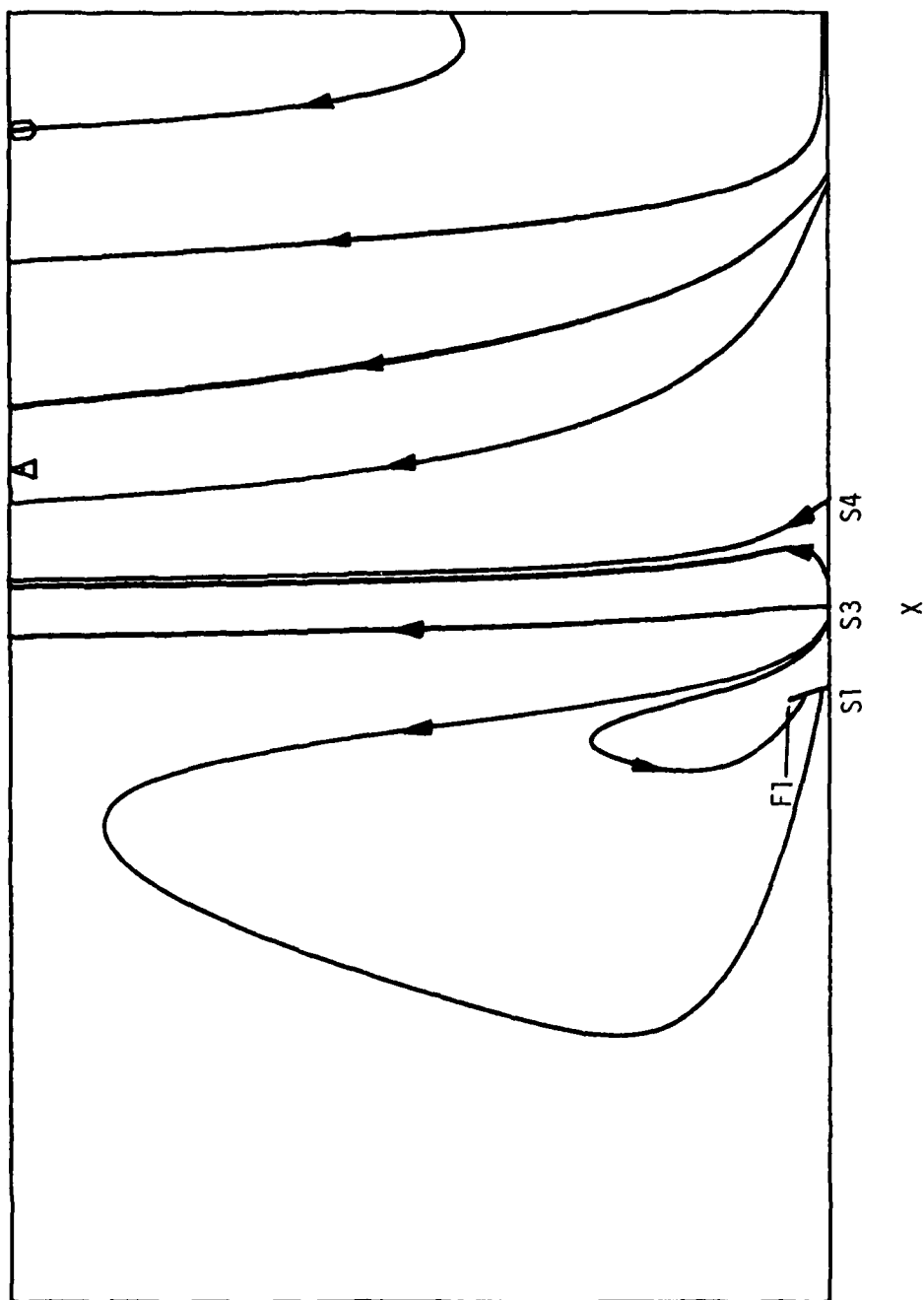
5.13(b) - Lines of constant θ at $t = 0.06$.



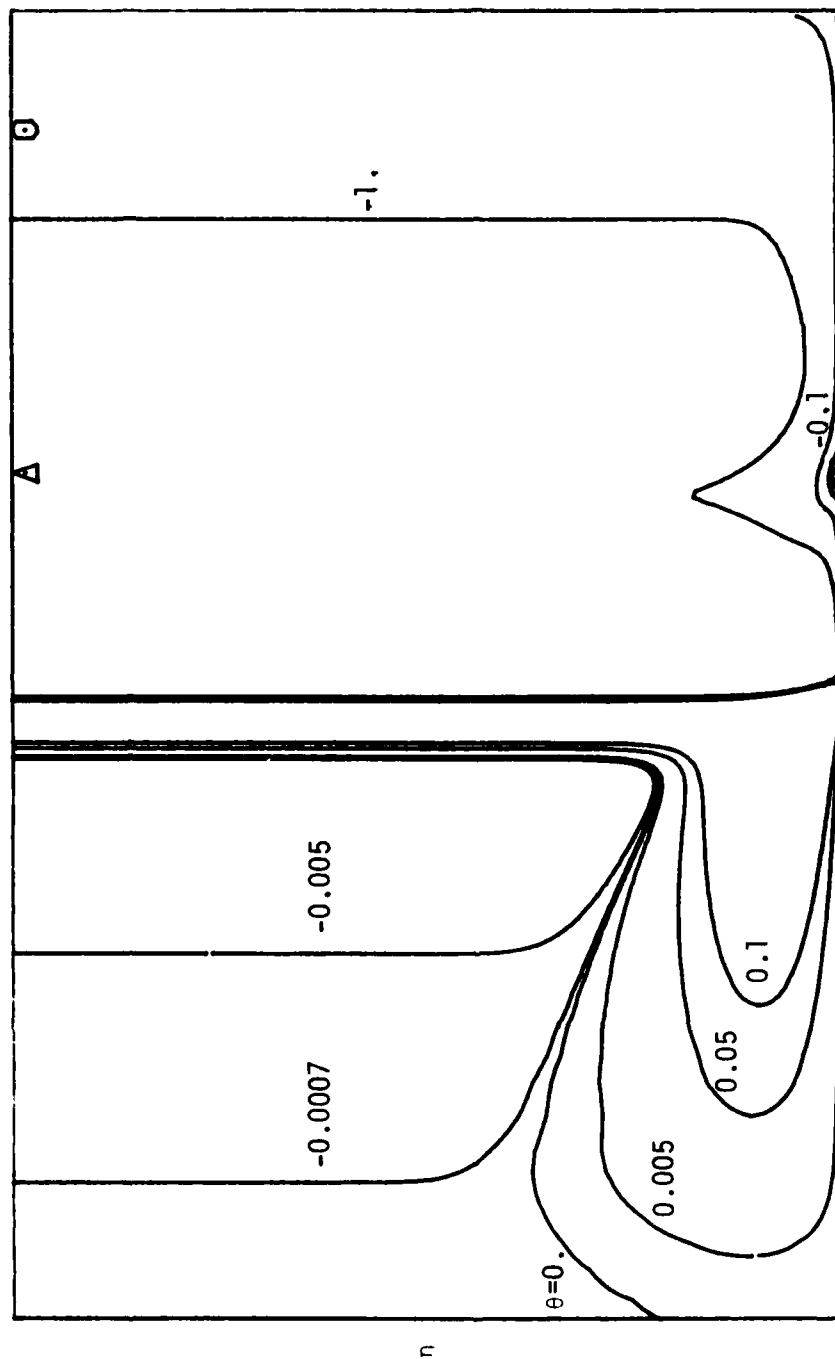
x

5.13(c) - Limiting surface streamlines in the xz plane at $t = 0.06$.

Figure 5.13 - Streamlines in the symmetry plane, constant θ contours and surface streamlines on the wall at $t = 0.06$.

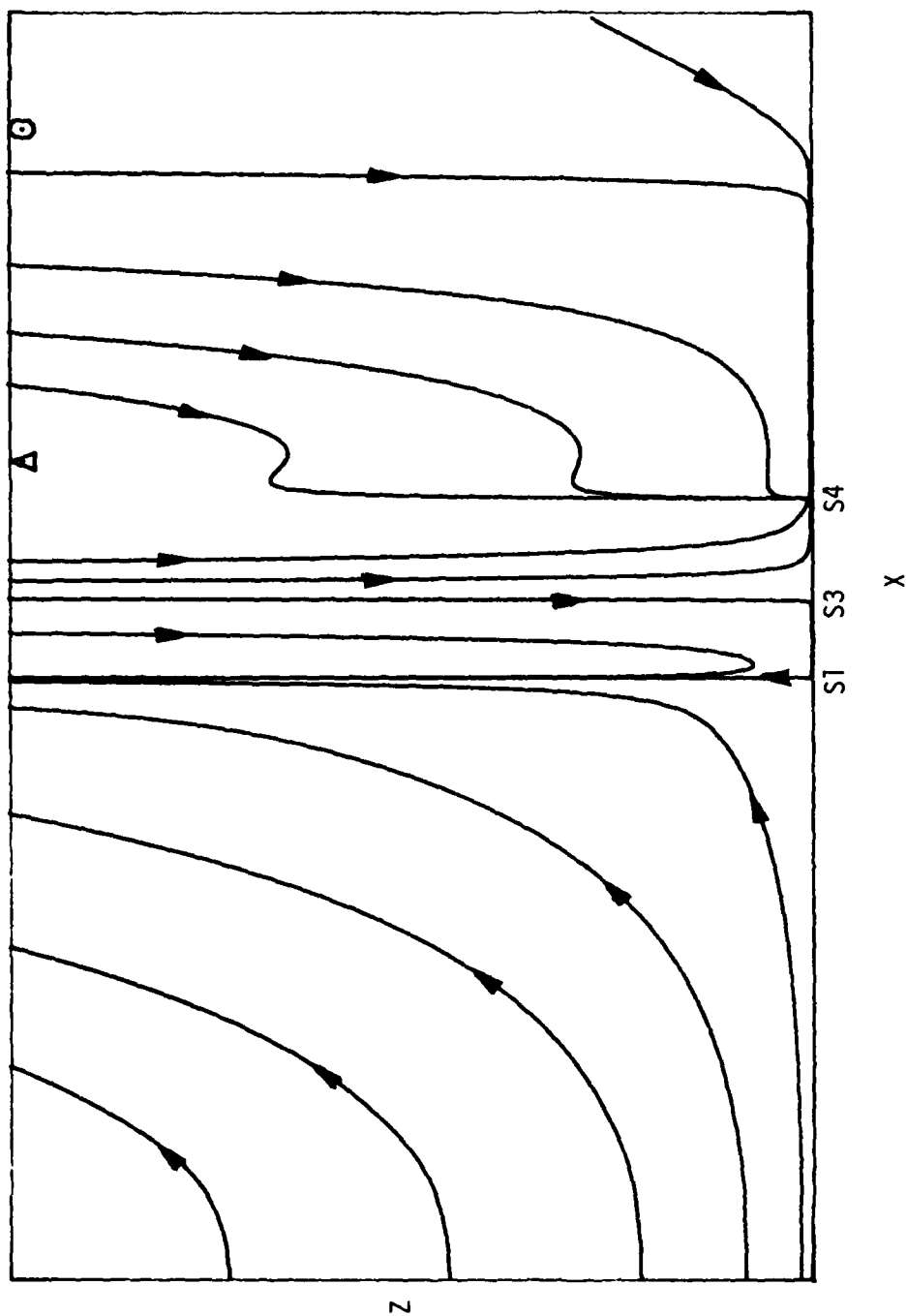


5.14(a) - Streamlines in the symmetry plane at $t = 0.07$.



x

5.14(b) - Lines of constant θ at $t = 0.07$.



5.14(c) - Limiting surface streamlines in the xz plane at $t = 0.07$.

Figure 5.14 - Streamlines in the symmetry plane, constant θ contours and surface streamlines on the wall at $t = 0.07$.

to develop in the constant θ contours and this is an indication that the numerical mesh is becoming inadequate. At this stage the hairpin vortex legs are rather close to the wall (c.f. Figure 4.8) and the inviscid velocity distributions are fairly complex (c.f. Figures 5.1 and 5.3). By $t = 0.07$, the legs of the vortex are moving fairly close to the wall and the inviscid calculation is nearing the end of its range of validity. For these reasons, the boundary-layer calculation was not extended much beyond $t = 0.07$. However it may be inferred from the present results that strong boundary-layer growth is occurring as a consequence of the imposed pressure distributions due to the moving hairpin vortex. This point is illustrated in Figure 5.15 where the temporal evolution of the displacement thickness,

$$\delta^* = 2\sqrt{t} \int_0^{\infty} (1-U) d\eta \quad , \quad (5.59)$$

on the symmetry plane is plotted. The initial hump that begins to develop and grow in Figure 5.14 is due to the expanding region of recirculating flow that develops on the symmetry plane at a fairly early stage in the integrations. The second and third humps that develop at a later stage are due to the approach of the legs to the wall and the formation of the secondary spanwise hairpins respectively.

5.7 Conclusions

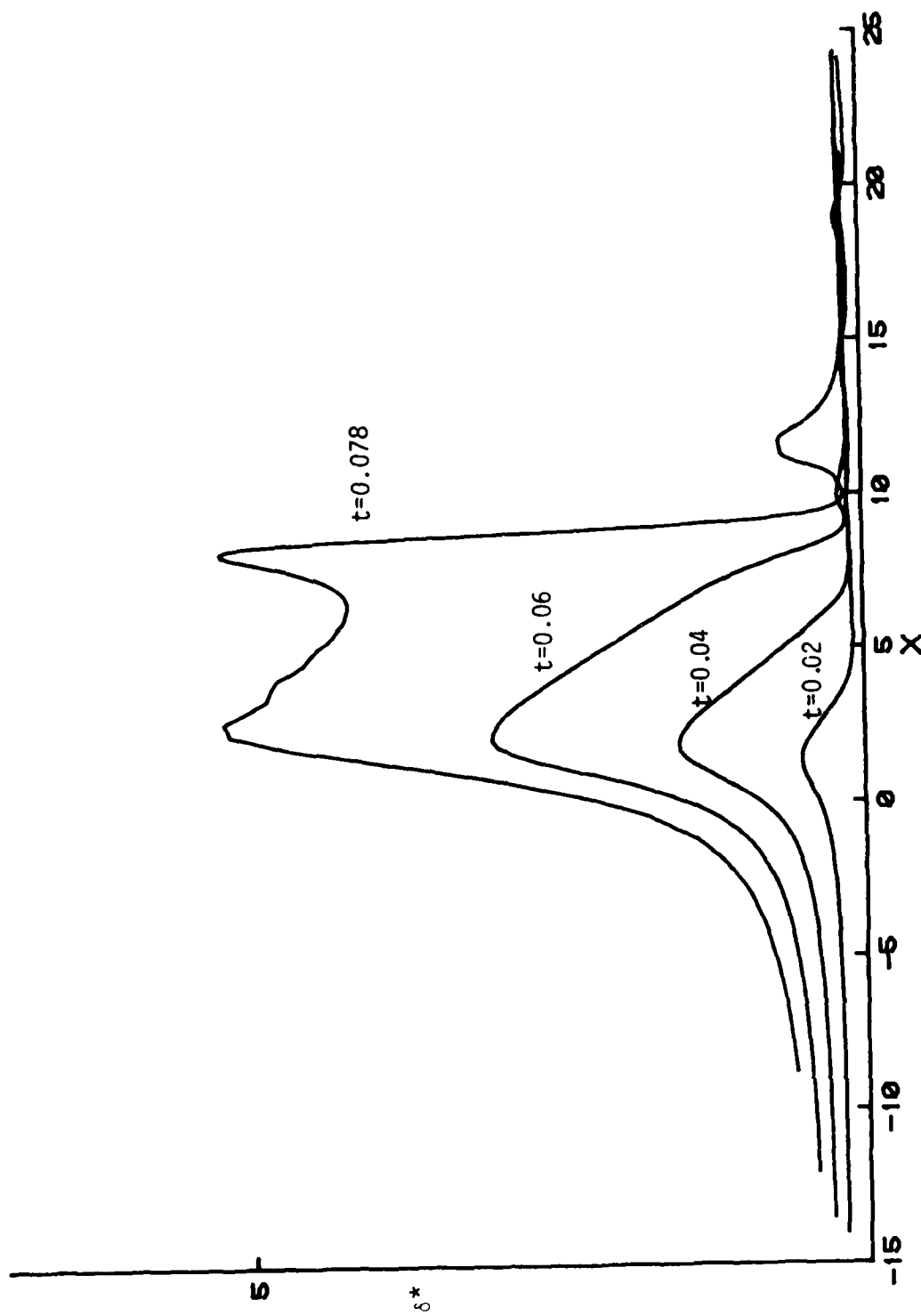


Figure 5.15 - Temporal development of displacement thickness.

In this chapter, a method has been described for the computation of the viscous response of a boundary layer to a moving and developing hairpin vortex in a shear flow. It is evident that the moving hairpin vortex gives rise to a very complex unsteady pressure field which in turn drives a complicated unsteady boundary-layer flow. The present results describe only the development of this viscous flow on the symmetry plane but it is evident that one consequence of the evolving flow is that strong outward growth of the boundary-layer flow occurs. It is reasonable to expect that as the thickening boundary-layer flow penetrates the cross flow in the inviscid region above the wall, a roll-over into a new secondary hairpin vortex will occur. This speculation is confirmed by the experimental observations of Acarlar and Smith (1984, 1987a, 1987b).

CHAPTER 6

CONCLUSIONS

In the present study, several aspects of the dynamics of hairpin vortices have been examined from a theoretical standpoint. The results of this study generally support the suggestions of the experimental studies of Acarlar and Smith (1984, 1987a, 1987b) and the idea that hairpin vortices are a basic building block in turbulent boundary-layer flows. Specific conclusions are as follows:

- (1) Hairpin vortices are streak creators.

This is borne out by the simulations described in Chapter 4 as well as the experiments of Acarlar and Smith.

- (2) Hairpin vortices in a shear flow develop secondary hairpin vortices which spread in the spanwise direction.

This was suggested by the experiments of Acarlar and Smith and is confirmed by the calculations in Chapter 4; this is a process of regeneration wherein a hairpin vortex can multiply itself in the spanwise direction.

- (3) Hairpin vortices induce a pressure gradient which evokes an eruptive response from the flow near the wall and leads to the creation of secondary hairpins through a strong viscous-inviscid interaction.

This phenomenon was clearly shown in the experiments of Acarlar and Smith in a variety of situations and is supported by the viscous calculations described in Chapter 5. This process is regenerative and offers a plausible explanation as to how new vorticity from the

region near the wall is continually introduced into the outer layer of a turbulent boundary layer.

(4) Pairs of hairpin vortices act to reinforce one another

In Chapter 4, it was demonstrated that two hairpin vortices in proximity to one another evolve in such a way that they intertwine and ultimately give the appearance of a single hairpin vortex. This phenomenon provides a possible explanation for the phenomenon of streak reinforcement described by Smith (1984). To understand this mechanism, assume that a hairpin vortex moves above a wall; as it does so, a streak occurs near the wall. After the flow near the wall is exposed to the pressure gradient induced by the moving vortex for a sufficient period of time, an eruption occurs and a secondary hairpin vortex is created in a strong viscous-inviscid interaction. As the eruption occurs the streak is obliterated near the point of ejection and at this stage there are two hairpin vortices within the flow. In view of the present results, the secondary and parent hairpin vortex would be expected to intertwine and reinforce one another. The next observable phase of the process should be the appearance of a new streak slightly downstream of the point of eruption as the pair of hairpins create a streak below them.

The present study is by no means complete and there is a variety of research directions that could be pursued in the future. First, the present vortex calculation method is believed to produce very accurate results for the motion of vortices having small

cores. However the calculation method is based on Moore's (1972) model of the vortex core which is probably not general enough to describe all of the vortex motions which are of interest in connection with the turbulent boundary layer. The theoretical model developed by Callegari and Ting (1978) for closed vortex loops is complex but is believed to be on firmer ground than all prior vortex calculation methods; this approach needs to be developed and extended to the types of vortices (of infinite extent) of interest in this study. In the second place, the present calculations have shown that hairpin vortices evolve in complex ways which are not easily predicted a priori on an intuitive basis; there is therefore a need to carry out further numerical integrations to develop an improved understanding of how hairpin vortices react with one another and also surface topography near walls. The present calculation method is fairly time consuming however and there is a need to develop new algorithmic approaches which will permit the accurate calculation the evolution of interacting vortices in three dimensions more efficiently. In the third place, there is a need to develop approaches which will permit the efficient calculation and prediction of physical situations where vortex cores merge locally; in the present study, it was necessary to terminate the computation of two interacting hairpin vortices when the two vortex cores touched (figure 4.25).

A fourth area of needed study is the calculation of the full

unsteady three-dimensional boundary layer under a moving hairpin vortex. In the present study, the boundary-layer calculations were restricted to the symmetry plane of the moving hairpin vortex; these calculations do suggest that the boundary-layer flow will become eruptive on the symmetry plane. However it is entirely possible that the boundary-layer flow will evolve toward interaction first at locations off the symmetry plane. In order to completely understand the viscous response at a wall to a moving hairpin vortex, the full boundary-layer problem must be addressed. Finally, the eruptive phase of the process, that is observed in experiments to lead to the creation of secondary hairpins, is of considerable interest. In order to compute such viscous-inviscid interactions, it will be necessary to develop new algorithmic approaches that will permit the calculation of a boundary-layer flow interacting strongly with an outer inviscid flow.

REFERENCES

- [1] Acarlar, M. S. and Smith, C. R. (1984), "An Experimental Study Hairpin-Type Vortices as a Potential Flow Structure of Turbulent Boundary Layers", Rept. FM-5, Dept. of Mechanical Engineering and Mechanics, Lehigh University.
- [2] Acarlar, M. S. and Smith, C. R. (1987a), "A Study of Hairpin Vortices in a Laminar Flow. Part 1. Hairpin Vortices Generated by a Hemisphere Protuberance", J. Fluid Mech., Vol. 175, pp. 1-41.
- [3] Acarlar, M. S. and Smith, C. R. (1987b), "A Study of Hairpin Vortices in a Laminar Flow. Part 2. Hairpin Vortices Generated by Fluid Injection", J. Fluid Mech., Vol. 175, pp. 43-83.
- [4] Aref, H. and Flinchem, E. P. (1984), "Dynamics of a Vortex Filament in a Shear Flow:", J. Fluid Mech., Vol. 148, pp. 477-497.
- [5] Arms, R. J. and Hama, F. R. (1965), "Localized-Induced Concept on a Curved Vortex and Motion of a Elliptic Vortex Ring", The Physics of Fluids, Vol. 8, No. 4., pp. 553-559.
- [6] Bakewell, H. P. and Lumley, J. L. (1967), "Viscous Sublayer and Adjacent Region in Turbulent Pipe Flow", Phys. of Fluids, Vol. 10, pp. 1880-89.
- [7] Batchelor, G. K. (1967), An Introduction to Fluid Dynamics, Cambridge University Press.
- [8] Blackwelder, R. F. (1978), "The Bursting Process in Turbulent Boundary Layers", AFOSR/Lehigh University Workshop on Coherent Structure in Turbulent Boundary Layers, C. R. Smith and D. E. Abbott (eds.), pp. 211-27.
- [9] Blackwelder, R. F. and Eckelmann, H. (1979), "Streamwise Vortices Associated with Bursting Phenomenon", J. Fluid Mech., Vol. 94, pp. 577-594.
- [10] Bliss, D. B. (1970), "The Dynamics of Curved Rotational Vortex Lines", M. S. Thesis, M. I. T.
- [11] Callegari, A. J. and Ting, L. (1978), "Motion of a Curved Vortex Filament with Decaying Vortical Core and Axial Velocity", SIAM J. of Applied Math., Vol. 35, pp. 148-174.

- [12] Cerra, A. W. and Smith, C. R. (1983), "Experimental Observation of Vortex Ring Interaction with Fluid Adjacent to a Surface", Report FM-4, Dept. of Mech. Engrg. and Mech., Lehigh University.
- [13] Crow, S. C. (1970), "Stability Theory for a Pair of Trailing Vortices", AIAA Journal, Vol. 8, pp. 2172-2179.
- [14] Dhanak, M. R. (1981), "Interaction Between a Vortex Filament and an Approaching Rigid Sphere", J. Fluid Mech., Vol. 110, pp. 129-147.
- [15] Dhanak, M. R. and De Bernardinis, B. (1981), "The Evolution of an Elliptic Vortex Ring", J. Fluid Mech., Vol. 109, pp. 189-216.
- [16] Didden, N. and Ho, C.-M. (1985), "Unsteady Separation in a Boundary Layer Produced by an Impinging Jet", J. Fluid Mech., Vol. 160, pp. 235-256.
- [17] Doligalski, T. L., Smith, C. R. and Walker, J.D.A. (1980), "A Production Mechanism for Turbulent Boundary-Layers", in Viscous Drag Reduction, G. Hough (ed.), AIAA Progress in Astronautics and Aeronautics, Vol. 72, pp. 47-72.
- [18] Doligalski, T. L. and Walker, J.D.A. (1978), "Shear Layer Breakdown Due to Vortex Motion", AFOSR/Lehigh University Workshop on Coherent Structure of Turbulent Boundary Layers, C. Smith and D. Abbott (eds.), pp. 288-339.
- [19] Doligalski, T. L. and Walker, J.D.A. (1984), "The Boundary Layer Induced by a Convected Two-Dimensional Vortex", J. Fluid Mech., Vol. 139, pp. 1-28.
- [20] Ersoy, S. and Walker, J.D.A. (1985a), "Viscous Flow Induced by Counter-Rotating Vortices", The Physics of Fluids, Vol. 28, No. 9, pp. 2687-2698.
- [21] Ersoy, S. and Walker, J.D.A., (1985b), "The Viscous Flow Near A Wall by Counter-Rotating Vortex Pairs and Vortex Loops", Report FM-8, Dept. of Mechanical Engineering and Mechanics, Lehigh University.
- [22] Ersoy, S. and Walker, J.D.A. (1986), "Flow Induced at a Wall by a Vortex Pair", AIAA Journal, Vol. 24, No. 10, pp. 1597-1605.
- [23] Falco, R. E. (1981), "Structural Aspects of Turbulence in Boundary Layer Flows", Proceedings of 6th Biennial Symposium on Turbulence, Rolla, Missouri, October 1979.
- [24] Falco, R. E. (1982), "A Synthesis and Model of Wall Region Turbulence Structure", in Structure of Turbulence in Heat and Mass Transfer, Z. Zaric (ed.), pp. 124-135, Hemisphere Press.

- [25] Falco, R. E. (1983), "New Results, A Review and Synthesis of the Mechanism of Turbulence Production in Boundary Layers and its Modification, AIAA Paper No. 83-0377.
- [26] Falco, R. E. and Wiggert, D. C. (1980), "The Effect of Dilute Polymer Additives on Vortex Ring/Wall Interactions - a Mechanism for Drag Reduction", in Viscous Flow Drag Reduction, G. Hough (ed.), AIAA Progress in Astronautics and Aeronautics, Vol. 72, pp. 275-289.
- [27] Hama, F. R. (1962), "Progressive Deformation of a Curved Vortex Filament by its Own Induction", The Physics of Fluids, Vol. 5, No. 10, pp. 1156-1162.
- [28] Harvey, J. K. and Perry, F. J. (1971), "Flowfield Produced by Trailing Vortices in the Vicinity of the Ground", AIAA Journal, Vol. 9, pp. 1659-1660.
- [29] Head, M. R. and Bandyopadhyay, P. (1981), "New Aspects of Turbulent Boundary-Layer Structure", J. Fluid Mech., Vol. 107, pp. 297-337.
- [30] Hinze, J. D. (1975), Turbulence, 2nd edition, McGraw-Hill, New York.
- [31] Kline, S. J. (1978), "The Role of Visualization in the Study of the Structure of the Turbulent Boundary Layer", AFOSR/Lehigh University Workshop on Coherent Structure of Turbulent Boundary Layers, C. R. Smith and D. E. Abbott (eds.), pp. 1-26.
- [32] Kline, S. J., Reynolds, W. C., Schroub, F. A. and Runstadler, P. W. (1967), "The Structure of Turbulent Boundary Layers", J. Fluid Mech., Vol. 30, pp. 741-774.
- [33] Leonard, E. A. (1975), "Numerical Simulation of Interacting Three-Dimensional Vortex Filament", Proc. 4th Int. Conf. on Numerical Methods in Fluid Dynamics, R. D. Richtmyer (ed.), Springer-Verlag, pp. 245-250.
- [34] Leonard, E. A. (1979), "Vortex Simulation of Three-Dimensional, Spotlike Disturbances in a Laminar Boundary Layer". NASA Tech. Mem. 78379.
- [35] Leonard, E. A. (1985), "Computing Three-Dimensional Incompressible Flows with Vortex Elements", Annual Review of Fluid Mech., Vol. 17, pp. 523-559.
- [36] Liu, C. H., Krause, E. and Ting, L. (1985), "Vortex-Dominated Flow with Viscous Core Structure", AIAA 18th Fluid Dynamics, Plasma Dynamics and Lasers Conference, Cincinnati, Ohio, AIAA Paper No. 85-1556.

- [37] Liu, C. H., Tavantzis, J. and Ting, L. (1984), "Numerical Studies of Motion of Vortex Filament-Implementing the Asymptotic Analysis", AIAA 17th Fluid Dynamics, Plasma Dynamics and Lasers Conference, Snowmass, Colorado, AIAA Paper 84-1542.
- [38] Liu, C. H., Ting, L. and Weston, R. P. (1986), "Boundary Conditions for Navier-Stokes Solution of the Merging of Vortex Filaments", Int. Symp. Compu. Fluid Dynamics, Tokyo, Japan.
- [39] Lu, L. J. (1987), Private Communications; Ph.D. Dissertation, Lehigh University.
- [40] Lu, L. J. and Smith, C. R. (1985), "Image Processing of Hydrogen Bubble Flow Visualization for Determination of Turbulence Statistics and Bursting Characteristics", Experiments in Fluids, Vol. 3, pp. 349-356.
- [41] Moin, P., Leonard, A. and Kim, J. (1986), "Evolution of a Curved Vortex Filament Into a Vortex Ring", The Physics of Fluids, Vol. 29, No. 4, pp. 955-963.
- [42] Moore, D. W. (1972), "Finite Amplitude Waves on Aircraft Trailing Vortices", Aeronautical Quarterly, Vol. 23, pp. 307-314.
- [43] Moore, D. W. and Saffman, P. G. (1972), "The Motion of a Vortex Filament with Axial Flow", Phil. Trans. Roy. Soc., Series A, Vol. 272, pp. 403-429.
- [44] Nychas, S. G., Hershey, H. C. and Brodkey, R. S., (1973), "A Visual Study of Turbulent Shear Flow", J. Fluid Mech., Vol. 61, pp. 513-540.
- [45] Offen, G. R. and Kline, S. J. (1973), "Experiments on the Velocity Characteristics of "Bursts" and in the Interactions Between the Inner and Outer Regions of a Turbulent Boundary Layer", Report MD-31, Stanford University.
- [46] Offen, G. R. and Kline, S. J. (1974), "Combined Dye-Streak and Hydrogen-Bubble Visual Observation of a Turbulent Boundary Layer", J. Fluid Mech., Vol. 62, pp. 223-239.
- [47] Offen, G. R. and Kline, S. J. (1975), "A Proposed Model of the Bursting Process in Turbulent Boundary Layers", J. Fluid Mech., Vol. 70, pp. 209-228.
- [48] Perry, A. E. and Chong, M. S. (1982), "On the Mechanisms of Wall Turbulence", J. Fluid Mech., Vol. 119, pp. 173-217.
- [49] Perry, A. E., Lim, T. T. and Teh, E. W. (1981), "A Visual Study of Turbulent Spots", J. Fluid Mech., Vol. 104, pp. 387-405.

- [50] Rosenhead, L. (1930), "The Spread of Vorticity in the Wake Behind a Cylinder", Proceedings of the Royal Society, Series A, Vol. 127, pp. 590-612.
- [51] Smith, C. R. (1978), "Visualization of Turbulent Boundary Layer Structure Using a Moving Hydrogen Bubble Wire Probe". Lehigh Workshop on Coherent Structure in Turbulent Boundary Layers, ed. C. R. Smith, D. E. Abbott, pp. 48-97.
- [52] Smith, C. R. (1984), "A Synthesized Model of the Near-Wall Behavior in Turbulent Boundary Layers", Proceedings of the 8th Biennial Symposium on Turbulence, ed. G. K. Patterson, J. L. Zakin, Dept. of Chem. Engrg., University of Missouri-Rolla.
- [53] Smith, C. R. and Metzler, S. P. (198), "The Characteristics of Low-Speed Streaks in the Near-Wall Region of a Turbulent Boundary Layer", J. Fluid Mech., Vol. 129, p. 27.
- [54] Tennekes, H. and Lumley, J. L. (1972), A First Course in Turbulence, MIT Press.
- [55] Theodersen, T. (1952), "Mechanism of Turbulence", Proc. 2nd Midwestern Conf. of Fluid Mechanics, Ohio State University, Columbus, Ohio.
- [56] Ting, L. and Tung, C. (1967), "Motion and Decay of a Vortex Ring", The Physics of Fluids, Vol. 10, pp. 901-910.
- [57] Walker, J.D.A. (1978), "The Boundary Layer Due to Rectilinear Vortex", Proc. R. Soc. Lond., A, Vol. 359, pp. 167-188.
- [58] Walker, J.D.A., Scharnhorst, R. K. and Weigand, G. G. (1986), "Wall Layer Models for the Calculation of Velocity and Heat Transfer in Turbulent Boundary Layers", AIAA 24th Aerospace Sciences Meeting, Reno, Nevada, AIAA Paper 86-0213.
- [59] Walker, J.D.A., Smith, C. R., Cerra, A. W. and Doligalski, T. L. (1987), "The Impact of a Vortex Ring on a Wall", J. Fluid Mech., in press.
- [60] Wallace, J. M. (1982), "On the Structure of Bounded Turbulent Shear Flow: A Personal View", Developments in Theoretical and Applied Mechanics, XI, T. J. Chung, G. R. Karr (eds.) Dept. of Mech. Engrg., University of Alabama in Huntsville, p. 509.
- [61] Weston, R. P., Ting, L. and Liu, C. H. (1986), "Numerical Studies of the Merging of Vortices", AIAA 24th Aerospace Sciences Meeting, Reno, Nevada, AIAA Paper No. 86-0557.

- [62] Widnall, S. E., Bliss, D. and Zelay, A. (1971), "Theoretical and Experimental Study of the Stability of a Vortex Pair", in Aircraft Wake Turbulence and Its Detection, Oslo, Goldberg and Rogers, (eds.), pp. 305-338.
- [63] Willmarth, W. W. and Tu, B. J. (1967), "Structure of Turbulence of the Boundary Layer Near the Wall", The Physics of Fluids, Suppl. Vol. 10, p. 3134.

APPENDIX A

In this appendix, it will be demonstrated that the anomalous behavior of the integrand in Moore's (1972) method which is depicted in Figure 2.3 for the circular ring may be associated with inaccuracy in the numerical differentiation. For a circular vortex ring, the position vector to any point on the ring may be written,

$$\vec{X}(s,t) = (R\cos\pi s, R\sin\pi s, Z_r), \quad -1 \leq s < 1, \quad (\text{A.1})$$

where $R = R(t)$, $Z_r = Z_r(t)$ are the dimensionless ring radius and normal distance from the wall. The first and second derivatives are,

$$\frac{\partial \vec{X}}{\partial s} = \pi \{-R\sin\pi s, R\cos\pi s, 0\}, \quad (\text{A.2})$$

$$\frac{\partial^2 \vec{X}}{\partial s^2} = \pi^2 \{-R\cos\pi s, -R\sin\pi s, 0\}. \quad (\text{A.3})$$

If \vec{X}_0 denotes the position vector to a point at $s = s_0$ on the vortex where the self-induced velocity of the vortex is to be evaluated, then

$$\vec{X}_0 - \vec{X} = \{R(\cos\pi s_0 - \cos\pi s), R(\sin\pi s_0 - \sin\pi s), 0\}. \quad (\text{A.4})$$

Suppose now that as a result of errors incurred in the numerical

differentiation, errors ϵ_1 and ϵ_2 occur in the evaluation of $\partial \vec{X}/\partial s$ and $\partial^2 \vec{X}/\partial s^2$ which have the following simple form,

$$\frac{\partial \vec{X}}{\partial s} = (\pi - \epsilon_1) \{-R \sin \pi s, R \cos \pi s, 0\}, \quad (A.5)$$

$$\frac{\partial^2 \vec{X}}{\partial s^2} = (\pi^2 - \epsilon_2) \{-R \cos \pi s, -R \sin \pi s, 0\}. \quad (A.6)$$

It is readily shown that,

$$\frac{\partial \vec{X}}{\partial s} \times \frac{(\vec{X}_0 - \vec{X})}{\{|\vec{X}_0 - \vec{X}|^2 + \mu^2\}^{3/2}} = \frac{(\pi - \epsilon_1) R^2 (1 - \cos \pi \Delta s)}{\{2 R^2 (1 - \cos \pi \Delta s) + \mu^2\}^{3/2}} \hat{k}, \quad (A.7)$$

where $\Delta s = s - s_0$ and \hat{k} is a unit vector in the z direction. Using equation (2.13), it may be shown that,

$$\frac{\partial \vec{X}}{\partial s} \times \frac{\partial^2 \vec{X}}{\partial s^2} P(s) = \frac{R^2 (\Delta s)^2 (\pi - \epsilon_1) (\pi^2 - \epsilon_2)}{2 \{R^2 (\Delta s)^2 (\pi - \epsilon_1)^2 + \mu^2\}^{3/2}} \hat{k}. \quad (A.8)$$

The Taylor series expansion of $\cos \pi \Delta s$ is

$$\cos \pi \Delta s = 1 - \frac{1}{2!} (\pi \Delta s)^2 + \frac{1}{4!} (\pi \Delta s)^4 + \dots, \quad (A.9)$$

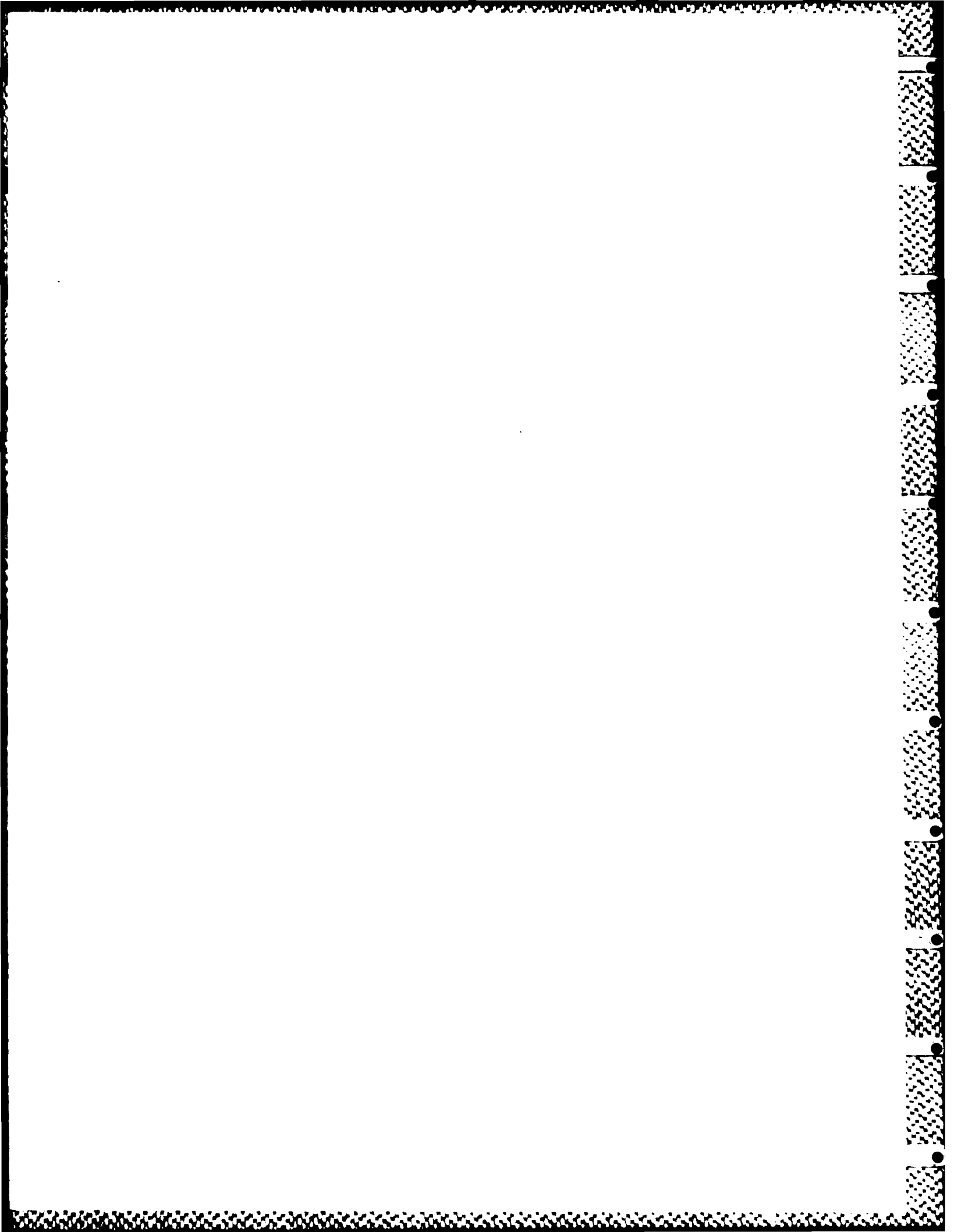
and assuming that $\mu^2 \ll \pi^2 R^2 \Delta s^2$ and that ϵ_1 and ϵ_2 are small, it may be shown that the difference I between equations (A.7) and (A.9) is,

$$I \sim \frac{1}{2 R \Delta s \pi} \left(-3 \epsilon_1 + \frac{\epsilon_2}{\pi} \right) + \frac{\pi^2 \Delta s}{4 R} + \dots. \quad (A.10)$$

It may be observed from equation (A.10) that if $\epsilon_1, \epsilon_2 = 0$,

$$I \rightarrow 0 \text{ as } \Delta s \rightarrow 0, \quad (\text{A.11})$$

which is the required behavior. On the other hand, if $\epsilon_1, \epsilon_2 \neq 0$, it may be observed that a large error for small Δs will occur in the evaluation of the integrand. Note that for $\epsilon_1 > 0$ (and $\epsilon_2 \leq 0$), the sign of the first term in equation (A.10) is different from the second term and the type of behavior depicted in Figure 2.3 will occur. It should be remarked that this analysis is heuristic and a complete error analysis was not carried out; the analysis in this Appendix is only an indication of the potential problems that may occur with Moore's (1972) method.



APPENDIX B

In this appendix, the details of the expansion of the integrand $R(s, s_0)$ in equation (2.18) are described. If s_0 denotes the location on the vortex where the self-induced velocity is being evaluated and s denotes any other location on the vortex, a Taylor series expansion of the position vector about s_0 is,

$$\begin{aligned} \vec{X}(s, t) = & \vec{X}(s_0, t) + (s-s_0) \left(\frac{\partial \vec{X}}{\partial s} \right)_0 + \frac{(s-s_0)^2}{2!} \left(\frac{\partial^2 \vec{X}}{\partial s^2} \right)_0 \\ & + \frac{(s-s_0)^3}{3!} \left(\frac{\partial^3 \vec{X}}{\partial s^3} \right)_0 + \dots, \end{aligned} \quad (B.1)$$

where the subscript 0 denotes that the derivative is evaluated at $s = s_0$; letting \vec{X}_0 denote $\vec{X}(s_0, t)$ it follows that

$$\vec{X}_0 - \vec{X} = - (s-s_0) \vec{X}'_0 - \frac{(s-s_0)^2}{2!} \vec{X}''_0 - \frac{(s-s_0)^3}{3!} \vec{X}'''_0 - \dots, \quad (B.2)$$

where a prime is used here to denote differentiation with respect to s . A similar expansion for $\partial \vec{X} / \partial s$ is,

$$\frac{\partial \vec{X}}{\partial s} = \vec{X}'_0 + (s-s_0) \vec{X}''_0 + \frac{(s-s_0)^2}{2!} \vec{X}'''_0 + \dots, \quad (B.3)$$

and consequently it is easily shown that,

$$\begin{aligned} \frac{\partial \vec{X}}{\partial s} \times (\vec{X}_0 - \vec{X}) &= \frac{1}{2} (s-s_0)^2 \vec{X}'_0 \times \vec{X}''_0 + \frac{1}{3} (s-s_0)^3 \vec{X}'_0 \times \vec{X}'''_0 \\ &+ \frac{(s-s_0)^4}{24} \{ 3\vec{X}''_0 \times \vec{X}''''_0 + 2\vec{X}'''_0 \times \vec{X}''''_0 \} + \dots \end{aligned} \quad (B.4)$$

In addition,

$$\begin{aligned} |\vec{X}_0 - \vec{X}|^2 &= (s-s_0)^2 \vec{X}'_0 \cdot \vec{X}'_0 + (s-s_0)^3 \vec{X}'_0 \cdot \vec{X}''_0 \\ &+ \frac{(s-s_0)^4}{12} \{ 3\vec{X}''_0 \cdot \vec{X}''_0 + 4\vec{X}'_0 \cdot \vec{X}'''_0 \} + \dots \end{aligned} \quad (B.5)$$

and the binomial expansion yields,

$$\begin{aligned} \{ |\vec{X}_0 - \vec{X}|^{2+\mu^2} \}^{-3/2} &= \alpha^{-3/2} \left[1 - \frac{3}{2\alpha} \{ (s-s_0)^3 \vec{X}'_0 \cdot \vec{X}''_0 \right. \\ &\left. + \frac{(s-s_0)^4}{12} (3\vec{X}''_0 \cdot \vec{X}''_0 + 4\vec{X}'_0 \cdot \vec{X}'''_0) \} + \dots \right], \end{aligned} \quad (B.6)$$

where,

$$\alpha = (s-s_0)^2 (\vec{X}'_0)^2 + \mu^2 \quad (B.7)$$

The expansion (B.6) is valid for $(s-s_0)$ sufficiently small.

An expression for the integrand for small $(s-s_0)$ given by equation (2.18) may now be obtained using equations (B.4) and (B.6); the result is,

$$R(s, s_0) = \vec{D}_3(s-s_0)^3 + \vec{D}_4(s-s_0)^4 + \dots, \quad (B.8)$$

where \vec{D}_3 and \vec{D}_4 are defined by,

$$\begin{aligned} \vec{D}_3 &= \frac{1}{3\alpha^{3/2}} \vec{X}'_0 \times \vec{X}'''_0 \\ &- \frac{3}{4\alpha^{5/2}} (\vec{X}'_0 \cdot \vec{X}''_0) (\vec{X}'_0 \times \vec{X}_0) (s-s_0)^2 + \dots, \end{aligned} \quad (B.9)$$

$$\begin{aligned} \vec{D}_4 &= \frac{1}{24\alpha^{3/2}} \{ 3\vec{X}'_0 \times \vec{X}''''_0 + 2\vec{X}''_0 \times \vec{X}'''_0 \} \\ &- \frac{1}{2\alpha^{5/2}} (\vec{X}'_0 \cdot \vec{X}''_0) (\vec{X}'_0 \times \vec{X}'''_0) (s-s_0)^2 \\ &- \frac{1}{16\alpha^{5/2}} (3\vec{X}''_0 \cdot \vec{X}''_0 + 4\vec{X}'_0 \cdot \vec{X}'''_0 \times \vec{X}'_0 \times \vec{X}''_0) (s-s_0)^2 + \dots. \end{aligned} \quad (B.10)$$

END

FEB.

1988

DTIC